

From pixels to puddles

Mapping surface melt on Antarctic ice shelves using satellite data and deep learning

de Roda Husman, S.

DOI

[10.4233/uuid:1d730e39-7f52-416c-bf0f-3c81a8af2ad5](https://doi.org/10.4233/uuid:1d730e39-7f52-416c-bf0f-3c81a8af2ad5)

Publication date

2025

Document Version

Final published version

Citation (APA)

de Roda Husman, S. (2025). *From pixels to puddles: Mapping surface melt on Antarctic ice shelves using satellite data and deep learning*. [Dissertation (TU Delft), Delft University of Technology]. <https://doi.org/10.4233/uuid:1d730e39-7f52-416c-bf0f-3c81a8af2ad5>

Important note

To cite this publication, please use the final published version (if applicable).
Please check the document version above.

Copyright

Other than for strictly personal use, it is not permitted to download, forward or distribute the text or part of it, without the consent of the author(s) and/or copyright holder(s), unless the work is under an open content license such as Creative Commons.

Takedown policy

Please contact us and provide details if you believe this document breaches copyrights.
We will remove access to the work immediately and investigate your claim.

Sophie de Roda Husman

From Pixels to Puddles

Mapping Surface Melt on
Antarctic Ice Shelves
using Satellite Data and
Deep Learning

FROM PIXELS TO PUDDLES

**MAPPING SURFACE MELT ON ANTARCTIC ICE SHELVES
USING SATELLITE DATA AND DEEP LEARNING**

Dissertation

for the purpose of obtaining the degree of doctor
at Delft University of Technology
by the authority of the Rector Magnificus, prof. dr. ir. T.H.J.J. van der Hagen,
chair of the Board for Doctorates
to be defended publicly on
Wednesday 22 January 2025 at 12:30 o'clock

by

Sophie DE RODA HUSMAN

Master of Science in Civil Engineering,
Delft University of Technology, The Netherlands,
born in Amsterdam, The Netherlands.

This dissertation has been approved by the promotors.

Composition of the doctoral committee:

| | |
|---------------------------------|---|
| Rector Magnificus, | chairperson |
| Prof. dr.-ing. habil. R. Klees, | Delft University of Technology, <i>promotor</i> |
| Dr. ir. B. Wouters, | Delft University of Technology, <i>copromotor</i> |
| Dr. ir. S.L.M. Lhermitte, | Katholieke Universiteit Leuven, Belgium, Delft University of Technology, <i>copromotor</i> |

Independent members:

| | |
|------------------------------------|---|
| Prof. dr. J.L. Bamber, | University of Bristol, United Kingdom |
| Prof. dr. M.R. van den Broeke, | Utrecht University |
| Dr. R. Datta, | Delft University of Technology |
| Prof. dr. ir. R.F. Hanssen, | Delft University of Technology |
| Prof. dr. ir. H.W.J. Russchenberg, | Delft University of Technology, <i>reserve member</i> |

This work was made possible by the Geoscience & Remote Sensing department of Delft University of Technology and is part of the HiRISE consortium, funded by the Netherlands Organization for Scientific Research (NWO).



Keywords: Antarctica, surface melt, ice shelves, remote sensing, deep learning

Printed by: Ridderprint | www.ridderprint.nl

Cover by: Studio Nina van Tuikwerd | www.ninavantuiikwerd.com

Copyright © 2025 by S. de Roda Husman

An electronic copy of this dissertation is available at
<https://repository.tudelft.nl/>.

I don't necessarily agree with everything I say.

Marshall McLuhan



CONTENTS

| | |
|--|-------------|
| Summary | ix |
| Samenvatting | xi |
| Preface | xiii |
| Acknowledgements | xv |
| 1 Introduction | 1 |
| 1.1 Distant land with close-to-home impacts | 2 |
| 1.2 The role of ice shelves in a warming climate | 3 |
| 1.3 Impact of surface melt on ice shelves | 5 |
| 1.4 Surface melt mapping using satellite observations | 8 |
| 1.5 Deep Learning and cloud computing in the big data realm | 10 |
| 1.6 Identifying and filling research gaps | 12 |
| 1.7 Structure of this dissertation | 15 |
| 2 Remote sensing of surface melt on Antarctica | 21 |
| 2.1 Introduction | 23 |
| 2.2 Background and related research | 25 |
| 2.3 Data | 28 |
| 2.3.1 Study area | 28 |
| 2.3.2 Satellite imagery | 28 |
| 2.3.3 Weather stations | 29 |
| 2.3.4 Precipitation data | 29 |
| 2.3.5 Sea ice concentration | 29 |
| 2.3.6 Contour lines | 30 |
| 2.4 Methods | 30 |
| 2.4.1 Melt detection methods | 30 |
| 2.4.2 Sensitivity studies | 32 |
| 2.5 Results | 34 |
| 2.5.1 Data availability | 34 |
| 2.5.2 Spatiotemporal sensitivity | 36 |
| 2.5.3 Overpass time sensitivity | 42 |
| 2.5.4 Sensitivity to liquid water | 42 |
| 2.5.5 Melt detection algorithm sensitivity | 44 |
| 2.6 Discussion | 44 |
| 2.6.1 Opportunities and challenges: perspectives of sensor characteristics | 44 |
| 2.6.2 Opportunities and challenges: perspectives of applied methods | 46 |

| | | |
|----------|---|-----------|
| 2.7 | Conclusions | 49 |
| 2.8 | Supplementary materials | 50 |
| 3 | A high-resolution Antarctic melting record | 59 |
| 3.1 | Introduction | 61 |
| 3.2 | Materials and methods | 63 |
| 3.2.1 | Study area | 63 |
| 3.2.2 | Melt masks | 64 |
| 3.2.3 | U-Net architecture | 65 |
| 3.2.4 | Preprocessing | 67 |
| 3.2.5 | Training, validation, and testing data | 71 |
| 3.2.6 | Post-processing | 71 |
| 3.2.7 | Accuracy assessment | 71 |
| 3.3 | Results | 72 |
| 3.3.1 | Surface melt over Shackleton Ice Shelf | 73 |
| 3.3.2 | Surface melt over Larsen C Ice Shelf | 76 |
| 3.3.3 | Antarctic-wide surface melt | 78 |
| 3.4 | Discussion | 80 |
| 3.4.1 | Opportunities of UMelt | 80 |
| 3.4.2 | Limitations of UMelt | 81 |
| 3.4.3 | Implications of selected training region | 82 |
| 3.4.4 | Implications of selected reference data | 83 |
| 3.4.5 | Downscaling other surface melt products | 84 |
| 3.5 | Conclusion | 84 |
| 3.6 | Supplementary materials | 86 |
| 4 | Downscaling of Antarctic surface melt volumes | 95 |
| 4.1 | Introduction | 97 |
| 4.2 | Data | 98 |
| 4.2.1 | RACMO 27 km and 5.5 km | 98 |
| 4.2.2 | Physical constraints | 100 |
| 4.2.3 | Validation data | 101 |
| 4.3 | Methods | 102 |
| 4.3.1 | Preprocessing | 102 |
| 4.3.2 | SUPREME model architecture | 103 |
| 4.3.3 | Training | 105 |
| 4.3.4 | Post-processing | 105 |
| 4.3.5 | Evaluation | 106 |
| 4.4 | Results | 106 |
| 4.4.1 | Performance on testing dataset | 107 |
| 4.4.2 | Comparison of SUPREME and RACMO 27 km | 108 |
| 4.4.3 | Comparison of SUPREME and AWS | 111 |
| 4.4.4 | Comparison of SUPREME and other surface melt products | 112 |
| 4.4.5 | Importance of physical constraints | 116 |
| 4.5 | Discussion | 118 |
| 4.6 | Conclusion | 120 |

| | | |
|----------|--|------------|
| 4.7 | Supplementary Materials | 121 |
| 5 | Seasonal evolution of Antarctic meltwater lakes | 133 |
| 5.1 | Introduction | 135 |
| 5.2 | Data and methods | 136 |
| 5.2.1 | Identifying locations of lakes | 136 |
| 5.2.2 | Sentinel-1 time series | 140 |
| 5.2.3 | Developing ConvLSTM model on Greenland Ice Sheet | 140 |
| 5.2.4 | Assessing sensitivity of ConvLSTM model | 142 |
| 5.2.5 | Applying ConvLSTM model on Antarctic Ice Sheet | 142 |
| 5.2.6 | Supraglacial lake and ice shelf parameters | 142 |
| 5.3 | Results | 142 |
| 5.3.1 | Testing the developed ConvLSTM | 142 |
| 5.3.2 | Predicted refreezing and draining lakes on Antarctica | 144 |
| 5.3.3 | Relation of refreezing and draining lakes to lake and ice shelf parameters | 146 |
| 5.4 | Discussion | 147 |
| 5.4.1 | From proof of concept to operational product | 147 |
| 5.4.2 | Greenland as training domain for predicting lake evolution on Antarctica | 148 |
| 5.4.3 | Inherent limitations of our model | 149 |
| 5.5 | Conclusion | 150 |
| 6 | Outlook | 155 |
| 6.1 | From where we were... | 156 |
| 6.2 | ... to where we are now | 157 |
| 6.2.1 | Summary of this research | 157 |
| 6.2.2 | Where the field stands today | 158 |
| 6.3 | ... and where to go from here | 158 |
| 6.3.1 | From surface melt extent to surface melt volume | 159 |
| 6.3.2 | Impact of detected lake drainages on ice shelf stability | 160 |
| 6.3.3 | Sensitivity of ice shelves to a changing climate | 161 |
| | Code and data availability | 167 |
| | List of publications | 169 |
| | Conference contributions | 171 |
| | Media coverage | 173 |
| | Curriculum Vitae | 175 |

SUMMARY

ANTARCTICA, the coldest, windiest, and most remote continent on our planet, plays a crucial role in the global climate system. Its ice mass loss is a major driver of rising sea levels, with projections indicating a potential rise of several meters in the coming centuries. However, there remains considerable uncertainty about the future trajectory of Antarctic mass loss. A major area of uncertainty is the fate of ice shelves—floating extensions of land ice that surround much of Antarctica and act as barriers, slowing the flow of glaciers into the ocean. Ice shelves are affected by warm water from below, which thins them and increases their vulnerability to cracking, as well as by warm air from above, which melts the surface and forms ponds of meltwater.

This research focuses on surface melt, a phenomenon where meltwater forms and either refreezes or accumulates on the ice shelf surface. When the water accumulates, it can seep into cracks, causing them to deepen and widen, which can weaken the ice shelves. In today's era of abundant satellite imagery and advanced deep learning techniques, we can efficiently process large volumes of data, enabling more comprehensive research on surface melt dynamics. The aim of this dissertation is to enhance the mapping and understanding of surface meltwater on Antarctic ice shelves using remote sensing and deep learning methods.

The introductory chapter provides an overview of the Antarctic Ice Sheet, emphasizing the continent's immense scale and importance. Written in an accessible style, it presents key concepts about Antarctica and explores how ice shelves and surface melt influence the continent. The chapter also describes the use of satellite data to map surface melt and discusses advancements in computational resources and deep learning, which have significantly improved our ability to analyze the expanding catalog of satellite data. It concludes with an overview of the research questions addressed in the thesis.

In the second chapter, various remote sensing datasets are compared to illustrate how and why satellite observations of surface melt differ. Using state-of-the-art melt detection algorithms, we analyze surface melt patterns and observe large differences, especially in icy areas, regions with subsurface melt, and during winter. These differences arise from factors such as satellite overpass times, spatial resolution, signal penetration, cloud cover, and detection methods. Despite these challenges, the variations create opportunities to combine data from multiple satellites, enhancing the overall accuracy of surface melt detection across Antarctica.

The third chapter builds on the previous findings and addresses the challenge of balancing spatial and temporal resolution in satellite observations. Surface melt in Antarctica is highly dynamic and varies regionally, making high-resolution mapping essential. To tackle this, we develop UMelt, a surface melt dataset for all Antarctic ice shelves with high spatial (500 m) and temporal (12 h) resolution, covering the period from 2016 to 2021. Our deep learning model integrates data from multiple satellites, allowing for de-

tailed detection of surface melt while maintaining high temporal resolution. UMelt offers the potential for new insights into how ice shelves respond to changing atmospheric conditions.

In the fourth chapter, we shift from mapping the presence of surface melt to estimating its volume. Since surface melt is mainly driven by local processes, high-resolution regional climate models (RCMs) are necessary. However, current RCMs have a coarse resolution (25–30 km) that is insufficient for capturing small-scale melt processes. To address this, we introduce SUPREME, a deep learning method that downscales surface melt to 5.5 km resolution using a physically-informed super-resolution model. This model combines remote sensing data on albedo and elevation with a 27 km resolution Regional Atmospheric Climate Model (RACMO), accounting for the diverse drivers of surface melt across Antarctica. SUPREME demonstrates the potential of super-resolution techniques with physical constraints for high-resolution surface melt mapping, providing valuable insights into localized melting patterns.

The fifth chapter examines the hydrology of surface meltwater lakes on Antarctica, investigating whether they refreeze or drain into fractures at the end of the melt season, potentially destabilizing ice shelves. Monitoring these lakes with optical satellite imagery is often limited by cloud cover, complicating the tracking of their changes over time. To overcome this, we develop a spatiotemporal deep learning model using radar imagery from Sentinel-1, which allows us to classify the evolution of meltwater lakes regardless of cloud conditions. Our findings reveal no clear connections between lake evolution and ice shelf parameters, highlighting the need for further research and model refinement. The study is an initial step in using deep learning and Sentinel-1 data to monitor the evolution of supraglacial lakes on Antarctic ice shelves.

The sixth and final chapter reflects on the research and outlines future directions. It begins by summarizing the state of Antarctic surface melt research at the start of my PhD. The chapter then highlights the key contributions of this thesis and concludes with three proposed research ideas aimed at advancing our understanding of surface melt processes in Antarctica.

SAMENVATTING

ANTARCTICA, het koudste, winderigste en meest afgelegen continent op onze planeet, speelt een cruciale rol in het mondiale klimaatstelsel. Het massaverlies van Antarctica is een belangrijke oorzaak van de verwachte wereldwijde zeespiegelstijging. Er is echter grote onzekerheid over hoe het massaverlies van Antarctica zich in de toekomst zal ontwikkelen. Dit is vooral te wijten aan het moeilijk te voorspellen lot van de ijsplaten, drijvende uitlopers van landijs die een groot deel van Antarctica omringen en fungeren als barrières die de stroom van gletsjers naar de oceaan vertragen. Ijsplaten worden zowel van onderaf beïnvloed door warm water, waardoor ze dunner worden en kwetsbaarder voor scheuren, als van bovenaf door warme lucht, die het oppervlak doet smelten.

Dit proefschrift richt zich op oppervlaktesmelt, waarbij smeltwater wordt gevormd dat ofwel opnieuw bevriest of zich verzamelt op het oppervlak van de ijsplaat. Wanneer het water zich verzamelt, kan het in scheuren sijpelen, waardoor deze dieper en breder worden, wat de ijsplaten kan verzwakken. Dankzij de beschikbaarheid van satellietbeelden en geavanceerde deep learning-technieken kunnen we grote hoeveelheden data efficiënt verwerken, wat uitgebreid onderzoek naar het smeltgedrag aan het ijsoppervlak mogelijk maakt. Het doel van dit proefschrift is om smeltwater op het oppervlak van Antarctica beter in kaart te brengen en te analyseren.

Het inleidende hoofdstuk geeft een overzicht van de Antarctische ijskap en benadrukt de immense schaal en het cruciale belang van dit continent. Het is geschreven in een toegankelijke stijl en introduceert belangrijke concepten over het continent, de rol van ijsplaten en het smelten van het ijsoppervlak. Daarnaast wordt beschreven hoe satellietdata worden gebruikt om oppervlaktesmelt in kaart te brengen en hoe deep learning de analyse van deze data heeft verbeterd. Het hoofdstuk sluit af met een overzicht van de onderzoeksvragen die in dit proefschrift worden behandeld.

In het tweede hoofdstuk worden data van verschillende satellieten vergeleken om te illustreren hoe en waarom data van oppervlaktesmelt verschillen. Met behulp van geavanceerde algoritmen voor smeltdetectie analyseren we smelt patronen, en vinden we grote verschillen in ijzige gebieden, regio's met smelt onder het oppervlak, en tijdens de winter. Deze verschillen zijn het gevolg van factoren zoals de overvliegtijden van de satellieten, ruimtelijke resolutie, dieptebereik van het satelliet signaal, bewolking en detectiemethoden. De verschillen in smeltdetectie bieden echter ook mogelijkheden om data van meerdere satellieten te combineren, waardoor de algehele nauwkeurigheid van de detectie van oppervlaktesmelt op Antarctica kan worden verbeterd.

Het derde hoofdstuk bouwt voort op de vorige bevindingen en gaat in op de uitdaging om een evenwicht te vinden tussen de ruimtelijke en temporele resolutie van satellietdata. Oppervlaktesmelt in Antarctica is zeer dynamisch en varieert regionaal, waardoor het belangrijk is het smelten met een hoge resolutie in kaart te brengen. In dit hoofdstuk

ontwikkelen we UMelt, een dataset voor oppervlaktesmelt voor alle Antarctische ijsplaten met een hoge ruimtelijke (500 m) en temporele (12 uur) resolutie, voor de periode van 2016 tot 2021. Ons deep learning-model integreert data van meerdere satellieten, waardoor oppervlaktesmelt gedetailleerd kan worden gedetecteerd met behoud van een hoge temporele resolutie. UMelt biedt nieuwe mogelijkheden om te begrijpen hoe ijsplaten reageren op veranderingen in atmosferische omstandigheden.

In het vierde hoofdstuk gaan we over van het in kaart brengen van de aanwezigheid van oppervlaktesmelt naar het bepalen van het smeltwatervolume. Oppervlaktesmelt wordt voornamelijk beïnvloed door lokale processen, waardoor regionale klimaatmodellen (RCM's) met een hoge resolutie nodig zijn. De huidige RCM's hebben echter een te lage ruimtelijke resolutie (25–30 km) om lokale smeltprocessen nauwkeurig in kaart te brengen. Daarom introduceren we SUPREME, een deep learning-methode die oppervlaktesmelt afschaalt naar een resolutie van 5.5 km met behulp van een fysisch onderbouwd superresolutie model. Dit model combineert satellietgegevens van albedo en hoogte met een regionaal atmosferisch klimaatmodel (RACMO) met een resolutie van 27 km, zodat de diverse factoren die de oppervlaktesmelt in Antarctica beïnvloeden worden meegenomen. SUPREME laat zien hoe superresolutie technieken met fysische randvoorwaarden kunnen worden toegepast om oppervlaktesmelt in hoge resolutie in kaart te brengen, wat waardevolle inzichten oplevert in lokale smeltpatronen.

Het vijfde hoofdstuk onderzoekt de hydrologie van smeltwatermeren in Antarctica en bekijkt of ze aan het einde van een smeltseizoen dichtvriezen of in scheuren in the ijs wegsijpelen, waardoor ijsplaten mogelijk instabiel kunnen worden. Het monitoren van deze meren met optische satellietbeelden is vaak beperkt door bewolking. Daarom ontwikkelen we een spatiotemporeel deep learning-model op basis van radarbeelden van Sentinel-1, waarmee we de evolutie van smeltwatermeren kunnen classificeren, ongeacht de bewolking. Onze resultaten tonen geen duidelijke verbanden tussen de evolutie van de meren en de eigenschappen van de ijsplaten, wat de noodzaak voor verder onderzoek en verfijning van het model benadrukt. De studie is een eerste stap in het gebruik van deep learning en Sentinel-1 data om de evolutie van smeltwatermeren op Antarctische ijsplaten te monitoren.

Het zesde en laatste hoofdstuk reflecteert op het verloop van het onderzoek en schetst perspectieven. Het begint met een overzicht van de staat van onderzoek naar Antarctische oppervlaktesmelt bij de aanvang van mijn proefschrift. Het hoofdstuk belicht vervolgens de belangrijkste wetenschappelijke bijdragen van dit proefschrift en sluit af met drie onderzoeksvoorstellen om ons begrip van de smeltprocessen in Antarctica te vergroten.

PREFACE

Sometimes you just need to distance yourself to see things more clearly.

This idea resonates deeply in the context of my dissertation. While Antarctica remains unexplored territory for me, and likely for you as well (given that only around one million out of eight billion people on Earth have been there, roughly translating to 0.01% of the global population), there's no cause for concern. Even from the confines of our desks, we have the opportunity to study Antarctica, perhaps even more effectively than if we were in the field. Seated at our desks, we can zoom out, draw comparisons over time and space, utilizing satellite data spanning the last 50 years, navigating across the pixels constituting the vast 14,000,000 km² known as the Antarctic Ice Sheet.

In this dissertation, I have delved into what I like best: translating satellite data into meaningful insights, data that resonate with us as human beings. These data products go beyond the confines of binary computer language. Allow me to present to you “From Pixels to Puddles: Mapping Surface Melt on Antarctic Ice Shelves using Satellite Data and Deep Learning”. From my desk to yours, I hope you enjoy it!

*Sophie de Roda Husman
Delft, December 2024*

ACKNOWLEDGEMENTS

I'll admit: when it comes to most PhD theses, the acknowledgments are often the only section I read. They offer a rare glimpse into the person behind the research—a reminder that every publication, booklet, and review has a human story behind it. That's why I'm glad to share my story here, which is really a collection of heartfelt thank-yous and messages of gratitude to the people who supported me along the way. In many ways, it feels absurd that my name alone is on the cover of this booklet. In truth, it should be filled from front to back with the names of everyone who made these roughly 200 pages possible. Oh and just a heads-up: I'm all about emotional speeches, love letters, sweeping drama, and everything sentimental. I realize not everyone shares that enthusiasm, so consider this your gentle warning if my acknowledgments come across as a little over the top!

It all began with an invitation to a job interview on 7 September 2020. My interviewers—and now PhD supervisors and copromotors—Bert and Stef, were inspiring from the very start: enthusiastic, empathetic, open-minded, incredibly smart, and the list of their qualities could go on. I want to thank them for the four-year rollercoaster that began on 1 January 2021, which was so much more than the 94 (and counting!) meetings. **Stef**, thank you for your (sometimes quirky!) metaphors and (always inspirational!) quotes, as well as the late-night deep discussions—whether at your BBQ, during EGU, or in No-orderheijde—that truly shaped me. Your ability to inspire scientists to be more than just their publications and to become well-rounded professionals was both motivating and admirable (see proposition 8 as proof!). **Bert**, thank you for always keeping your door open. Somehow, despite your overflowing agenda, you manage to make time for everyone. Your thoughtfulness—remembering birthdays, giving meaningful Christmas gifts like a beautiful book, or offering a reassuring wink during tough presentations—gave me so much confidence and lifted my spirits. There were times when I doubted whether a PhD was the right path for me, but both of you made sure I always knew I was exactly where I belonged.

Thank you, **Roland**, my promotor, for all your faith in me. While we sometimes disagreed, you always gave me the time to express my thoughts, share my opinions, and explore different perspectives. I truly appreciate all your help, especially during the final stages of my PhD. Knowing I could fully trust you and count on your unwavering support made all the difference in crossing the finish line.

A deep thank you also goes to my committee. Thanks to **Jonathan, Michiel, Tri, Ramon**, and **Herman**. As we work in the same country and/or field, I have had the pleasure of meeting you over the past few years. Each of you has been such an inspiration, and I consider it an incredible honor that you agreed to be part of my committee.

A very special thanks goes to the students I had the opportunity to work with. Thank you, **Gillis, Marijn, Wytse, Adriaan, Julius, Meike**, and **Fenia**. It was such a joy to actively

collaborate with you in gaining a better understanding of Antarctica, and you may all recognize parts of your work in this dissertation.

To the technical and support staff, our work would not be possible without you. **Natasha, Debbie, Cindy, Suzanne, Lidwien, Mariska, and Josien**, thank you for always keeping your door open. A special thank you to Natascha. On a particularly difficult day, I came into your office feeling overwhelmed. You calmly guided me to a chair, closed the door, and kept bringing me tea until I felt better. I'm so grateful for that, and for all the fun and laughter we shared along the way. **Niels**, thank you for your support when I was struggling with VRLab. You can't imagine how much your statement—"You are not leaving this office until we have fixed this issue"—meant to me.

My officemates were truly indispensable on this journey. Let me begin with two very special officemates, **Maike** and **Wietske**, my paranims. Now that Wietske is in China and Maike is splitting her time between Brussels and Antarctica, I realize more than ever how valuable you are. You made my office days so much more enjoyable, and beyond the office, you've become such dear friends. I'm beyond grateful for all our adventures together, from Herkingen to the Grand Canyon, the Phoenixstraat to Labs, and from Vienna to Newcastle. A warm thank you also goes to the Cozy Cocktail Complexes, which, along with Maike and Wietske, also included **Valerie** and **Ann-Sofie**. Our dinner and cocktail evenings were always a blessing. Thanks to **all my GRS colleagues**, too. I've had the pleasure of meeting so many fantastic people over the past four years. As we move beyond the Covid years, our group has only grown closer, and it's been truly wonderful to be part of it. Also, a big thank you to the colleagues at the **AI4EO lab** in Munich for hosting me during my research stay in early 2024.

A big thank you to the HiRISE consortium, including **Aimée, Ann-Sofie, Bert, Carleen, Dewi, Erwin, Frank, Franka, Javier, Jeemijn, Maike, Maurice, Michiel, Paul, Peter, Sanne, Shashwat, Stef, and Willem Jan**. I truly enjoyed working with all of you and feeling like part of such an incredible team. Our getaway to Noorderheijde, a magical spot in the Veluwe, was undoubtedly the highlight of my PhD.

Thanks to all the contributors to the publications I (co-)authored during my PhD. A special shout-out to **Zhongyang, Becky, Jordi, Marijn, Valeria, Peter, and Shashwat**. You were all such inspiring, supportive, and incredibly pleasant people to work with.

A heartfelt thank you to all the science friends I've met along the way. To my **Karthus** friends, thank you for an unforgettable time at the summer school in May 2023 and for all the wonderful encounters that followed. A special shout-out to **Meghan**, a truly warm-hearted and one-of-a-kind person. I'll never forget the half-marathon in Beaujolais with Karthus friends **Maxence, Flo, Jan, Mikkil, Niklas, and Rebekka**—stopping for wine and cheese every few minutes, all while dressed as penguins. I probably laughed more that day than I ever thought possible! A big thanks as well to the conference friends I kept running into, including **Alex, Raf, Kali, Ben, and Andrew**. You were all fantastic conference buddies, and I thoroughly enjoyed getting to know each of you.

And of course, a huge thank you to all my non-science friends. To **Yordi, Sophie, Fox, Mitchel, and Ayla**—thank you for the endless board games, the crazy sports adventures, and the unforgettable holidays from Limburg to Flachau. To Club Aubi—**Moffel, Room, Maart, Sos, Ei, Meyk, Aggie**—thank you for so much more than just the aubi's. Every time I see you, I leave feeling energized and full of joy. A heartfelt thanks to **Kasteel**

Oosteinde, my Delft brothers and sisters, and to **B122** and the **Goudvisjes** for all the incredible adventures. To **Anna**, thank you for being such a wonderful friend, someone with whom I can share absolutely anything. To my friends from way, way back, **Nena**, you have a way of understanding me with just half a word; **Iris**, **Kim**, **Merlijn**, it means the world to me that we're forever connected. **Nina**, we became friends more than twenty years ago, and it means so much to me that you were willing to create the cover for this booklet. Thank you, **Maxim**, for always being there. I feel completely myself when I'm with you. Thank you for walking (99% of) the Pieterpad, for all our adventures from Tübingen to Croatia, for those cozy pyjama days with sushi and yoga, and for the random calls. I am beyond grateful for our friendship.

Finally, a heartfelt word of thanks to my family. First, to **my parents**, who have always been there to offer support whenever I needed it. Thanks to **Rob** and **Mariska** for bringing so much happiness into the life of my mom and dad. A thousand thanks to **Hannah**, my little sister who is wiser than me in so many ways. Thank you for supporting me through both the big and small challenges life throws at us. Special shout-out to your voice messages—always random, chaotic, and yet never failing to brighten my day. Thank you to my **mis abuelos**. My opa passed away during my PhD, but I have so many warm memories of him, from hugging trees to the fun rides in my little red car. Thanks to my oma, the most knowledgeable person I know. You are simply fantastic! A huge thank you to the **van Dijkjes** for welcoming me with open arms and including me in your cherished traditions. The Sinterklaas poems and yearly Texel trips, which I once thought might get repetitive, have turned into the highlights of my year. And last but not least, thank you, thank you, thank you to **Mathijs**. Life is so much more fun with you! I treasure all our big and small adventures, and the daily races down the stairs followed by a hug when one of us comes home are proof that you are truly my “lievelings”.

1

INTRODUCTION

This chapter was written to introduce the topics of this dissertation to the general public. Therefore, the language used in this chapter is different from the language used in Chapters 2–5, each containing an academic introduction to their contents.

1.1. DISTANT LAND WITH CLOSE-TO-HOME IMPACTS

ANTARCTICA stands as a challenging concept to fathom—a place of extreme remoteness and isolation on our densely populated planet. Spanning an immense territory approximately 1.5 times the size of Europe, it ranks among the most extraordinary places on Earth.

As someone who has never set foot on Antarctica but has spent hours studying satellite images, let me attempt to describe what this remote continent looks like. The continent's foundation, contrary to popular belief that Antarctica consists of solely ice, is a bedrock resembling a rugged mountain range (Figure 1.1a). Atop the bedrock, an impressive layer of ice covers 98% of the surface, averaging 2160 meters thick (Figure 1.1b). Traveling across the Antarctic Ice Sheet—using Google Earth in my case—your gaze will mostly be met by this layer of ice, interrupted only occasionally by isolated rock outcrops. This immense mass of ice that covers the continent's bedrock is what we refer to as an ice sheet.

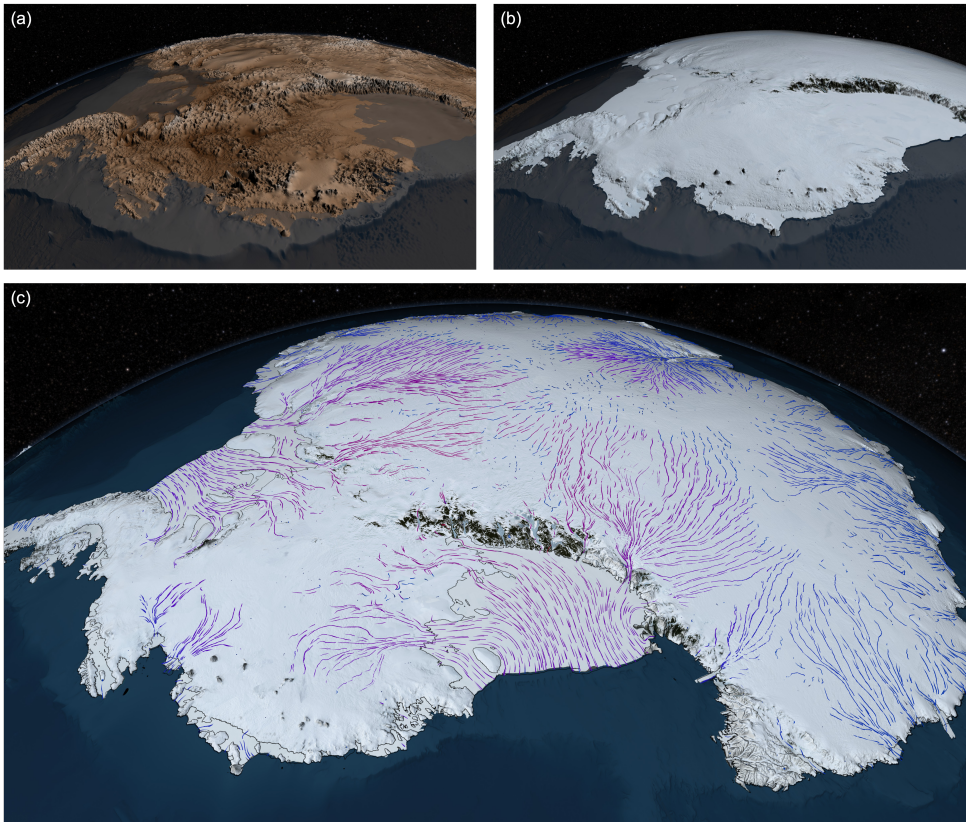


Figure 1.1: Topography and motion of Antarctica. (a) Bed topography, (b) surface elevation, and (c) flow lines illustrating ice sheet motion. Flow lines are color-coded by velocity, with pink indicating faster flows and blue indicating slower flows. Data is from BEDMAP2, visualizations are from NASA's Goddard Space Flight Center Scientific Visualization Studio.

Antarctica is not just a static ice cube; much of its ice constantly flows towards the ocean under its own weight (Figure 1.1c). Moving away from the ice sheet towards the ocean, you encounter the result of this constant movement – floating ice shelves (Figure 1.2). Ice shelves, some of them being the size of France, are attached to the land-based ice and rest on the ocean's waters. They are anchored by lateral mountains and grounding points in the ocean and can therefore provide a 'buttressing' force, acting as barriers that hold back land-based ice. The ice shelves fringe approximately 75% of Antarctica's 17,968-kilometer coastline (Rignot *et al.*, 2013), roughly the distance from the Netherlands to New Zealand.

Throughout history, Antarctica has been referred to as the 'sleeping giant'. Compared to the only other significant ice sheet on Earth, the Greenland Ice Sheet, Antarctica has shown less mass loss. Between 2002 and 2023, the Greenland Ice Sheet experienced a noticeable decrease in mass, averaging 270 billion metric tons of ice lost per year, contributing to a global sea level rise of 0.8 millimeters annually (NASA, 2023). In contrast, Antarctica experienced only half of Greenland's mass loss during the same period.

Nevertheless, when focusing on the coming centuries, the sea level contribution due to mass loss from the Antarctic Ice Sheet is extensive, holding the capacity to significantly shape Earth's climate. Antarctica has the remarkable potential to elevate sea levels by an astounding 57 meters (Swithinbank, 1988). It is worth noting that the complete disappearance of Antarctica is not a projection within the foreseeable centuries, if ever. However, the latest Intergovernmental Panel on Climate Change (IPCC) report estimates that the Antarctic Ice Sheet could contribute to a sea level rise of more than a meter by 2100 and more than 15 meters by 2500, if emissions continue without restraint (IPCC, 2023).

The potential sea level rise from Antarctica is particularly significant for countries like the Netherlands. Not only does a third of the Netherlands lie below sea level, making it vulnerable to rising seas, but also because Antarctica's massive ice sheet exerts a gravitational pull that currently holds water away from the northern hemisphere. As Antarctica melts, its gravitational pull weakens, paradoxically causing sea levels near Antarctica to decrease. As a result, waters far from Antarctica, such as the North Sea, rise more than the global average. This underscores the far-reaching consequences of Antarctica's mass loss on countries like the Netherlands. Despite being distant, Antarctica's impact hits close to home.

1.2. THE ROLE OF ICE SHELVES IN A WARMING CLIMATE

The greatest uncertainty in forecasting global sea level rise comes from Antarctica's ice loss (IPCC, 2023). This uncertainty primarily stems from the unknown future of Antarctica's approximately 300 ice shelves (Figure 1.2). As previously explained, ice shelves buttress the land-based ice; acting as a 'band-aid', they prevent Antarctica from 'bleeding' ice into the oceans.

Similar to land-based ice, ice shelves are constantly in motion. For an ice shelf in equilibrium, growth occurs from the incoming ice flow from the ice sheet and snowfall on its surface. Deterioration occurs as ice calves off at its edges, a cycle

comparable to the continuous renewal and shedding of fingernails. This natural cycle of replenishment and calving helps maintain their size relatively constant over the long term. However, in recent decades, the warming ocean and atmosphere have destabilized Antarctica's ice shelves, resulting in thinner and weaker structures. It was recently reported that more than 40% of Antarctica's ice shelves have been shrinking since 1997, with nearly half showing no signs of recovery (Davison *et al.*, 2023).

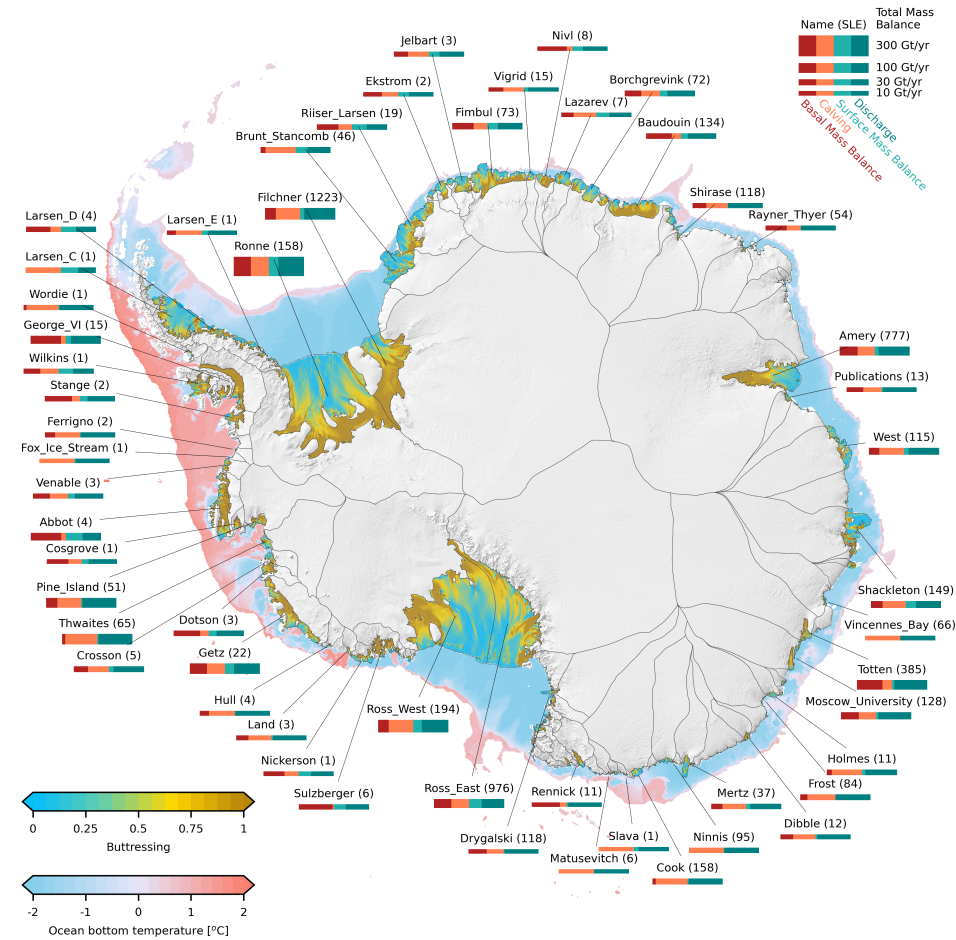


Figure 1.2: Overview of main Antarctic ice shelves. For each ice shelf, the sea level equivalent of the upstream basin is shown in centimeters. The bar charts display the equilibrium mass balance (bar thickness) and the separation of mass sources (surface mass balance and discharge) and mass sinks (basal mass balance and calving) from Davison *et al.* (2023). Buttressing is shown along flow (Fürst *et al.*, 2016), and observation-based ocean temperatures are shown at continental shelf depth (Jourdain *et al.* (2020), prepared by Clara Burgard). Credit: Erwin Lambert.

In a warming climate, more ice shelves fall out of equilibrium, leading to increased mass loss. Figure 1.3 illustrates several reasons for the increased mass loss of Antarctica. One major factor is basal melting, where warmer ocean waters thin the ice shelves from below (Paolo *et al.*, 2015; Pritchard *et al.*, 2012). The most rapid thinning occurs in West Antarctica, where ocean temperatures are the highest compared to the surrounding Antarctic Ice Sheet waters (Paolo *et al.*, 2015; Rignot *et al.*, 2014), see also Figure 1.2. A second reason for Antarctic mass loss is calving at the edges of ice shelves, where large chunks of ice break off. While this process also occurs for ice shelves in equilibrium (recall the fingernail metaphor), calving is projected to increase in a warming climate (Y. Liu *et al.*, 2015). Due to reduced thickness from basal melting, ice shelves have become weaker and more prone to damage and fracture (Greene *et al.*, 2022; Lhermitte *et al.*, 2020), leading to this increased calving. Currently, mass loss from Antarctica due to calving has been approximately equal to the mass loss from ice shelf thinning caused by basal melting (Greene *et al.*, 2022). Lastly, surface melt can destabilize ice shelves through various mechanisms, as elaborated upon in the following section.

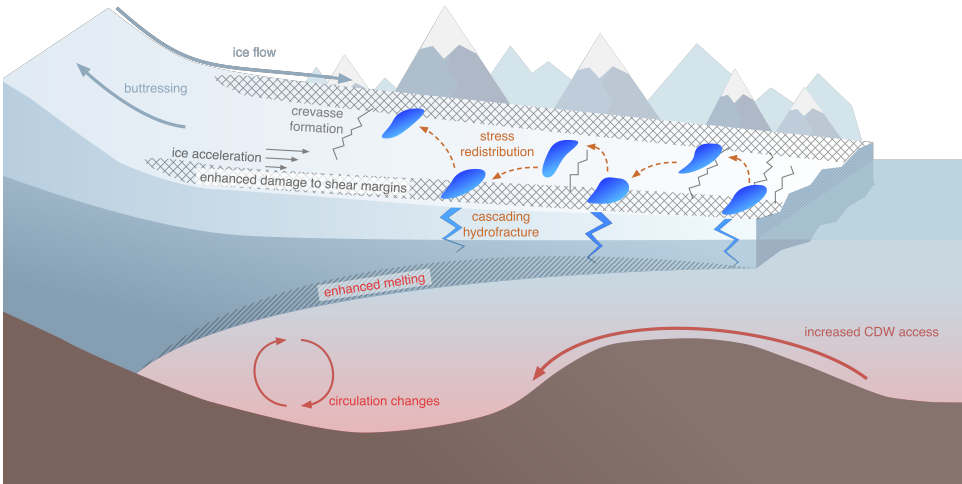


Figure 1.3: Conceptual overview of an ice shelf, highlighting destabilizing processes: basal melting resulting in ice shelf thinning, surface melting leading to hydrofracturing, and structural damage reducing overall ice shelf integrity. Credit: Alexander Bradley.

1.3. IMPACT OF SURFACE MELT ON ICE SHELVES

Surface melt occurs when the top layer of an ice shelf reaches temperatures above freezing, causing the snow and ice to melt. In this dissertation, the term ‘surface melt’ encompasses all forms of liquid water, from wet snow to accumulated meltwater in ponds and streams (Figure 1.4). While surface melt has always been a part of Antarctica’s natural cycle, its intensity and extent are expected to increase due to rising local temperatures (Gilbert & Kittel, 2021; Trusel *et al.*, 2015).

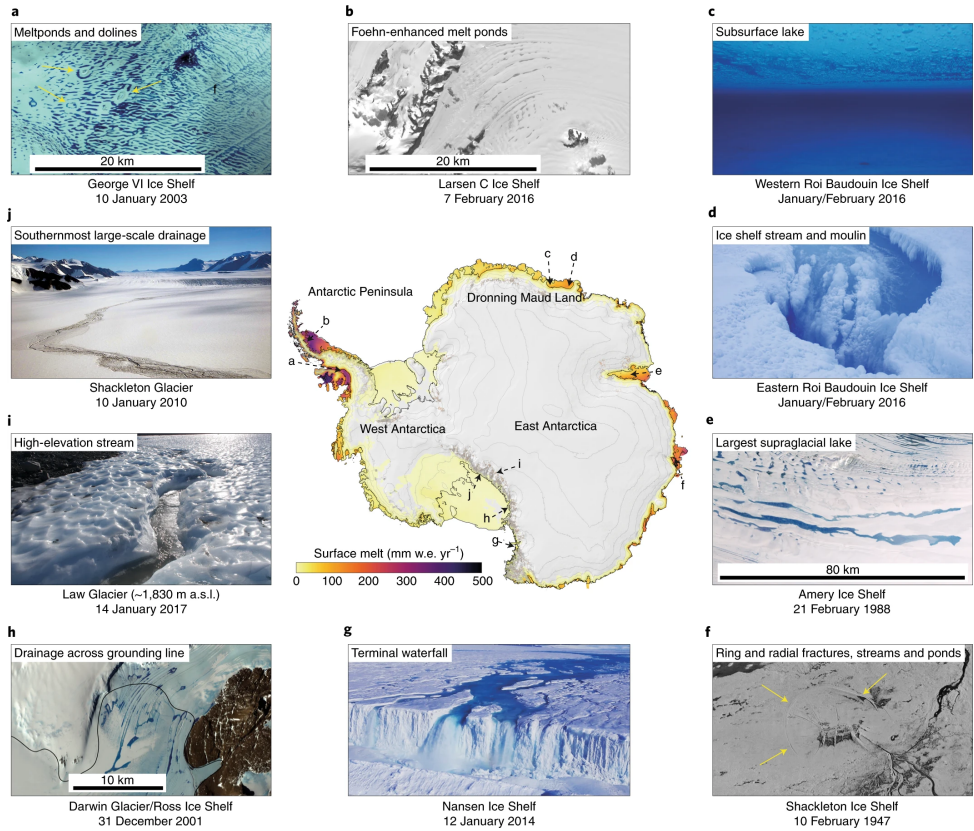


Figure 1.4: Overview of surface melt on the Antarctic Ice Sheet. The central map shows the surface melt of Antarctica from 2000–2009, based on satellite observations (Quick Scatterometer, QuikSCAT) by Trusel *et al.* (2013). Panels a–j display photos of various surface melt formations, with their locations indicated on the central map. Credit: Bell *et al.* (2018).

Surface melting in Antarctica leads to the gradual formation of liquid water, which can be understood as progressing through a series of stages, much like moving up a ladder. At the first rung, when the icy or snowy surface begins to melt, it forms ‘wet snow’ (see Figure 1.5). Beneath this layer of fresh snow lies the firn layer—a multi-year accumulation of snow with air-filled pores. The wet snow can seep into these pores and refreeze. As new snow accumulates, it replenishes the firn layer, creating additional pore spaces where the wet snow can refreeze (Kuipers Munneke *et al.*, 2014).

When the firn’s pore spaces become saturated, we ascend to the next rung on the ladder: ‘slush’. Antarctic slush has a wet texture but maintains a semi-solid form, similar to slush puppies enjoyed on a hot day. As the slush continues to melt, the water starts to pool, moving us to the next stage.

At this last stage, we reach the ‘ponded meltwater’. During peak melt season, the extent of ponded meltwater in Antarctica can be comparable to the slush area, each covering roughly an area equivalent to the size of South Holland in the Netherlands (Dell *et al.*, 2024). Ponded meltwater collects in low-lying areas, forming pools that can range from bathtub-sized ponds to vast lakes, with the largest recorded at 71.5 km². (Corr *et al.* (2022); see also Figure 1.4e), comparable in size to The Hague. These pools can quickly expand as more ice and snow melt, leading to the formation of streams and rivers on the ice surface.

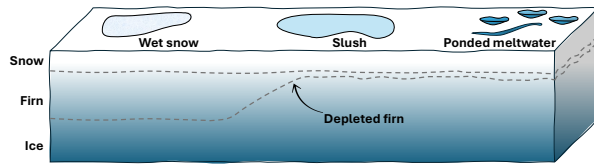


Figure 1.5: Progression of meltwater stages: from wet snow, to slush, to ponded meltwater.

Surface melt primarily impacts ice shelves through ‘hydrofracturing’, a process of water-induced fracturing, as its name suggests. When ponded meltwater seeps into fractures in the ice surface, it exerts pressure, causing them to grow unstoppably (Nye, 1957; Weertman, 1973). This process can transform stable ice shelves into structures that resemble Swiss cheese, filled with numerous holes. After a lake has drained, that location on the ice shelf experiences a sudden release of pressure, causing it to uplift, leading to more fractures around the areas where the lakes used to be (Banwell *et al.*, 2013, 2024; MacAyeal & Sergienko, 2013; Scambos *et al.*, 2009). If these fractures intersect with other nearby lakes, they can trigger a chain reaction of further lake-drainage events, potentially leading to large-scale ice shelf break-up (Banwell *et al.*, 2013, 2024). The disintegration of the Larsen B Ice Shelf on the Antarctic Peninsula in 2002 is a notable example of how surface melt-induced weakening can cause rapid ice shelf collapse (Banwell *et al.*, 2013; Glasser & Scambos, 2008; Scambos *et al.*, 2003). The ice shelf, comparable in size to the province of Utrecht, rapidly disappeared after a series of lake drainage events (Sergienko & Macayeal, 2005).

Additionally, there are two processes that enhance surface melt formation and ponding, making hydrofracturing increasingly likely in the future (Gilbert & Kittel, 2021; Jourdain *et al.*, 2024). Firstly, surface melt alters the reflectivity of the ice surface. White snow and ice reflect sunlight, helping to maintain cooler surface temperatures. However, as meltwater accumulates, it darkens the ice surface, reducing its reflectivity and accelerating the melting process. This forms a feedback loop: increased melt darkens the ice, leading to greater heat absorption, which in turn causes further melting (Budyko, 1969; Sellers, 1969).

Secondly, surface melt can deplete the firn layer of the Antarctic Ice Sheet, resulting in more surface melt ponding. Currently, around 94% of Antarctica is covered by firn (Medley *et al.*, 2022; van Wessem *et al.*, 2018). However, if meltwater repeatedly refreezes without sufficient replenishment from snowfall, the firn air content decreases, reducing its capacity to absorb future meltwater. This process, known as firn air depletion, leads to more ponded meltwater, increasing the risk of hydrofracturing (Kuipers Munneke *et al.*, 2014).

1.4. SURFACE MELT MAPPING USING SATELLITE OBSERVATIONS

Understanding the complex interplay between surface melt and ice shelf stability is essential for accurate sea level predictions. Ongoing research aims to quantify the effects of surface melt on ice shelves and improve climate models that simulate their behavior in a changing climate. Early studies mapping surface melt and its hydrology relied on direct measurements taken on the ice. In 1909, Ernest Shackleton and his team were among the first to observe surface meltwater on Antarctica, on a small ice shelf known as the Nansen Ice Shelf. They recorded the presence of meltwater in their logbook, describing it as a ‘thaw-water stream could be heard roaring’ (David & Priestley, 1909). Three years later, in 1912, Robert Falcon Scott’s team followed up on Shackleton’s observations by producing the first detailed map of Antarctic meltwater, including channels, streams, and melt ponds (Priestley, 1915).

To date, in-situ measurements and observations remain invaluable sources of information. Over the last fifty years, in addition to visual observations, roughly 300 automatic weather stations have been deployed on the Antarctic Ice Sheet (Wang *et al.*, 2023), continuously measuring incoming energy to estimate surface melt, along with many other relevant climate processes. Additionally, field campaigns have been set up, for example, to track ice movement following lake drainage (Banwell *et al.*, 2024) and study the hydrology of meltwater flowing up and through ice shelves (Lenaerts *et al.*, 2017). While in-situ measurements are indispensable for understanding Antarctic meltwater, mapping the entire Antarctic Ice Sheet this way is too costly and time-consuming, resulting in sparse measurements both temporally and spatially. Fortunately, over the last 50 years, the abundance of remote sensing data has enabled us to study the Antarctic Ice Sheet in its entirety.

In this thesis, when discussing remote sensing data, I specifically refer to satellite observations. However, officially remote sensing encompasses all measurements taken from a distance, so including those from aircraft and drones, though these are not utilized in this dissertation. Satellites are devices moving around Earth at altitudes of hundreds of kilometers, capturing images and measurements of our planet. Satellites are equipped with powerful sensors that detect different types of light and energy. They orbit Earth in a carefully planned path and send their data back to Earth. These data are used to learn about our planet’s changing climate, how cities are growing, and how forests are shrinking. We use the data to predict weather patterns, monitor pollution levels, and in my case, help us understand how the ice on Antarctica is melting.

Surface melt on Antarctica can be mapped using a range of satellite data, and like every data source, each satellite comes with its opportunities and limitations. Some satellites take images of our Earth like the cameras on our phones, but with these images we can only detect accumulated meltwater, such as melt ponds and streams. Other satellites can measure all types of meltwater, including meltwater below the surface and in snow, which is not visible to the human eye. However, these satellites often cannot determine the exact amount of liquid water, resulting in a binary melt/no-melt classification. To get a full overview of the different types of

satellites used for monitoring surface melt, see Figure 1.6 and Figure 1.7.

Figure 1.6 illustrates a timeline of the various satellite types, the effective horizontal resolution (essentially the smallest ground area that a satellite can distinguish and measure), and the depth beneath the surface from which the satellites can gather information. Figure 1.7 shows how different satellites “see” surface melt in various ways. Active sensors, such as synthetic aperture radar (SAR) sensors, scatterometers, and altimeters, send signals to the surface and analyze the returned signals to detect binary surface melt presence (SAR sensors and scatterometers) or measure pond depths (altimeter sensors). In contrast, passive sensors, such as radiometers and optical sensors, do not emit signals; they instead measure natural emissions from the Earth (radiometers) or sunlight reflections (optical sensors).

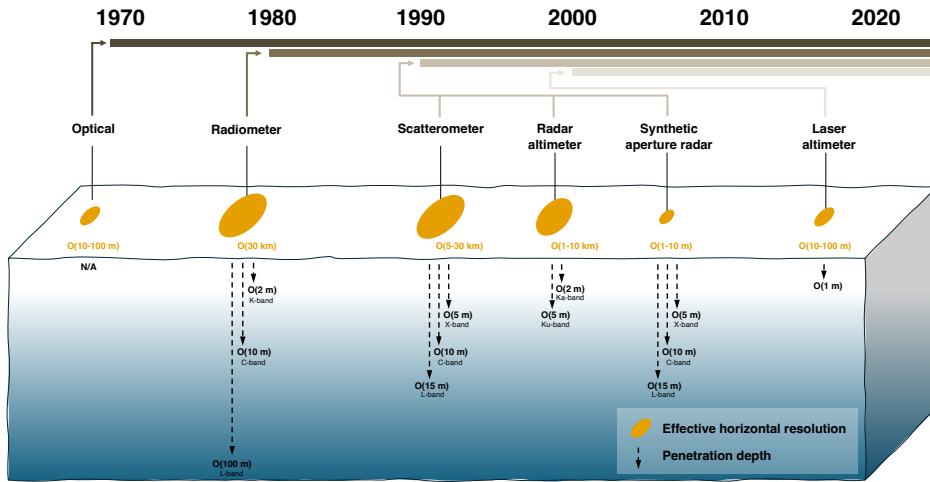


Figure 1.6: Overview of satellites used to study Antarctic surface dynamics, including the start dates of their use, their effective horizontal resolution, and their penetration depth. This figure is adapted from Figure 5 of The Firm Symposium team (2024).

Figure 1.8 provides an overview of the George VI Ice Shelf, one of the wettest ice shelves in Antarctica, during the first week of January (the peak of the Antarctic melt season) for the years 2021 to 2024. Each satellite image represents a different year of my PhD research. The figure includes images captured by four primary sensors used in my dissertation: January 2021 by a radiometer, January 2022 by a scatterometer, January 2023 by an optical sensor, and January 2024 by a SAR sensor.

Finally, a short remark on the term ‘surface melt’. While this term is widely accepted in scientific literature, and for this reason, also continuously used by me, I would argue the term is not entirely used correctly by the remote sensing community. As you know by now, surface melt from satellites is derived by looking at how much light or energy the sensors measure, which implicitly means that we can only study ‘properties’ using satellites, not ‘processes’. Since surface melt is an energy conversion process in which snow and ice are transformed into water, we

are actually not measuring the process itself but only its outcome—the presence of liquid water.

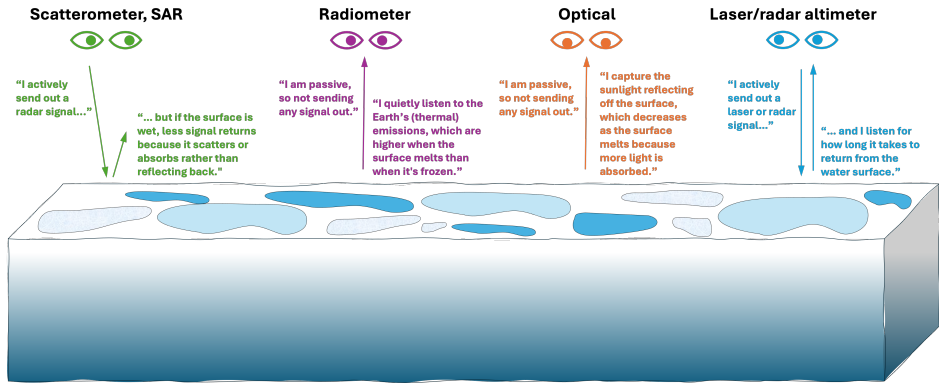


Figure 1.7: Visual summary of satellites used for surface melt observation in Antarctica.

1.5. DEEP LEARNING AND CLOUD COMPUTING IN THE BIG DATA REALM

The abundance of satellite data opens many doors for studying surface melt on Antarctica, as well as countless other processes. It is believed by some that “Data is the new science. Big data holds the answers” (quote by Patrick P. Gelsinger, CEO of Intel). While I don’t think data will solve all our problems, there is much to learn and discover from big data. Big data refers to very large datasets that keep growing rapidly. These datasets are so large that traditional data management systems can’t store or analyze them effectively. Each day, satellites capture hundreds of terabytes of data. In a quest to analyze these trillions of pixels, cloud computing and deep learning serve as invaluable tools.

Over the past 15 years, numerous cloud-based platforms have emerged, including commercial options like Microsoft Planetary Computer, Amazon Web Services GeoSpatial Services, Microsoft Azure Maps, and Google Earth Engine, as well as free, open-source platforms such as Open Data Cube and Pangeo. These cloud-based platforms let you use computer resources like storage and processing power without needing to rely on your own computer. Instead, you use external resources stored in data centers that you can access over the internet.

One of the most popular cloud-based platforms for storing and analyzing remote sensing data, and the one I used in my research, is Google Earth Engine. Google Earth Engine enables users to conduct geospatial analyses in the cloud using Google’s servers (Gorelick *et al.*, 2017). By executing tasks in parallel across multiple servers, large computational jobs can be completed quickly. Google Earth Engine hosts a large catalog of ready-to-use, cloud-hosted geospatial data products, spanning over thirty years of satellite data, making it an ideal solution for large-scale remote sensing analysis of, for example, surface meltwater in Antarctica.

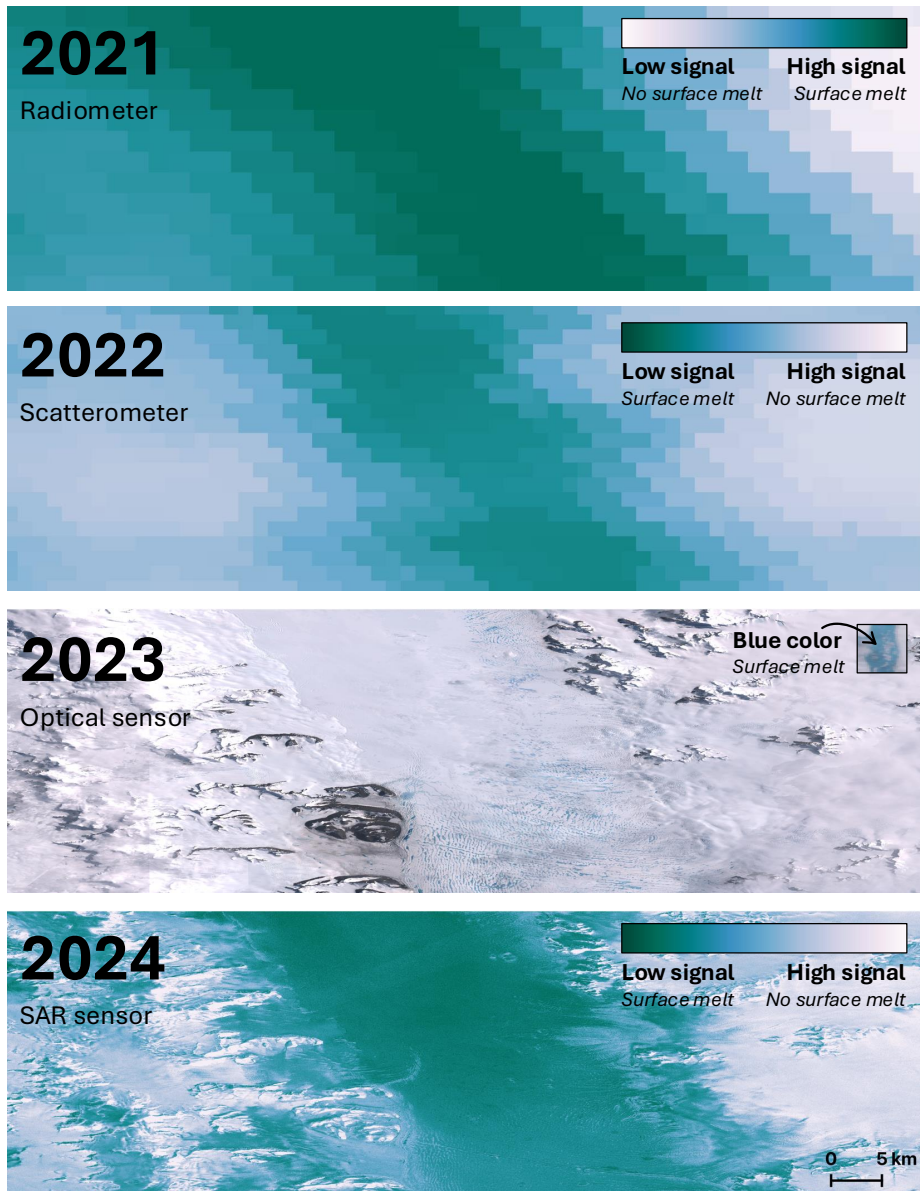


Figure 1.8: Satellite images of the George VI Ice Shelf in Antarctica, taken during the first week of January from 2021 to 2024, each marking a year of my PhD research. The images are medium composites from various sensors: 2021 shows SSMIS 19 GHz horizontally polarized data, with a color bar ranging from 195 K (white) to 235 K (green); 2022 shows ASCAT data, vertically polarized, with a range from -20 dB (green) to 0 dB (white); 2023 shows Sentinel-2 imagery using red, green, and blue bands; and 2024 shows Sentinel-1 horizontally polarized data, with a range from -20 dB (green) to 0 dB (white). These images illustrate the variation in surface conditions over time and across different sensing methods.

Cloud-based platforms can be compared to a well-stocked kitchen, providing us with the necessary storage space and ingredients. However, just like in cooking, we also need recipes to create excellent dishes. This is where I believe deep learning comes in, providing us with the tools to creatively analyze and interpret the data. Deep learning is a specialized type of artificial intelligence and, more specifically, a subset of machine learning. Machine learning techniques learn from data to improve performance over time. For several decades, techniques like support vector machines and ensemble classifiers, such as random forests, have been popular in the scientific community (Lary *et al.*, 2016). In the past decade, the remote sensing community has increasingly focused on deep learning (X. Zhu *et al.*, 2017). Deep learning is characterized by neural network architectures with multiple layers—hence the term ‘deep’. This approach is particularly advantageous for remote sensing problems involving complex, nonlinear, poorly understood, or hard-to-generalize physical models (X. Zhu *et al.*, 2017).

For surface melt monitoring, the rise of cloud computing and deep learning has led the community to shift from monitoring surface melt using a few satellite images and statistically-based threshold approaches (e.g., Zwally & Fiegles, 1994) to large-scale analyses employing non-linear deep learning methods (e.g., Q. Zhu *et al.*, 2024). While cloud computing and deep learning offer exciting possibilities, they also introduce new challenges. We must be cautious to ensure that deep learning models do not learn from noise or spurious relationships, as this can lead to incorrect results and, in some cases, even disastrous consequences (such as the Dutch childcare benefits scandal, known as the “toeslagenaffaire” in Dutch; Hadwick & Lan, 2021). Ongoing research is crucial to navigate these challenges and optimize the use of deep learning for addressing societal issues.

1.6. IDENTIFYING AND FILLING RESEARCH GAPS

Despite the availability of extensive satellite data, advanced computational resources and deep learning techniques, the contribution of Antarctica to sea level rise remains uncertain. To reduce this uncertainty, it is crucial to predict the future behavior of Antarctic ice shelves by understanding their potential destabilization processes. This understanding hinges on a thorough analysis of historical data and past destabilization events. This dissertation delves into the dynamics of ice shelf melt in Antarctica using satellite data, examining the timing, location, and hydrology of surface meltwater. Four key research gaps are identified, and the objectives of this dissertation are presented to address these gaps and enhance our understanding of Antarctic surface melt.

Research gap 1: Surface melt mapping relies on one sensor

To determine where and when Antarctica is melting, satellite data have been extensively used to map the extent of surface melt. Traditionally, surface melt detection relied primarily on passive microwave data and a single threshold to

identify melting events (H. Liu *et al.*, 2006; Picard & Fily, 2006; Torinesi *et al.*, 2003; Zwally & Fiegles, 1994). More recently, surface melt extent maps have also been developed using other sensors, such as active microwave data from SAR sensors (Johnson *et al.*, 2020; Liang *et al.*, 2021; Luckman *et al.*, 2014) and scatterometers (Barrand *et al.*, 2013; Bothale *et al.*, 2015; Trusel *et al.*, 2012).

However, when comparing surface melt extents derived from different satellites, large differences arise. Trusel *et al.* (2012) demonstrated that, from 2000 to 2009, the accumulated surface melt extent detected by passive microwave sensors was approximately 50–75% less than that detected by scatterometers over the Antarctic Peninsula. This raises important questions about whether different satellites are detecting the same phenomena and why they might provide different numbers. Understanding these differences is crucial for determining whether it is valid to rely on a single satellite for assessing Antarctic surface melt extent and for identifying the limitations of a specific satellite. This will ensure that the most accurate surface melt products are used in climate models for sea level rise projections.

PhD objective 1 - Evaluating the strengths and weaknesses of remote sensing techniques for surface melt detection on Antarctica

The first objective of my PhD is to evaluate the consistency of different satellites in detecting surface melt. I compare the extent of surface melt across Antarctica using a passive microwave sensor, two active microwave sensors (SAR and scatterometer), and an optical sensor. Melt extents are determined by applying state-of-the-art melt detection algorithms to the satellite data. This comparison aims to reveal differences in timing, location, and reasons for inconsistencies among the satellites, providing insights into the opportunities and challenges associated with each sensor.

Research gap 2: Surface melt maps – either infrequent or coarse resolution

When working with satellite data, one key consideration is the trade-off between spatial resolution and temporal frequency. Satellites either provide frequent imagery of the same location with coarse pixels or detailed imagery with less frequent overpasses. Surface melt, being a dynamic process both spatially and temporally, requires frequent and high-resolution mapping.

Passive microwave studies, such as those by Torinesi *et al.* (2003), H. Liu *et al.* (2006), and Picard and Fily (2006), provide Antarctic surface melt data with a pixel resolution of 25 km and a temporal frequency of twice daily. In contrast, SAR studies, including those by Luckman *et al.* (2014), Johnson *et al.* (2020), and Liang *et al.* (2021), offer high spatial resolution maps with pixel sizes ranging from 10 m to 1000 m. However, these SAR images typically become available every other day, which is about four times less frequent than the passive microwave studies mentioned earlier. The limitations of remote sensing data, whether due to infrequent coverage or coarse resolution, pose difficulties in accurately mapping the dynamic surface melt in Antarctica.

PhD objective 2 - Develop a high-resolution surface melt record for Antarctica with both high spatial and temporal resolution

The second objective of my PhD is to address the spatial-temporal trade-offs inherent in satellite observations and develop a high-resolution surface melt record for Antarctica. This involves identifying locations where different types of satellites pass over at the same time, ensuring they capture the same surface melt conditions. These simultaneous observations will serve as training data for a deep learning model. The goal is to enable the coarse but frequent satellite images to replicate the detailed melt patterns observed in the high-resolution but infrequent data. By incorporating additional input data, such as a detailed elevation map, along with the coarse-resolution images, the deep learning model can learn these relationships. This approach will allow me to generate an Antarctic-wide melt product that offers both high temporal and high spatial resolution.

Research gap 3: Surface melt maps – from presence to volume

The previous research gaps and dissertation objectives focused on surface melt *presence*, but to fully understand Antarctic surface melt, it is also crucial to assess surface melt *volume*. While recent efforts have attempted to estimate surface melt volume using remote sensing data in Greenland (Zheng *et al.*, 2022) and Antarctica (Banwell *et al.*, 2023), surface melt volume is typically studied through models, particularly regional climate models. Regional climate models use equations to represent the processes and interactions driving regional climate. For Antarctica, commonly used regional climate models include the Modèle Atmosphérique Régional (MAR) (Agosta *et al.*, 2019) and the Regional Atmospheric Climate Model (RACMO) (van Wessem *et al.*, 2018). Although these models provide an Antarctic-wide overview of surface melt volume, their horizontal resolution (approximately 25–30 km) is insufficient for capturing the small-scale melt processes across Antarctica.

PhD objective 3 - Enhance the spatial resolution of Antarctic surface melt data from a regional climate model

The third objective of my PhD is to enhance the spatial resolution of the regional climate model RACMO, which is currently run at a relatively coarse resolution of 27 km (van Wessem *et al.*, 2018). The goal is to develop a method for downscaling RACMO's surface melt volumes using a deep learning architecture, leveraging 'ground truth' data from a RACMO simulation at 5.5 km resolution available for the Antarctic Peninsula (van Wessem *et al.*, 2016). Previous research has shown that downscaling using only the coarse-resolution data (i.e., RACMO at 27 km) produces inadequate results, as Antarctic surface melt processes vary across the continent (Hu *et al.*, 2021). Therefore, the aim is to improve the downscaling deep learning algorithm by incorporating additional data that are physically related to surface melt, such as elevation and albedo obtained from remote sensing. This approach will provide insights into the impacts of localized melting on ice shelf integrity, including processes like hydrofracturing.

Research gap 4: Unexplored dynamics of meltwater lakes

The final research gap addressed in this dissertation pertains to the hydrology of Antarctic meltwater. There are still many unknowns on this topic, such as whether meltwater from hydrofracturing can reach the bottom of the ice sheet, how much meltwater refreezes in the firn layer versus how much remains liquid, and the behavior of meltwater lakes—whether they drain or refreeze. This dissertation specifically tackles this last question; what happens to meltwater lakes at the end of a melt season. Although previous studies have monitored the presence and volume of Antarctic meltwater lakes using optical imagery (Arthur *et al.*, 2020; Moussavi *et al.*, 2020), tracking meltwater lakes throughout a melt season remains difficult due to the persistent cloud cover in Antarctica.

Understanding the behavior of meltwater lakes is crucial because rapid drainage (i.e., hydrofracturing), can destabilize ice shelves, as demonstrated by the Larsen B ice shelf collapse in 2002. Without a comprehensive Antarctic-wide map of draining and refreezing lakes, further investigation into the effects of lake dynamics on ice shelf stability is challenging.

PhD objective 4 - Develop a methodology to map the evolution of supraglacial lakes in Antarctica

The fourth objective of my PhD is to develop a method for assessing the evolution of meltwater lakes in Antarctica, specifically to determine whether they drain or refreeze. While similar analyses have been conducted in Greenland using optical data (Langley *et al.*, 2016; Leeson *et al.*, 2013; McMillan *et al.*, 2007), frequent cloud cover in Antarctica often makes optical imagery unusable. Benedek and Willis (2021) have shown that SAR data can effectively analyze lake evolution, as they demonstrated for several lakes on Greenland. My goal is to determine if a deep learning algorithm trained on SAR time series data from Greenland can be adapted and applied to analyze meltwater lake dynamics on Antarctica.

1.7. STRUCTURE OF THIS DISSERTATION

Now that you have completed the introduction to this dissertation, let me provide you an overview of the research. The goal of this dissertation is to improve our understanding of surface melt on the Antarctic Ice Sheet by leveraging satellite data and deep learning techniques. This overarching goal is divided into four specific sub-goals, addressed in Chapters 2–5, each aimed at tackling one of the research gaps outlined in Section 1.6.

Chapter 2 evaluates the opportunities and challenges of various remote sensing techniques for detecting surface melt on Antarctica. Chapter 3 presents a product that merges the different satellite data discussed in Chapter 2, using deep learning to create a high-resolution surface meltwater record. Chapter 4 shifts the focus from meltwater presence to meltwater volume, introducing a method for creating

a high-resolution surface melt volume product by downscaling a regional climate model with a physically-informed deep learning architecture. Chapter 5 delves into the hydrology of meltwater, presenting a method for distinguishing between refreezing and draining lakes using SAR observations and deep learning.

Like any dissertation, this study began with a few questions and has led to many more questions and new research directions. In Chapter 6, I summarize the main findings of my PhD work and propose three new research ideas to further advance the field of mapping the dynamic surface meltwater on Antarctica.

BIBLIOGRAPHY

- Agosta, C., Amory, C., Kittel, C., Orsi, A., Favier, V., Gallée, H., Van den Broeke, M. R., Lenaerts, J., van Wessem, J. M., Van de Berg, W. J., et al. (2019). Estimation of the Antarctic surface mass balance using the regional climate model MAR (1979–2015) and identification of dominant processes. *The Cryosphere*, 13(1), 281–296.
- Arthur, J. F., Stokes, C. R., Jamieson, S. S., Carr, J. R., & Leeson, A. A. (2020). Distribution and seasonal evolution of supraglacial lakes on Shackleton Ice Shelf, East Antarctica. *The Cryosphere*, 14(11), 4103–4120.
- Banwell, A. F., MacAyeal, D. R., & Sergienko, O. V. (2013). Breakup of the Larsen B Ice Shelf triggered by chain reaction drainage of supraglacial lakes. *Geophysical Research Letters*, 40(22), 5872–5876.
- Banwell, A. F., Wever, N., Dunmire, D., & Picard, G. (2023). Quantifying Antarctic-Wide Ice-Shelf Surface Melt Volume Using Microwave and Firn Model Data: 1980 to 2021. *Geophysical Research Letters*, 50(12), e2023GL102744.
- Banwell, A. F., Willis, I. C., Stevens, L. A., Dell, R. L., & MacAyeal, D. R. (2024). Observed meltwater-induced flexure and fracture at a doline on George VI Ice Shelf, Antarctica. *Journal of Glaciology*, 1–14.
- Barrand, N. E., Vaughan, D. G., Steiner, N., Tedesco, M., Kuipers Munneke, P., Van den Broeke, M. R., & Hosking, J. S. (2013). Trends in Antarctic Peninsula surface melting conditions from observations and regional climate modeling. *Journal of Geophysical Research: Earth Surface*, 118(1), 315–330.
- Bell, R. E., Banwell, A. F., Trusel, L. D., & Kingslake, J. (2018). Antarctic surface hydrology and impacts on ice-sheet mass balance. *Nature Climate Change*, 8(12), 1044–1052.
- Benedek, C. L., & Willis, I. C. (2021). Winter drainage of surface lakes on the Greenland Ice Sheet from Sentinel-1 SAR imagery. *The Cryosphere*, 15(3), 1587–1606.
- Bothale, R. V., Rao, P., Dutt, C., & Dadhwal, V. K. (2015). Detection of snow melt and freezing in Himalaya using OSCAT data. *Journal of Earth System Science*, 124(1), 101–113.
- Budyko, M. I. (1969). The effect of solar radiation variations on the climate of the Earth. *tellus*, 21(5), 611–619.
- Corr, D., Leeson, A., McMillan, M., Zhang, C., & Barnes, T. (2022). An inventory of supraglacial lakes and channels across the West Antarctic Ice Sheet. *Earth System Science Data*, 14(1), 209–228.
- David, T. W. E., & Priestley, R. E. (1909). *Geological Observations in Antarctica by the British Antarctic Expedition 1907–1909*. JP Lippincott.
- Davison, B. J., Hogg, A. E., Gourmelen, N., Jakob, L., Wuite, J., Nagler, T., Greene, C. A., Andreasen, J., & Engdahl, M. E. (2023). Annual mass budget of Antarctic ice shelves from 1997 to 2021. *Science Advances*, 9(41), eadi0186.
- Dell, R., Willis, I., Arnold, N., Banwell, A., & de Roda Husman, S. (2024). Substantial contribution of slush to meltwater area across Antarctic ice shelves. *Nature Geoscience*, 1–7.

- Fürst, J. J., Durand, G., Gillet-Chaulet, F., Tavard, L., Rankl, M., Braun, M., & Gagliardini, O. (2016). The safety band of Antarctic ice shelves. *Nature Climate Change*, 6(5), 479–482.
- Gilbert, E., & Kittel, C. (2021). Surface melt and runoff on Antarctic ice shelves at 1.5 C, 2 C, and 4 C of future warming. *Geophysical Research Letters*, 48(8), e2020GL091733.
- Glasser, N., & Scambos, T. A. (2008). A structural glaciological analysis of the 2002 Larsen B ice-shelf collapse. *Journal of Glaciology*, 54(184), 3–16.
- Gorelick, N., Hancher, M., Dixon, M., Ilyushchenko, S., Thau, D., & Moore, R. (2017). Google Earth Engine: Planetary-scale geospatial analysis for everyone. *Remote sensing of Environment*, 202, 18–27.
- Greene, C. A., Gardner, A. S., Schlegel, N.-J., & Fraser, A. D. (2022). Antarctic calving loss rivals ice-shelf thinning. *Nature*, 609(7929), 948–953.
- Hadwick, D., & Lan, S. (2021). Lessons to be learned from the dutch childcare allowance scandal: a comparative review of algorithmic governance by tax administrations in the Netherlands, France and Germany. *World tax journal.-Amsterdam*, 13(4), 609–645.
- Hu, Z., Kuipers Munneke, P., Lhermitte, S., Izeboud, M., & Van den Broeke, M. (2021). Improving surface melt estimation over the Antarctic Ice Sheet using deep learning: a proof of concept over the Larsen Ice Shelf. *The Cryosphere*, 15(12), 5639–5658.
- IPCC. (2023). Summary for Policymakers. In: Climate Change 2023: Synthesis Report. Contribution of Working Groups I, II and III to the Sixth Assessment Report of the Intergovernmental Panel on Climate Change [Core Writing Team, H. Lee and J. Romero (eds.)]
- Johnson, A., Fahnestock, M., & Hock, R. (2020). Evaluation of passive microwave melt detection methods on Antarctic Peninsula ice shelves using time series of Sentinel-1 SAR. *Remote Sensing of Environment*, 250, 112044.
- Jourdain, N. C., Amory, C., Kittel, C., & Durand, G. (2024). Changes in Antarctic surface conditions and potential for ice shelf hydrofracturing from 1850 to 2200. *EGUsphere*, 2024, 1–34.
- Jourdain, N. C., Asay-Davis, X., Hattermann, T., Straneo, F., Seroussi, H., Little, C. M., & Nowicki, S. (2020). A protocol for calculating basal melt rates in the ISMIP6 Antarctic ice sheet projections. *The Cryosphere*, 14(9), 3111–3134.
- Kuipers Munneke, P., Ligtenberg, S. R., Van den Broeke, M. R., & Vaughan, D. G. (2014). Firn air depletion as a precursor of antarctic ice-shelf collapse. *Journal of Glaciology*, 60(220), 205–214.
- Langley, E. S., Leeson, A. A., Stokes, C. R., & Jamieson, S. S. (2016). Seasonal evolution of supraglacial lakes on an East Antarctic outlet glacier. *Geophysical Research Letters*, 43(16), 8563–8571.
- Lary, D. J., Alavi, A. H., Gandomi, A. H., & Walker, A. L. (2016). Machine learning in geosciences and remote sensing. *Geoscience Frontiers*, 7(1), 3–10.
- Leeson, A. A., Shepherd, A., Sundal, A. V., Johansson, A. M., Selmes, N., Briggs, K., Hogg, A. E., & Fettweis, X. (2013). A comparison of supraglacial lake observations derived from MODIS imagery at the western margin of the Greenland Ice Sheet. *Journal of Glaciology*, 59(218), 1179–1188.
- Lenaerts, J., Lhermitte, S., Drews, R., Ligtenberg, S., Berger, S., Helm, V., Smeets, C., Van den Broeke, M., Van de Berg, W. J., Van Meijgaard, E., et al. (2017). Meltwater produced by wind–albedo interaction stored in an East Antarctic ice shelf. *Nature climate change*, 7(1), 58–62.

- Lhermitte, S., Sun, S., Shuman, C., Wouters, B., Pattyn, F., Wuite, J., Berthier, E., & Nagler, T. (2020). Damage accelerates ice shelf instability and mass loss in Amundsen Sea Embayment. *Proceedings of the National Academy of Sciences*, 117(40), 24735–24741.
- Liang, D., Guo, H., Zhang, L., Cheng, Y., Zhu, Q., & Liu, X. (2021). Time-series snowmelt detection over the Antarctic using Sentinel-1 SAR images on Google Earth Engine. *Remote Sensing of Environment*, 256, 112318.
- Liu, H., Wang, L., & Jezek, K. C. (2006). Spatiotemporal variations of snowmelt in Antarctica derived from satellite scanning multichannel microwave radiometer and Special Sensor Microwave Imager data. *Journal of Geophysical Research*, 111(F1).
- Liu, Y., Moore, J. C., Cheng, X., Gladstone, R. M., Bassis, J. N., Liu, H., Wen, J., & Hui, F. (2015). Ocean-driven thinning enhances iceberg calving and retreat of Antarctic ice shelves. *Proceedings of the National Academy of Sciences*, 112(11), 3263–3268.
- Luckman, A., Elvidge, A., Jansen, D., Kulesa, B., Kuipers Munneke, P., King, J., & Barrand, N. E. (2014). Surface melt and ponding on Larsen C Ice Shelf and the impact of föhn winds. *Antarctic Science*, 26(6), 625–635.
- MacAyeal, D. R., & Sergienko, O. V. (2013). The flexural dynamics of melting ice shelves. *Annals of Glaciology*, 54(63), 1–10.
- McMillan, M., Nienow, P., Shepherd, A., Benham, T., & Sole, A. (2007). Seasonal evolution of supra-glacial lakes on the Greenland Ice Sheet. *Earth and Planetary Science Letters*, 262(3–4), 484–492.
- Medley, B., Neumann, T. A., Zwally, H. J., Smith, B. E., & Stevens, C. M. (2022). Simulations of firn processes over the Greenland and Antarctic ice sheets: 1980–2021. *The Cryosphere*, 16(10), 3971–4011.
- Moussavi, M., Pope, A., Halberstadt, A. R. W., Trusel, L. D., Cioffi, L., & Abdalati, W. (2020). Antarctic supraglacial lake detection using Landsat 8 and Sentinel-2 imagery: Towards continental generation of lake volumes. *Remote Sensing*, 12(1), 134.
- NASA. (2023). Greenland ice sheet mass loss (2002–2023) [Accessed: 2023-07-23].
- Nye, J. F. (1957). The distribution of stress and velocity in glaciers and ice-sheets. *Proceedings of the Royal Society of London. Series A. Mathematical and Physical Sciences*, 239(1216), 113–133.
- Paolo, F. S., Fricker, H. A., & Padman, L. (2015). Volume loss from Antarctic ice shelves is accelerating. *Science*, 348(6232), 327–331.
- Picard, G., & Fily, M. (2006). Surface melting observations in Antarctica by microwave radiometers: Correcting 26-year time series from changes in acquisition hours. *Remote sensing of environment*, 104(3), 325–336.
- Priestley, R. E. (1915). *Antarctic Adventure: Scott's Northern Party*. E.P. Dutton; Company.
- Pritchard, H., Ligtenberg, S. R., Fricker, H. A., Vaughan, D. G., Van den Broeke, M. R., & Padman, L. (2012). Antarctic ice-sheet loss driven by basal melting of ice shelves. *Nature*, 484(7395), 502–505.
- Rignot, E., Jacobs, S., Mouginot, J., & Scheuchl, B. (2013). Ice-shelf melting around Antarctica. *Science*, 341(6143), 266–270.
- Rignot, E., Mouginot, J., Morlighem, M., Seroussi, H., & Scheuchl, B. (2014). Widespread, rapid grounding line retreat of Pine Island, Thwaites, Smith, and Kohler glaciers, West Antarctica, from 1992 to 2011. *Geophysical Research Letters*, 41(10), 3502–3509.
- Scambos, T. A., Fricker, H. A., Liu, C.-C., Bohlander, J., Fastook, J., Sargent, A., Massom, R., & Wu, A.-M. (2009). Ice shelf disintegration by plate bending and hydro-fracture: Satellite observations and model results of the 2008 Wilkins ice shelf break-ups. *Earth and Planetary Science Letters*, 280(1–4), 51–60.

- Scambos, T. A., Hulbe, C., & Fahnestock, M. (2003). Climate-induced ice shelf disintegration in the Antarctic Peninsula. *Antarctic Peninsula climate variability: Historical and paleoenvironmental perspectives*, 79, 79–92.
- Sellers, W. D. (1969). A global climatic model based on the energy balance of the earth-atmosphere system. *Journal of Applied Meteorology (1962-1982)*, 392–400.
- Sergienko, O., & Macayeal, D. R. (2005). Surface melting on Larsen ice shelf, Antarctica. *Annals of Glaciology*, 40, 215–218.
- Swithinbank, C. (1988). Satellite image atlas of glaciers of the world-Antarctica.
- The Firm Symposium team. (2024). Firm on ice sheets. *Nature Reviews Earth & Environment*, 5(2), 79–99.
- Torinesi, O., Fily, M., & Genthon, C. (2003). Variability and trends of the summer melt period of Antarctic ice margins since 1980 from microwave sensors. *Journal of Climate*, 16(7), 1047–1060.
- Trusel, L., Frey, K. E., & Das, S. B. (2012). Antarctic surface melting dynamics: Enhanced perspectives from radar scatterometer data. *Journal of Geophysical Research: Earth Surface*, 117(F2).
- Trusel, L., Frey, K. E., Das, S. B., Karnauskas, K. B., Kuipers Munneke, P., Van Meijgaard, E., & Van den Broeke, M. R. (2015). Divergent trajectories of Antarctic surface melt under two twenty-first-century climate scenarios. *Nature Geoscience*, 8(12), 927–932.
- Trusel, L., Frey, K. E., Das, S. B., Kuipers Munneke, P., & Van den Broeke, M. (2013). Satellite-based estimates of Antarctic surface meltwater fluxes. *Geophysical Research Letters*, 40(23), 6148–6153.
- van Wessem, J. M., Ligtenberg, S. R. M., Reijmer, C. H., Van de Berg, W. J., Van den Broeke, M. R., Barrand, N. E., Thomas, E. R., Turner, J., Wuite, J., Scambos, T. A., & van Meijgaard, E. (2016). The modelled surface mass balance of the Antarctic Peninsula at 5.5 km horizontal resolution. *The Cryosphere*, 10(1), 271–285.
- van Wessem, J. M., Van de Berg, W. J., Noël, B. P., Van Meijgaard, E., Amory, C., Birnbaum, G., Jakobs, C. L., Krüger, K., Lenaerts, J., Lhermitte, S., et al. (2018). Modelling the climate and surface mass balance of polar ice sheets using RACMO2–Part 2: Antarctica (1979–2016). *The Cryosphere*, 12(4), 1479–1498.
- Wang, Y., Zhang, X., Ning, W., Lazzara, M. A., Ding, M., Reijmer, C. H., Smeets, P. C., Grigioni, P., Heil, P., Thomas, E. R., et al. (2023). The AntAWS dataset: a compilation of Antarctic automatic weather station observations. *Earth System Science Data*, 15(1), 411–429.
- Weertman, J. (1973). Can a water-filled crevasse reach the bottom surface of a glacier. *IASH publ*, 95, 139–145.
- Zheng, L., Cheng, X., Shang, X., Chen, Z., Liang, Q., & Wang, K. (2022). Greenland Ice Sheet daily surface melt flux observed from space. *Geophysical Research Letters*, 49(6), e2021GL096690.
- Zhu, Q., Guo, H., Zhang, L., Liang, D., Wu, Z., de Roda Husman, S., & Du, X. (2024). Automated surface melt detection over the Antarctic from Sentinel-1 imagery using deep learning. *International Journal of Applied Earth Observation and Geoinformation*, 130, 103895.
- Zhu, X., Tuia, D., Mou, L., Xia, G.-S., Zhang, L., Xu, F., & Fraundorfer, F. (2017). Deep learning in remote sensing: A comprehensive review and list of resources. *IEEE geoscience and remote sensing magazine*, 5(4), 8–36.
- Zwally, H. J., & Fiegles, S. (1994). Extent and duration of Antarctic surface melting. *Journal of Glaciology*, 40(136), 463–475.

2

REMOTE SENSING OF SURFACE MELT ON ANTARCTICA: OPPORTUNITIES AND CHALLENGES

**Sophie de Roda Husman, Zhongyang Hu, Bert Wouters,
Peter Kuipers Munneke, Sanne Veldhuijsen, Stef Lhermitte**

This chapter has been published in IEEE Journal of Selected Topics in Applied Earth Observations and Remote Sensing as **de Roda Husman *et al.*, 2022**.

ABSTRACT

Surface melt is an important driver of ice shelf disintegration and its consequent mass loss over the Antarctic Ice Sheet. Monitoring surface melt using satellite remote sensing can enhance our understanding of ice shelf stability. However, the sensors do not measure the actual physical process of surface melt, but rather observe the presence of liquid water. Moreover, the sensor observations are influenced by the sensor characteristics and surface properties. Therefore, large inconsistencies can exist in the derived melt estimates from different sensors. In this study, we apply state-of-the-art melt detection algorithms to four frequently used remote sensing instruments: two active microwave instruments, ASCAT (Advanced Scatterometer) and Sentinel-1, a passive microwave sensor SSMIS (Special Sensor Microwave Imager/Sounder), and an optical sensor MODIS (Moderate Resolution Imaging Spectroradiometer). We intercompare the melt detection results over the entire Antarctic Ice Sheet and four selected study regions for the melt seasons 2015–2020. Our results show large spatiotemporal differences in detected melt between the sensors, with particular disagreement in blue ice areas, in aquifer regions, and during wintertime surface melt. We discuss that discrepancies between sensors are mainly due to (1) cloud obstruction and polar darkness, (2) frequency-dependent penetration of satellite signals, (3) temporal resolution, and (4) spatial resolution, as well as (5) the applied melt detection methods. Nevertheless, we argue that different sensors can complement each other, enabling improved detection of surface melt over the Antarctic Ice Sheet.

2.1. INTRODUCTION

LARGE uncertainty about the future viability of the Antarctic ice shelves leads to an enormous spread in sea level rise projections (Bakker *et al.*, 2017; Church *et al.*, 2013; Edwards *et al.*, 2021; Pörtner *et al.*, 2019, 2022). Estimates on the contribution of the Antarctic Ice Sheet over the next century range from +0.03 to +0.34 m of sea level equivalent under Representative Concentration Pathway (RCP) 8.5 according to the Sixth Assessment Report (Pörtner *et al.*, 2022). By far the largest direct contribution to the present-day Antarctic Ice Sheet mass loss is enhanced basal melt and increased iceberg calving. In the mass balance of Antarctica, direct mass loss by surface melt and subsequent runoff currently play a marginal role (Donat-Magnin *et al.*, 2021; Rignot *et al.*, 2019). However, surface melt can lead to enhanced mass loss indirectly, by destabilization of ice shelves (Bell *et al.*, 2018; Gilbert & Kittel, 2021; Kuipers Munneke *et al.*, 2014; Scambos *et al.*, 2009). When melt ponds drain into crevasses in the ice shelf, the stress of the meltwater column exerted on the crevasse tip can promote fracture, resulting in a weakened ice shelf (Nye, 1957; Weertman, 1973). Moreover, the load of meltwater lakes causes flexural stresses in the ice shelf, that generate fractures, further weakening the ice shelf (Banwell *et al.*, 2019; MacAyeal *et al.*, 2015; van der Veen, 2007). Recent climate models that incorporate the impact of meltwater on ice shelf instability (e.g., DeConto & Pollard, 2016) suggest that surface meltwater will result in widespread melting and hydrofracturing during this century, leading to a significant increase in the contribution of the Antarctic Ice Sheet to sea level rise. Regardless of the ice shelf processes in these models, Antarctic surface melt is projected to double by 2050 due to atmospheric warming (Gilbert & Kittel, 2021; Trusel *et al.*, 2015). In this context, monitoring the presence of surface melt on the Antarctic ice shelves can improve our understanding of the fundamental processes involved in the coupling between meltwater production and future Antarctic mass loss, ultimately improving our sea level rise projections and reducing their uncertainties.

At present, there are three methods to estimate surface melt, using automatic weather stations (AWSs), physics-based (regional) climate models (RCMs), and remote sensing. First, AWS observations can be used to compute the surface energy balance and estimate the excess energy available for surface melt. For instance, Vaughan (2006) studied observations from nine AWSs dating back to 1947, solely using temperature data. Studies followed that used more sophisticated AWSs equipped with radiation sensors (Kuipers Munneke *et al.*, 2018; Kuipers Munneke *et al.*, 2014). While AWS observations are widely used and considered ‘ground truth’ (Jakobs *et al.*, 2020), the main drawback of AWS observations is that the data are point-based on a limited number of locations, making them insufficient for continent-wide melt studies. Moreover, AWS locations are heavily biased towards homogeneous snow surface types, disregarding more challenging surface types like blue ice, slush, and other wet surface types.

The second approach to estimate surface melt is using RCMs, such as Modèle Atmosphérique Régional (MAR) (e.g., Agosta *et al.*, 2019) or Regional Atmospheric Climate Model (RACMO2) (e.g., van Wessem *et al.*, 2018). RCMs can simulate surface melt on a continental scale. Nevertheless, the accuracy of models relies on the

resolution and accuracy of its forcing data, which are often unsatisfactory for the Antarctic Ice Sheet (Zheng *et al.*, 2019). Moreover, melt features over low albedo regions are often more detailed than the model resolution and can therefore not accurately be captured by RCMs (Hu *et al.*, 2021; Kingslake *et al.*, 2017; Lenaerts *et al.*, 2017).

Remote sensing is an alternative to derive long-term (back to 1970s) melt dynamics at various spatiotemporal resolutions. Optical sensors have been used not only to detect meltwater presence, such as supraglacial streams, lakes (Dirscherl *et al.*, 2020; Kingslake *et al.*, 2017; Spergel *et al.*, 2021), and slush (Dell *et al.*, 2022), but also to estimate meltwater extent (D. K. Hall *et al.*, 2006; D. K. Hall *et al.*, 2008, 2013; Lenaerts *et al.*, 2017) and volume (Arthur *et al.*, 2022; Dell *et al.*, 2020; Moussavi *et al.*, 2020). Microwave sensors have also been used for detecting the presence of meltwater, for example the active microwave Ku-band (12–18 GHz) from Quick Scatterometer (QuikSCAT) (Trusel *et al.*, 2012), C-band (4–8 GHz) from Advanced Scatterometer (ASCAT) (Bevan *et al.*, 2018) and satellite mission Sentinel-1 (Datta *et al.*, 2019; Dirscherl *et al.*, 2021; Dunmire *et al.*, 2020; Li *et al.*, 2021; D. Liang *et al.*, 2021), and passive microwave K-band (18–27 GHz) and K_a -band (27–40 GHz) from Scanning Multichannel Microwave Radiometer (SSMR) and Special Sensor Microwave/Imagers (SSM/I) (Liu *et al.*, 2006; Picard & Fily, 2006; Tedesco *et al.*, 2007; Tedesco & Monaghan, 2009; Torinesi *et al.*, 2003), and L-band (1–2 GHz) sensors like Soil Moisture Active Passive (SMAP) (Colliander *et al.*, 2022; Mousavi *et al.*, 2022) and Soil Moisture and Ocean Salinity (SMOS) (Leduc-Leballeur *et al.*, 2020). Attempts to convert binary detected surface melt to continuous estimates of meltwater volume have been carried out using QuikSCAT (Trusel *et al.*, 2013) and Special Sensor Microwave Imager/Sounder (SSMIS) (over Greenland, Zheng *et al.*, 2022).

Remote sensing satellites provide information on the Antarctic surface in the visible to the microwave part of the electromagnetic spectrum, i.e., surface reflectance, backscatter intensity (σ^0), and brightness temperature (T_b). The value of surface reflectance, σ^0 , and T_b are altered under the presence of liquid water. These parameters therefore are indicators for the presence of liquid water, rather than for the actual physical process of surface melt, which is in fact an energy (conversion) process. Except perhaps, in the case of thermal infrared-derived surface temperature, which defines the occurrence of surface melt at the melting point. Yet, the term ‘surface melt’ is widely used in the remote sensing community (e.g., Banwell *et al.*, 2019; Gilbert & Kittel, 2021; Kuipers Munneke *et al.*, 2018; Trusel *et al.*, 2015), and we will adopt it here, although we do acknowledge that sensors measure the presence of liquid water. Apart from this, spaceborne observations of backscatter intensity, brightness temperature, and surface reflectance depend on sensor characteristics and surface properties. In this regard, large inconsistencies can exist in derived surface melt estimates from different sensors (Zheng *et al.*, 2019).

This study aims to identify the opportunities and challenges for melt detection over the Antarctic Ice Sheet using remote sensing, focusing on currently operating instruments that are capable of detecting wet surfaces (e.g., wet snow, slush, melt ponds, and streams). We compare differences in melt detection among a frequently used radiometer (SSMIS), scatterometer (ASCAT), Synthetic Aperture

Radar (SAR) (Sentinel-1), and optical sensor (MODIS, Moderate Resolution Imaging Spectroradiometer). In this study, we exclude satellites that are no longer operational (such as QuikSCAT). Moreover, L-band sensors (such as SMOS and SMAP) are not considered, as they are less sensitive to surface melt than K-band and K_a -band sensors (such as SSMIS) (Leduc-Leballeur *et al.*, 2020). In Section 2.2, we introduce the background of monitoring surface melt using different sensors and related research. Next, we introduce the satellite and auxiliary data sets in Section 2.3. Then, we summarize the state-of-the-art methods we applied for surface melt detection in Section 2.4 separately for each sensor type. In Section 2.5, we apply the melt detection methods to MODIS, Sentinel-1, ASCAT, and SSMIS over the entire Antarctic Ice Sheet for melt seasons 2015–2020. We compare spatial and temporal patterns of retrieved surface melt and assess the sensitivity of the methods. Based on this intercomparison, we discuss the possibilities and challenges of the different sensors and methods in Section 2.6. Finally, we summarize the main opportunities and challenges for remote sensing of surface melt in Section 2.7.

2.2. BACKGROUND AND RELATED RESEARCH

Before applying melt detection algorithms to the sensor observations, we illustrate *what* satellite sensors are detecting, and *how* this is linked to surface melt. Figure 2.1 shows the measuring principles of optical, active microwave, and passive microwave sensors under different atmospheric and melting conditions. In this study, we focus on active microwave instruments (i.e., ASCAT and Sentinel-1) that operate at frequencies between 5.2 and 5.4 GHz (C-band; wavelength of 5.6 cm), and passive microwave sensors at 19 GHz (K-band; wavelength: 1.6 cm) and at 37 GHz (K_a -band; wavelength of 0.8 cm). Figure 2.1a shows a dry snowpack, in which active microwave sensors can penetrate to a depth of around 10 m (Ulaby *et al.*, 1986), passive microwave sensors to a smaller penetration depth of around 2.5 m for 19 GHz (and 0.5 m for 37 GHz, not shown in Figure 2.1a) (Ulaby *et al.*, 1986), whereas optical sensors only measure surface reflectance. Figure 2.1b shows a snowpack under melting conditions under daylight and cloud-free conditions, and Figure 2.1c shows the same melt situations but in a cloudy and/or night situation. Signals from active and passive microwave sensors are (almost) unaffected by atmospheric conditions, whereas optical sensors depend on reflected sunlight. Figure 2.1d denotes near-surface melt presence, which can form due to near-surface melting (Brandt & Warren, 1993; Colbeck, 1989), after a snowfall event or after meltwater percolation from the surface (Lenaerts *et al.*, 2017).

Optical sensors measure the surface reflectance when atmospheric and topographical effects are removed from the visible through the shortwave infrared spectral bands. Since the total surface reflectance depends on the surface properties, the reflectance of snow, ice, water, and bare rocks can be used to discriminate between land surface types (D. K. Hall & Martinec, 1985; Hui *et al.*, 2014; Tedesco, 2014). The refractive indices of water and ice are similar and therefore do not directly change the surface reflectance when snow melts. However, the presence of liquid water changes the surface reflectance indirectly, because liquid water increases the snow

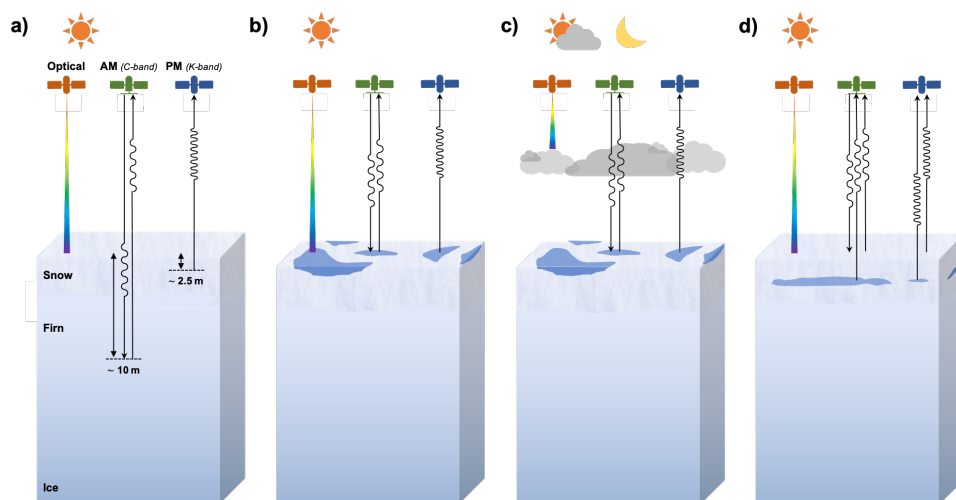


Figure 2.1: Conceptual overview of working principles of optical, active, and passive microwave sensors under different atmospheric and melting conditions. (a) no melt and sunlight, (b) surface melt and sunlight, (c) surface melt and no sunlight due to cloudy and/or nighttime conditions, (d) near-surface melt and sunlight. AM indicates active microwave sensors and PM passive microwave sensors.

grain size (Dozier *et al.*, 1981; Tedesco, 2014). Ponding water on the other hand changes the spectral properties of the surface, causing a drop in near-infrared, red and green reflectance (Choudhury & Chang, 1979; Luckman *et al.*, 2014). This results in a blue appearance of melt components in true-color imagery, such as slush, melt ponds, and streams (Dell *et al.*, 2022; Dirscherl *et al.*, 2020).

Active microwave sensors detect the reflected portion of a radar signal emitted by the satellite, known as the backscatter intensity. The backscatter intensity depends on the snow dielectric properties and the surface roughness, and hence is very sensitive to liquid water content within the snowpack (Ulaby *et al.*, 1986). Liquid water increases the absorption of the microwave radiation and also increases forward scattering, both leading to a decreased backscatter intensity compared to dry surfaces (Ashcraft & Long, 2006; Liu *et al.*, 2006). Therefore, a drop in the backscatter intensity is associated with melt presence. Nevertheless, melt detection on surfaces with a very high or low roughness can be challenging. Surfaces may become rougher under the presence of liquid water, for example by creating small meltwater streams (D. Hall *et al.*, 2000; Shi & Dozier, 1995). This process increases the backscatter intensity, thereby confusing meltwater detection algorithms that look for a drop in backscatter intensity under melting conditions. Over very flat surfaces (e.g., blue ice), active microwave sensors might fail to detect surface melt, because sensors receive (almost) no backscattered signal during non-melt periods (Nagler *et al.*, 2016; Ulaby *et al.*, 1981). Hence, an increased liquid water content does not further reduce the backscatter intensity.

Passive microwave sensors detect the brightness temperature, which is a function of the liquid water content, temperature, density, and grain size of the snowpack (Mote & Anderson, 1995). From all these factors, the liquid water content is assumed to have the largest influence on the brightness temperature (Hofer & Mätzler, 1980; Tedesco *et al.*, 2007). When snow melts, the liquid water content increases the imaginary part of the electromagnetic permittivity, which results in an increased brightness temperature (Hallikainen *et al.*, 1987; Ulaby *et al.*, 1986). However, other factors such as larger grain size, may also increase the brightness temperature, potentially leading to falsely detected melt.

Changes in remote sensing data form the basis for many melt detection algorithms. Most optical algorithms rely on thresholds based on a modified normalized difference water index adapted for ice ($NDWI_{ice}$) (Bell *et al.*, 2017; Dell *et al.*, 2020; Williamson *et al.*, 2018; Yang & Smith, 2012), occasionally also including some additional thresholds (Moussavi *et al.*, 2020). Recently, machine learning techniques have been deployed for the detection of meltwater (Dirscherl *et al.*, 2020; Halberstadt *et al.*, 2020) and slush (Dell *et al.*, 2022). However, it should be noted that besides the slush detection of Dell *et al.* (2022), the listed methods focus on supraglacial lakes and streams, instead of the broader focus of this research on all meltwater types.

Meltwater detection algorithms using microwave signals allow for studying the seasonal variations of backscatter intensity and brightness temperature, as observations are also retrieved during winter (Figure 2.1c). For C-band active microwave sensors, Ashcraft and Long (2006) developed a method that assumed melt when the backscatter intensity is lower than the annual winter mean minus 3 dB. The threshold of 3 dB aligns well with theoretical results and direct observations (Stiles & Ulaby, 1980). While this approach is widely used for melt detection in Antarctica (e.g., Banwell *et al.*, 2019; Johnson *et al.*, 2020; Zhou *et al.*, 2019), also other thresholds have been used, for example using multiple thresholds (Trusel *et al.*, 2012) or adaptive thresholds (Bothale *et al.*, 2015).

Most passive microwave-based melt detection methods make use of the 19 GHz horizontally polarized channel, since this frequency and polarization show the lowest T_b over dry firn, thereby maximizing the increase in T_b by an increased liquid water content (Liu *et al.*, 2006). Already in the 1990s, Zwally and Fiegles (Zwally & Fiegles, 1994) developed a method for melt detection over Antarctica using the 19 GHz horizontal channel. They assumed melt to occur when the measured brightness temperature exceeds the annual winter mean by 30 K, similar to the method proposed in Mote *et al.* (1993) for melt detection over the Greenland Ice Sheet. We refer to this method as M+30. Torinesi *et al.* (2003) suggested a more advanced method, referred to as M+3S, in which they used a dynamic threshold based on the standard deviation of the T_b signal. In 2002, Ramage and Isacks (2002) developed the diurnal amplitude variations (DAV) method, which has been successfully applied to study surface melt (Tedesco *et al.*, 2009; Zheng *et al.*, 2018, 2020). The high revisit time of twice a day for many passive microwave sensors allows making use of the difference between the morning and afternoon T_b signal, when melt and subsequent refreezing occurs. Tedesco *et al.* (2009) found that the DAV algorithm reduces the underestimation of surface melt that can exist for the M+30 and M+3S methods. The

DAV algorithm works best for the 37 GHz vertically polarized channel, as it is less noisier than the 19 GHz channel (Semmens *et al.*, 2013). Besides the M+30, M+3S, and DAV algorithms, other studies applied statistical K-means clustering (Johnson *et al.*, 2020) and the cross-polarization (horizontal and vertical) gradient ratio (XPGR) of the 19 GHz and 37 GHz frequencies (Abdalati & Steffen, 1995) for surface melt detection.

2.3. DATA

2.3.1. STUDY AREA

In this study, we assessed the spatiotemporal melt patterns on a continental scale, but specifically focused on four regions over which meltwater has been detected in previous studies: the Amery Ice Shelf, Roi Baudouin Ice Shelf, Shackleton Ice Shelf, and the Antarctic Peninsula (among others Larsen B and C, George VI, and Wilkins ice shelves) (see Figure 2.3).

2.3.2. SATELLITE IMAGERY

Data from four widely-used sensors and satellite missions (ASCAT, MODIS, Sentinel-1, and SSMIS) were acquired and preprocessed using the Google Earth Engine (Gorelick *et al.*, 2017). Table 2.1 provides an overview of the properties of the four types of satellite imagery.

The 4.45 km ASCAT enhanced resolution product with vertical polarization, developed by the NASA Scatterometer Climate Record Pathfinder Project (D. G. Long *et al.*, 1993), was downloaded from Brigham Young University Microwave Earth Remote Sensing Laboratory (D. Long, 2022). Over dry snowpacks in the interior of the Antarctic Ice Sheet the backscatter intensity is very weak, due to deep penetration of the microwave signals (Arigony-Neto *et al.*, 2009). These low signal-to-noise pixels were therefore masked. We followed Zheng and Zhou (2020) and assumed a low signal-to-noise ratio when a pixel fulfilled one of the following conditions: (1) the winter (June to August) mean was lower than -14 dB or (2) the minimum winter backscatter intensity was less than 3 dB smaller than the minimum summer (December to February) backscatter intensity.

For MODIS, the MOD09GA (MODIS/Terra Surface Reflectance Daily L2G Global 1 km and 500 m SIN Grid) and MYD09GA (MODIS/Aqua Surface Reflectance Daily L2G Global 1 km and 500 m SIN Grid) products were acquired and combined into daily composites based on the least cloudy observation. This data set provides a daily visible and near-infrared reflectance over the Antarctic Ice Sheet, in which cloud pixels were masked out according to the *1 km Reflectance Data State QA* band.

This study used Sentinel-1 Level-1 Ground Range Detected (GRD) scenes available in Google Earth Engine, where they were preprocessed using the Sentinel-1 Toolbox to generate a calibrated, orthorectified product (Gorelick *et al.*, 2017). All available horizontally polarized GRD scenes over the Antarctic Ice Sheet for the five melt seasons were selected, giving a combination of Interferometric (IW) and Extra Wide (EW) overpasses, for which the melt detection algorithm was applied per orbit.

Similar to ASCAT, pixels with a low signal-to-noise ratio in the interior of the Antarctic Ice Sheet were masked.

For SSMIS two melt detection algorithms were implemented, i.e., M+3S (abbreviated to SSMIS_{M+3S}) and DAV (abbreviated to SSMIS_{DAV}), with each algorithm requiring different input data. The SSMIS_{M+3S} results were computed using horizontally polarized 19 GHz observations with a spatial resolution of 6.25 km, the finest enhanced resolution product available for the 19 GHz frequency. Observations from platform F17 were ingested, which has the highest orbit stability (Remote Sensing Systems (RSS), 2022). The SSMIS_{DAV} algorithm gives best results for vertically polarized 37 GHz observations (Semmens *et al.*, 2013). Observations with a spatial resolution of 3.125 km were used, the finest spatial resolution for the 37 GHz frequency. The vertically polarized 37 GHz data of platform F17 are corrupted from April 2016 onward. Therefore, data from the F18 platform were used instead, which have a lower orbit stability than data from the F17 platform, but nevertheless a similar overpass time as platform F17 when averaged over the study period. All SSMIS observations were obtained from the National Snow and Ice Data Center (Meier *et al.*, 2022).

2.3.3. WEATHER STATIONS

Three hourly 2 m air temperature observations from AWS14, located at the Larsen C Ice Shelf, were used. The daily minimum and maximum values were selected and compared to the satellite observations and derived melt predictions. We used the temperature observations to interpret the disagreement between the sensors in detected melt over AWS14. Even though surface temperatures below freezing point can occasionally also lead to melt (Koh & Jordan, 1995), the positive air temperatures from the weather station were used as first indication for melt presence, similar to many studies (e.g., L. Liang *et al.*, 2013; Steiner & Tedesco, 2014; Tedesco & Monaghan, 2009; Trusel *et al.*, 2012).

2.3.4. PRECIPITATION DATA

Precipitation data from RACMO version 2.3p2, which are dynamically downscaled ERA-5 (van Wessem *et al.*, 2018), were compared to the detected melt of the four remote sensing satellites. Surface melt can turn into near-surface melt after a snowfall event (Liston & Winther, 2005) and therefore remain unnoticed by MODIS. For that reason, we examined whether precipitation events could explain some of the disagreement in detected melt between MODIS and the other three satellites.

2.3.5. SEA ICE CONCENTRATION

The global 4 km sea ice concentration product PFV53 (AVHRR Pathfinder Sea Surface Temperature Version 5.3), available in the Google Earth Engine (Kilpatrick *et al.*, 2001), was compared to SSMIS_{M+3S} observations. The large measurement response function of SSMIS 19 GHz, with a footprint of ~72 km by ~44 km (Brodzik *et al.*, 2016), means that the reported T_b may be contaminated by the pixel surroundings.

Table 2.1: Properties of the remote sensing sensors and satellite missions deployed in this study.

| | ASCAT | MODIS | Sentinel-1 | SSMIS |
|----------------------------|--------------|-------------------------------------|------------------------------------|----------------------------------|
| Start date | October 2006 | Feb 2000 (Terra) Jul 2002 (Aqua) | Apr 2014 (S-1A) Apr 2016 (S-1B) | Mar 2008 (F17) Mar 2010 (F18) |
| Spatial resolution | 4.45 km | 250–1000 m | 5–40 m | 3.125–6.25 km |
| Temporal resolution | Twice a day | Twice a day | 1–7 days | Twice a day |
| Overpass time | 6:00, 18:00 | 10:30, 13:30 | Orbit-dependent | 6:00, 18:00 |

In the case of a near-coastal pixel surrounded by open water, the effect on the T_b observation can be large, since open water has a very low T_b compared to (sea) ice.

The allocated sea ice concentration for a near-coastal SSMIS pixel was presumed to be the average sea ice concentration of all ocean pixels in the buffering area with a radius of 58 km around the pixel of interest, corresponding to the mean of the measurement response function.

2.3.6. CONTOUR LINES

The grounding line, coastline, and outlines of the ice shelves were obtained from the National Snow and Ice Data Center MEaSUREs campaign created between 2007 and 2009 (Mouginot *et al.*, 2017). The outlines of the individual ice shelves were clipped using the more up-to-date coastline product of the British Antarctic Survey from 2021 (Gerrish *et al.*, 2021). Finally, we used a digital elevation model (DEM) of Antarctica based on CryoSat-2 observations between July 2010 and July 2016 (Slater *et al.*, 2018) to eliminate elevations over 1700 meters (similar to e.g., Banwell *et al.*, 2021), at which melt is not expected.

2.4. METHODS

2.4.1. MELT DETECTION METHODS

We computed the binary melt presence, $m(t)$ (0: no melt, 1: melt), for the four studied remote sensing instruments using state-of-the-art melt detection algorithms. We focused on austral summers (December, January, February) for five melt seasons, between (December) 2015 and (February) 2020.

Since both ASCAT and Sentinel-1 operate with C-band sensors, the same widely used melt detection algorithm was applied, proposed by Ashcraft and Long (2006). Melt presence is assumed when the backscatter intensity is smaller than the annual winter mean minus a certain threshold, by using Eq. (2.1) with

$$m(t) = \begin{cases} 1, & \sigma^0(t) < \sigma_{\text{winter}}^0 + \Delta\sigma^0 \\ 0, & \sigma^0(t) \geq \sigma_{\text{winter}}^0 + \Delta\sigma^0 \end{cases} \quad (2.1)$$

where σ_{winter}^0 is the average backscatter intensity of the previous winter (June to August) months and $\Delta\sigma^0$ is the threshold which is set to -3 dB. Sentinel-1 observations were processed on a per relative orbit basis.

For MODIS, we used the NDWI_{ice} to detect meltwater. Over Antarctica, different thresholds are used for detecting (1) supraglacial lakes, e.g., greater than 0.25 (Arthur *et al.*, 2020; Banwell *et al.*, 2019; Bell *et al.*, 2017; Yang & Smith, 2012); (2) slush, e.g., greater than 0.12 (Bell *et al.*, 2017; Dell *et al.*, 2022); and (3) meltwater, e.g., greater than 0.07 (Banwell *et al.*, 2019). In this study, we lowered the NDWI_{ice} threshold to 0.05 to include more potentially wet pixels, according to the spectral measurement of wet snow from Hannula and Pulliainen (Hannula & Pulliainen, 2019). Melt is assumed when a pixel agreed with the following equation,

$$m(t) = \begin{cases} 1, & \text{NDWI}_{\text{ice}}(t) > 0.05 \\ 0, & \text{NDWI}_{\text{ice}}(t) \leq 0.05 \end{cases} \quad (2.2)$$

where NDWI_{ice} is the normalized difference between the observed surface reflectance in red and blue bands ($\text{NDWI}_{\text{ice}} = (\text{BLUE} - \text{RED})/(\text{BLUE} + \text{RED})$).

For SSMIS observations, we applied two melt detection algorithms, referred to as $\text{SSMIS}_{\text{M+3S}}$ and $\text{SSMIS}_{\text{DAV}}$. The $\text{SSMIS}_{\text{M+3S}}$ algorithm, developed by Torinesi *et al.* (2003), is comparable to the active microwave algorithm as it is also based on the annual winter mean plus a certain threshold. Torinesi *et al.* (2003) proposed a three-step approach to define a threshold. When the brightness temperature exceeds the winter mean plus the derived threshold, melt is assumed, using

$$m(t) = \begin{cases} 1, & T_b(t) > T_{b,\text{winter}} + \Delta T_b \\ 0, & T_b(t) \leq T_{b,\text{winter}} + \Delta T_b \end{cases} \quad (2.3)$$

where ΔT_b is the threshold which is set to at least 30 K, but can be as large as three times the standard deviation (Tedesco *et al.*, 2007). The standard deviation is obtained by computing the mean T_b over all observations of a melt year (from 1 April to 31 March), then excluding all observations exceeding the mean by at least 30 K, and repeating this process in three iterations. In this way, the high brightness temperatures are removed, and the standard deviation is computed using the filtered data set.

The second algorithm applied to SSMIS observations, referred to as $\text{SSMIS}_{\text{DAV}}$, makes use of the difference between morning and afternoon T_b . The method was first used by Ramage and Isacks (2002) over Alaska. Zheng *et al.* (2018) found that a threshold of 9 K was optimal for detecting surface melt over the Antarctic Ice Sheet. According to the $\text{SSMIS}_{\text{DAV}}$ algorithm, melt is assumed when a pixel agreed with the following equation,

$$m(t) = \begin{cases} 1, & |T_{b,\text{morning}}(t) - T_{b,\text{afternoon}}(t)| > \Delta\text{DAV} \\ 0, & |T_{b,\text{morning}}(t) - T_{b,\text{afternoon}}(t)| \leq \Delta\text{DAV} \end{cases} \quad (2.4)$$

where $T_{b,\text{morning}}$ and $T_{b,\text{afternoon}}$ are the brightness temperature of the morning and afternoon overpasses, and ΔDAV equals 9 K.

2.4.2. SENSITIVITY STUDIES

Multiple sensitivity studies were applied to assess the differences in detected melt for the four sensors. Our sensitivity analyses consisted of four parts, i.e., (1) spatiotemporal sensitivity, (2) overpass time sensitivity, (3) sensitivity to liquid water, and (4) melt detection algorithm sensitivity.

SPATIOTEMPORAL SENSITIVITY

Once the surface melt was detected in the satellite observations, we compared the results in both spatial and temporal domains. To study the spatial patterns, we calculated a summer melt occurrence (SMO; in percentage), a statistical representation to intercompare the detected melt, using

$$\text{SMO} = \frac{\# \text{ melt}}{\# \text{ observations}} \times 100 \text{ [\%]} \quad (2.5)$$

in which the number of melt observations ($\# \text{ melt}$) and the total number of observations ($\# \text{ observations}$) were computed per pixel. To calculate the $\# \text{ melt}$ we summed all the observations for which melt was detected over the five studied melt seasons, using the state-of-the-art melt detection algorithms as described in Section 2.4.1. We computed the $\# \text{ observations}$ by summing all the available observations over the studied melt seasons. An SMO of 0% means that there was no melt observed over the studied period, whereas an SMO of 100% holds that over all the observations melt was detected.

For ASCAT, Sentinel-1, and SSMIS, we used all the observations. For MODIS, SMO is solely calculated based on cloud-free pixels. While the role of clouds on melt is still under debate, clouds alter shortwave/longwave energy budget which could lead to (additional) melting (Bintanja & Van den Broeke, 1996; Hofer & Mätzler, 1980; Izeboud *et al.*, 2020; Van den Broeke *et al.*, 2006; Van Tricht *et al.*, 2016). Therefore, MODIS likely underestimates melt in cloudy regions, preventing an unbiased comparison between MODIS and the other sensors.

For the temporal analysis, time series were created to analyze the satellite signals over seven locations. These locations were selected based on their large difference in SMO between the sensors. For all the points, we compared both the input signals in the used melt detection algorithms (i.e., σ^0 , NDWI_{ice} , and T_b) as the derived melt. Again note that, especially for optical imagery, this can lead to biased results, as surface melt is possibly correlated to cloudiness.

OVERPASS TIME SENSITIVITY

To assess the sensitivity of the melt detection algorithms to overpass time, we analyzed the SMO for both ASCAT and $\text{SSMIS}_{\text{M}+3\text{S}}$ for morning and afternoon observations separately. This analysis was performed over the four study areas described in Section 2.3.1, where for the Antarctic Peninsula only the ice shelf pixels were analyzed.

The overpass time sensitivity analysis was not applied to Sentinel-1 and MODIS due to the lack of balanced morning and afternoon datasets. In case of Sentinel-1,

the data availability depends on the acquisition strategy, resulting in unbalanced global coverage. For example, over the Larsen C Ice Shelf, 58% of the observations were captured in the early morning (3 AM – 6 AM), compared to 42% in the evening (6 PM – 9 PM). Similarly, MODIS lacks an equal number of cloud-free observations for the morning (10:30 AM) and afternoon (1:30 PM). Frequent cloud cover over the Antarctic Ice Sheet leads to seasonal differences in the number of Aqua and Terra observations (King *et al.*, 2005). Finally, the melt results from SSMIS_{DAV} were excluded from the overpass time sensitivity analysis, as the algorithm combines morning and afternoon observations into a single daily melt product.

SENSITIVITY TO LIQUID WATER

The Snow Microwave Radiative Transfer (SMRT) (Picard *et al.*, 2018) model was used to study the sensitivity of microwave sensors to the presence of liquid water. SMRT is a one-dimensional model that simulates the interaction of microwave signals with a stack of horizontal layers, each with its specific properties (such as density, temperature, liquid water) (Picard *et al.*, 2018, 2022). Similar to Picard *et al.* (2022), the exponential representation was selected to model the microstructure of the snowpack. This representation assumes an exponential function for the correlation function, therefore information about the grain size did not have to be provided, and only the correlation length of each layer was required. The implemented model framework was similar to other SMRT studies (Picard *et al.*, 2018, 2022; Vargel *et al.*, 2020). The improved Born approximation (IBA) theory (Mätzler, 1998) was selected to compute the scattering and absorption coefficients per layer, and the radiative transfer equation for the whole snowpack was solved according to the discrete ordinate and eigenvalue (DORT) method (Picard *et al.*, 2018).

The SMRT model was used to simulate the backscatter intensity of ASCAT and Sentinel-1, and brightness temperature of SSMIS, for a snowpack with varying liquid water contents. The sensitivity of the sensors and satellites to liquid water was assessed with the following settings: ASCAT (frequency: 5.4 GHz; polarization: VV; incidence angle: 40°), Sentinel-1 (frequency: 5.2 GHz; polarization: HH; incidence angle: 40°), SSMIS for SSMIS_{M+3S} algorithm (frequency: 19 GHz; polarization: H; incidence angle: 55°), and SSMIS for SSMIS_{DAV} algorithm (frequency: 37 GHz; polarization: V; incidence angle: 55°). The default snowpack parameters for the upper layer (i.e., snow), middle layer (i.e., firn), and bottom layer (i.e., ice) are summarized in Table 2.2. The sensitivity of these parameters (i.e., thickness, density, correlation length, and temperature) was assessed by adjusting them one by one.

MELT DETECTION ALGORITHM SENSITIVITY

Since the assessed melt detection algorithms rely on thresholds to derive a binary no melt / melt estimate, we evaluated the sensitivity of the selected thresholds by comparing the SMO for different thresholds. This is important because smaller thresholds result in more melt, as smaller deviations are classified as melt, whereas larger thresholds result in less melt. To assess the threshold sensitivity we varied the thresholds applied in Eq. (2.1), (2.2), and (2.3). For ASCAT and Sentinel-1, we varied $\Delta\sigma^0$ from -5 dB to -1 dB with steps of 0.1 dB. For MODIS, we varied the threshold

Table 2.2: Default snowpack parameters for SMRT simulations.

| | Upper layer <i>Snow</i> | Middle layer <i>Firn</i> | Bottom layer <i>Ice</i> |
|-----------------------------------|----------------------------|-----------------------------|----------------------------|
| Thickness [m] | 0.1 | 10 | 100 |
| Density [kg/m³] | 200 | 600 | 900 |
| Correlation length [m] | 1e-4 | 5e-4 | 6e-4 |
| Temperature [K] | 270 | 250 | 240 |

of $NDWI_{ice}$ for melt detection from 0 to 0.1 with steps of 0.01. For $SSMIS_{M+3S}$, we varied ΔT_b from 20 K to 40 K with steps of 1 K. The ΔDAV threshold applied in the $SSMIS_{DAV}$ algorithm was varied from 5 K to 13 K with steps of 0.1 K.

Then, for each sensor/satellite we selected the thresholds that resulted in 10% more summed melt pixels compared to the default thresholds, which we defined as $SMO_{10\%}^+$. The same method was repeated to obtain the thresholds that resulted in 10% less melt, which we defined as $SMO_{10\%}^-$. Finally, the threshold sensitivity (TS) was computed using

$$TS = SMO_{10\%}^+ - SMO_{10\%}^- \quad (2.6)$$

in which TS is a value between 0 and 100%. When TS equaled 0%, the melt occurrence for a pixel was insensitive for the threshold, and the same SMO was obtained for the small and large threshold. For larger TS values, more melt was computed using the small threshold than for the large threshold.

2.5. RESULTS

2.5.1. DATA AVAILABILITY

Figure 2.2 shows the data availability of the four sensors and satellites over the examined melt seasons, covering the austral summers (December, January, February) from 2015 to 2020. The results indicate large differences in the number of observations for each sensor/satellite.

ASCAT has almost complete coverage over the entire Antarctic Ice Sheet, with accurate parameter retrieval to ~ 88 degrees south. However, there are some data gaps in the ASCAT data set, i.e., 22 days in the melt season of 2017–2018 and 30 days in melt season 2018–2019, are missing. Most of the data is missing over West Antarctica and Dronning Maud Land, resulting in ~ 450 overpasses in melt seasons 2015–2020, whereas over Victoria Land and Wilkes Land in East Antarctica ~ 600 observations can be studied. Besides periods of data gaps, ASCAT overpasses twice a day (~ 6 AM, ~ 6 PM local time) on alternating days.

MODIS has frequent coverage over the interior of Antarctica with approximately 400 acquisitions during the study period. However, over the ice shelves, MODIS is severely impacted by cloud cover. The Antarctic Peninsula is especially affected by

the persistent clouds. Over Larsen C ~85% of the observations are unusable as they are covered by clouds, translating to only 66 observations for the five melt seasons,

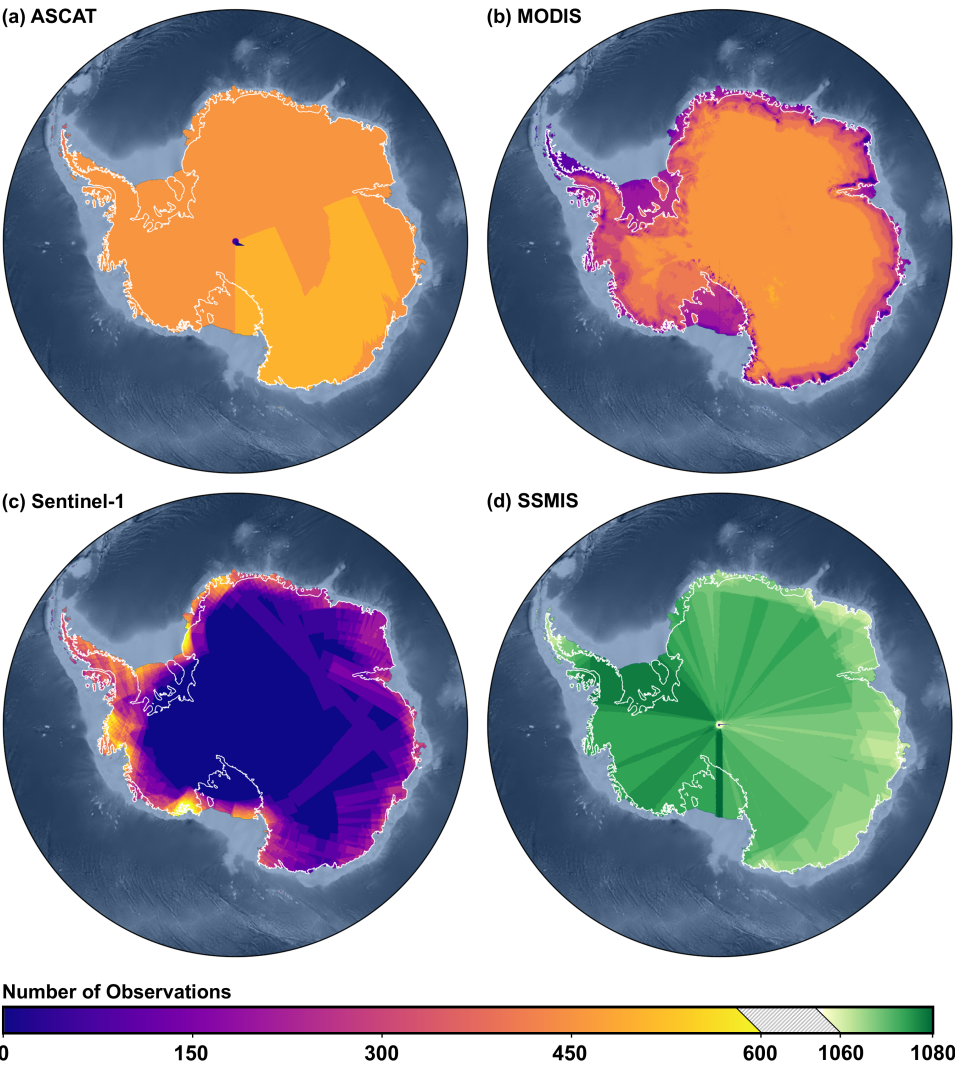


Figure 2.2: Large difference in the number of overpasses during the melt seasons (December, January, February) from 2015 to 2020 for (a) Advanced Scatterometer (ASCAT), (b) Moderate Resolution Imaging Spectroradiometer (MODIS), (c) Sentinel-1, and (d) Special Sensor Microwave Imager/Sounder (SSMIS). The number of overpasses for SSMIS shown in (d) is based on the observations of the F17 platform for the horizontally polarized 19 GHz channel (used for $SSMIS_{M+3S}$). SSMIS observations from the vertically polarized 37 GHz channel from the F18 platform (used for $SSMIS_{DAY}$) have a comparable number of overpasses (1082, without data gaps).

equivalent to an observation once every week.

Similar to MODIS, the number of observations for Sentinel-1 varies strongly between the interior of the Antarctic Ice Sheet and ice shelves. Sentinel-1 retrieves more observations over the ice shelves than over the interior of the ice sheet, as Sentinel-1 is a right-viewing satellite. Over the Antarctic Peninsula, there are ~450 overpasses, translating to more or less one overpass per day. The Sentinel-1 mission plan prescribes storing fewer observations over ice shelves in East Antarctica compared to West Antarctica, with ~200 overpasses over Amery, Roi Baudouin, and Shackleton Ice Shelves, translating to ~1 overpass every 2–3 days.

SSMIS has the highest overpass frequency, with ~1060 overpasses in total in East Antarctica and ~1080 in West Antarctica, for the 19 GHz horizontally polarized observations (used for the SSMIS_{M+3S} algorithm). The difference in overpass frequency is a result of some rare failures mostly influencing East Antarctica. For the SSMIS_{DAV} algorithm, for which 37 GHz vertically polarized observations were used, there is an overpass frequency of 1082 over the entire Antarctic Ice Sheet. It should be noted that the SSMIS_{DAV} algorithm combines a morning and an afternoon overpass for one melt observation, hence the total number of melt observations equals 541 for the study period.

2.5.2. SPATIOTEMPORAL SENSITIVITY

Figure 2.3 shows the spatial pattern of SMO for melt seasons from 2015 to 2020 over the Antarctic Ice Sheet and the four selected study regions. To further demonstrate the differences in melt detection between the sensors, we present the discrepancies in Figure 2.4.

When comparing the ASCAT SMO to the SMO of the other sensors, we find large variation over blue ice regions. The blue ice region located south-east on the Roi Baudouin Ice Shelf is the most clear example. At the location indicated with point *a* in Figure 2.4, ASCAT detects an SMO of 11%, whereas an SMO of 84%, 25%, and 43% are found for MODIS, SSMIS_{M+3S}, and SSMIS_{DAV}, respectively. Similar to ASCAT, also Sentinel-1 detects a low SMO of 12% over point *a*.

Large discrepancies between MODIS and the other sensors occur both over the center of the ice shelves and along the grounding lines. Over the center of the ice shelves, most of the MODIS observations are cloud-covered (see Figure 2.2), therefore the SMO was computed on a limited number of observations. MODIS detects an SMO of around 25% over the ice shelves, whereas the other sensors detect an SMO of at least 50% over the studied ice shelves.

On the contrary, MODIS results show an SMO exceeding 75% over the grounding lines of the Amery Ice Shelf, Roi Baudouin Ice Shelf, and Shackleton Ice Shelf, whereas the other sensors detect a lower SMO around 50%. These areas coincide with the blue ice areas as found by Winther *et al.* (2001). Over the location indicated with point *b* in Figure 2.4, MODIS detects an average SMO of 74%, whereas the SMO equals to 20% for MODIS, 7% for Sentinel-1, 0% for SSMIS_{M+3S}, and 9% for SSMIS_{DAV}. Due to the optical nature of MODIS, there are differences in SMO between MODIS and the other sensors over regions with near-surface melt, such as over a firn aquifer (point *c* in Figure 2.4) and surface melt covered by snowfall (point

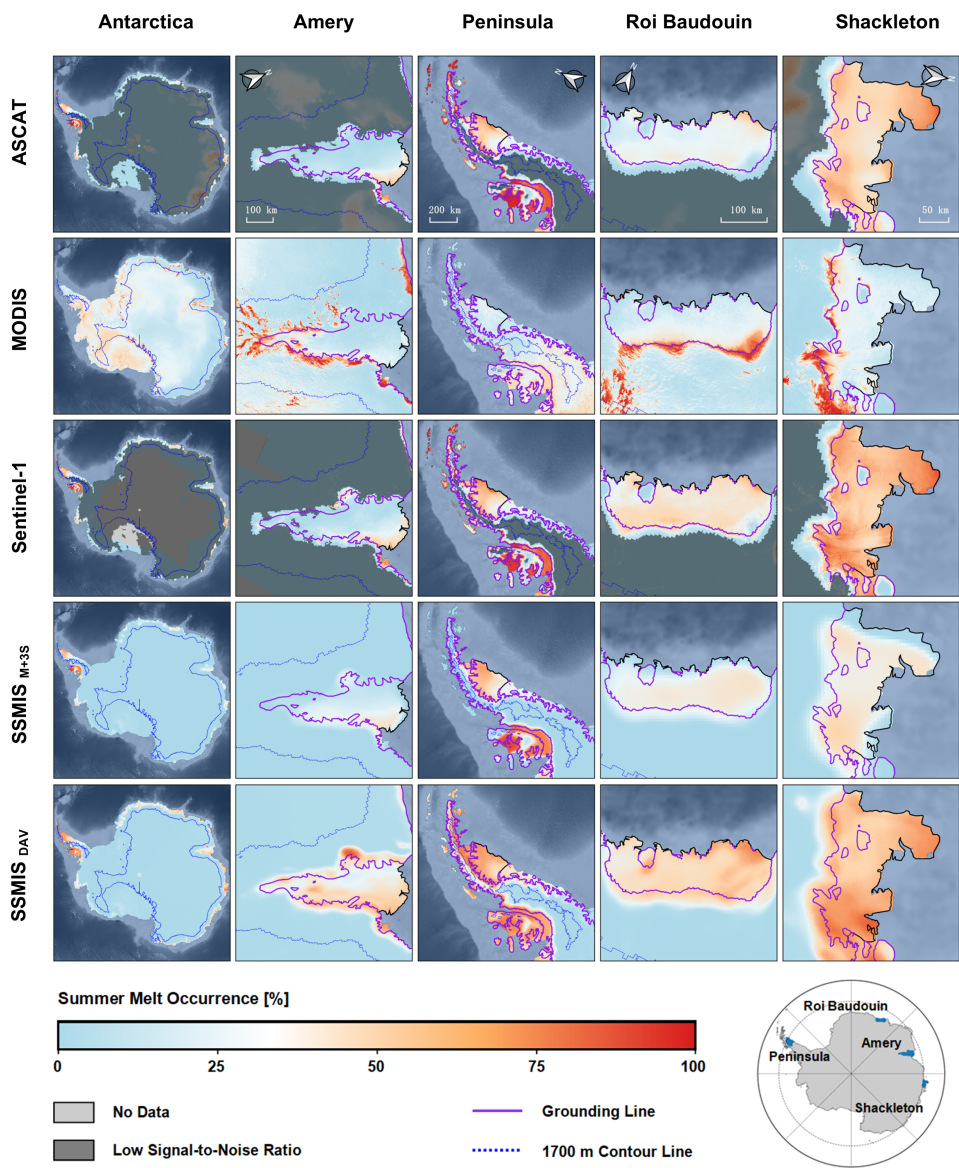


Figure 2.3: Melt occurrence for melt seasons 2015–2020 for Advanced Scatterometer (ASCAT), Moderate Resolution Imaging Spectroradiometer (MODIS), Sentinel-1, and Special Sensor Microwave Imager/Sounder (SSMIS) over the Antarctic Ice Sheet and four selected ice shelves. For the latter, two melt detection methods were applied, i.e., SSMIS_{M+3S} and SSMIS_{DAY}. The light gray areas have no overpasses over the study period. The dark gray areas in ASCAT and Sentinel-1 highlight the low signal-to-noise ratio areas in which the algorithm is unreliable.

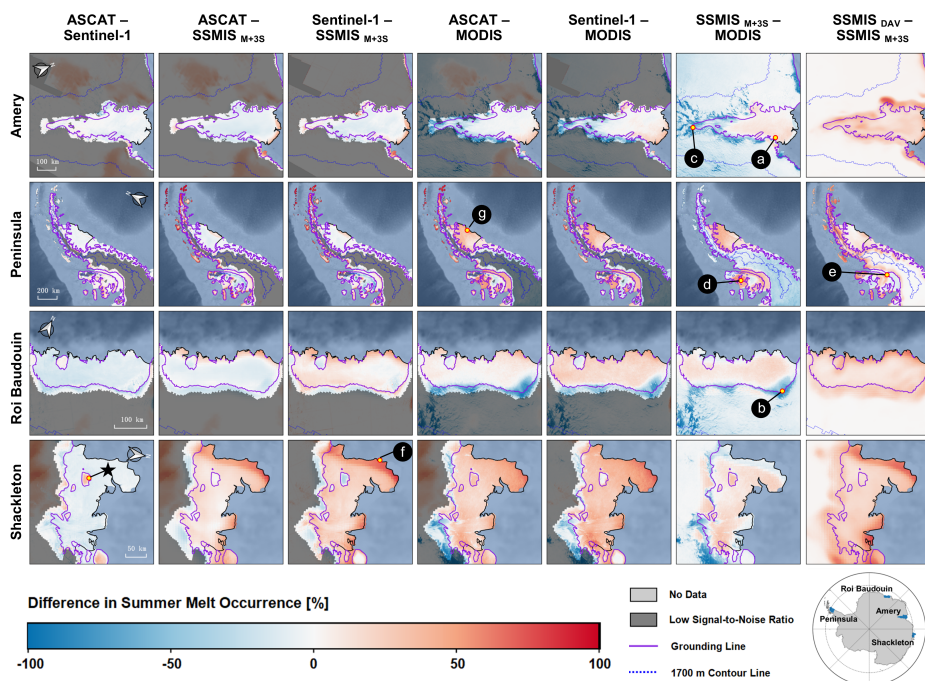


Figure 2.4: Difference in melt occurrence for melt seasons 2015–2020 between Advanced Scatterometer (ASCAT), Moderate Resolution Imaging Spectroradiometer (MODIS), Sentinel-1 and Special Sensor Microwave Imager/Sounder (SSMIS) over the four selected ice shelves. For the latter, two melt detection methods were applied, i.e., $SSMIS_{M+3S}$ and $SSMIS_{DAV}$. The results of $SSMIS_{M+3S}$ are compared to the other three sensors, and the last column compares $SSMIS_{M+3S}$ and $SSMIS_{DAV}$. Seven locations are selected for further analysis, i.e., (a) blue ice, (b) outlet glacier, (c) firn aquifer, (d) snowfall, (e) winter melt, (f) near-shore, and (g) persistent melt. The location indicated with a black star is discussed in the text.

d in Figure 2.4). Also winter melt events are missed by MODIS (point e in Figure 2.4).

Sentinel-1—with the finest spatial resolution of the four studied instruments—captures more detailed melt features than the other sensors. This is clearly visible for the most northern ice rise at the Shackleton Ice Shelf (indicated with a black star in Figure 2.4) that has an average elevation of 300 m. ASCAT and SSMIS (both $SSMIS_{M+3S}$ and $SSMIS_{DAV}$), with a coarser spatial resolution, detect a similar SMO over the ice rise as over the surrounding pixels, with values between 30% and 35% melt. A much lower SMO for Sentinel-1 is found over the ice rise, corresponding to an average SMO of 4%. Such a low SMO value would be expected at higher (and thus colder) elevations.

$SSMIS_{M+3S}$ differs from the other sensors over some near-coast regions. For example, at the pixels near the coast at the western part of Shackleton (the pixels surrounding point f in Figure 2.4), $SSMIS_{M+3S}$ does not detect any melt. Over

this location $\text{SSMIS}_{\text{M}+3\text{S}}$ has an SMO of 0%, whereas a higher SMO is found for ASCAT, MODIS, Sentinel-1, and $\text{SSMIS}_{\text{DAV}}$ with values of 62%, 14%, 70%, and 69%, respectively.

$\text{SSMIS}_{\text{DAV}}$ shows a low SMO over areas with persistent melt. An example is the George VI Ice Shelf on the Antarctic Peninsula, with an average SMO of 55% over point g in Figure 2.4, whereas values of 80%, 77%, and 72% are detected by ASCAT, Sentinel-1, and $\text{SSMIS}_{\text{M}+3\text{S}}$, respectively. Again, also MODIS results in a lower SMO (i.e., 41%) over the often clouded George VI Ice Shelf.

To better understand the discrepancies and similarities between the sensors, the time series of seven locations were compared. The locations of points a–g can be found on the maps of Figure 2.4. The satellite signals and detected melt over these locations are presented in Figure 2.5.

Figure 2.5a and 2.5b show that there are large discrepancies in melt detection over bare ice regions, such as a blue ice area and an outlet glacier. MODIS detects more melt over the blue ice location (Figure 2.5a) (95%) than ASCAT (32%), Sentinel-1 (31%), $\text{SSMIS}_{\text{M}+3\text{S}}$ (18%) and $\text{SSMIS}_{\text{DAV}}$ (66%) in melt season 2019–2020. Also over the outlet glacier (Figure 2.5b) more melt is detected by MODIS (100%) than by ASCAT (30%), Sentinel-1 (33%), $\text{SSMIS}_{\text{M}+3\text{S}}$ (6%), and $\text{SSMIS}_{\text{DAV}}$ (19%), here computed for melt season 2016–2017. MODIS detects a persistently high NDWI_{ice} over the bare ice regions (0.10 for Figure 2.5a; 0.16 for Figure 2.5b), resulting in detected melt for (almost) all observations. On the other hand, almost no drop in backscatter intensity of ASCAT and Sentinel-1 is visible during the melt seasons relative to winter period values, and no clear peak presents in the brightness temperature of SSMIS, explaining the less frequent melt detection by the microwave sensors.

Figure 2.5c illustrates the sensor signals over a firn aquifer (subsurface meltwater stored in pore spaces in the firn layer) at the Wilkins Ice Shelf. Montgomery *et al.* (2020) detected a firn aquifer here, starting at 13.4 m depth with a total thickness of 16.2 m in December 2018, which indicates that the climatic conditions are in general favorable for liquid water storage below the surface. ASCAT and Sentinel-1 detect melt for the longest period (up to April 2019) over this location, which may hint at the detection of near-surface melt instead of surface melt, as ASCAT and Sentinel-1 have relatively large penetration depths. Both $\text{SSMIS}_{\text{M}+3\text{S}}$ and $\text{SSMIS}_{\text{DAV}}$ detect melt for a shorter period than ASCAT and Sentinel-1, until mid-February. MODIS only detects melt during the end of December and January, thereafter no melt is detected.

We also see differences in melt detection after snowfall events (Figure 2.5d), potentially also due to confusion between surface and near-surface melt. Again, MODIS only measures surface melt, therefore it fails to detect melt covered by snow after precipitation events (11 January, 15 February), whereas other sensors do detect (near-surface) melt.

Since MODIS depends on reflected sunlight, no melt observations can be performed during the winter season. However, there are locations in Antarctica where up to 20 to 25% of the melt occurs during the winter season, driven by foehn winds (Kuipers Munneke *et al.*, 2018). Figure 2.5e shows an example of such a winter melt event (reported in Datta *et al.*, 2019). Both $\text{SSMIS}_{\text{M}+3\text{S}}$ and $\text{SSMIS}_{\text{DAV}}$ detect melt during the three periods of elevated temperature, at the beginning of March,

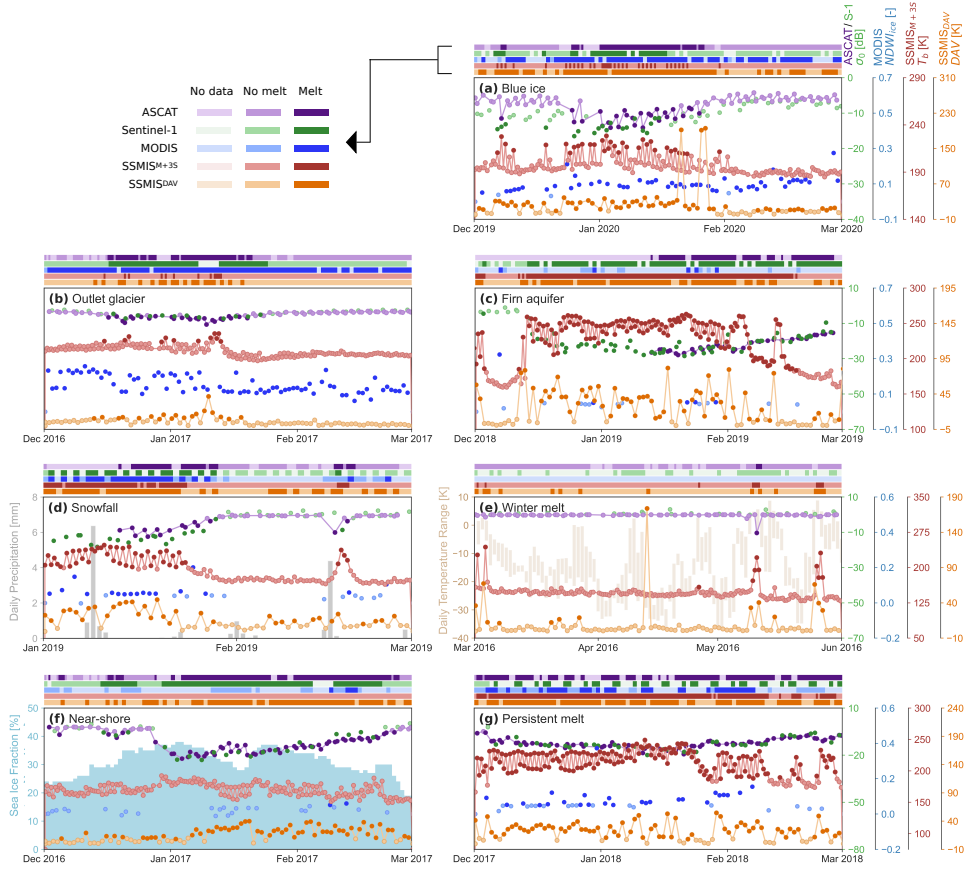


Figure 2.5: Time series of backscatter intensity (σ^0), normalized difference water index adapted for ice (NDWI_{ice}), brightness temperature (T_b), and diurnal amplitude variation (DAV) for the four studied sensors/satellites. The comparison shows the measured σ^0 of Advanced Scatterometer (ASCAT) (in purple), σ^0 of Sentinel-1 (in green), NDWI_{ice} of Moderate Resolution Imaging Spectroradiometer (MODIS) (in blue), T_b of Special Sensor Microwave Imager/Sounder (SSMIS) SSMIS_{M+3S} (in red), and DAV for SSMIS_{DAV} (in orange). When melt is detected, the signals are overlaid with a darker scatter. The flags on top of each subfigure facilitate intercomparison of the melt results, indicating no data (light color), no melt (medium color), and melt (dark color), see the legend in the left upper corner for the specific colors used per melt detection method. The locations of (a)–(g) are shown in Figure 2.4.

mid-May, and end-May. ASCAT detects melt once, on May 10 at 6 PM. Sentinel-1 does not detect melt, however there are also no overpasses at times where SSMIS detects melt (i.e., 1, 3 March, 9–11, and 25–27 May).

SSMIS_{M+3S} detects no melt during the melt seasons for near-coastal pixels at locations where sea ice strongly decreases during summer. Figure 2.5f shows that

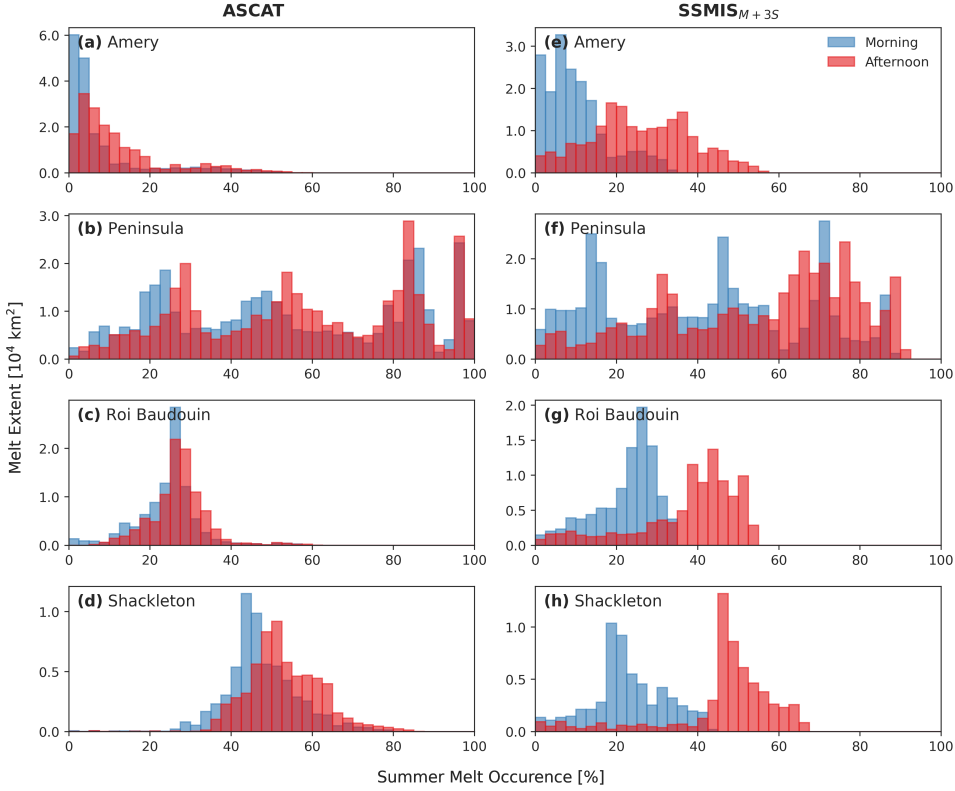


Figure 2.6: Melt occurrence for morning and afternoon observations for Advanced Scatterometer (ASCAT) (a–d) and Special Sensor Microwave Imager/Sounder (SSMIS) SSMIS_{M+3S} (e–h).

changes in sea ice concentration and SSMIS brightness temperature correspond. When the sea ice concentration decreases (e.g., in the beginning of January 2017), the SSMIS brightness temperature follows. This is because the large footprint of SSMIS_{M+3S} results in mixed pixels, where open water masks the increased brightness temperature during melt. For SSMIS_{DAV} this problem is minimized, because (1) the 37 GHz has a smaller footprint than the 19 GHz channel, and (2) the SSMIS_{DAV} algorithm compensates for the low T_b signal by subtracting morning from afternoon overpasses.

Extensive areas of ponded surface water have been observed over the northern part of the George VI Ice Shelf since the early 1940s (Banwell *et al.*, 2021; Reynolds, 1981; Wager, 1972). Where ASCAT, Sentinel-1, and SSMIS_{M+3S} detect melt of 99%, 97%, and 85% averaged over melt season 2017–2018, this is lower for SSMIS_{DAV} (i.e., 72%) in Figure 2.5g. The applied SSMIS_{DAV} algorithm detects melt when the difference between morning and afternoon observation exceeds 9 K, however, for areas with persistent melt throughout the summer the difference between morning

and afternoon observations is too small to pass this threshold.

2.5.3. OVERPASS TIME SENSITIVITY

When we compare the SMO for morning and afternoon overpasses for ASCAT and SSMIS_{M+3S} in Figure 2.6, afternoon observations show higher SMO than morning observations with differences of 16% (4%) over Amery Ice Shelf, 15% (3%) over the Antarctic Peninsula, 14% (4%) over Roi Baudouin Ice Shelf, and 23% (6%) over Shackleton Ice Shelf for SSMIS_{M+3S} (for ASCAT between brackets). This shows that the overpass time can have a large influence on the detected melt.

The differences between ASCAT and SSMIS_{M+3S} are small for morning observations. However, SSMIS_{M+3S} detects more melt than ASCAT during afternoon observations. The Antarctic Peninsula forms an exception here, where meltwater is abundant also during nighttime (for example shown by the small diurnal variation in detected melt over the Antarctic Peninsula in Picard & Fily, 2006), thereby explaining the high SMO during both morning and afternoon observations for both sensors.

While we did not assess the influence of overpass time for MODIS and Sentinel-1 due to a lack of variations of overpass times, Figure 2.5e shows how mismatching overpass timing and a lower temporal resolution result in potential missed melt events for Sentinel-1.

2.5.4. SENSITIVITY TO LIQUID WATER

The backscatter intensity and brightness temperature sensitivity to liquid water for different thicknesses of the upper layer are assessed in Figure 2.7, the sensitivity to the other three parameters (i.e., density, correlation length, and temperature) are evaluated in Supplementary Figure 2.1. Results from our radiative transfer model SMRT suggest that SSMIS (19 GHz and 37 GHz) is highly sensitive to small liquid water contents. The brightness temperature increases with 80/95 K for 19/37 GHz, respectively, for a total liquid water content of 0.10 kg/m² compared to a dry snowpack, with a snow layer thickness of 0.10 m. After reaching a maximum brightness temperature (approximately at a total liquid water content of 0.10 kg/m²), the brightness temperature slowly decreases because the surface becomes more reflective. The backscatter intensities of ASCAT and Sentinel-1, which slightly differ due to small differences in polarization and frequency, require approximately a tenfold larger liquid water content (approximately 1.0 kg/m²) than SSMIS to become fully saturated.

As illustrated in Figure 2.7, the increase in brightness temperature for SSMIS 19 GHz is largest for thicker snow layers (i.e., 75/86 K for 0.05/0.25 m, respectively, when comparing a dry snowpack to a snowpack with a total liquid water content of 0.10 kg/m²). For SSMIS 37 GHz, the brightness temperatures are (almost) identical for different snow layer thicknesses. For ASCAT and Sentinel-1, the drop in backscatter intensity is small, especially for shallow snow layers (i.e., -2.5 dB/-7.1 dB for 0.05 m/0.25 m, respectively, when comparing a dry snowpack to a snowpack with a total liquid water content of 1.0 kg/m²) making ASCAT and Sentinel-1 less sensitive to liquid water in shallow snow layers, but also to snow layers with lower densities,

larger correlation lengths, and higher temperatures (see Supplementary Figure 2.1).

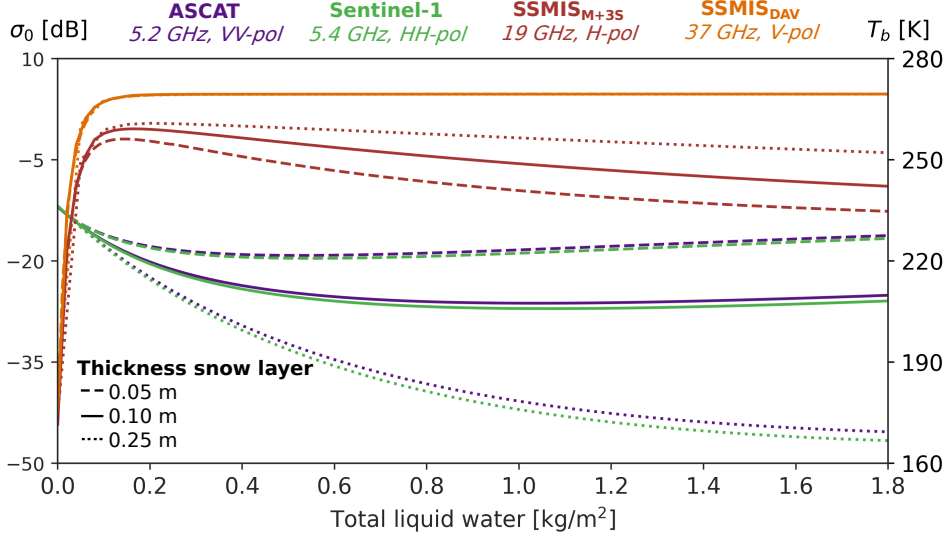


Figure 2.7: Modeled backscatter intensity (σ^0) from Advanced Scatterometer (ASCAT) vertically polarized (in purple), and Sentinel-1 horizontally polarized (in green), and brightness temperature (T_b) from Special Sensor Microwave Imager/Sounder (SSMIS) 19 GHz horizontally polarized (in red) and 37 GHz vertically polarized (in orange) as a function of the total liquid water content in the top 0.05 m (dashed lines), 0.10 m (solid lines), or 0.25 m (dotted lines) of the snowpack.

The high sensitivity of SSMIS to small liquid water contents might explain the previously observed difference in afternoon SMO between ASCAT and SSMIS_{M+3S} (Figure 2.6). Especially over the Amery Ice Shelf and Roi Baudouin Ice Shelf, the afternoon observations of SSMIS_{M+3S} show a higher SMO than ASCAT. According to Figure 2.6, over Amery Ice Shelf the difference in SMO is 14% (ASCAT afternoon mean: 12%, SSMIS afternoon mean: 26%) and over Roi Baudouin 11% (ASCAT afternoon mean: 27%, SSMIS_{M+3S} afternoon mean: 38%). This difference can be linked to the small mean surface melt flux over these ice shelves (around 100 mm w.e. year⁻¹), whereas the fluxes are larger over the Antarctic Peninsula and the Shackleton Ice Shelf (between 200–400 mm w.e. year⁻¹, and around 200 mm w.e. year⁻¹, respectively) according to satellite-based estimates (Trusel *et al.*, 2013) and RACMO2 simulations (van Wessem *et al.*, 2018).

The higher sensitivity of SSMIS might also explain the discrepancies in Figure 2.5e. Both SSMIS_{M+3S} and SSMIS_{DAV} detect more melt than ASCAT and Sentinel-1 during the melt events in the winter of 2016. However, this might also be linked to the lower overpass frequency of ASCAT and Sentinel-1 as stated in the previous Section 2.5.3.

Table 2.3: Summary of the perturbed thresholds for threshold sensitivity analysis.

| Sensor/mission | Threshold for $\text{SMO}_{10\%}^+$ | Threshold for $\text{SMO}_{10\%}^-$ |
|-----------------------|-------------------------------------|-------------------------------------|
| ASCAT | -3.9 [dB] | -2.3 [dB] |
| MODIS | 0.045 [-] | 0.055 [-] |
| Sentinel-1 | -4.0 [dB] | -2.4 [dB] |
| SSMIS _{M+3S} | 26 [K] | 34 [K] |
| SSMIS _{DAV} | 8.0 [K] | 10.4 [K] |

2.5.5. MELT DETECTION ALGORITHM SENSITIVITY

Figure 2.8 shows the threshold sensitivity for ASCAT, MODIS, Sentinel-1, SSMIS_{M+3S}, and SSMIS_{DAV}. The used thresholds for $\text{SMO}_{10\%}^+$ and $\text{SMO}_{10\%}^-$ are summarized in Table 2.3. The highest threshold sensitivity for ASCAT, Sentinel-1, SSMIS_{M+3S}, and SSMIS_{DAV} arise along the grounding lines. Especially for SSMIS_{M+3S} and SSMIS_{DAV}, more melt is detected inward from the grounding line, where we find that on average $\text{SMO}_{10\%}^+$ results in ~10–15% more melt than $\text{SMO}_{10\%}^-$. For MODIS, ~15–20% more melt is detected over the center of ice shelves when using the $\text{SMO}_{10\%}^+$ threshold. The original threshold of NDWI_{ice} shows a low SMO compared to the other sensors over these regions (Figure 2.3), hence a lower threshold of NDWI_{ice} might result in more comparable melt results as the other sensors. Nevertheless, areas that showed a relatively high SMO compared to the microwave sensors (Figure 2.3) (i.e., blue ice regions) are less sensitive to the selected threshold, and would also overestimate melt presence with a $\text{SMO}_{10\%}^-$ threshold compared to the other sensors.

2.6. DISCUSSION

2.6.1. OPPORTUNITIES AND CHALLENGES: PERSPECTIVES OF SENSOR CHARACTERISTICS

Based on the comparison of the detected melt for the four sensors, we identify four opportunities and challenges in relation to the sensor characteristics, including: cloud obstruction and polar darkness, surface penetration, temporal resolution and overpass time, and spatial resolution.

CLOUD OBSTRUCTION AND POLAR DARKNESS

Our results showed that cloud obstruction and polar darkness are fundamental limitations for optical data. MODIS does not detect winter melt events (Figure 2.5e), whereas especially over the Antarctic Peninsula several melt events have been reported during winter (Datta *et al.*, 2019; Kuipers Munneke *et al.*, 2018; Turton *et al.*, 2020). Moreover, MODIS is unable to capture melt events during cloudy days. This is probably one of the main reasons for the underestimation of melt over the ice shelves, where clouds are abundant.

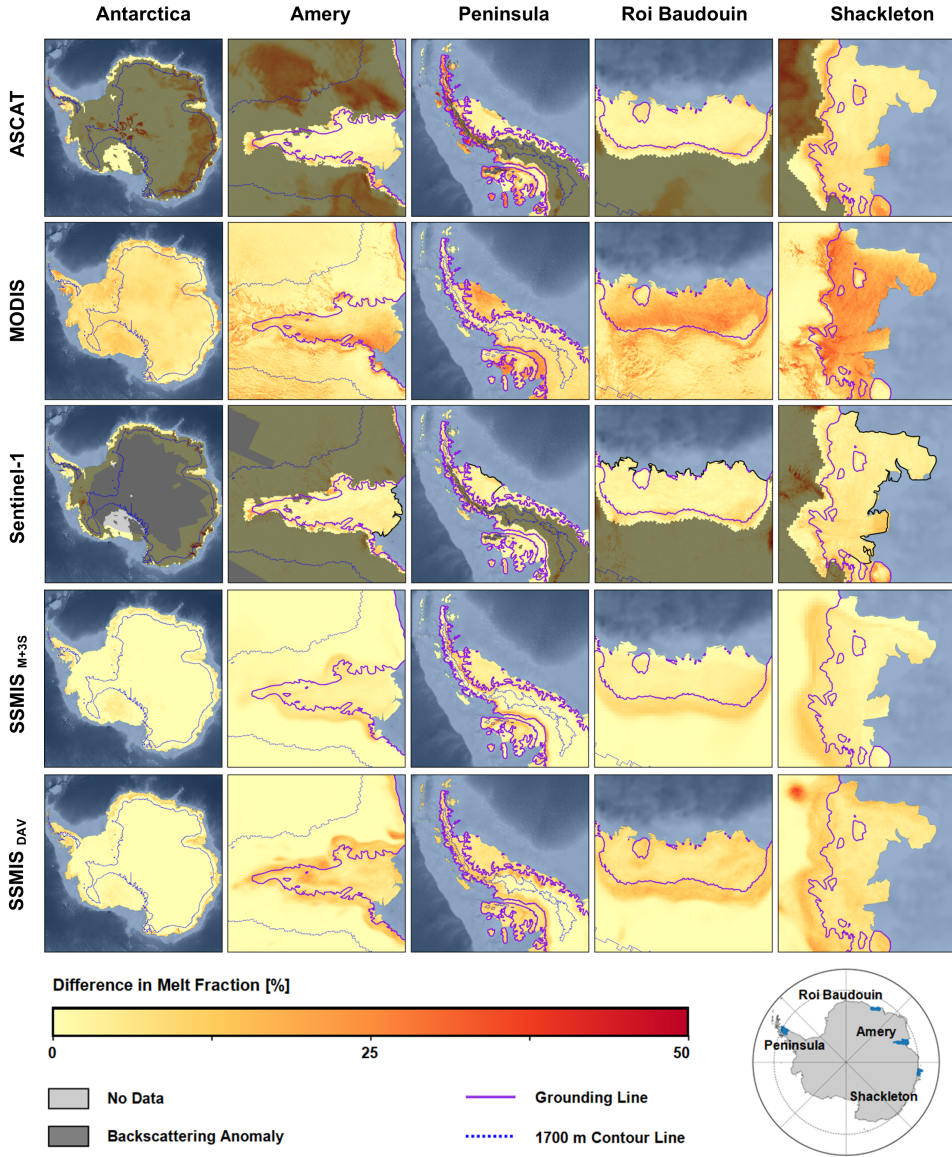


Figure 2.8: Melt sensitivity for melt seasons 2015–2020 for Advanced Scatterometer (ASCAT), Moderate Resolution Imaging Spectroradiometer (MODIS), Sentinel-1, and Special Sensor Microwave Imager/Sounder (SSMIS) using algorithm SSMIS_{M+3S} and SSMIS_{DAV} over the four selected ice shelves. The difference in melt occurrence is computed by comparing a small and large threshold, compared to the default thresholds used in the state-of-the-art melt detection algorithms.

SURFACE PENETRATION

Our analysis showed that large differences in SMO between sensors can result from differences in penetration depth. The active and passive microwave sensors receive signals from dry snowpacks to depths of ~10 m, ~2.5 m, and ~0.5 m for C-band active microwave, K-band passive microwave, and K_a -band passive microwave, respectively. Therefore, microwave sensors are not only detecting surface melt, but also liquid water in deeper layers. At locations where we expect near-surface melt to be present (Figure 2.5c and 2.5d), ASCAT and Sentinel-1 detected more melt than SSMIS. In contrast, MODIS does not penetrate the surface and therefore gives the opportunity to purely focus on surface melt. Moreover, the different frequencies of active and microwave sensors provide the opportunity to derive the depth of the meltwater. A recent study attempted to discriminate between surface and near-surface melt over the Greenland Ice Sheet using multiple frequencies of passive microwave sensors (Colliander *et al.*, 2022). When combining optical, active, and passive microwave signals, an even more detailed profile of meltwater depths might be acquired.

TEMPORAL RESOLUTION AND OVERPASS TIME

Our results showed that melt over Antarctica can occur for very short periods. Sentinel-1, which has a lower temporal resolution than ASCAT and SSMIS, missed such short melt events (e.g., in Figure 2.5e). We indicated that afternoon overpasses resulted in a higher SMO than morning overpasses (Figure 2.6). Picard and Fily (2006) found that when comparing passive microwave sensors, the differences in overpass time have the most significant effect on SMO, more than other characteristics such as frequency, incidence angle, and spatial resolution. Bevan *et al.* (2018) compared QuikSCAT and ASCAT melt observations, and showed that QuikSCAT detected more melt than ASCAT over the Larsen C Ice Shelf, among others due to the preferable overpass time of QuikSCAT (~4 PM local time) over ASCAT (~6 PM local time). These findings highlight the importance of available sensor observations during noon, when melt over Antarctica is most likely.

2.6.2. OPPORTUNITIES AND CHALLENGES: PERSPECTIVES OF APPLIED METHODS

Apart from sensor-characteristic-related opportunities and challenges, we also identify opportunities and challenges considering the applied methods. We discuss opportunities and challenges related to (1) the sensitivity to the applied thresholds in the melt detection algorithms, (2) the two melt detection algorithms applied to SSMIS, and (3) discuss implications due to the absence of ground truth data.

SPATIAL RESOLUTION

We demonstrated that coarse spatial resolution observations—such as the 4.45 km observations of ASCAT, the 6.25 km observations of SSMIS_{M+3S}, and the 3.125 km observations of SSMIS_{DAY}—failed to detect smaller-scale melt features. ASCAT, SSMIS_{M+3S}, and SSMIS_{DAY} detected melt over the small ice rises at Shackleton Ice

Table 2.4: Summary of the identified advantages and disadvantages in detecting surface melt over Antarctica using different remote sensing sensors and methods.

| Sensor | Advantages | Disadvantages |
|------------|--|--|
| ASCAT | <ul style="list-style-type: none"> • Overpasses twice a day (on alternate days) • Continental coverage | <ul style="list-style-type: none"> • Coarse spatial resolution of 4.45 km • Low signal-to-noise ratio over ~75% of the Antarctic Ice Sheet • Fails to detect melt over blue ice • Can confuse surface melt and near-surface melt |
| MODIS | <ul style="list-style-type: none"> • Fine spatial resolution of 500 m • Daily overpasses over the interior of the Antarctic Ice Sheet (almost always cloud-free) • (Almost) daily overpasses over grounding line (less clouds than over ice shelves) • Captures melt over blue ice regions | <ul style="list-style-type: none"> • No observations during winter • Between 15–75% of the observations over ice shelves are cloud-covered during melt season • High threshold sensitivity over the center of ice shelves |
| Sentinel-1 | <ul style="list-style-type: none"> • Fine spatial resolution of 10–40 m • (Almost) daily overpasses over the West Antarctic ice shelves | <ul style="list-style-type: none"> • No coverage over the interior of the Antarctic Ice Sheet • One overpass every two/three days over East Antarctica • Overpass time varies per orbit • Low signal-to-noise ratio over ~75% of the Antarctic Ice Sheet • Fails to detect melt over blue ice • Can confuse surface melt and near-surface melt |
| SSMIS | <ul style="list-style-type: none"> • Overpasses twice a day • Continental coverage • High sensitivity to low liquid water contents | <ul style="list-style-type: none"> • Coarse spatial resolution of 3.125 km (K_a-band) or 6.25 km (K-band) • Can confuse surface melt and near-surface melt |

Shelf (Figure 2.4), opposed to MODIS and Sentinel-1. Besides, in heterogeneous pixels, their coarse spatial resolution leads to mixing up the surface melt signals with signals from sea ice or open water (Figure 2.5f). As a consequence, coarse spatial resolution sensors might fail threshold-based surface melt detection methods.

MELTWATER DETECTION THRESHOLDS

ASCAT, Sentinel-1, SSMIS_{M+3S} and SSMIS_{DAV} show the highest threshold sensitivity along the grounding lines, where MODIS has the highest threshold sensitivity over the center of ice shelves. Over locations with a high threshold sensitivity, thorough research is desired to select optimal thresholds. An example is a study by Trusel *et al.* (2012), in which they proposed to use a decision tree method to determine the

appropriate $\Delta\sigma^0$. Since they used QuikSCAT data, future research is required to show the applicability of the proposed thresholds to ASCAT and Sentinel-1 data.

We also found areas where MODIS detected an SMO exceeding $\sim 75\%$ (e.g., over blue ice regions), but had a low sensitivity to the selected threshold. Due to the bluish appearance over blue ice regions, the NDWI_{ice} -based detection method is likely to overestimate surface melt over these regions. Moreover, misclassification of aged snow can result in an overestimation of SMO along the grounding lines detected by MODIS. Based on spectral measurements and simulations (Hannula *et al.*, 2020; Libois *et al.*, 2013), the NDWI_{ice} of either wet snow or aged snow range from 0.05 to 0.1. Therefore, there is a trade-off between the detection of wet snow and overestimation of melt over aged snow areas. The MODIS melt detection could potentially be refined by including additional constraints (for example based on snow grain size or blue ice presence) to the melt detection algorithm. Nevertheless, it should be noted that surface melt can occur in these low albedo areas (Hu *et al.*, 2021, 2022), and optical sensors are able to detect surface melt over these areas (albeit an overestimation), whereas blue ice regions are often underestimated or neglected by regional climate models (van Wessem *et al.*, 2018) and the melt detection algorithms applied to microwave sensors.

SSMIS MELT DETECTION ALGORITHMS

Besides the frequently used M+3S algorithm (i.e., $\text{SSMIS}_{\text{M+3S}}$), also the DAV algorithm (i.e., $\text{SSMIS}_{\text{DAV}}$) was applied to the SSMIS data in this research. It was possible to also study the daily brightness temperature variations using the DAV algorithm, because SSMIS observes the Antarctic Ice Sheet twice a day with constant local overpass times. Similar to Tedesco *et al.* (2009), it was found that $\text{SSMIS}_{\text{M+3S}}$ tends to underestimate melt compared to the other sensors for most of the Antarctic Ice Sheet. Therefore, $\text{SSMIS}_{\text{DAV}}$ is preferred over the $\text{SSMIS}_{\text{M+3S}}$ algorithm, however, over persistent melt regions (such as Figure 2.5g) the $\text{SSMIS}_{\text{DAV}}$ algorithm underestimates melt compared to the other sensors. Here the difference between morning and afternoon observation is often smaller than 9 K, whereas the individual brightness temperature of morning and afternoon overpasses are high (i.e., exceeding the previous winter mean plus 30 K). Therefore, it is recommended to extent the $\text{SSMIS}_{\text{DAV}}$ algorithm, and not only detect melt when DAV exceeds 9 K, but also when the morning and afternoon overpasses both exceed a certain threshold. (Tedesco *et al.*, 2007) used such a dual-condition approach to detect melt over the Greenland Ice Sheet, however, these thresholds highly underestimate melt over the Antarctic Ice Sheet, so an additional study over Antarctica would be desired.

LIMITED GROUND TRUTH DATA

Last but not least, validating the SMO results per sensor was hampered by the absence of ground truth data. Therefore the results could be compared (between sensors and to auxiliary data), but it remained difficult to explain the discrepancies among the results. AWSs provide a way to validate the absolute value at pixel size. However, given the spatial resolution of sensors, the representativeness over a pixel with heterogeneous melt patterns is still difficult to verify, as well as the spatial

patterns of surface melt. Moreover, over areas with the largest SMO differences between sensors, such as blue ice regions, there are no AWSs in place yet.

2.7. CONCLUSIONS

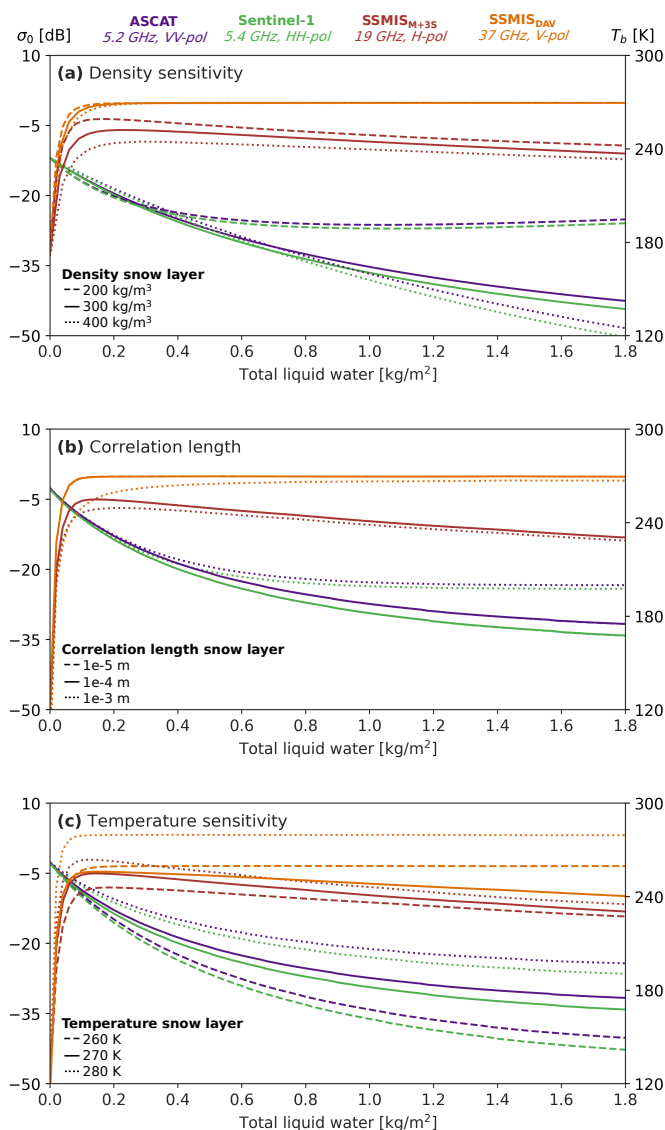
In this study, we presented an overview of opportunities and challenges in detecting surface melt over Antarctica. We applied a range of methods to four frequently used sensors: ASCAT, MODIS, Sentinel-1, and SSMIS. The comparison showed large SMO differences, especially over blue ice regions, in the case of near-surface melt, and during winter melt. In this study, we identified five opportunities and challenges when detecting surface melt over Antarctica, which include: (1) cloud obstruction and darkness, (2) surface penetration, (3) temporal resolution, (4) spatial resolution, and (5) the applied melt detection methods. We also summarize the identified opportunities and challenges in Table 2.4.

Table 2.4 shows that an opportunity for one sensor is often a challenge for another. We foresee a promising future for combining sensors, in particular by applying machine learning methods. However, there is a need for machine learning methods that can handle the differences in time and space between the satellites. Standard machine learning techniques will not be sufficient to merge the diverse satellite observations.

There are multiple scenarios in which synergizing satellite data can improve the mapping of surface melt over the Antarctic Ice Sheet. There are four opportunities for which we foresee that combining satellite data could be beneficial. First, melt detection over blue ice could be improved by combining MODIS and microwave data. Second, MODIS could help separating surface and near-surface melt, due to its inability to penetrate the surface. When one would be interested in near-surface melt, different microwave frequencies could be compared to assess the depth of meltwater. Third, temporal and spatial resolution could be enhanced when sensors with different resolutions are combined into one high-resolution melt presence product. Finally, machine learning provides the opportunity to combine multiple input features, including multiple satellite observations or auxiliary data sets, which might lead to an improved melt detection product.

In this study, we performed an intercomparison of surface melt detected by four satellites. A more varied collection of ground truth data from automatic weather stations, including sensors for observing liquid water presence in the snowpack, would be required for a thorough validation study.

2.8. SUPPLEMENTARY MATERIALS



Supplementary Figure 2.1: Modeled backscatter intensity (σ^0) from Advanced Scatterometer (ASCAT) vertically polarized (in purple), and Sentinel-1 horizontally polarized (in green), and brightness temperature (T_b) from Special Sensor Microwave Imager/Sounder (SSMIS) 19 GHz horizontally polarized (in red) and 37 GHz vertically polarized (in orange) as a function of the total liquid water content for a varying (a) density, (b) correlation length, and (c) temperature of the snowpack.

BIBLIOGRAPHY

- Abdalati, W., & Steffen, K. (1995). Passive microwave-derived snow melt regions on the Greenland Ice Sheet. *Geophysical Research Letters*, 22(7), 787–790. <https://doi.org/10.1029/95GL00433>
- Agosta, C., Amory, C., Kittel, C., Orsi, A., Favier, V., Gallée, H., Van den Broeke, M. R., Lenaerts, J., van Wessem, J. M., Van de Berg, W. J., et al. (2019). Estimation of the Antarctic surface mass balance using the regional climate model MAR (1979–2015) and identification of dominant processes. *The Cryosphere*, 13(1), 281–296.
- Arigony-Neto, J., Saurer, H., Simões, J. C., Rau, F., Jaña, R., Vogt, S., & Gossmann, H. (2009). Spatial and temporal changes in dry-snow line altitude on the Antarctic Peninsula. *Climatic change*, 94(1), 19–33.
- Arthur, J. E., Stokes, C. R., Jamieson, S. S., Carr, J. R., & Leeson, A. A. (2020). Distribution and seasonal evolution of supraglacial lakes on Shackleton Ice Shelf, East Antarctica. *The Cryosphere*, 14(11), 4103–4120.
- Arthur, J. E., Stokes, C. R., Jamieson, S. S., Rachel Carr, J., Leeson, A. A., & Verjans, V. (2022). Large interannual variability in supraglacial lakes around East Antarctica. *Nature communications*, 13(1), 1–12.
- Ashcraft, I. S., & Long, D. G. (2006). Comparison of methods for melt detection over Greenland using active and passive microwave measurements. *International Journal of Remote Sensing*, 27(12), 2469–2488.
- Bakker, A. M., Wong, T. E., Ruckert, K. L., & Keller, K. (2017). Sea-level projections representing the deeply uncertain contribution of the West Antarctic ice sheet. *Scientific reports*, 7(1), 1–7.
- Banwell, A. F., Datta, R. T., Dell, R. L., Moussavi, M., Brucker, L., Picard, G., Shuman, C. A., & Stevens, L. A. (2021). The 32-year record-high surface melt in 2019/2020 on the northern George VI Ice Shelf, Antarctic Peninsula. *The Cryosphere*, 15(2), 909–925.
- Banwell, A. F., Willis, I. C., Macdonald, G. J., Goodsell, B., & MacAyeal, D. R. (2019). Direct measurements of ice-shelf flexure caused by surface meltwater ponding and drainage. *Nature communications*, 10(1), 1–10.
- Bell, R. E., Banwell, A. F., Trusel, L. D., & Kingslake, J. (2018). Antarctic surface hydrology and impacts on ice-sheet mass balance. *Nature Climate Change*, 8(12), 1044–1052.
- Bell, R. E., Chu, W., Kingslake, J., Das, I., Tedesco, M., Tinto, K. J., Zappa, C. J., Frezzotti, M., Boghosian, A., & Lee, W. S. (2017). Antarctic ice shelf potentially stabilized by export of meltwater in surface river. *Nature*, 544(7650), 344–348.
- Bevan, S. L., Luckman, A. J., Kuipers Munneke, P., Hubbard, B., Kullessa, B., & Ashmore, D. W. (2018). Decline in surface melt duration on Larsen C Ice Shelf revealed by the advanced scatterometer (ASCAT). *Earth and Space Science*, 5(10), 578–591.
- Bintanja, R., & Van den Broeke, M. R. (1996). The influence of clouds on the radiation budget of ice and snow surfaces in Antarctica and Greenland in summer. *International Journal of Climatology: A Journal of the Royal Meteorological Society*, 16(11), 1281–1296.

- Bothale, R. V., Rao, P., Dutt, C., & Dadhwal, V. K. (2015). Detection of snow melt and freezing in Himalaya using OSCAT data. *Journal of Earth System Science*, 124(1), 101–113.
- Brandt, R. E., & Warren, S. G. (1993). Solar-heating rates and temperature profiles in Antarctic snow and ice. *Journal of Glaciology*, 39(131), 99–110.
- Brodzik, M., Long, D., Hardman, M., Paget, A., & Armstrong, R. (2016). MEaSURES calibrated enhanced-resolution passive microwave daily EASE-grid 2.0 brightness temperature ESDR, version 1. *NASA National Snow and Ice Data Center Distributed Active Archive Center*.
- Choudhury, B., & Chang, A. T. (1979). Two-stream theory of reflectance of snow. *IEEE Transactions on Geoscience Electronics*, 17(3), 63–68.
- Church, J. A., Clark, P. U., Cazenave, A., Gregory, J. M., Jevrejeva, S., Levermann, A., Merrifield, M. A., Milne, G. A., Nerem, R. S., Nunn, P. D., et al. (2013). *Sea level change* (tech. rep.). PM Cambridge University Press.
- Colbeck, S. (1989). Snow-crystal growth with varying surface temperatures and radiation penetration. *Journal of Glaciology*, 35(119), 23–29.
- Colliander, A., Mousavi, M., Marshall, S., Samimi, S., Kimball, J. S., Miller, J. Z., Johnson, J., & Burgin, M. (2022). Ice Sheet Surface and Subsurface Melt Water Discrimination Using Multi-Frequency Microwave Radiometry. *Geophysical Research Letters*, 49(4), e2021GL096599.
- Datta, R. T., Tedesco, M., Fettweis, X., Agosta, C., Lhermitte, S., Lenaerts, J. T., & Wever, N. (2019). The effect of Foehn-induced surface melt on firn evolution over the northeast Antarctic peninsula. *Geophysical Research Letters*, 46(7), 3822–3831.
- DeConto, R. M., & Pollard, D. (2016). Contribution of Antarctica to past and future sea-level rise. *Nature*, 531(7596), 591–597.
- Dell, R., Arnold, N., Willis, I., Banwell, A., Williamson, A., Pritchard, H., & Orr, A. (2020). Lateral meltwater transfer across an Antarctic ice shelf. *The Cryosphere*, 14(7), 2313–2330.
- Dell, R., Banwell, A. F., Willis, I. C., Arnold, N. S., Halberstadt, A. R. W., Chudley, T. R., & Pritchard, H. D. (2022). Supervised classification of slush and ponded water on Antarctic ice shelves using Landsat 8 imagery. *Journal of Glaciology*, 68(268), 401–414.
- de Roda Husman, S., Hu, Z., Wouters, B., Kuipers Munneke, P., Veldhuisen, S., & Lhermitte, S. (2022). Remote Sensing of Surface Melt on Antarctica: Opportunities and Challenges. *IEEE Journal of Selected Topics in Applied Earth Observations and Remote Sensing*.
- Dirscherl, M., Dietz, A. J., Kneisel, C., & Kuenzer, C. (2020). Automated mapping of Antarctic supraglacial lakes using a machine learning approach. *Remote Sensing*, 12(7), 1203.
- Dirscherl, M., Dietz, A. J., Kneisel, C., & Kuenzer, C. (2021). A novel method for automated supraglacial lake mapping in Antarctica using Sentinel-1 SAR imagery and deep learning. *Remote Sensing*, 13(2), 197.
- Donat-Magnin, M., Jourdain, N. C., Kittel, C., Agosta, C., Amory, C., Gallée, H., Krinner, G., & Chekki, M. (2021). Future surface mass balance and surface melt in the Amundsen sector of the West Antarctic Ice Sheet. *The Cryosphere*, 15(2), 571–593.
- Dozier, J., Schneider, S. R., & McGinnis Jr, D. F. (1981). Effect of grain size and snowpack water equivalence on visible and near-infrared satellite observations of snow. *Water Resources Research*, 17(4), 1213–1221.
- Dunmire, D., Lenaerts, J., Banwell, A., Wever, N., Shragge, J., Lhermitte, S., Drews, R., Pattyn, F., Hansen, J., Willis, I., et al. (2020). Observations of buried lake drainage on the Antarctic Ice Sheet. *Geophysical research letters*, 47(15), e2020GL087970.

- Edwards, T. L., Nowicki, S., Marzeion, B., Hock, R., Goelzer, H., Seroussi, H., Jourdain, N. C., Slater, D. A., Turner, F. E., Smith, C. J., et al. (2021). Projected land ice contributions to twenty-first-century sea level rise. *Nature*, 593(7857), 74–82.
- Gerrish, L., Fretwell, P., & Cooper, P. (2021). High resolution vector polylines of the Antarctic coastline (7.4), UK Polar Data Centre, Natural Environment Research Council, UK Research & Innovation [Online; accessed 20 April 2022].
- Gilbert, E., & Kittel, C. (2021). Surface melt and runoff on Antarctic ice shelves at 1.5 C, 2 C, and 4 C of future warming. *Geophysical Research Letters*, 48(8), e2020GL091733.
- Gorelick, N., Hancher, M., Dixon, M., Ilyushchenko, S., Thau, D., & Moore, R. (2017). Google Earth Engine: Planetary-scale geospatial analysis for everyone. *Remote sensing of Environment*, 202, 18–27.
- Halberstadt, A. R. W., Gleason, C. J., Moussavi, M. S., Pope, A., Trusel, L. D., & DeConto, R. M. (2020). Antarctic supraglacial lake identification using Landsat-8 image classification. *Remote Sensing*, 12(8), 1327.
- Hall, D., Williams, R., Barton, J., Sigurdsson, O., Smith, L., & Garvin, J. (2000). Evaluation of remote-sensing techniques to measure decadal-scale changes of Hofsjökull ice cap, Iceland. *Journal of Glaciology*, 46(154), 375–388.
- Hall, D. K., Williams Jr, R., Casey, K. A., DiGirolamo, N. E., & Wan, Z. (2006). Satellite-derived, melt-season surface temperature of the Greenland Ice Sheet (2000–2005) and its relationship to mass balance. *Geophysical Research Letters*, 33(11).
- Hall, D. K., Comiso, J. C., DiGirolamo, N. E., Shuman, C. A., Box, J. E., & Koenig, L. S. (2013). Variability in the surface temperature and melt extent of the Greenland ice sheet from MODIS. *Geophysical Research Letters*, 40(10), 2114–2120.
- Hall, D. K., & Martinec, J. (1985). An introduction to the optical, thermal and electrical properties of ice and snow. In *Remote sensing of ice and snow* (pp. 1–9). Springer.
- Hall, D. K., Williams, R. S., Luthcke, S. B., & DiGirolamo, N. E. (2008). Greenland ice sheet surface temperature, melt and mass loss: 2000–06. *Journal of Glaciology*, 54(184), 81–93.
- Hallikainen, M. T., Ulaby, F. T., & Van Deventer, T. E. (1987). Extinction behavior of dry snow in the 18-to 90-GHz range. *IEEE Transactions on Geoscience and Remote Sensing*, 6(6), 737–745.
- Hannula, H.-R., Heinilä, K., Böttcher, K., Mattila, O.-P., Salminen, M., & Pulliainen, J. (2020). Laboratory, field, mast-borne and airborne spectral reflectance measurements of boreal landscape during spring. *Earth System Science Data*, 12(1), 719–740.
- Hannula, H.-R., & Pulliainen, J. (2019). Spectral reflectance behavior of different boreal snow types. *Journal of Glaciology*, 65(254), 926–939.
- Hofer, R., & Mätzler, C. (1980). Investigations on snow parameters by radiometry in the 3-to 60-mm wavelength region. *Journal of Geophysical Research: Oceans*, 85(C1), 453–460.
- Hu, Z., Kuipers Munneke, P., Lhermitte, S., Dirscherl, M., Ji, C., & Van den Broeke, M. (2022). FABIAN: A daily product of Fractional Austral-summer Blue Ice over Antarctica during 2000–2021 based on MODIS imagery using Google Earth Engine. *Remote Sensing of Environment*, 280, 113202.
- Hu, Z., Kuipers Munneke, P., Lhermitte, S., Izeboud, M., & Van den Broeke, M. (2021). Improving surface melt estimation over the Antarctic Ice Sheet using deep learning: a proof of concept over the Larsen Ice Shelf. *The Cryosphere*, 15(12), 5639–5658.
- Hui, F., Ci, T., Cheng, X., Scambo, T. A., Liu, Y., Zhang, Y., Chi, Z., Huang, H., Wang, X., Wang, F., et al. (2014). Mapping blue-ice areas in Antarctica using ETM+ and MODIS data. *Annals of Glaciology*, 55(66), 129–137.

- Izeboud, M., Lhermitte, S., Van Tricht, K., Lenaerts, J., Van Lipzig, N., & Wever, N. (2020). The spatiotemporal variability of cloud radiative effects on the Greenland Ice Sheet surface mass balance. *Geophysical Research Letters*, 47(12), e2020GL087315.
- Jakobs, C. L., Reijmer, C. H., Smeets, C. P., Trusel, L. D., Van de Berg, W. J., Van den Broeke, M. R., & van Wessem, J. M. (2020). A benchmark dataset of in situ Antarctic surface melt rates and energy balance. *Journal of Glaciology*, 66(256), 291–302.
- Johnson, A., Fahnestock, M., & Hock, R. (2020). Evaluation of passive microwave melt detection methods on Antarctic Peninsula ice shelves using time series of Sentinel-1 SAR. *Remote Sensing of Environment*, 250, 112044.
- Kilpatrick, K. A., Podestá, G. P., & Evans, R. (2001). Overview of the NOAA/NASA advanced very high resolution radiometer Pathfinder algorithm for sea surface temperature and associated matchup database., 106(C5), 9179–9197. <https://doi.org/10.1029/1999JC000065>
- King, M., Platnick, S., Menzel, W. P., Ackerman, S. A., & Paul, A. H. (2005). Spatial and Temporal Distribution of Tropospheric Clouds Observed by MODIS On-board the Terra and Aqua Satellites. *IEEE Transactions on Geoscience and Remote Sensing*, 51, 3826–3851.
- Kingslake, J., Ely, J. C., Das, I., & Bell, R. E. (2017). Widespread movement of meltwater onto and across Antarctic ice shelves. *Nature*, 544(7650), 349–352.
- Koh, G., & Jordan, R. (1995). Sub-surface melting in a seasonal snow cover. *Journal of Glaciology*, 41(139), 474–482.
- Kuipers Munneke, P., Luckman, A., Bevan, S., Smeets, C., Gilbert, E., Van den Broeke, M., Wang, W., Zender, C., Hubbard, B., Ashmore, D., et al. (2018). Intense winter surface melt on an Antarctic ice shelf. *Geophysical Research Letters*, 45(15), 7615–7623.
- Kuipers Munneke, P., Ligtenberg, S. R., Van den Broeke, M. R., & Vaughan, D. G. (2014). Firn air depletion as a precursor of antarctic ice-shelf collapse. *Journal of Glaciology*, 60(220), 205–214.
- Leduc-Leballeur, M., Picard, G., Macelloni, G., Mialon, A., & Kerr, Y. H. (2020). Melt in Antarctica derived from Soil Moisture and Ocean Salinity (SMOS) observations at L band. *The Cryosphere*, 14(2), 539–548.
- Lenaerts, J., Lhermitte, S., Drews, R., Ligtenberg, S., Berger, S., Helm, V., Smeets, C., Van den Broeke, M., Van de Berg, W. J., Van Meijgaard, E., et al. (2017). Meltwater produced by wind–albedo interaction stored in an East Antarctic ice shelf. *Nature climate change*, 7(1), 58–62.
- Li, W., Lhermitte, S., & López-Dekker, P. (2021). The potential of synthetic aperture radar interferometry for assessing meltwater lake dynamics on Antarctic ice shelves. *The Cryosphere*, 15(12), 5309–5322.
- Liang, D., Guo, H., Zhang, L., Cheng, Y., Zhu, Q., & Liu, X. (2021). Time-series snowmelt detection over the Antarctic using Sentinel-1 SAR images on Google Earth Engine. *Remote Sensing of Environment*, 256, 112318.
- Liang, L., Guo, H., Li, X., & Cheng, X. (2013). Automated ice-sheet snowmelt detection using microwave radiometer measurements. *Polar Research*, 32(1), 19746.
- Libois, Q., Picard, G., France, J., Arnaud, L., Dumont, M., Carmagnola, C., & King, M. (2013). Influence of grain shape on light penetration in snow. *The Cryosphere*, 7(6), 1803–1818.
- Liston, G. E., & Winther, J.-G. (2005). Antarctic surface and subsurface snow and ice melt fluxes. *Journal of Climate*, 18(10), 1469–1481.

- Liu, H., Wang, L., & Jezek, K. C. (2006). Spatiotemporal variations of snowmelt in Antarctica derived from satellite scanning multichannel microwave radiometer and Special Sensor Microwave Imager data. *Journal of Geophysical Research*, 111(F1).
- Long, D. (2022). NASA Scatterometer Climate Record Pathfinder (SCP) [Accessed 4 April 2022].
- Long, D. G., Hardin, P. J., & Whiting, P. T. (1993). Resolution enhancement of spaceborne scatterometer data. *IEEE Transactions on Geoscience and Remote Sensing*, 31(3), 700–715.
- Luckman, A., Elvidge, A., Jansen, D., Kulesa, B., Kuipers Munneke, P., King, J., & Barrand, N. E. (2014). Surface melt and ponding on Larsen C Ice Shelf and the impact of föhn winds. *Antarctic Science*, 26(6), 625–635.
- MacAyeal, D. R., Sergienko, O. V., & Banwell, A. F. (2015). A model of viscoelastic ice-shelf flexure. *Journal of Glaciology*, 61(228), 635–645.
- Mätzler, C. (1998). Improved Born approximation for scattering of radiation in a granular medium. *Journal of Applied Physics*, 83(11), 6111–6117.
- Meier, W., Wilcox, H., Scott, D., Stewart, J., & Calme, J. (2022). Near-Real-Time DMSP SSM/I-SSMIS Daily Polar Gridded Brightness Temperatures, Version 2 [Accessed 14 April 2022].
- Montgomery, L., Miège, C., Miller, J., Scambos, T. A., Wallin, B., Miller, O., Solomon, D. K., Forster, R., & Koenig, L. (2020). Hydrologic properties of a highly permeable firn aquifer in the Wilkins Ice Shelf, Antarctica. *Geophysical Research Letters*, 47(22), e2020GL089552.
- Mote, T. L., & Anderson, M. R. (1995). Variations in snowpack melt on the Greenland ice sheet based on passive-microwave measurements. *Journal of Glaciology*, 41(137), 51–60.
- Mote, T. L., Anderson, M. R., Kuivinen, K. C., & Rowe, C. M. (1993). Passive microwave-derived spatial and temporal variations of summer melt on the Greenland ice sheet. *Annals of Glaciology*, 17, 233–238.
- Mouginot, J., Scheuchl, B., & Rignot, E. (2017). MEaSUREs Antarctic Boundaries for IPY 2007-2009 from Satellite Radar, Version 2. Subsets: GroundingLine_Antarctica_v02, IceShelf_Antarctica_v02, NASA National Snow and Ice Data Center Distributed Active Archive Center [Online; accessed 16 February 2022].
- Mousavi, M., Colliander, A., Miller, J. Z., & Kimball, J. S. (2022). A novel approach to map the intensity of surface melting on the Antarctica ice sheet using SMAP L-band microwave radiometry. *IEEE Journal of Selected Topics in Applied Earth Observations and Remote Sensing*, 15, 1724–1743.
- Moussavi, M., Pope, A., Halberstadt, A. R. W., Trusel, L. D., Cioffi, L., & Abdalati, W. (2020). Antarctic supraglacial lake detection using Landsat 8 and Sentinel-2 imagery: Towards continental generation of lake volumes. *Remote Sensing*, 12(1), 134.
- Nagler, T., Rott, H., Ripper, E., Bippus, G., & Hetzenecker, M. (2016). Advancements for snowmelt monitoring by means of Sentinel-1 SAR. *Remote Sensing*, 8(4), 348.
- Nye, J. F. (1957). The distribution of stress and velocity in glaciers and ice-sheets. *Proceedings of the Royal Society of London. Series A. Mathematical and Physical Sciences*, 239(1216), 113–133.
- Picard, G., & Fily, M. (2006). Surface melting observations in Antarctica by microwave radiometers: Correcting 26-year time series from changes in acquisition hours. *Remote sensing of environment*, 104(3), 325–336.
- Picard, G., Leduc-Leballeur, M., Banwell, A. F., Brucker, L., & Macelloni, G. (2022). The sensitivity of satellite microwave observations to liquid water in the Antarctic snowpack. *The Cryosphere Discussions*, 1–34.

- Picard, G., Sandells, M., & Löwe, H. (2018). SMRT: An active–passive microwave radiative transfer model for snow with multiple microstructure and scattering formulations (v1. 0). *Geoscientific Model Development*, 11(7), 2763–2788.
- Pörtner, H.-O., Roberts, D. C., Adams, H., Adler, C., Aldunce, P., Ali, E., Begum, R. A., Betts, R., Kerr, R. B., Biesbroek, R., et al. (2022). *Climate change 2022: impacts, adaptation and vulnerability*. IPCC.
- Pörtner, H.-O., Roberts, D. C., Masson-Delmotte, V., Zhai, P., Tignor, M., Poloczanska, E., & Weyer, N. (2019). The ocean and cryosphere in a changing climate. *IPCC Special Report on the Ocean and Cryosphere in a Changing Climate*.
- Ramage, J. M., & Isacks, B. L. (2002). Determination of melt-onset and refreeze timing on southeast Alaskan icefields using SSM/I diurnal amplitude variations. *Annals of Glaciology*, 34, 391–398.
- Remote Sensing Systems (RSS). (2022). Satellite Equator Crossing Times [Accessed 31 August 2022].
- Reynolds, J. M. (1981). Lakes on George VI Ice Shelf, Antarctica. *Polar Record*, 20(128), 425–432.
- Rignot, E., Mouginot, J., Scheuchl, B., Van den Broeke, M., van Wessem, J. M., & Morlighem, M. (2019). Four decades of Antarctic Ice Sheet mass balance from 1979–2017. *Proceedings of the National Academy of Sciences*, 116(4), 1095–1103.
- Scambos, T. A., Fricker, H. A., Liu, C.-C., Bohlander, J., Fastook, J., Sargent, A., Massom, R., & Wu, A.-M. (2009). Ice shelf disintegration by plate bending and hydro-fracture: Satellite observations and model results of the 2008 Wilkins ice shelf break-ups. *Earth and Planetary Science Letters*, 280(1–4), 51–60.
- Semmens, K. A., Ramage, J., Bartsch, A., & Liston, G. E. (2013). Early snowmelt events: detection, distribution, and significance in a major sub-arctic watershed. *Environmental Research Letters*, 8(1), 014020.
- Shi, J., & Dozier, J. (1995). Inferring snow wetness using C-band data from SIR-C's polarimetric synthetic aperture radar. *IEEE transactions on geoscience and remote sensing*, 33(4), 905–914.
- Slater, T., Shepherd, A., McMillan, M., Muir, A., Gilbert, L., Hogg, A. E., Konrad, H., & Parrinello, T. (2018). A new digital elevation model of Antarctica derived from CryoSat-2 altimetry. *The Cryosphere*, 12(4), 1551–1562.
- Spergel, J. J., Kingslake, J., Creyts, T., van Wessem, M., & Fricker, H. A. (2021). Surface meltwater drainage and ponding on Amery Ice Shelf, East Antarctica, 1973–2019. *Journal of Glaciology*, 67(266), 985–998.
- Steiner, N., & Tedesco, M. (2014). A Wavelet Melt Detection Algorithm Applied to Enhanced Resolution Scatterometer Data over Antarctica (2000–2009). *The Cryosphere*, 8, 25–40. <https://doi.org/10.5194/tc-8-25-2014>
- Stiles, W. H., & Ulaby, E. T. (1980). The active and passive microwave response to snow parameters: 1. Wetness. *Journal of Geophysical Research: Oceans*, 85(C2), 1037–1044.
- Tedesco, M., Abdalati, W., & Zwally, H. J. (2007). Persistent surface snowmelt over Antarctica (1987–2006) from 19.35 GHz brightness temperatures. *Geophysical Research Letters*, 34(18). <https://doi.org/10.1029/2007GL031199>
- Tedesco, M. (2014). *Remote sensing of the cryosphere*. John Wiley & Sons.
- Tedesco, M., Brodzik, M., Armstrong, R., Savoie, M., & Ramage, J. (2009). Pan arctic terrestrial snowmelt trends (1979–2008) from spaceborne passive microwave data and correlation with the Arctic Oscillation. *Geophysical Research Letters*, 36(21).

- Tedesco, M., & Monaghan, A. J. (2009). An updated Antarctic melt record through 2009 and its linkages to high-latitude and tropical climate variability. *Geophysical Research Letters*, 36(18).
- Torinesi, O., Fily, M., & Genthon, C. (2003). Variability and trends of the summer melt period of Antarctic ice margins since 1980 from microwave sensors. *Journal of Climate*, 16(7), 1047–1060.
- Trusel, L., Frey, K. E., & Das, S. B. (2012). Antarctic surface melting dynamics: Enhanced perspectives from radar scatterometer data. *Journal of Geophysical Research: Earth Surface*, 117(F2).
- Trusel, L., Frey, K. E., Das, S. B., Karnauskas, K. B., Kuipers Munneke, P., Van Meijgaard, E., & Van den Broeke, M. R. (2015). Divergent trajectories of Antarctic surface melt under two twenty-first-century climate scenarios. *Nature Geoscience*, 8(12), 927–932.
- Trusel, L., Frey, K. E., Das, S. B., Kuipers Munneke, P., & Van den Broeke, M. (2013). Satellite-based estimates of Antarctic surface meltwater fluxes. *Geophysical Research Letters*, 40(23), 6148–6153.
- Turton, J. V., Kirchgassner, A., Ross, A. N., King, J. C., & Kuipers Munneke, P. (2020). The influence of föhn winds on annual and seasonal surface melt on the Larsen C Ice Shelf, Antarctica. *The Cryosphere*, 14(11), 4165–4180.
- Ulaby, F. T., Moore, R. K., & Fung, A. K. (1981). *Microwave remote sensing: Active and passive. Volume 1—microwave remote sensing fundamentals and radiometry*.
- Ulaby, F. T., Moore, R. K., & Fung, A. K. (1986). *Microwave remote sensing: Active and passive. Volume 3—From theory to applications*.
- Van den Broeke, M., Reijmer, C., Van As, D., & Boot, W. (2006). Daily cycle of the surface energy balance in Antarctica and the influence of clouds. *International Journal of Climatology: A Journal of the Royal Meteorological Society*, 26(12), 1587–1605.
- van der Veen, C. J. (2007). Fracture propagation as means of rapidly transferring surface meltwater to the base of glaciers. *Geophysical Research Letters*, 34(1).
- Van Tricht, K., Lhermitte, S., Lenaerts, J. T., Gorodetskaya, I. V., L'Ecuyer, T. S., Noël, B., Van den Broeke, M. R., Turner, D. D., & van Lipzig, N. P. (2016). Clouds enhance Greenland ice sheet meltwater runoff. *Nature communications*, 7(1), 1–9.
- van Wessem, J. M., Van de Berg, W. J., Noël, B. P., Van Meijgaard, E., Amory, C., Birnbaum, G., Jakobs, C. L., Krüger, K., Lenaerts, J., Lhermitte, S., et al. (2018). Modelling the climate and surface mass balance of polar ice sheets using RACMO2—Part 2: Antarctica (1979–2016). *The Cryosphere*, 12(4), 1479–1498.
- Vargel, C., Royer, A., St-Jean-Rondeau, O., Picard, G., Roy, A., Sasseville, V., & Langlois, A. (2020). Arctic and subarctic snow microstructure analysis for microwave brightness temperature simulations. *Remote Sensing of Environment*, 242, 111754.
- Vaughan, D. G. (2006). Recent trends in melting conditions on the Antarctic Peninsula and their implications for ice-sheet mass balance and sea level. *Arctic, Antarctic, and Alpine Research*, 38(1), 147–152.
- Wager, A. (1972). Flooding of the ice shelf in George VI Sound. *British Antarctic Survey Bulletin*, 28, 71–74.
- Weertman, J. (1973). Can a water-filled crevasse reach the bottom surface of a glacier. *IAASH publ*, 95, 139–145.
- Williamson, A. G., Banwell, A. F., Willis, I. C., & Arnold, N. S. (2018). Dual-satellite (Sentinel-2 and Landsat 8) remote sensing of supraglacial lakes in Greenland. *The Cryosphere*, 12(9), 3045–3065.
- Winther, J.-G., Jespersen, M. N., & Liston, G. E. (2001). Blue-ice areas in Antarctica derived from NOAA AVHRR satellite data. *Journal of Glaciology*, 47(157), 325–334.

- Yang, K., & Smith, L. C. (2012). Supraglacial streams on the Greenland Ice Sheet delineated from combined spectral–shape information in high-resolution satellite imagery. *IEEE Geoscience and Remote Sensing Letters*, 10(4), 801–805.
- Zheng, L., Cheng, X., Shang, X., Chen, Z., Liang, Q., & Wang, K. (2022). Greenland Ice Sheet daily surface melt flux observed from space. *Geophysical Research Letters*, 49(6), e2021GL096690.
- Zheng, L., & Zhou, C. (2020). Comparisons of snowmelt detected by microwave sensors on the shackleton ice shelf, east antarctica. *International Journal of Remote Sensing*, 41(4), 1338–1348.
- Zheng, L., Zhou, C., & Liang, Q. (2019). Variations in Antarctic Peninsula snow liquid water during 1999–2017 revealed by merging radiometer, scatterometer and model estimations. *Remote Sensing of Environment*, 232, 111219.
- Zheng, L., Zhou, C., Liu, R., & Sun, Q. (2018). Antarctic snowmelt detected by diurnal variations of AMSR-E brightness temperature. *Remote Sensing*, 10(9), 1391.
- Zheng, L., Zhou, C., Zhang, T., Liang, Q., & Wang, K. (2020). Recent changes in pan-Antarctic region surface snowmelt detected by AMSR-E and AMSR2. *The Cryosphere*, 14(11), 3811–3827.
- Zhou, C., Zheng, L., Sun, Q., & Liu, R. (2019). Amery Ice Shelf surface snowmelt detected by ASCAT and Sentinel-1. *Remote Sensing Letters*, 10(5), 430–438.
- Zwally, H. J., & Fiegles, S. (1994). Extent and duration of Antarctic surface melting. *Journal of Glaciology*, 40(136), 463–475.

3

A HIGH-RESOLUTION RECORD OF SURFACE MELT ON ANTARCTIC ICE SHELVES USING MULTI-SOURCE REMOTE SENSING & DEEP LEARNING

**Sophie de Roda Husman, Stef Lhermitte, Jordi Bolibar,
Maaïke Izeboud, Zhongyang Hu, Shashwat Shukla, Marijn
van der Meer, David Long, Bert Wouters**

This chapter has been published in IEEE Journal of Selected Topics in Applied Earth Observations and Remote Sensing as **de Roda Husman *et al.*, 2024**.

ABSTRACT

While the influence of surface melt on Antarctic ice shelf stability can be large, the duration and affected area of melt events are often small. Therefore, melt events are difficult to capture with remote sensing, as satellite sensors always face the trade-off between spatial and temporal resolution. To overcome this limitation, we developed UMelt: a surface melt record for all Antarctic ice shelves with a high spatial (500 m) and high temporal (12 h) resolution for the period 2016–2021. Our approach is based on a deep learning model, specifically a U-Net, which was developed in Google Earth Engine. The U-Net combines microwave remote sensing observations from three sources: Sentinel-1, Special Sensor Microwave Imager/Sounder (SSMIS), and Advanced Scatterometer (ASCAT). The U-Net was trained on the Shackleton Ice Shelf for melt seasons 2017–2021, using the fine-scale melt patterns of Sentinel-1 as reference data and SSMIS, ASCAT, a digital elevation model, and multi-year Sentinel-1 melt fraction as predictors. The trained U-Net performed well on the Shackleton Ice Shelf for test melt season 2016–2017 (accuracy: 91.3%; F1-score: 86.9%), and the Larsen C Ice Shelf, which was not considered during training (accuracy: 91.0%; F1-score: 89.3%). Using the trained U-Net model, we have successfully developed the UMelt record. UMelt allows Antarctic-wide surface melt to be detected at a small scale while preserving a high temporal resolution, which could lead to new insights into the response of ice shelves to a changing atmospheric forcing.

3.1. INTRODUCTION

ANTARCTICA'S ice shelves, the floating extensions of the grounded ice sheet, are crucial in regulating sea level rise (Dupont & Alley, 2005). However, these ice shelves are increasingly vulnerable to disintegration due to a mix of factors, including atmospheric-driven surface melt (J. Lenaerts *et al.*, 2017; Van den Broeke, 2005), ocean-driven basal melt (Pritchard *et al.*, 2012), and loss of structural integrity from ocean forcing (Massom *et al.*, 2018; Wilmes *et al.*, 2017) and surface velocity differences (Lhermitte *et al.*, 2020). While surface melt has played a marginal role in the past (Rignot *et al.*, 2019), it is becoming more important to the Antarctic Ice Sheet's fate as temperatures continue to rise (Gilbert & Kittel, 2021; L. Trusel *et al.*, 2015; van Wessem *et al.*, 2023). Therefore, it is essential to closely monitor surface melt on Antarctic ice shelves to better comprehend and anticipate climate change impacts.

Satellite remote sensing enables long-term and frequent mapping of the extent and dynamics of surface meltwater over the Antarctic ice shelves. Microwave remote sensing is particularly suited for this purpose because microwave signals are very sensitive to liquid water, and observations can be acquired even during cloudy conditions or at night (de Roda Husman *et al.*, 2022). Microwave remote sensing techniques can be separated into two classes: active microwave sensors, which measure backscatter intensity, i.e., the normalized radar cross-section (σ^0), and passive microwave sensors, which observe the brightness temperature (T_b) (Ulaby & Long, 2014). When melting starts, the emissivity and absorptivity of snow and ice increase significantly because of the abrupt increase of the dielectric constant, leading to a sudden decrease in backscatter intensity and an increase in brightness temperature (Ashcraft & Long, 2006; Liu *et al.*, 2006).

Many recent studies have developed methods to detect surface meltwater over the Antarctic ice shelves using active or passive microwave satellite data (e.g., Johnson *et al.*, 2020; Mousavi *et al.*, 2022; L. Trusel *et al.*, 2012). Even though these methods have shown widespread surface melt over the Antarctic ice shelves, detecting melt using data from a single satellite has limitations (see Figure 3.1). Microwave sensors such as Special Sensor Microwave Imager/Sounder (SSMIS) and Advanced Scatterometer (ASCAT) cover the entire Antarctic Ice Sheet at a high, twice-daily temporal resolution. Nevertheless, their coarse, kilometer-scale spatial resolutions are insufficient to observe small-scale melt features, such as complex surface melt patterns induced by topography at the grounding line (J. T. Lenaerts *et al.*, 2018). Data from synthetic aperture radar (SAR) sensors, such as aboard Sentinel-1, can be obtained with a much finer, meter-scale spatial resolution but often miss melt events that occur only during short periods of time due to the low revisit time of the satellite (i.e., a few times per week).

Deep learning techniques provide a promising solution to tackle the trade-off between temporal and spatial resolution in satellite imagery. U-Nets (Ronneberger *et al.*, 2015), in particular, have gained widespread recognition in various fields, including cryospheric research (e.g., Baumhoer *et al.*, 2019; Mohajerani *et al.*, 2019; Niu *et al.*, 2023; Radhakrishnan *et al.*, 2021; van der Meer *et al.*, 2023). The aforementioned studies have showcased the ability of U-Nets to identify and capture

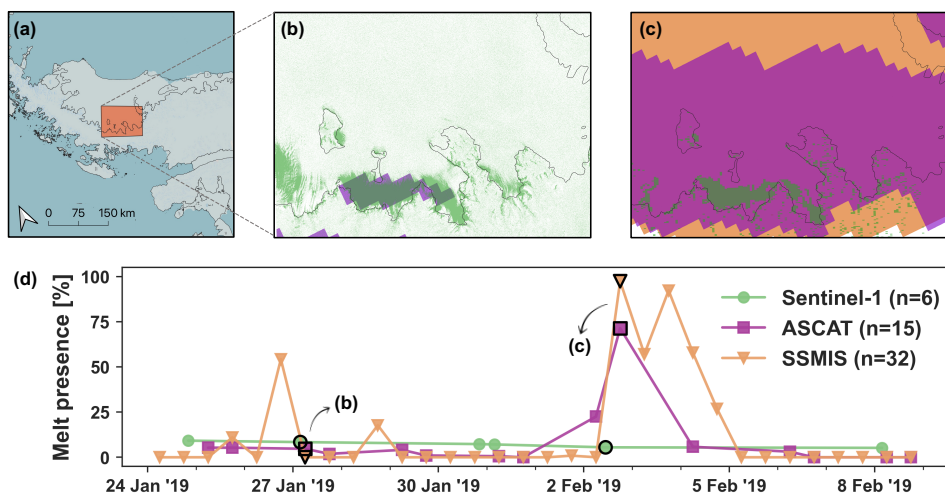


Figure 3.1: Illustration of the temporal-spatial resolution trade-off for surface melt detection. A small part of the Larsen C Ice Shelf is selected as the area of interest, shown in (a). Spatial plots of detected surface melt by Sentinel-1 (green), ASCAT (purple), and SSMIS (orange) are presented for 27 January 2019 in (b) and 2 February 2019 in (c). Panel (d) displays a time series illustrating the percentage of pixels within the study region where melt was detected. Melt is determined using threshold-based melt detection algorithms, developed by (Ashcraft & Long, 2006) for Sentinel-1 and ASCAT, and by (Zwally & Fiegles, 1994) for SSMIS.

spatial patterns, positioning them as a promising tool for effectively capturing the complex spatial melt patterns observed on Antarctica. Additionally, by processing data at frequent time intervals, U-Nets enable valuable insights into the duration, frequency, and evolution of melt events.

In this study, we present a U-Net to combine data from multiple microwave satellites into a high-resolution surface melt record, referred to as UMelt. In this way, we overcome specific sensor limitations, related to the trade-off between spatial and temporal resolution, which allows us to establish a record of surface melt over the Antarctic ice shelves at a high spatial (500 m) and high temporal (12 h) resolution for the period 2016–2021. The record is based on a combination of three microwave satellites with varying spatiotemporal resolutions, namely Sentinel-1, ASCAT, and SSMIS. Combining these data, the U-Net learned to recognize the fine-scale Sentinel-1 melt patterns, enabling the production of detailed melt maps from the coarse spatial resolution ASCAT and SSMIS observations, a digital elevation model (DEM), and multi-year Sentinel-1 melt fractions. In Section 3.2, the satellite and auxiliary data sets are introduced, and the training and validation of the U-Net are discussed. In Section 3.3, the performance of the model over training and testing ice shelves is presented, along with its application to all Antarctic ice shelves. The strengths and limitations of the developed U-Net are discussed in Section 3.4. The conclusion demonstrates how the high-resolution melt record can enhance our

understanding of the impact of surface melt on Antarctic ice shelf stability in Section 3.5.

3.2. MATERIALS AND METHODS

3.2.1. STUDY AREA

We developed a U-Net to create UMelt, a high-resolution surface melt record for all Antarctic ice shelves. Like most deep learning algorithms, U-Nets require both training and testing data to effectively learn and make accurate predictions (Ronneberger *et al.*, 2015). During the training phase, a U-Net is fed with a large data set consisting of input features (see Section 3.2.4) and their corresponding reference data (see Section 3.2.4), see Figure 3.3. By exposing the U-Net to diverse training data, it becomes more capable of recognizing and generalizing spatial patterns in the data, allowing it to make informed predictions. After training, the U-Net's performance is evaluated using a separate set of testing data that it has never encountered before. This helps assess its ability to accurately segment unseen images.

Our U-Net model was trained on the Shackleton Ice Shelf, and subsequently tested on both the Shackleton and Larsen C ice shelves. The Shackleton Ice Shelf, a large ice shelf fronting the coast of East Antarctica, was selected as a training region based on three main factors. First, the Shackleton Ice Shelf has the most “matching overpasses” (Figure 3.2a), where Sentinel-1, ASCAT, and SSMIS overpasses were acquired with less than two hours difference. These matching overpasses ensure comparable melt patterns between Sentinel-1, ASCAT, and SSMIS (see Section 3.2.5 for an elaborate description). Secondly, (Saunderson *et al.*, 2022) identified nine different melt patterns on the Shackleton Ice Shelf, which exhibited significant variability in the timing and spread of surface melt. This large variability in melt patterns on the Shackleton Ice Shelf provides a diverse and representative training data set for the U-Net model. Finally, the Shackleton Ice Shelf experiences substantial surface melting, averaging between 100–200 mm w.e. per year (L. Trusel *et al.*, 2013). Among Antarctic ice shelves, it ranks as one of the most susceptible to surface melting, except for those located on the Antarctic Peninsula (Gilbert & Kittel, 2021; L. Trusel *et al.*, 2013). Consequently, the peak melting months (December to February) closely mirror the melt patterns and corresponding remote sensing signals seen on the ice shelves with relatively high surface melt. Conversely, the months marking the beginning and end of the melting season (i.e., November and March) align with ice shelves that experience less frequent surface melting.

We tested the U-Net on the Larsen C Ice Shelf, which yielded valuable insights into the performance of the trained U-Net for three primary reasons. First, the geographic location of the two ice shelves on opposite sides of the Antarctic Ice Sheet meant that different melt patterns were expected, allowing for a robust assessment of the U-Net's transferability (i.e., the ability to apply knowledge gained from the training region to other regions without significant loss in performance). Secondly, the topography of the two ice shelves is markedly different. Large parts of the Shackleton Ice Shelf are surrounded by the ocean and buttressed by several ice

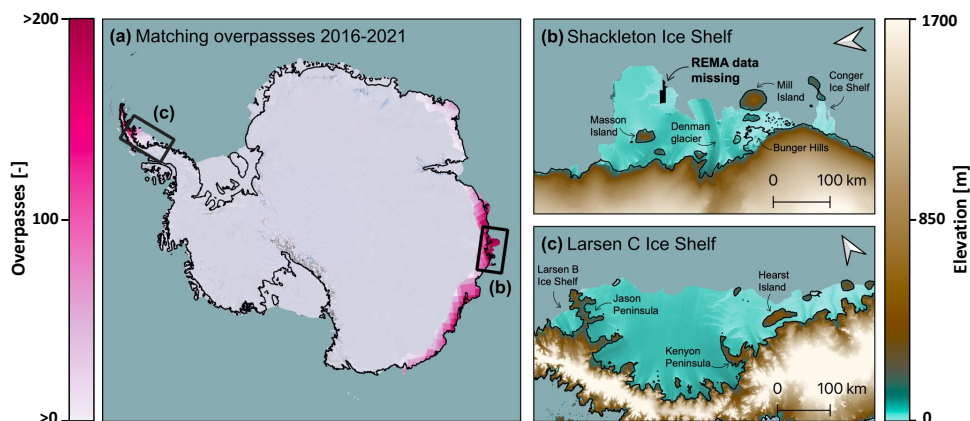


Figure 3.2: The number of matching overpasses in (a), indicating instances where the time difference between Sentinel-1, ASCAT, and SSMIS overpasses is less than two hours. The elevations of the training and testing regions, namely the Shackleton and Larsen C ice shelves, are depicted in panels (b) and (c). The Shackleton Ice Shelf has a small data gap, as indicated by the label “REMA data missing”. Other labels on the map indicate various place names on the ice shelves.

risers, while the Larsen C Ice Shelf is mostly confined by land ice and has a more homogeneous elevation over its center but a notably steep grounding line (Figure 3.2b and 3.2c). Finally, a more practical consideration was that, with around 50 matching overpasses over the Larsen C Ice Shelf, a sufficiently large testing data set was available to evaluate the U-Net’s performance.

After training and testing, the U-Net model was applied on all Antarctic ice shelves between 2016 and 2021 to generate an Antarctic-wide high-resolution surface melt record: UMelt. Because there are (almost) no matching overpasses for most of the Antarctic ice shelves (Figure 3.2a), the accuracy of our UMelt record was only determined for the Shackleton and Larsen C ice shelves.

3.2.2. MELT MASKS

UMELT MASK

Our UMelt record is available on a large part of the Antarctic Ice Sheet, but we have excluded some areas. The considered area of interest, referred to as the “UMelt mask”, is provided in Supplementary Figure 3.1a. First, extensive parts of the interior of the Antarctic Ice Sheet where high accumulation rates result in a low backscatter intensity (around -15 dB) were omitted, following the approach of (Zheng & Zhou, 2020). Under such conditions, surface melt detection algorithms may classify pixels erroneously as surface melting, whereas no surface melt has been observed on the interior of the ice sheet (e.g., van Wessem *et al.*, 2018). Moreover, pixels with an elevation over 1700 meters were ignored, as surface melt is unlikely to occur there (Banwell *et al.*, 2021; de Roda Husman *et al.*, 2022). Finally, areas with no Sentinel-1

overpasses were removed (refer to Figure 2.2 in Chapter 2), because we were unable to generate the multi-year Sentinel-1 melt fraction input feature. After implementing these exclusions, the study area was reduced to 1.8 million km², which accounts for 12.7% of the total area of the Antarctic Ice Sheet.

U-NET DEVELOPMENT MASK

To test and train the U-Net model, we excluded additional regions beyond those covered by the UMelt mask (described in Section 3.2.2). Specifically, we omitted damaged regions, which are known to confuse melt detection algorithms on the reference product, Sentinel-1 (Dirscherl *et al.*, 2021; Zhou *et al.*, 2019). Damaged regions, i.e., regions containing fractures, rifts, or crevasses on the ice surface, lead to distortions in SAR images. These distortions result in high backscatter intensities for slopes facing toward the sensor (known as radar foreshortening) and low backscatter intensities for slopes facing away from the sensor (known as radar shadows). These radar shadows can be mistakenly identified as surface melt. Therefore, we created a “damage mask” using the damage detection method developed by (Izeboud & Lhermitte, 2023). This method detects the presence of a fracture feature within a group of pixels based on a line detection algorithm. Noise is removed using a sensor- and processing-resolution specific threshold, for which we used $\tau = 0.1$ (damage detection applied to Sentinel-1 EW images, processed on 100 m resolution with 10x10 pixel groups). Furthermore, a buffer with a radius of 5 km was applied to mask neighboring pixels.

In comparison to the UMelt mask (Section 3.2.2), removing the damage pixels for the Shackleton Ice Shelf resulted in an 8% reduction, transforming the UMelt mask from 52×10^3 km² to a UMelt development mask of approximately 48×10^3 km². Similarly, for the Larsen C Ice Shelf, about 9% of pixels were removed from the UMelt mask to derive the UMelt development mask, decreasing from 84×10^3 km² to 77×10^3 km².

3.2.3. U-NET ARCHITECTURE

We used an Attention U-Net architecture for our image segmentation task, which is an extension of the traditional U-Net (Ronneberger *et al.*, 2015) that incorporates attention gates to selectively highlight relevant features (Oktay *et al.*, 2018; Trebing *et al.*, 2021). Our network consisted of two main parts: the contracting path for encoding and the expansive path for decoding (see Figure 3.3).

In the contracting path, the input features were progressively downsampled by convolutional layers and max-pooling operations, allowing the network to extract high-level features (Girshick *et al.*, 2014). These high-level features capture information about the rough outlines of surface melt events, disregarding small-scale melt details. These features are analogous to the large-scale melt patterns observed by (Saunderson *et al.*, 2022), who studied surface melt using satellite data with a 25 km spatial resolution on the Shackleton Ice Shelf. In the expansive path, the features coming from the encoder are upsampled by transposed convolutions. Furthermore, they are concatenated with features from the contracting path through

skip connections, which connect corresponding encoder and decoder layers. This preserves low-level features, such as the spatial arrangements of melt pixels on a small scale. The attention gates were added to these skip connections to allow the network to selectively focus on important features while filtering out irrelevant information (Oktay *et al.*, 2018).

We conducted hyperparameter tuning on the validation data set (See Section 3.2.5) to optimize the performance of our Attention U-Net model. We did a grid search over all possible combinations of hyperparameters (Bengio, 2012), which included the learning rate (0.05, 0.01, 0.005, 0.001, 0.0005, 0.0001), batch size (16, 32, 64, 128), the number of filters for the first layer, which was doubled in each subsequent layer (16, 32, 64, 128), and the dropout rate (constant rate of 0.5 applied to the different convolution layers). For each combination of hyperparameters, we trained the model on the training data set and evaluated its performance (i.e., segmentation accuracy) on the validation data set to identify the optimal configuration. The optimal hyperparameters maximized the segmentation accuracy (learning rate: 0.001; batch size: 32; number of channels: 32; dropout rate of 0.5: applied to the fourth and fifth convolution layers). In cases where the difference in validation accuracy was less than 1% for different hyperparameters, we selected the most computationally efficient ones.

We employed commonly used and standard algorithms for activation, loss, and optimization, which are (almost) similar to those employed in previous works such as (Dahle *et al.*, 2022), (Mastrofini *et al.*, 2023), and (Zhao *et al.*, 2022). Specifically, the Rectified Linear Unit (ReLU) activation function was utilized for the hidden layers, effectively eliminating negative values within the neural network and allowing only positive values to propagate. Additionally, the sigmoid activation function, commonly employed in binary classification tasks, was employed in the final layer to compress the output within the range of 0 to 1, representing the probability. To address the class imbalance issue in the training data, where non-melt pixels outnumbered melt pixels by a factor of four, we incorporated class weighting based on the melt and non-melt pixels ratio into the binary cross-entropy loss function. This ensured that missing a surface melt event incurred a higher penalty compared to missing a non-melt event. The Adam optimization algorithm was used, which allowed efficient training and parameter optimization.

The model was trained for a maximum of 30 epochs, with each epoch taking approximately 10 minutes. Early stopping was implemented to stop training when the validation loss did not improve for three consecutive epochs. The default early stopping settings were used, considering any improvement, regardless of magnitude, as progress. As a result, the U-Net model used for generating the UMelt record was trained for 10 epochs. However, for other models used to evaluate spatial and temporal performance, the number of epochs varied between 5 and 12.

To perform the training, we utilized Google Colab, a cloud-based platform that offers GPU access for deep learning tasks. TensorFlow, the deep learning framework used to code our model, is integrated into Google Colab, simplifying the process of building and training the model.

3.2.4. PREPROCESSING

REFERENCE DATA

Sentinel-1 observations were used to create the reference data (sometimes referred to as target or ground truth data) for the U-Net. We used Sentinel-1 Level-1 Ground Range Detected (GRD) scenes in the linear scale that were preprocessed in the Google Earth Engine (Gorelick *et al.*, 2017). This preprocessing included orthorectification, radiometric calibration, thermal noise removal, and border noise removal. It is worth noting that border noise removal was applied to scenes from January 2018 onwards in the preprocessed images available in the Google Earth Engine. This occasionally leads to noisy pixels at the edges of scenes prior to January 2018.

We selected all available horizontally polarized GRD scenes over the Antarctic Ice Sheet for melt seasons 2016–2021, allowing a combination of Interferometric (IW) and Extra Wide (EW) overpasses. The scenes were resampled to a 500 m resolution using bilinear interpolation and reprojected to WGS 84 Antarctic Polar Stereographic projection (EPSG:3031). The utilization of a 500 m spatial resolution enabled the detection of surface melt features at a small scale, while concurrently ensuring the data could be processed efficiently.

Then, we derived the binary melt presence (i.e., melt/non-melt) for the Sentinel-1 observations using the widely used melt detection algorithm proposed by Ashcraft and Long (2006). Melt presence was assumed when the backscatter intensity was smaller than the annual winter mean minus a certain threshold by using the following equation:

$$m(t) = \begin{cases} 1, & \sigma^0(t) < \sigma_{\text{winter}}^0 + \Delta\sigma^0 \\ 0, & \sigma^0(t) \geq \sigma_{\text{winter}}^0 + \Delta\sigma^0 \end{cases} \quad (3.1)$$

where σ_{winter}^0 is the average backscatter intensity of the previous winter months, and $\Delta\sigma^0$ is the threshold which was set to -3 dB (similar to Ashcraft and Long, 2006). To address the substantial disparities in backscatter intensity across different orbits, we implemented Equation (3.1) on a per Sentinel-1 orbit basis. This approach accounts for the variations in backscatter intensities stemming from differences in incidence angles.

INPUT FEATURES

The U-Net input received four input features: ASCAT, SSMIS, elevation, and the multi-year Sentinel-1 melt fraction (see Figure 3.3), offering diverse information related to surface melt patterns and characteristics. ASCAT, similar to Sentinel-1, is an active microwave satellite. However, it exhibits lower spatial resolution (kilometer-scale instead of meters) and a higher revisit time (twice a day instead of a few times per week) when compared to Sentinel-1. Consequently, we expect that ASCAT will provide valuable information on the dynamic changes in melt patterns over time, although it may primarily capture coarse-scale patterns. Similar to ASCAT, SSMIS also provides information on liquid water presence on a coarse spatial scale but with a high temporal resolution. However, it is important to consider that

SSMIS measures the brightness temperature instead of the backscatter intensity. This distinction means that SSMIS is influenced by various parameters beyond just liquid water content, which can result in significant differences in large-scale patterns compared to Sentinel-1 and ASCAT (Hofer & Mätzler, 1980; Mote & Anderson, 1995). Nevertheless, SSMIS is highly sensitive to detecting even small amounts of liquid water, enabling valuable insights into less intense melt events (Picard *et al.*, 2022). The role of elevation data is also crucial in this study, given its high spatial resolution and well-established inverse correlation with melt patterns (L. Trusel *et al.*, 2013). In addition to the aforementioned input features, multi-year melt fractions from Sentinel-1 are also utilized to provide insights into spatial details. Although these details may not be critical for capturing day-to-day variations, which are significant in Antarctica, they offer valuable information about the most common fine-scale melt patterns. The subsequent paragraphs will sequentially elaborate on the details of the four input features.

For the ASCAT input feature, we utilized vertically polarized observations with a 4.45 km resolution, consistent with prior studies (e.g., S. L. Bevan *et al.*, 2018; de Roda Husman *et al.*, 2022; L. Trusel *et al.*, 2012), obtained from the Brigham Young University Microwave Earth Remote Sensing Laboratory (Long, 2022). ASCAT captures observations of the Antarctic Ice Sheet every other day at 6 AM (morning) and 6 PM (evening). We calculated averages to address days without observations by combining the morning before and after a missing morning observation (and similarly for missing afternoon observations). This process allowed the creation of a twice-daily ASCAT time series. Then, instead of generating binary melt presence from ASCAT observations by applying a threshold (i.e., $\Delta\sigma^0$ in Eq. (3.1)), we only subtracted σ_{winter}^0 from the ASCAT observations. Continuous data carry more information than binary data, allowing the U-Net to learn the most appropriate threshold depending on the situation rather than relying on a specific threshold value. Finally, we normalized these values between the low (5th percentile) and high (95th percentile) values of ASCAT minus the winter mean over the Shackleton Ice Shelf for the melt seasons from 2016–2021, without capping values below zero or larger than one.

We utilized horizontally polarized 19 GHz SSMIS observations from the NASA MEaSUREs project (Brodzik *et al.*, 2016) as the second input feature, with a spatial resolution of 6.25 km (similar to, e.g., X. Wang *et al.*, 2022; Wei *et al.*, 2022). Observations from the F17 sensor were selected, which consistently passed over at approximately 6 AM and 6 PM during our study period. We applied a similar approach as for ASCAT and created continuous and normalized melt observations by subtracting the average brightness temperature of the previous winter months and scaling the values between the 5th and 95th percentiles.

As for the third input, we utilized the Reference Elevation Model of Antarctica (REMA) mosaic to inform the model on the elevation of the Antarctic Ice Sheet (Howat *et al.*, 2019). The REMA mosaic has a high resolution of two or eight meters, depending on the location. For this study, the resampled version with a resolution of 200 meters was used, which was sufficient for our purposes. While the REMA mosaic provides extensive coverage of the continent, there are some gaps

in coverage, including a small area of the Shackleton Ice Shelf (as shown in Figure 3.2b). We disregarded the data gaps, predominantly located along the edges of ice shelves with minimal surface melt.

The fourth input feature consisted of the multi-year melt fractions of Sentinel-1 data, derived from the reference data discussed in Section 3.2.4. The multi-year Sentinel-1 melt fractions were computed by summing the monthly melt pixels obtained using Equation (3.1) and then dividing the sum by the total number of observations in that specific month. We are aware that using Sentinel-1 as reference and input data may raise concerns about information leakage. To address this, we ensured the exclusion of the month of interest from the calculation, aiming to eliminate any potential correlation between the input features and reference data. For instance, when calculating the multi-year melt fraction for November 2016, the melt fraction was derived from the November months of 2017 until 2021. To validate that the U-Net model was not simply replicating the monthly melt fractions of Sentinel-1, we conducted an assessment of the importance of each feature, as described in Section 3.2.7.

Finally, the four input features were resampled to match the scale and projection of the preprocessed Sentinel-1 scenes, which were in the WGS 84 Antarctic Polar Stereographic projection with a resolution of 500 meters.

COMPARISON UMelt TO SENTINEL-1, ASCAT, AND SSMIS

To facilitate a comparison between the UMelt record and surface melt observations from Sentinel-1, ASCAT, and SSMIS, binary melt products were also derived from ASCAT and SSMIS observations. The approach used for Sentinel-1 was explained in Section 3.2.4, while continuous values were utilized as input for ASCAT and SSMIS (as described in Section 3.2.4). A further step was required to compare these data with the UMelt record: converting the continuous ASCAT and SSMIS data to binary melt estimates using thresholding algorithms. We applied the same melt detection algorithm used for Sentinel-1 (Eq. (3.1)) to ASCAT to achieve this. For SSMIS, a melt detection algorithm suggested by (Torinesi *et al.*, 2003) was implemented, which has been used in several previous studies (e.g., Banwell *et al.*, 2021; Johnson *et al.*, 2020; Wille *et al.*, 2019). The algorithm defines surface melt based on the observed brightness temperature surpassing an empirical threshold, typically between 30 K and 40 K. This dynamic threshold is determined using the mean and variability of the brightness temperatures recorded during the preceding winter.

In addition to comparing UMelt with single observations from Sentinel-1, ASCAT, and SSMIS, we calculated the “summer melt occurrence” following the methodology of (de Roda Husman *et al.*, 2022). The summer melt occurrence, computed for each melt season spanning November through March, represents the ratio of the number of melt observations to the total number of observations per pixel. The metric is expressed as a percentage and was computed using binary products obtained from UMelt, Sentinel-1, ASCAT, and SSMIS.

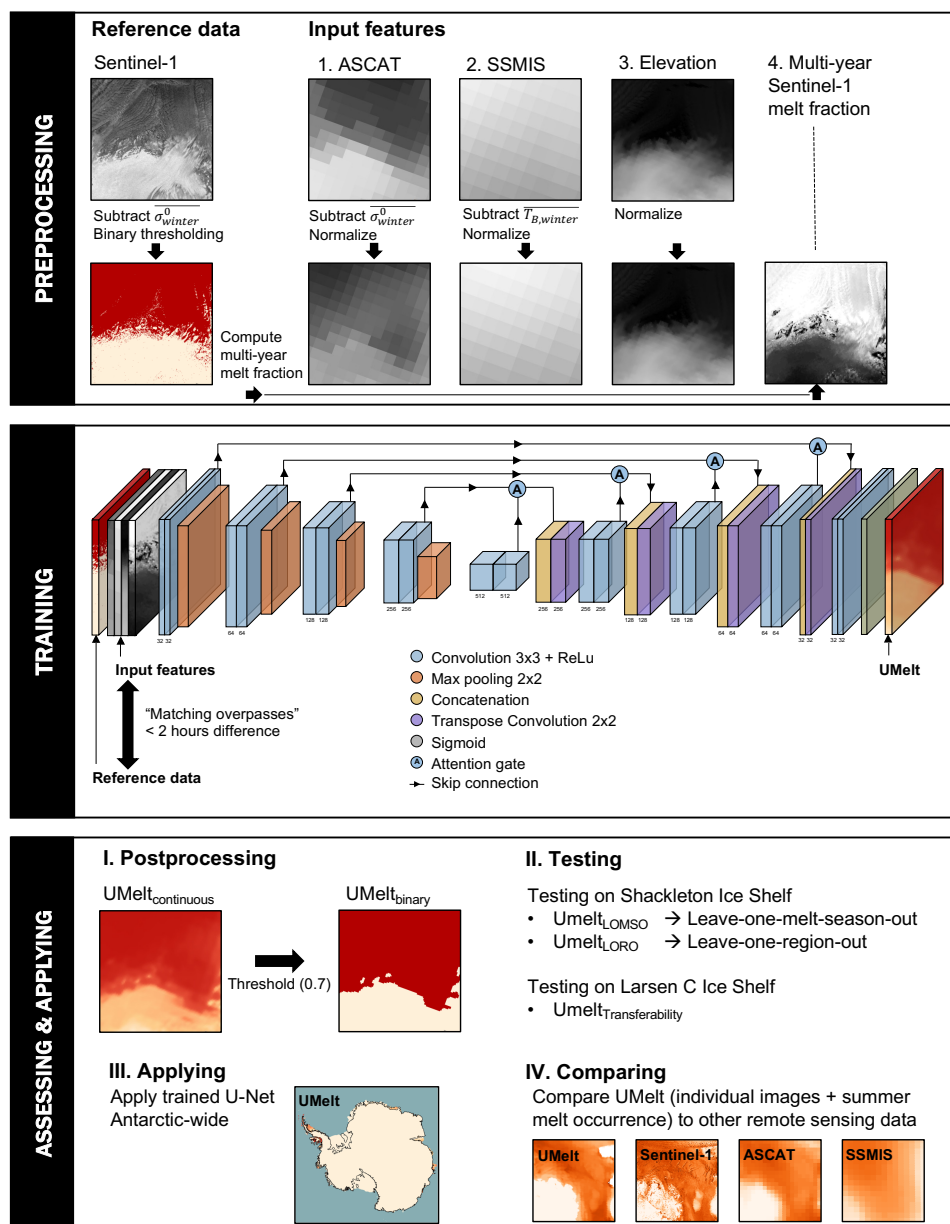


Figure 3.3: Conceptual overview of the method employed in this study, which is divided into three key steps: preprocessing, training, and assessing & applying. The details of this method are discussed in Sections 3.2.4–3.2.7.

3.2.5. TRAINING, VALIDATION, AND TESTING DATA

The training, validation, and testing data were selected according to the criterion that the temporal difference in Sentinel-1, ASCAT, and SSMIS overpass times was less than two hours. This criterion was important as surface melt can occur for a very short duration, and larger differences in overpass time may lead to disparities in the detected surface melt among the satellite observations. The matching overpasses of Sentinel-1, ASCAT, and SSMIS were then combined with the elevation and Sentinel-1 multi-year melt fraction data sets, creating a 5-band (i.e., channels) image comprising reference labels (i.e., Sentinel-1 binary melt) and four input features (i.e., ASCAT, SSMIS, elevation, and multi-year Sentinel-1 melt fraction).

We employed stratified sampling to achieve a balanced data set for effective learning and recognition of melt patterns by the U-Net model. This process involved randomly selecting points on the Shackleton Ice Shelf, all within the U-Net development mask (Supplementary Figure 3.1b). For each matching overpass, a total of 10 points were selected, comprising an equal number of melt pixels (5) and non-melt pixels (5), determined by the Sentinel-1 labels. It is worth noting that only non-melt pixels were selected if a Sentinel-1 scene did not contain any melt pixels. Subsequently, we generated patches of input features and labels by selecting neighboring pixels around the sampled points. As the stratified sampling points were randomly distributed, patches could overlap. Each patch was sized at 64 x 64 pixels, equivalent to 32 x 32 kilometers, ensuring they captured sufficient detail to represent the melt patterns accurately and guaranteeing an appropriate distribution of melt locations. Finally, all patches from one matching overpass were assigned to either the training data set (80%), the validation data set (10%), or the testing data set (10%). Each set's approximate number of pixels was 15 million for training, 2 million for validation, and 2 million for testing.

3.2.6. POST-PROCESSING

After training the U-Net, the model was applied to create the UMelt record. We stacked the input features (i.e., ASCAT, SSMIS, elevation, and multi-year Sentinel-1 melt fraction) and tiled the data into patches of 64 x 64 pixels (similar to in Section 3.2.5), using an 8-pixel overlap on all sides. In overlap regions, prediction results were calculated as the mean of the prediction probabilities.

Next, we converted the prediction probabilities into a binary product using a threshold of 0.7. We determined that this specific threshold value yielded the best performance on the validation set (see Supplementary Figure 3.3). Pixels with probability values exceeding the 0.7 threshold were identified as melt pixels, whereas those below the threshold were labeled as non-melt.

3.2.7. ACCURACY ASSESSMENT

To assess the performance of our U-Net model, we utilized the test data set, which was not used during the training and validation phases. Several performance metrics, including precision, recall, F1-score, and accuracy, were calculated. Precision measures the fraction of true positive predictions among the total predicted positive

instances, while recall measures the fraction of true positive predictions among the total actual positive instances. The F1-score is the harmonic mean of precision and recall, providing a single value that combines both measures. Accuracy measures the overall proportion of correct predictions over all instances.

Cross-validation is essential for training the U-Net model as it enables reliable performance evaluation, prevents overfitting, and improves our understanding of its effectiveness (Bolibar *et al.*, 2020; Roberts *et al.*, 2017). Specifically, to assess the temporal performance of the U-Net, we performed a ‘leave-one-melt-season-out’ (LOMSO) analysis. We evaluated the model’s performance when applied to the melt season that was excluded from training. In Section 3.3, we discuss the accuracies over a very wet season (2019–2020), a very dry season (2020–2021), and an average melt season (2016–2017). High accuracies over unseen melt seasons hint at a good performance of the U-Net over other ice shelves with more or less extreme melt intensities than at the Shackleton Ice Shelf.

In order to evaluate the model’s spatial performance, we partitioned the Shackleton Ice Shelf into four distinct parts with similar areas (see Supplementary Figure 3.1d). Then, we implemented a ‘leave-one-region-out’ (LORO) approach to assess the model’s accuracy when applied to an unseen region. The melt patterns are very diverse over the ice shelf. Therefore, a high accuracy over an unseen region means the model is probably well-capable over other Antarctic ice shelves.

We assessed the transferability of the U-Net by applying the model to the Larsen C Ice Shelf for melt season 2016–2017. We applied the trained model for which melt season 2016–2017 was excluded, so that we could assess the performance for both an unseen spatial and temporal domain. Please be aware that our model’s transferability was exclusively evaluated over the Larsen C Ice Shelf. This is due to a lack of matching overpasses on other ice shelves (see Figure 3.2a). Consequently, accuracy computations for ice shelves other than Shackleton and Larsen C were hindered.

In the final stage of the accuracy assessment, the significance of the four input features was evaluated by training four separate models, with each model excluding one feature at a time. The training was conducted over melt seasons 2017–2021, and the performance was assessed on the unseen melt season 2016–2017. By comparing the accuracies and spatial patterns of these models, we could determine the importance of each input feature. If a model exhibited notably lower performance compared to the model utilizing all four features, it indicated the excluded input feature’s significance.

3.3. RESULTS

We evaluated the performance of the U-Net model using varying spatial and temporal domains of the training, validation, and testing data sets. We present the results over the Shackleton Ice Shelf, Larsen C Ice Shelf, and Antarctic-wide in Sections 3.3.1, 3.3.2, and 3.3.3, respectively. Supplementary Table 3.1 contains the accuracy assessment results for all experiments.

3.3.1. SURFACE MELT OVER SHACKLETON ICE SHELF

TEMPORAL PERFORMANCE

We first evaluated the performance of the U-Net model on the Shackleton Ice Shelf in terms of temporal performance. Specifically, we examined the model's ability to predict melt events during unseen seasons, which we refer to as UMelt_{LOMSO}. Figure 3.4 shows that UMelt_{LOMSO} performed well on three distinct days at the beginning, middle, and end of the 2016–2017 melt season, despite not being trained on data from the 2016–2017 season (see Supplementary Video in the published manuscript for melt observations for all days with matching overpasses). The model accurately identifies the complex melt patterns over the Shackleton Ice Shelf, resulting in an F1-score of 86.9% and an accuracy of 91.3% when compared to Sentinel-1. Notably, ASCAT and SSMIS (Figure 3.4, column 4 and 5, respectively) detect mostly larger melt patterns, with the exception of the western part of the Shackleton Ice Shelf. Here, SSMIS tends to underestimate melt due to the presence of a frequently occurring polynya that results in lower brightness temperatures, as noted by (Nihashi & Ohshima, 2015). However, both sensors often miss the detailed melt patterns captured by the reference product Sentinel-1. Our UMelt product is well able to detect these small-scale patterns, especially along the grounding line and on Masson Island (location indicated in Figure 3.2).

The accuracy of UMelt, ASCAT, and SSMIS melt observations compared to the reference product Sentinel-1 is displayed in Figure 3.4d. UMelt achieved an average accuracy of 91.3% for the 2016–2017 melt season, which is higher than the average accuracies of ASCAT and SSMIS, with 90.0% and 82.3%, respectively.

UMelt is particularly effective in detecting small-scale patterns, such as those found on the grounding line and on Masson and Mill islands (Figure 3.5). In contrast, ASCAT and SSMIS incorrectly detect melt at Masson Island (Figure 3.5f), where the elevation is over 1000 meters and Sentinel-1 does not indicate any surface melt. In addition, Sentinel-1 shows a wide range of melt patterns over the grounding line (Figure 3.5e and i), which UMelt_{LOMSO} accurately simulates. The detected melt on the Bunger Hills (Figure 3.5h) demonstrates the most notable difference, with Sentinel-1 revealing complex melt patterns, while ASCAT and UMelt show minimal detection of melt. In contrast, SSMIS detects melt throughout the entire Bunger Hills region but lacks the expected level of detail considering the diverse terrain and varying elevations.

Additionally, our findings indicate that UMelt outperformed ASCAT and SSMIS for the 2019–2020 and 2020–2021 melt seasons (Supplementary Figure 3.2). In the 2019–2020 melt season, UMelt obtained an average accuracy of 90.9%, while in the 2020–2021 melt season, it achieved a higher accuracy of 95.7%. However, it is important to note that the F1-score for the 2020–2021 melt season was significantly lower (33.5%) than that of the 2016–2017 (86.9%) and 2019–2020 (82.7%) melt seasons. The 2020–2021 melt season experienced minimal melting, which is clearly reflected in the cumulative yearly melt maps by (Picard, 2022) (more details on the melt maps in Picard & Fily, 2006). Out of the small amount of melt that did occur, only 55.3% of the identified melt pixels were accurately classified.

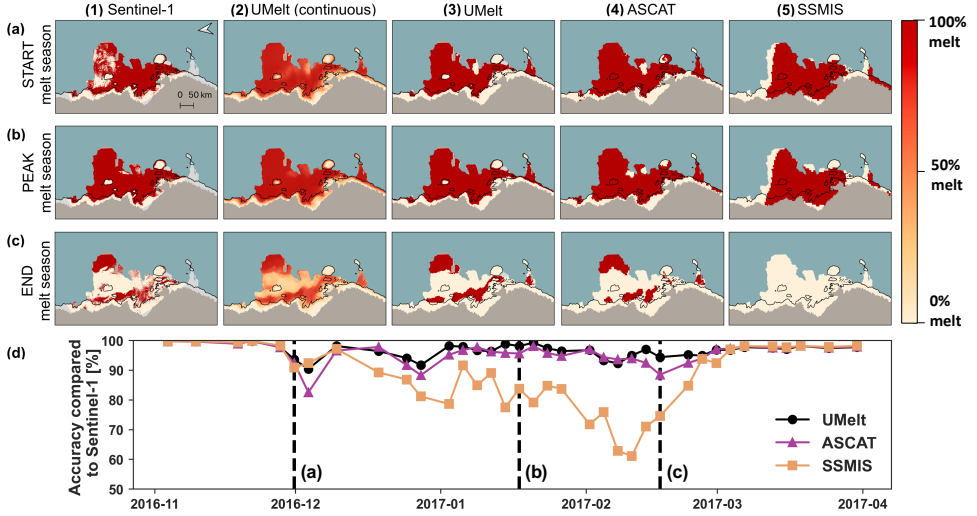


Figure 3.4: The maps in (a), (b), and (c) present a comparison of reference data Sentinel-1 (first column) and our $\text{UMelt}_{\text{LOMSO}}$ product, visualized in both continuous format without threshold (third column) and binary format with a 0.7 threshold (second column), ASCAT (fourth column), and SSMIS (fifth column), at the beginning (30 November 2016, 6 PM), peak (17 January 2017, 6 PM), and end (16 February 2017, 6 PM) of the melt season of 2016–2017. The time series in (d) present the melt accuracy of UMelt (black), ASCAT (orange), and SSMIS (pink) compared to Sentinel-1 for melt season 2016–2017 on the Shackleton Ice Shelf.

SPATIAL PERFORMANCE

The model also showed a solid performance when regions of the ice shelf were not included during training, as shown in Figure 3.6. In particular, we found that for the two regions located at the center of the ice shelf (Region 1 and Region 3), the accuracies of UMelt trained on all regions and $\text{UMelt}_{\text{LORO}}$ were comparable, with an average difference in accuracies of 0.3% and 0.4%, respectively. However, Region 3 resulted in the lowest accuracy of the four regions, both for UMelt (i.e., 87.6%) and $\text{UMelt}_{\text{LORO}}$ (i.e., 87.2%), whereas all the other regions resulted in accuracies exceeding 90%.

In the case of Regions 2 and 4, which are situated at the grounding line, we observed similar discrepancies in accuracy between UMelt and $\text{UMelt}_{\text{LORO}}$ as for Regions 1 and 3, ranging from 0.2–0.4%. However, when examining specific pixels along the grounding line, $\text{UMelt}_{\text{LORO}}$ exhibited over- or underestimation of surface melt occurrence by -25% to $+25\%$ compared to UMelt. In general, UMelt predicts a melt presence further inland, whereas the melt presence predicted by $\text{UMelt}_{\text{LORO}}$ for Regions 2 and 4 ends closer to the grounding line. However, it comes as no surprise that the most significant discrepancy is evident along the grounding line. This region showcases exceptionally intricate melt patterns that ASCAT and SSMIS struggle to resolve adequately because of their limited spatial resolution. Despite this, the comparable performance of UMelt and $\text{UMelt}_{\text{LORO}}$ is promising for the application of

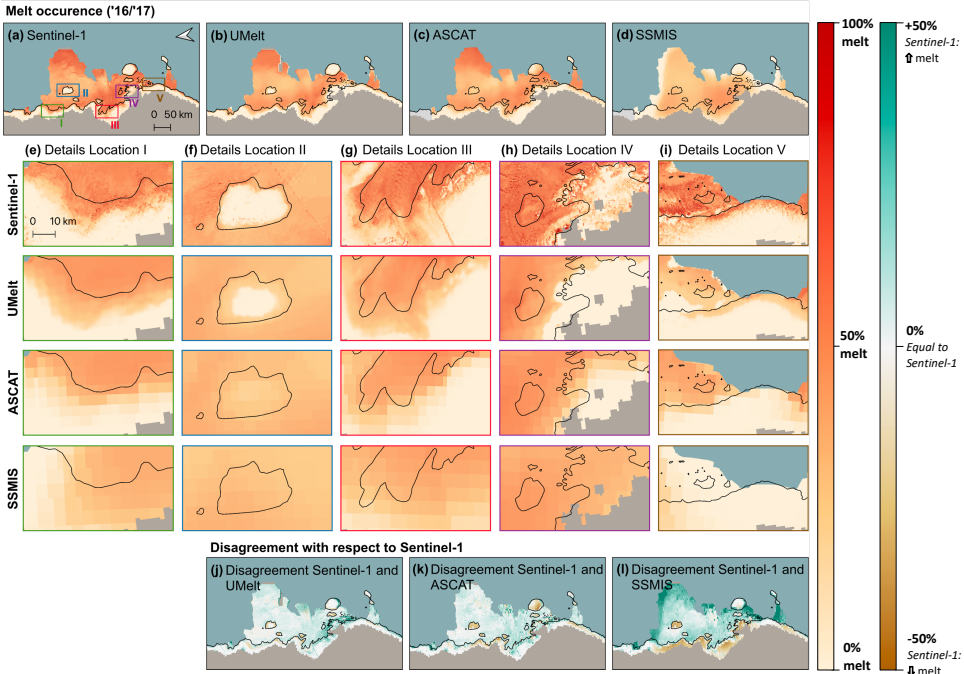


Figure 3.5: The summer melt occurrence on Shackleton Ice Shelf for testing melt season 2016–2017 for Sentinel-1 (a), UMelt (b), ASCAT (c), and SSMIS (d). Details of five locations are shown in (e–i). The disagreements between Sentinel-1 and UMelt, Sentinel-1 and ASCAT, and Sentinel-1 and SSMIS are shown in (j–l).

UMelt on an Antarctic-wide scale, showcasing that the U-Net demonstrates favorable performance even on untrained regions.

FEATURE IMPORTANCE

Convolutional neural networks are black-box algorithms, and their lack of transparency regarding feature importance remains a challenge (Olden & Jackson, 2002). However, we can get an estimate of the importance of features by iteratively removing them during the training of the model and evaluating its performance (Zhang *et al.*, 2018).

Figure 3.7 demonstrates the importance of the four input features used for the development of UMelt: ASCAT, SSMIS, elevation, and multi-year Sentinel-1 melt fraction. The results show that ASCAT is the most important feature, as evidenced by the drop in accuracy from 91.3% to 80.2% when ASCAT is removed from the training phase (Supplementary Table 3.1). The exclusion of ASCAT reduces surface melt across the entire study area, emphasizing its significance as an input feature. This is not surprising as both ASCAT and the reference data Sentinel-1 are C-band active microwave sensors, and therefore result in melt patterns that are comparable on a

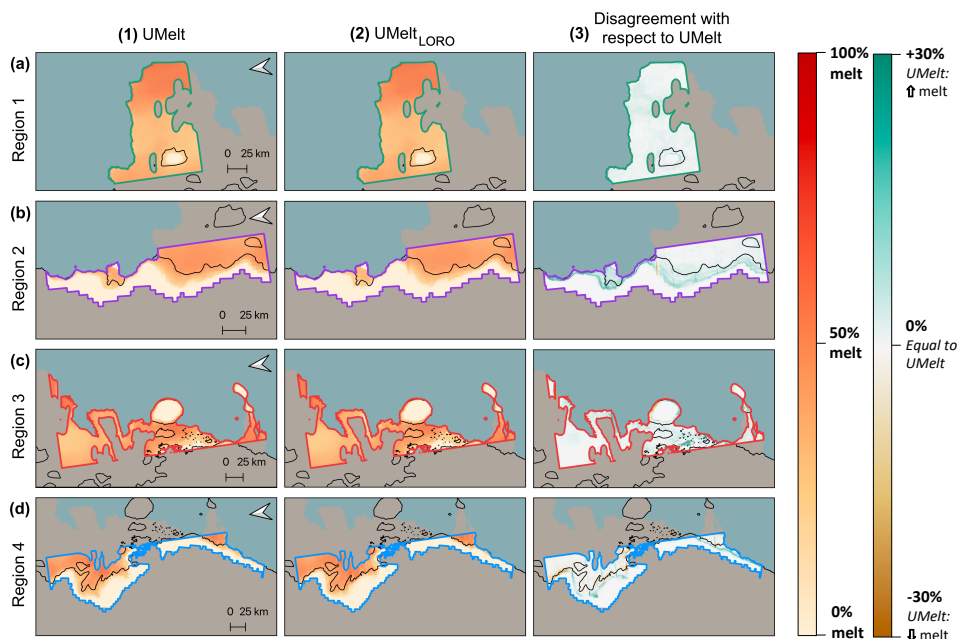


Figure 3.6: Summer melt occurrence of UMelt (1) and UMelt_{LORO} (2) for melt season 2016–2017 on the Shackleton Ice Shelf for the four leave-one-region-out (LORO) regions (a–d). UMelt (1) was trained on the entire ice shelf using data from melt seasons 2017–2021. UMelt_{LORO} (2) was trained on the same period, but one region was excluded at a time. Then, the trained model was tested on the excluded region to evaluate the spatial transferability of the model. The disagreement between UMelt and UMelt_{LORO} is shown in (3).

larger scale (although smaller details may differ due to spatial resolution differences).

In contrast, SSMIS, elevation, and multi-year Sentinel-1 melt fraction are less important, and their exclusion results in comparable disagreement with Sentinel-1 as the model trained on all input features (Supplementary Table 3.1). However, including these features results in the identification of detailed melt patterns similar to those in Sentinel-1. Additionally, multi-year Sentinel-1 melt fraction is important for melt detection on the eastern part of the Shackleton Ice Shelf (Figure 3.7e), where small surface lakes are present annually (Arthur *et al.*, 2020), but are not detected by ASCAT and SSMIS due to their low spatial resolution.

3.3.2. SURFACE MELT OVER LARSEN C ICE SHELF

In order to ensure that the U-Net model is applicable on an Antarctic-wide scale, we assessed its performance on the Larsen C Ice Shelf during the 2016–2017 melt season. We applied the UMelt_{LOMSO}, which was trained on the Shackleton Ice Shelf for the melt seasons between 2017–2021. This provides a fully out-of-sample performance estimate of our model since the trained model has neither seen the spatial region nor the temporal period of the target data set.

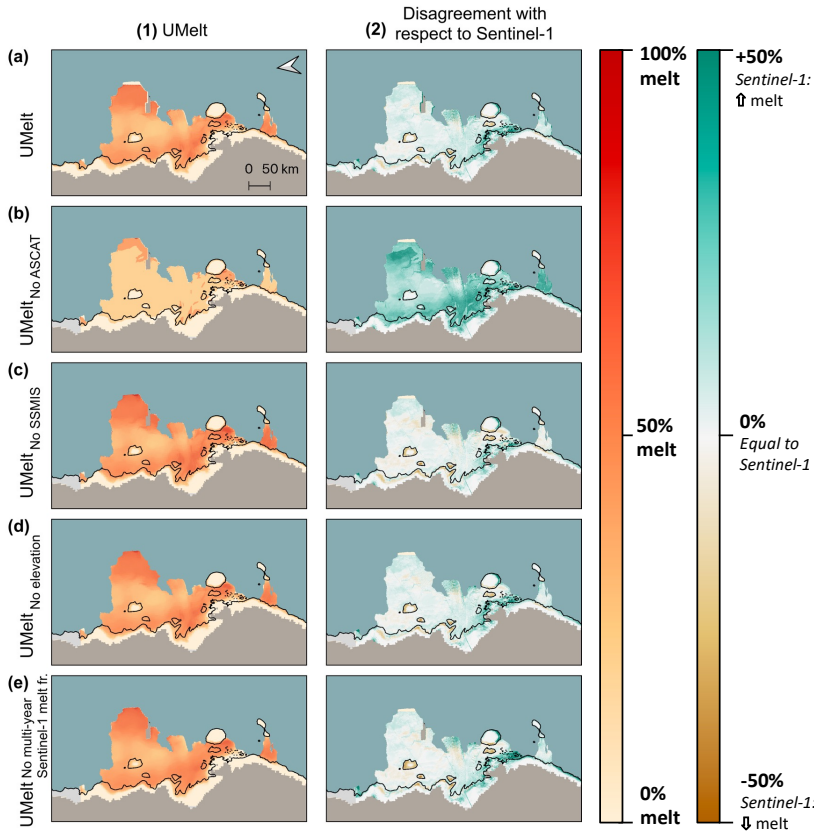


Figure 3.7: Surface melt occurrence and performance compared to Sentinel-1 over the Shackleton Ice Shelf for the melt season 2016–2017 for different input features. Column 1 (a–e) displays the UMelt summer melt occurrence trained on different input features, where UMelt trained on all input features is presented in (a), and panels (b)–(e) correspond to UMelt with one of the input features excluded (ASCAT, SSMIS, elevation, and multi-year Sentinel-1 melt fraction, respectively). Column 2 (a)–(e) demonstrates the comparison of UMelt and Sentinel-1 performance, where the disagreements between Sentinel-1 and UMelt models trained with different input features are presented.

The general melt patterns from UMelt on Larsen C overlap well with the Sentinel-1 patterns, showing most melt in the western part of the ice shelf. However, in Figures 3.8d and 3.8g, UMelt tends to overestimate surface melt landward of the grounding line where the elevation rapidly increases. There are two plausible explanations for this overestimation. First, the multi-year Sentinel-1 melt fraction, which is one of the input features, was derived from melt seasons spanning 2017 to 2021. During this period, surface melt was present landward of the grounding line. Hence, certain sections of the grounding line experienced an overestimation of surface melt during the 2016–2017 melt season, due to the comparatively wetter melt seasons observed

between 2017 and 2021 (S. Bevan *et al.*, 2020). Secondly, the Shackleton Ice Shelf, on which UMelt was trained, experiences surface melt at elevations up to around 300 meters. The regions along Larsen C's grounding line where UMelt overestimated the surface melt are situated at elevations of 100–300 meters, within the range where the UMelt model was trained to detect melting. Nevertheless, UMelt demonstrated a strong overall performance during the 2016–2017 melt season with an average F1-score of 89.3% with many UMelt patterns that matched with Sentinel-1. This is a better performance compared to Sentinel-1 than ASCAT and SSMIS, which have F1-scores of 85.9% and 80.0%, respectively.

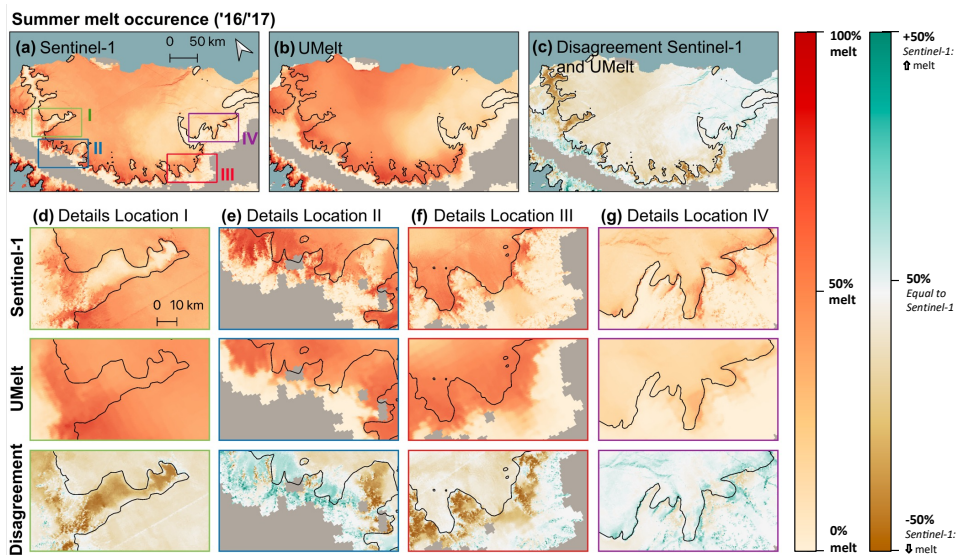


Figure 3.8: The summer melt occurrence on Larsen C Ice Shelf for testing melt season 2016–2017 for Sentinel-1 (a), UMelt (b), and the disagreements between Sentinel-1 and UMelt (c). Details of four locations are shown in (d–g).

3.3.3. ANTARCTIC-WIDE SURFACE MELT

The U-Net was trained on the Shackleton Ice Shelf using data from all five melt seasons (i.e., 2016–2021) and subsequently applied to the entire Antarctic region, with the exception of the masked areas (see Section 3.2.2 and Supplementary Figure 3.1a), resulting in an observation area of 1.8 million km². The UMelt product for melt season 2016–2017 is presented in Figure 3.9, while the summer melt occurrence derived from the melt observations of seasons 2017–2021 are shown in Supplementary Figure 3.4.

In the aggregated summer melt occurrence maps (Figure 3.9), it becomes more difficult to identify the small-scale melt features captured by UMelt that were visible in earlier figures (Figures 3.4, 3.5, and 3.6). However, almost all large-scale spatial melt patterns are consistent across UMelt, Sentinel-1, ASCAT, and SSMIS. Notably,

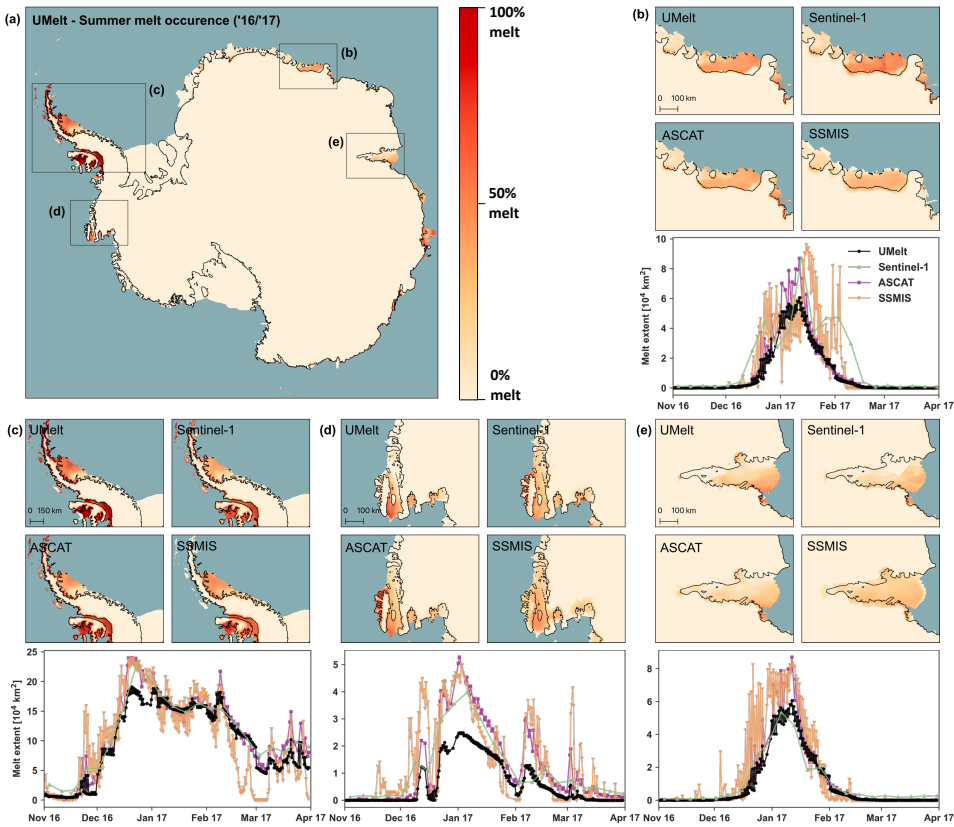


Figure 3.9: The UMelt record, showing Antarctic-wide summer melt occurrence for melt season 2016–2017 (a), with details of Dronning Maud Land (b), the Antarctic Peninsula (c), Mary Byrd Land (d), and Amery Ice Shelf (e). The time series show a comparison in melt extent for the four regions between UMelt (black), Sentinel-1 (green), ASCAT (purple), and SSMIS (orange).

the presence of melt in blue ice regions in the southeastern part of the Roi Baudouin Ice Shelf (Figure 3.9b) and the western part of the Amery Ice Shelf (Figure 3.9e) are only captured by the passive microwave satellite SSMIS. This discrepancy in detecting melt over blue ice areas is a recognized limitation of active microwave sensors (de Roda Husman *et al.*, 2022; Zheng & Zhou, 2020; Zhou *et al.*, 2019), including UMelt, which utilizes Sentinel-1 as the reference data. In the case of the Amery Ice Shelf (Figure 3.9e), the Sentinel-1 summer melt occurrence map shows a clear boundary between areas with and without melt along the northern part of the grounding line. This distinction arises from the absence of Sentinel-1 observations in the northernmost region of the ice shelf during the 2016–2017 melt season. In the northern part of the Abbot Ice Shelf in Mary Byrd Land (Figure 3.9d), UMelt successfully captures small-scale melt details that ASCAT and SSMIS are unable to

capture. However, it is worth noting that UMelt tends to underestimate surface melt when compared to Sentinel-1, ASCAT, and SSMIS. Unfortunately, there are no matching overpasses over Mary Byrd Land, including Abbot Ice Shelf, which prevents further evaluation of UMelt to Sentinel-1 in this region.

The time series plots in Figure 3.9b–e illustrate the melt extent over the four regions throughout the 2016–2017 melt season. To account for the limited coverage of Sentinel-1, we created weekly aggregates representing the maximum melt extent. The time series analysis of Dronning Maud Land (Figure 3.9b), Antarctic Peninsula (Figure 3.9c), and Amery Region (Figure 3.9e) reveals a close resemblance in total melt extent throughout the melt season among UMelt, Sentinel-1, ASCAT, and SSMIS. However, as we approach the conclusion of the melt season in Dronning Maud Land (Figure 3.9b) and throughout the entire melt season in Mary Byrd Land (Figure 3.9d), the time series indicate that UMelt tends to underestimate the extent of melt compared to the other sensors, especially compared to Sentinel-1 and SSMIS. It is crucial to take into account the restricted number of Sentinel-1 observations over Dronning Maud Land and Mary Byrd Land (de Roda Husman *et al.*, 2022). This means that the weekly averages are based on a limited data set, which may impact their reliability. The discrepancies with SSMIS could be attributed to the substantial difference in penetration depth between SSMIS and ASCAT/Sentinel-1 (Ulaby *et al.*, 1986).

Figure 3.9 demonstrates that UMelt serves as a viable alternative to existing satellite observations. In the context of high spatial resolution images of surface melt, Sentinel-1 observations have been commonly used (e.g., Liang *et al.*, 2021). However, UMelt offers a significant advantage in terms of high temporal resolution. UMelt presents a notable advantage over Sentinel-1 by offering complete coverage without missing locations due to limited overpasses, a limitation observed in certain areas of the Amery Ice Shelf. Additionally, UMelt's twice-daily observation frequency eliminates the gaps in time that exist in Sentinel-1's time series.

Traditionally, sensors like ASCAT or SSMIS have been relied upon for high temporal resolution images (e.g., S. L. Bevan *et al.*, 2018; Liu *et al.*, 2006). However, their drawback lies in their low spatial resolution. In contrast, UMelt not only provides high temporal resolution but also captures spatial details that ASCAT and SSMIS fail to capture. Notably, UMelt reveals intricate features along the grounding lines of Larsen C and George VI ice shelves (Figure 3.9c), as well as the western part of the grounding line on the Amery Ice Shelf (Figure 3.9e). Therefore, UMelt proves to be a valuable tool in obtaining both detailed temporal and spatial information in melt observations, surpassing the limitations of Sentinel-1, ASCAT, and SSMIS.

3.4. DISCUSSION

3.4.1. OPPORTUNITIES OF UMELT

The UMelt record demonstrates great potential as a new data product for surface melt monitoring, offering a viable alternative to existing remote sensing data sets such as Sentinel-1, ASCAT, and SSMIS. UMelt offers a significant advantage over ASCAT and SSMIS by effectively overcoming the limitations related to coarse spatial

resolution while maintaining a high temporal resolution. By providing surface melt information at a higher spatial resolution of 500 meters, UMelt allows for more precise and accurate detection of melt events. Additionally, UMelt captures short-lived melt events that may be missed by Sentinel-1 due to its low revisit time. This enhanced capability makes UMelt a valuable tool for studying and monitoring surface melt dynamics.

The UMelt record has the potential to provide valuable insights into specific melt dynamics that may be challenging to capture using Sentinel-1, ASCAT, or SSMIS. One notable application is the improved understanding of diurnal melt cycles, which provide valuable insights into the drivers and impacts of melt processes (Van den Broeke *et al.*, 2006). While ASCAT and SSMIS also provide temporal information, their coarse spatial resolution limits the ability to establish precise connections between surface melt patterns and local drivers. In contrast, UMelt enables us to examine highly localized melt triggers and track the evolving melt patterns throughout the day.

Another compelling research direction that utilizes the UMelt record involves monitoring surface melt on highly heterogeneous terrains, such as the Larsen C Ice Shelf. The Larsen C Ice Shelf is the largest remaining ice shelf on the Antarctic Peninsula and is vulnerable to potential collapse in a warming climate (S. Wang *et al.*, 2022). Notably, past disintegrations of Larsen A and Larsen B were preceded by elevated air temperatures and intense surface melt, underscoring the importance of understanding melt dynamics for assessing ice shelf stability (Banwell *et al.*, 2013; Scambos *et al.*, 2000, 2003). However, the spatial resolutions of ASCAT and SSMIS might be inadequate for accurately mapping surface melt along the grounding line of the Larsen C Ice Shelf. Depending solely on infrequent Sentinel-1 images that pass over the region a few times a week may restrict our comprehensive understanding of the intricate melt dynamics (see Figure 3.1). Therefore, the UMelt record offers a promising addition to the currently existing remote sensing data for studying surface melt on highly heterogeneous ice shelves such as Larsen C.

3.4.2. LIMITATIONS OF UMELT

Despite its promising capabilities, the UMelt product has inherent limitations due to the complex nature of its deep learning approach. The intricate workings of the model make it challenging to precisely identify the factors that contribute to the estimation of surface melt. While we have conducted assessments of the temporal performance (Figure 3.5 and Supplementary Figure 3.2), spatial performance (Figure 3.6), feature importance (Figure 3.7), and transferability (Figure 3.8) of the model, a complete understanding of its inner workings remains elusive. This is particularly evident in cases like Mary Byrd Land, where underestimation of surface melt is observed in melt season 2016–2017 (Figure 3.9d). This highlights the need for further research and investigation to unravel the underlying mechanisms and improve the accuracy and performance of the UMelt product and/or the machine learning methods to develop such products.

Another limitation of deep learning networks is their tendency to mimic the patterns and characteristics they have been trained on. While UMelt incorporates

inputs such as ASCAT and SSMIS, which provide real-time information about liquid water presence, it also considers elevation and multi-year Sentinel-1 melt fraction as input features. Given the current availability of Sentinel-1 data, the multi-year Sentinel-1 melt fraction input feature encompasses observations from both Sentinel-1A and -B, covering the period from 2016 (when Sentinel-1B was launched) to 2021 (when Sentinel-1B ceased operation). The model applies downscaling patterns based on past observations where ASCAT, SSMIS, elevation, and multi-year Sentinel-1 melt fraction collectively resulted in specific melt patterns. This means that when faced with unprecedented and dissimilar events that significantly deviate from its training data, the model may generate inaccurate results. This aligns with the insights presented in the study by (Picard *et al.*, 2007), which demonstrates that in regions with frequent melting, the number of melting days exhibits an almost continuous distribution, varying from year to year. Conversely, in areas where melting is infrequent, the distribution adopts an exponential pattern. In these cases, only a few years encounter a high number of melting days.

Finally, we utilized a basic Attention U-Net framework, which is renowned for its effectiveness in capturing spatial patterns in data (Oktay *et al.*, 2018). A prospective advancement could involve integrating temporal information into the deep learning model, offering significant value for tasks that require the consideration of both spatial and temporal contexts to achieve accurate predictions. This holds true for surface melt prediction, as certain melt trends and patterns exhibit temporal dependencies throughout a melt season (Saunderson *et al.*, 2022). A common approach for incorporating temporal information into U-Nets is through the utilization of 3D convolutional operations (Çiçek *et al.*, 2016). While the 2D convolutions employed in our study operate on spatial dimensions (i.e., width and height), 3D convolutions additionally incorporate the temporal dimension (i.e., time or sequence). By leveraging these 3D convolutions, U-Nets can effectively capture spatiotemporal patterns, enabling the analysis and processing of data with combined spatial and temporal variations.

3.4.3. IMPLICATIONS OF SELECTED TRAINING REGION

The Shackleton Ice Shelf was selected as the training region, as it provided us with sufficient training data. While training a U-Net model on each individual ice shelf would be preferable, there are insufficient (or no) matching overpasses available on most ice shelves to accomplish this (Figure 3.2). Another advantage is that the Shackleton Ice Shelf exhibits a wide range of fine-scale melt patterns, especially along the grounding line and ice rises. The U-Net captured and represented these patterns well, and the results can be extrapolated to other ice shelves, as shown in Figures 3.8 and 3.9.

One of the encountered limitations of selecting the Shackleton Ice Shelf as the training region is the presence of surface melt at relatively high elevations (up to 300 meters), due to strong katabatic winds. This aligns with earlier research that identified that low-elevation regions near the grounding line in East Antarctica are frequently exposed to persistent katabatic winds (Arthur *et al.*, 2020; J. Lenaerts *et al.*, 2017; Stokes *et al.*, 2019). As a consequence, UMelt could potentially overestimate

surface melt in regions with less pronounced or absent katabatic winds. A study by (Laffin *et al.*, 2023) demonstrates that along the grounding line of the Shackleton Ice Shelf, roughly 50% of the melt is linked to downslope winds. Conversely, for the Larsen C Ice Shelf and the Abbot Ice Shelf, this proportion drops to less than 20%. A potential solution to address this issue is adjusting the current binary melt threshold, which is consistently set to 0.7, by implementing a region-specific threshold. Since the model is able to capture fine-scale melt patterns accurately, this approach may be effective.

3.4.4. IMPLICATIONS OF SELECTED REFERENCE DATA

UMelt was developed using Sentinel-1 as the reference data. We filled the observational gaps of Sentinel-1 and created a simulated Antarctic-wide product with a much higher temporal resolution (12h) than the original Sentinel-1 data (1–7 days). However, while Sentinel-1 is a reliable source for melt detection, it has limitations.

First, Sentinel-1 fails to accurately detect the presence of liquid water in icy regions without snow cover (de Roda Husman *et al.*, 2022; Zheng & Zhou, 2020; Zhou *et al.*, 2019), such as on the southeast part of Shackleton or southeast part of Roi Baudouin ice shelves. Over these regions, Sentinel-1 is unable to differentiate between a dry and melting ice surface, as for both cases the backscatter intensity is very low (de Roda Husman *et al.*, 2022). Consequently, in our UMelt product, we also encounter limitations in detecting melt over these regions, as demonstrated in Figure 3.9b and 3.9e of our study. Using Sentinel-1 as the reference data has a further limitation regarding damaged ice. Damaged ice has heterogeneous surface orientations and thus different local incidence angles than the surrounding ice, leading to potential over- or underestimation of surface melt. We addressed this issue by excluding damaged areas from the U-Net development mask. A potential path for future improvement could be to use a different reference product for blue ice regions (e.g., using the blue ice maps of Hu *et al.*, 2022; Jawak *et al.*, 2023) and damaged areas (e.g., using the damage map of Izeboud & Lhermitte, 2023). Multispectral imagers, such as Landsat, MODIS, or Sentinel-2, may be suitable for this purpose. If such a merged, optimized reference product were available, the U-Net could be retrained to improve its performance.

Using Sentinel-1 as reference data presents another limitation, as it, like all microwave sensors, detects the presence of liquid water rather than directly observing the underlying energy conversion process of surface melt. It is important to highlight that both ASCAT and Sentinel-1 have a significant penetration depth, theoretically reaching up to 10 meters (Ulaby *et al.*, 1986). These large penetration depths enable them to potentially detect more residual water in the snowpack compared to SSMIS, which is limited to a theoretical penetration depth of 2.5 meters (Ulaby *et al.*, 1986). This could potentially explain the surface melt overestimation for ASCAT and Sentinel-1 (along with UMelt) compared to SSMIS over the Wilkins Ice Shelf, particularly at the end of the melt season (Figure 3.9c). This is especially plausible given the known tendency of the Wilkins Ice Shelf to retain meltwater in the subsurface (Montgomery *et al.*, 2020). A potential avenue for improving the UMelt record could involve assigning greater weight to SSMIS for locations with higher

levels of retained melt. One possible approach to identifying these locations could involve examining the ASCAT and SSMIS time series and assessing the disparity between morning and afternoon observations. In areas with no active surface melt and only retained meltwater, it is more likely that the difference between morning and afternoon observations would be minimal towards the end of a melt season.

3.4.5. DOWNSCALING OTHER SURFACE MELT PRODUCTS

The findings of this study demonstrate the value of deep learning as a tool for monitoring surface melt with a high spatial and temporal resolution, offering insights into both historical and current ice shelf conditions. Additionally, other surface melt products, such as regional climate model data, can be utilized for downscaling surface melt.

Regional climate models typically operate at a resolution of tens of kilometers (e.g., Agosta *et al.*, 2019; van Wessem *et al.*, 2018), which often fails to capture small-scale surface melt events occurring in Antarctica (Barrand *et al.*, 2013). By incorporating deep learning models, it becomes possible to explore the relationship between large-scale melt patterns derived from regional climate models and fine-scale variations found in additional data sets, such as elevation data or multi-year Sentinel-1 melt fractions employed in this study. Hence, deep learning provides the capability to downscale coarse surface melt data derived from regional climate models.

The application of a U-Net proves to be a promising method for this purpose. By downscaling regional climate model data using deep learning techniques, we can gain a more comprehensive understanding of high-resolution surface melt. This not only encompasses the analysis of historical surface melt patterns but also enables the exploration of future projections.

3.5. CONCLUSION

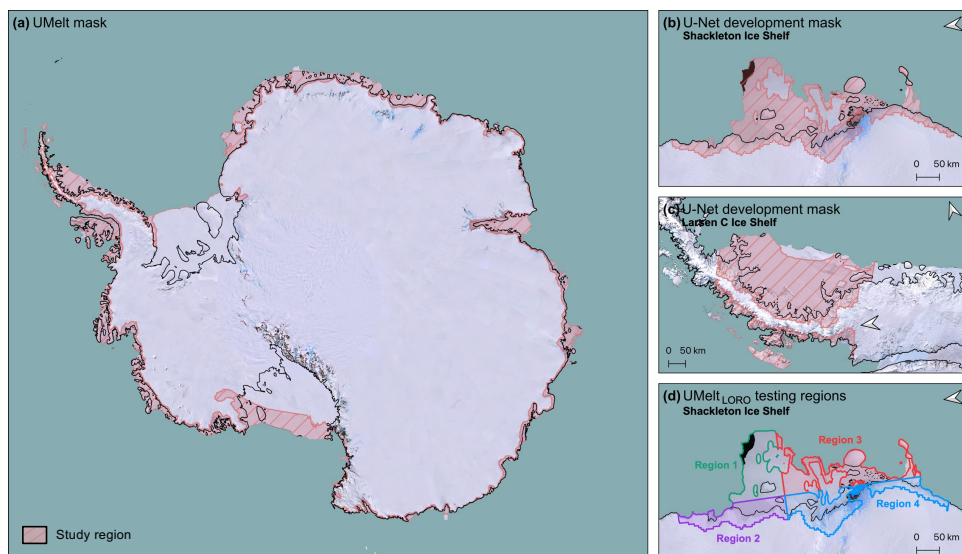
This study presents a novel workflow to create a record of high-resolution surface melt on the Antarctic ice shelves, UMelt. The core of our approach is a modified U-Net that learns the patterns from high temporal (i.e., ASCAT and SSMIS) and high spatial (i.e., elevation and multi-year Sentinel-1 melt fraction) data. The trained model mimics the detailed Sentinel-1 melt observations but on a much higher temporal resolution, resulting in melt maps with a high spatial (500 m) and temporal (12 h) resolution.

We demonstrated the spatial and temporal transferability of the U-Net on the Shackleton Ice Shelf, achieving accuracies ranging from 87.2% to 95.5% for spatial transferability and 90.9% to 95.7% for temporal transferability. The U-Net also performed well in terms of spatiotemporal transferability, with good performance over the Larsen C Ice Shelf (91.0%). This spatiotemporal transferability allows for the assessment of surface melt on the entire Antarctic continent. The U-Net can provide maps of surface melt with a high resolution for all previous years with available input data, meaning we could study surface melt in high detail from 2006 (when ASCAT was launched) until present day. However, for both past and future scenarios,

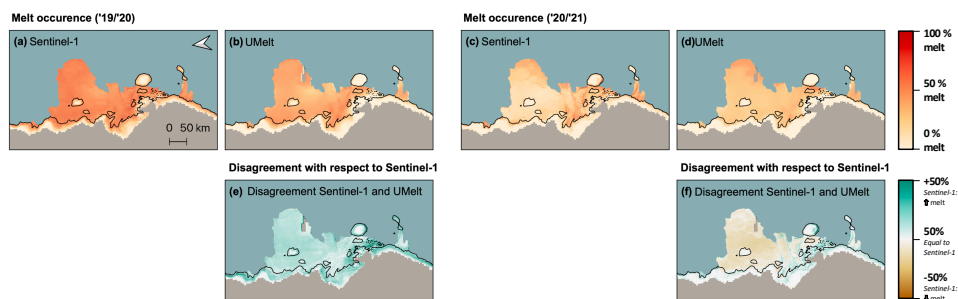
it is important to acknowledge that the model may necessitate re-training, especially when confronted with surface melt patterns that significantly differ from the training data used for the U-Net model.

High-resolution observations are crucial to monitor surface melt on the Antarctic ice shelves because of the short duration and fine melt patterns. Therefore, the high-resolution surface melt record on the Antarctic ice shelves UMelt provides a valuable product to be used in further studies, uncovering melt dynamics and potential consequent ice shelf instability that remains hidden in low-resolution satellite imagery.

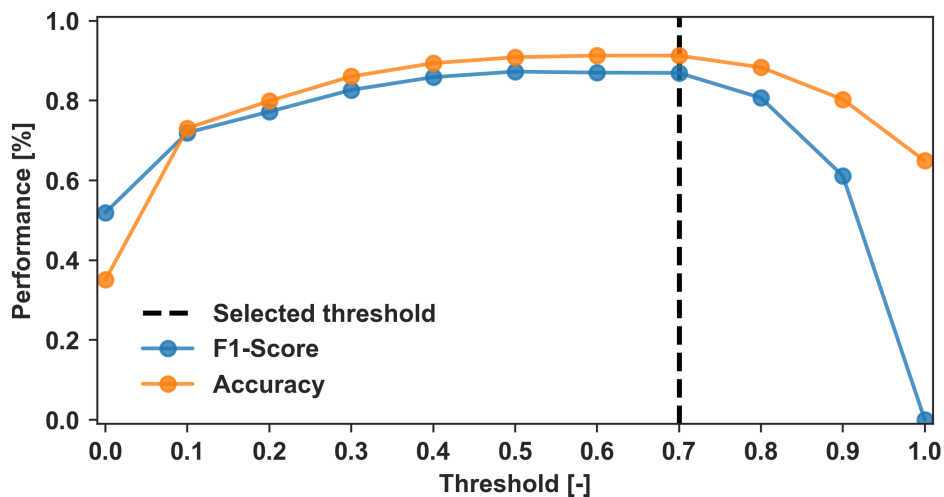
3.6. SUPPLEMENTARY MATERIALS



Supplementary Figure 3.1: Overview of used masks. The UMelt product is available over the highlighted, red area, seen in (a). The U-Net development mask, used for training and testing, is presented in (b) and (c) for the Shackleton and Larsen C ice shelves, respectively. The four regions used for leave-one-region-out (LORO) cross-validation are shown in (d).



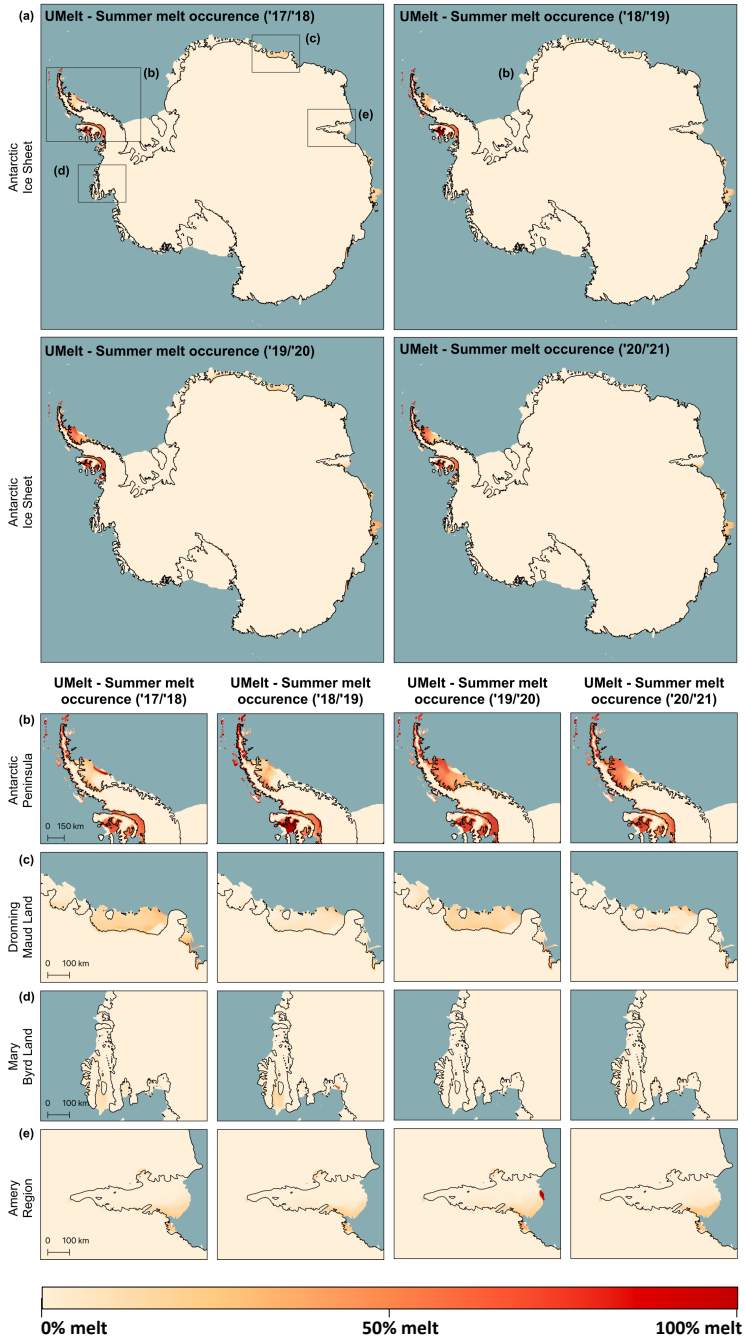
Supplementary Figure 3.2: The summer melt occurrence on Shackleton Ice Shelf for Sentinel-1 (a, c), UMelt (b, d), and the disagreements between Sentinel-1 and UMelt (e, f) for a relatively wet (2019–2020) and a relatively dry (2020–2021) melt season.



Supplementary Figure 3.3: To convert the UMelt probabilities into binary values, a range of thresholds was tested on the validation data set over the Shackleton Ice Shelf. A threshold of 0.7 (dashed black line) resulted in the highest F1-score (blue) and accuracy (orange).

Supplementary Table 3.1: An overview of the performance metrics, including F1-score, accuracy, precision, and recall, evaluated during the development of UMelt. The cross-validation tests were conducted for the average melt season of 2016–2017, with additional temporal performance assessments conducted for the melt seasons of 2019–2020 and 2020–2021.

| Test data set | F1-score | Accuracy | Precision | Recall |
|--|----------|----------|-----------|--------|
| Temporal performance - UMelt _{LOMSO} | | | | |
| Melt season 2016–2017 | 86.9% | 91.3% | 82.8% | 91.6% |
| Melt season 2019–2020 | 82.7% | 90.9% | 74.1% | 93.6% |
| Melt season 2020–2021 | 33.5% | 95.7% | 24.0% | 55.3% |
| Spatial performance (assessment for 2016–2017) - UMelt _{LORO} | | | | |
| Region 1 | 94.8% | 95.5% | 92.8% | 97.0% |
| Region 2 | 85.7% | 93.3% | 78.6% | 94.3% |
| Region 3 | 83.8% | 87.2% | 78.1% | 90.4% |
| Region 4 | 83.4% | 90.6% | 78.4% | 89.2% |
| Feature importance (assessment for 2016–2017) | | | | |
| No ASCAT | 61.8% | 80.2% | 45.3% | 97.1% |
| No SSMIS | 88.1% | 91.5% | 89.1% | 87.1% |
| No Elevation | 87.4% | 91.3% | 85.1% | 89.8% |
| No multi-year Sentinel-1 melt fraction | 86.3% | 90.6% | 84.2% | 88.5% |
| Transferability (assessment for 2016–2017) | | | | |
| Larsen C | 89.3% | 91.0% | 90.5% | 88.0% |



Supplementary Figure 3.4: The UMelT record, showing Antarctic-wide summer melt occurrence for melt season 2017–2021 (a), with details of the Antarctic Peninsula (b), Dronning Maud Land (c), Mary Byrd Land (d), and Amery Ice Shelf (e). The UMelT summer melt occurrence for melt season 2016–2017 can be found in Figure 3.9.

BIBLIOGRAPHY

- Agosta, C., Amory, C., Kittel, C., Orsi, A., Favier, V., Gallée, H., Van den Broeke, M. R., Lenaerts, J., van Wessem, J. M., Van de Berg, W. J., et al. (2019). Estimation of the Antarctic surface mass balance using the regional climate model MAR (1979–2015) and identification of dominant processes. *The Cryosphere*, 13(1), 281–296.
- Arthur, J. F., Stokes, C. R., Jamieson, S. S., Carr, J. R., & Leeson, A. A. (2020). Distribution and seasonal evolution of supraglacial lakes on Shackleton Ice Shelf, East Antarctica. *The Cryosphere*, 14(11), 4103–4120.
- Ashcraft, I. S., & Long, D. G. (2006). Comparison of methods for melt detection over Greenland using active and passive microwave measurements. *International Journal of Remote Sensing*, 27(12), 2469–2488.
- Banwell, A. F., Datta, R. T., Dell, R. L., Moussavi, M., Brucker, L., Picard, G., Shuman, C. A., & Stevens, L. A. (2021). The 32-year record-high surface melt in 2019/2020 on the northern George VI Ice Shelf, Antarctic Peninsula. *The Cryosphere*, 15(2), 909–925.
- Banwell, A. F., MacAyeal, D. R., & Sergienko, O. V. (2013). Breakup of the Larsen B Ice Shelf triggered by chain reaction drainage of supraglacial lakes. *Geophysical Research Letters*, 40(22), 5872–5876.
- Barrand, N. E., Vaughan, D. G., Steiner, N., Tedesco, M., Kuipers Munneke, P., Van den Broeke, M. R., & Hosking, J. S. (2013). Trends in Antarctic Peninsula surface melting conditions from observations and regional climate modeling. *Journal of Geophysical Research: Earth Surface*, 118(1), 315–330.
- Baumhoer, C. A., Dietz, A. J., Kneisel, C., & Kuenzer, C. (2019). Automated extraction of Antarctic glacier and ice shelf fronts from Sentinel-1 imagery using deep learning. *Remote Sensing*, 11(21), 2529.
- Bengio, Y. (2012). Practical recommendations for gradient-based training of deep architectures. *Neural Networks: Tricks of the Trade: Second Edition*, 437–478.
- Bevan, S., Luckman, A., Hendon, H., & Wang, G. (2020). The 2020 Larsen C Ice Shelf surface melt is a 40-year record high. *The Cryosphere*, 14(10), 3551–3564.
- Bevan, S. L., Luckman, A. J., Kuipers Munneke, P., Hubbard, B., Kulesa, B., & Ashmore, D. W. (2018). Decline in surface melt duration on Larsen C Ice Shelf revealed by the advanced scatterometer (ASCAT). *Earth and Space Science*, 5(10), 578–591.
- Bolibar, J., Rabatel, A., Gouttevin, I., Galiez, C., Condom, T., & Sauquet, E. (2020). Deep learning applied to glacier evolution modelling. *The Cryosphere*, 14(2), 565–584.
- Brodzik, M., Long, D., Hardman, M., Paget, A., & Armstrong, R. (2016). MEaSUREs calibrated enhanced-resolution passive microwave daily EASE-grid 2.0 brightness temperature ESDR, version 1. NASA National Snow and Ice Data Center Distributed Active Archive Center.
- Çiçek, Ö., Abdulkadir, A., Lienkamp, S. S., Brox, T., & Ronneberger, O. (2016). 3D U-Net: learning dense volumetric segmentation from sparse annotation. *Medical Image Computing and Computer-Assisted Intervention–MICCAI 2016: 19th International Conference, Athens, Greece, October 17–21, 2016, Proceedings, Part II* 19, 424–432.

- Dahle, F., Tanke, J., Wouters, B., Lindenberg, R., Dahle, F., Tanke, J., Wouters, B., & Lindenberg, R. (2022). Semantic segmentation of historical photographs of the Antarctica Peninsula. *ISPRS Annals of the Photogrammetry, Remote Sensing and Spatial Information Sciences*, 2, 237–244.
- de Roda Husman, S., Hu, Z., Wouters, B., Kuipers Munneke, P., Veldhuijsen, S., & Lhermitte, S. (2022). Remote Sensing of Surface Melt on Antarctica: Opportunities and Challenges. *IEEE Journal of Selected Topics in Applied Earth Observations and Remote Sensing*.
- de Roda Husman, S., Lhermitte, S., Bolibar, J., Izeboud, M., Hu, Z., Shukla, S., van der Meer, M., Long, D., & Wouters, B. (2024). A high-resolution record of surface melt on Antarctic ice shelves using multi-source remote sensing data and deep learning. *Remote Sensing of Environment*, 301, 113950.
- Dirscherl, M., Dietz, A. J., Kneisel, C., & Kuenzer, C. (2021). A novel method for automated supraglacial lake mapping in Antarctica using Sentinel-1 SAR imagery and deep learning. *Remote Sensing*, 13(2), 197.
- Dupont, T., & Alley, R. (2005). Assessment of the importance of ice-shelf buttressing to ice-sheet flow. *Geophysical Research Letters*, 32(4).
- Gilbert, E., & Kittel, C. (2021). Surface melt and runoff on Antarctic ice shelves at 1.5 C, 2 C, and 4 C of future warming. *Geophysical Research Letters*, 48(8), e2020GL091733.
- Girshick, R., Donahue, J., Darrell, T., & Malik, J. (2014). Rich feature hierarchies for accurate object detection and semantic segmentation. *Proceedings of the IEEE conference on computer vision and pattern recognition*, 580–587.
- Gorelick, N., Hancher, M., Dixon, M., Ilyushchenko, S., Thau, D., & Moore, R. (2017). Google Earth Engine: Planetary-scale geospatial analysis for everyone. *Remote sensing of Environment*, 202, 18–27.
- Hofer, R., & Mätzler, C. (1980). Investigations on snow parameters by radiometry in the 3-to 60-mm wavelength region. *Journal of Geophysical Research: Oceans*, 85(C1), 453–460.
- Howat, I. M., Porter, C., Smith, B. E., Noh, M.-J., & Morin, P. (2019). The reference elevation model of Antarctica. *The Cryosphere*, 13(2), 665–674.
- Hu, Z., Kuipers Munneke, P., Lhermitte, S., Dirscherl, M., Ji, C., & Van den Broeke, M. (2022). FABIAN: A daily product of Fractional Austral-summer Blue Ice over Antarctica during 2000–2021 based on MODIS imagery using Google Earth Engine. *Remote Sensing of Environment*, 280, 113202.
- Izeboud, M., & Lhermitte, S. (2023). Damage detection on Antarctic ice shelves using the normalised radon transform. *Remote Sensing of Environment*, 284, 113359.
- Jawak, S. D., Luis, A. J., Pandit, P. H., Wankhede, S. F., Convey, P., & Fretwell, P. T. (2023). Exploratory mapping of blue ice regions in Antarctica using very high-resolution satellite remote sensing data. *Remote Sensing*, 15(5), 1287.
- Johnson, A., Fahnestock, M., & Hock, R. (2020). Evaluation of passive microwave melt detection methods on Antarctic Peninsula ice shelves using time series of Sentinel-1 SAR. *Remote Sensing of Environment*, 250, 112044.
- Laffin, M. K., Zender, C. S., van Wessem, M., Noël, B., & Wang, W. (2023). Wind-Associated Melt Trends and Contrasts Between the Greenland and Antarctic Ice Sheets. *Geophysical Research Letters*, 50(16), e2023GL102828.
- Lenaerts, J. T., Ligtenberg, S. R., Medley, B., Van de Berg, W. J., Konrad, H., Nicolas, J. P., van Wessem, J. M., Trusel, L. D., Mulvaney, R., Tuckwell, R. J., et al. (2018). Climate and surface mass balance of coastal West Antarctica resolved by regional climate modelling. *Annals of Glaciology*, 59(76pt1), 29–41.
- Lenaerts, J., Lhermitte, S., Drews, R., Ligtenberg, S., Berger, S., Helm, V., Smeets, C., Van den Broeke, M., Van de Berg, W. J., Van Meijgaard, E., et al. (2017). Meltwater

- produced by wind–albedo interaction stored in an East Antarctic ice shelf. *Nature climate change*, 7(1), 58–62.
- Lhermitte, S., Sun, S., Shuman, C., Wouters, B., Pattyn, F., Wuite, J., Berthier, E., & Nagler, T. (2020). Damage accelerates ice shelf instability and mass loss in Amundsen Sea Embayment. *Proceedings of the National Academy of Sciences*, 117(40), 24735–24741.
- Liang, D., Guo, H., Zhang, L., Cheng, Y., Zhu, Q., & Liu, X. (2021). Time-series snowmelt detection over the Antarctic using Sentinel-1 SAR images on Google Earth Engine. *Remote Sensing of Environment*, 256, 112318.
- Liu, H., Wang, L., & Jezek, K. C. (2006). Spatiotemporal variations of snowmelt in Antarctica derived from satellite scanning multichannel microwave radiometer and Special Sensor Microwave Imager data. *Journal of Geophysical Research*, 111(F1).
- Long, D. (2022). NASA Scatterometer Climate Record Pathfinder (SCP) [Accessed 4 April 2022].
- Massom, R. A., Scambos, T. A., Bennetts, L. G., Reid, P., Squire, V. A., & Stammerjohn, S. E. (2018). Antarctic ice shelf disintegration triggered by sea ice loss and ocean swell. *Nature*, 558(7710), 383–389.
- Mastrofini, M., Agostinelli, I., & Curti, F. (2023). Design and validation of a U-Net-based algorithm for star sensor image segmentation. *Applied Sciences*, 13(3), 1947.
- Mohajerani, Y., Wood, M., Velicogna, I., & Rignot, E. (2019). Detection of glacier calving margins with convolutional neural networks: A case study. *Remote Sensing*, 11(1), 74.
- Montgomery, L., Miège, C., Miller, J., Scambos, T. A., Wallin, B., Miller, O., Solomon, D. K., Forster, R., & Koenig, L. (2020). Hydrologic properties of a highly permeable firn aquifer in the Wilkins Ice Shelf, Antarctica. *Geophysical Research Letters*, 47(22), e2020GL089552.
- Mote, T. L., & Anderson, M. R. (1995). Variations in snowpack melt on the Greenland ice sheet based on passive-microwave measurements. *Journal of Glaciology*, 41(137), 51–60.
- Mousavi, M., Colliander, A., Miller, J. Z., & Kimball, J. S. (2022). A novel approach to map the intensity of surface melting on the Antarctica ice sheet using SMAP L-band microwave radiometry. *IEEE Journal of Selected Topics in Applied Earth Observations and Remote Sensing*, 15, 1724–1743.
- Nihashi, S., & Ohshima, K. I. (2015). Circumpolar mapping of Antarctic coastal polynyas and landfast sea ice: Relationship and variability. *Journal of climate*, 28(9), 3650–3670.
- Niu, L., Tang, X., Yang, S., Zhang, Y., Zheng, L., & Wang, L. (2023). Detection of Antarctic surface meltwater using sentinel-2 remote sensing images via U-net with attention blocks: A case study over the amery ice shelf. *IEEE Transactions on Geoscience and Remote Sensing*, 61, 1–13.
- Oktay, O., Schlemper, J., Folgoc, L. L., Lee, M., Heinrich, M., Misawa, K., Mori, K., McDonagh, S., Hammerla, N. Y., Kainz, B., et al. (2018). Attention U-Net: Learning where to look for the pancreas. *arXiv preprint arXiv:1804.03999*.
- Olden, J. D., & Jackson, D. A. (2002). Illuminating the “black box”: a randomization approach for understanding variable contributions in artificial neural networks. *Ecological modelling*, 154(1–2), 135–150.
- Picard, G., & Fily, M. (2006). Surface melting observations in Antarctica by microwave radiometers: Correcting 26-year time series from changes in acquisition hours. *Remote sensing of environment*, 104(3), 325–336.
- Picard, G. (2022). Surface melt on the Antarctic and Greenland Ice Sheets (1979 - 2021) [[Accessed 21 June 2023]].

- Picard, G., Fily, M., & Gallée, H. (2007). Surface melting derived from microwave radiometers: a climatic indicator in Antarctica. *Annals of Glaciology*, 46, 29–34.
- Picard, G., Leduc-Leballeur, M., Banwell, A. F., Brucker, L., & Macelloni, G. (2022). The sensitivity of satellite microwave observations to liquid water in the Antarctic snowpack. *The Cryosphere Discussions*, 1–34.
- Pritchard, H., Ligtenberg, S. R., Fricker, H. A., Vaughan, D. G., Van den Broeke, M. R., & Padman, L. (2012). Antarctic ice-sheet loss driven by basal melting of ice shelves. *Nature*, 484(7395), 502–505.
- Radhakrishnan, K., Scott, K. A., & Clausi, D. A. (2021). Sea ice concentration estimation: Using passive microwave and SAR data with a U-net and curriculum learning. *IEEE Journal of Selected Topics in Applied Earth Observations and Remote Sensing*, 14, 5339–5351.
- Rignot, E., Mouginot, J., Scheuchl, B., Van den Broeke, M., van Wessem, J. M., & Morlighem, M. (2019). Four decades of Antarctic Ice Sheet mass balance from 1979–2017. *Proceedings of the National Academy of Sciences*, 116(4), 1095–1103.
- Roberts, D. R., Bahn, V., Ciuti, S., Boyce, M. S., Elith, J., Guillerá-Arroita, G., Hauenstein, S., Lahoz-Monfort, J. J., Schröder, B., Thuiller, W., et al. (2017). Cross-validation strategies for data with temporal, spatial, hierarchical, or phylogenetic structure. *Ecography*, 40(8), 913–929.
- Ronneberger, O., Fischer, P., & Brox, T. (2015). U-net: Convolutional networks for biomedical image segmentation. *Medical Image Computing and Computer-Assisted Intervention–MICCAI 2015: 18th International Conference, Munich, Germany, October 5–9, 2015, Proceedings, Part III*, 18, 234–241.
- Saunderson, D., Mackintosh, A., McCormack, F., Jones, R. S., & Picard, G. (2022). Surface melt on the Shackleton Ice Shelf, East Antarctica (2003–2021). *The Cryosphere*, 16(10), 4553–4569.
- Scambos, T. A., Hulbe, C., & Fahnestock, M. (2003). Climate-induced ice shelf disintegration in the Antarctic Peninsula. *Antarctic Peninsula climate variability: Historical and paleoenvironmental perspectives*, 79, 79–92.
- Scambos, T. A., Hulbe, C., Fahnestock, M., & Bohlander, J. (2000). The link between climate warming and break-up of ice shelves in the Antarctic Peninsula. *Journal of Glaciology*, 46(154), 516–530.
- Stokes, C. R., Sanderson, J. E., Miles, B. W., Jamieson, S. S., & Leeson, A. A. (2019). Widespread distribution of supraglacial lakes around the margin of the East Antarctic Ice Sheet. *Scientific reports*, 9(1), 13823.
- Torinesi, O., Fily, M., & Genthon, C. (2003). Variability and trends of the summer melt period of Antarctic ice margins since 1980 from microwave sensors. *Journal of Climate*, 16(7), 1047–1060.
- Trebing, K., Stańczyk, T., & Mehrkanoon, S. (2021). SmaAt-UNet: Precipitation nowcasting using a small attention-UNet architecture. *Pattern Recognition Letters*, 145, 178–186.
- Trusel, L., Frey, K. E., & Das, S. B. (2012). Antarctic surface melting dynamics: Enhanced perspectives from radar scatterometer data. *Journal of Geophysical Research: Earth Surface*, 117(F2).
- Trusel, L., Frey, K. E., Das, S. B., Karnauskas, K. B., Kuipers Munneke, P., Van Meijgaard, E., & Van den Broeke, M. R. (2015). Divergent trajectories of Antarctic surface melt under two twenty-first-century climate scenarios. *Nature Geoscience*, 8(12), 927–932.
- Trusel, L., Frey, K. E., Das, S. B., Kuipers Munneke, P., & Van den Broeke, M. (2013). Satellite-based estimates of Antarctic surface meltwater fluxes. *Geophysical Research Letters*, 40(23), 6148–6153.

- Ulaby, F. T., & Long, D. (2014). *Microwave radar and radiometric remote sensing*. University of Michigan Press.
- Ulaby, F. T., Moore, R. K., & Fung, A. K. (1986). *Microwave remote sensing: Active and passive*. Volume 3-From theory to applications.
- Van den Broeke, M. (2005). Strong surface melting preceded collapse of Antarctic Peninsula ice shelf. *Geophysical Research Letters*, 32(12).
- Van den Broeke, M., Reijmer, C., Van As, D., & Boot, W. (2006). Daily cycle of the surface energy balance in Antarctica and the influence of clouds. *International Journal of Climatology: A Journal of the Royal Meteorological Society*, 26(12), 1587–1605.
- van der Meer, M., de Roda Husman, S., & Lhermitte, S. (2023). Deep learning regional climate model emulators: A comparison of two downscaling training frameworks. *Journal of Advances in Modeling Earth Systems*, 15(6), e2022MS003593.
- van Wessem, J. M., Van de Berg, W. J., Noël, B. P., Van Meijgaard, E., Amory, C., Birnbaum, G., Jakobs, C. L., Krüger, K., Lenaerts, J., Lhermitte, S., et al. (2018). Modelling the climate and surface mass balance of polar ice sheets using RACMO2–Part 2: Antarctica (1979–2016). *The Cryosphere*, 12(4), 1479–1498.
- van Wessem, J. M., Van den Broeke, M. R., Wouters, B., & Lhermitte, S. (2023). Variable temperature thresholds of melt pond formation on Antarctic ice shelves. *Nature Climate Change*, 13(2), 161–166.
- Wang, S., Liu, H., Jezek, K., Alley, R. B., Wang, L., Alexander, P., & Huang, Y. (2022). Controls on Larsen C Ice Shelf Retreat From a 60-Year Satellite Data Record. *Journal of Geophysical Research: Earth Surface*, 127(3), e2021JF006346.
- Wang, X., Qiu, Y., Zhang, Y., Lemmetyinen, J., Cheng, B., Liang, W., & Leppäranta, M. (2022). A lake ice phenology dataset for the Northern Hemisphere based on passive microwave remote sensing. *Big Earth Data*, 1–19.
- Wei, Y., Li, X., Gu, L., Zheng, X., Jiang, T., & Zheng, Z. (2022). A fine-resolution snow depth retrieval algorithm from enhanced-resolution passive microwave brightness temperature using machine learning in Northeast China. *IEEE Geoscience and Remote Sensing Letters*, 19, 1–5.
- Wille, J. D., Favier, V., Dufour, A., Gorodetskaya, I. V., Turner, J., Agosta, C., & Codron, F. (2019). West Antarctic surface melt triggered by atmospheric rivers. *Nature Geoscience*, 12(11), 911–916.
- Wilmes, S.-B., Green, J. M., Gomez, N., Rippeth, T. P., & Lau, H. (2017). Global tidal impacts of large-scale ice sheet collapses. *Journal of Geophysical Research: Oceans*, 122(11), 8354–8370.
- Zhang, Q., Wu, Y. N., & Zhu, S.-C. (2018). Interpretable convolutional neural networks. *Proceedings of the IEEE conference on computer vision and pattern recognition*, 8827–8836.
- Zhao, J., Liang, S., Li, X., Duan, Y., & Liang, L. (2022). Detection of surface crevasses over Antarctic ice shelves using SAR imagery and deep learning method. *Remote Sensing*, 14(3), 487.
- Zheng, L., & Zhou, C. (2020). Comparisons of snowmelt detected by microwave sensors on the shackleton ice shelf, east antarctica. *International Journal of Remote Sensing*, 41(4), 1338–1348.
- Zhou, C., Zheng, L., Sun, Q., & Liu, R. (2019). Amery Ice Shelf surface snowmelt detected by ASCAT and Sentinel-1. *Remote Sensing Letters*, 10(5), 430–438.
- Zwally, H. J., & Fiegles, S. (1994). Extent and duration of Antarctic surface melting. *Journal of Glaciology*, 40(136), 463–475.

4

PHYSICALLY-INFORMED SUPER-RESOLUTION DOWNSCALING OF ANTARCTIC SURFACE MELT

**Sophie de Roda Husman, Zhongyang Hu, Maurice van
Tiggelen, Rebecca Dell, Jordi Bolibar, Stef Lhermitte, Bert
Wouters, Peter Kuipers Munneke**

This chapter has been published in Journal of Advances in Modeling Earth Systems as de Roda Husman, Hu, *et al.* (2024).

ABSTRACT

Because Antarctic surface melt is mostly driven by local processes, its simulation necessitates high-resolution regional climate models (RCMs). However, the current horizontal resolution of RCMs ($\approx 25\text{--}30$ km) is inadequate for capturing small-scale melt processes. To address this limitation, we present SUPREME (SUPER-REsolution-based Melt Estimation over Antarctica), a deep learning method to downscale surface melt to 5.5 km resolution using a physically-informed super-resolution model. The physical information integrated into the model originates from observations tied to surface melt, specifically remote sensing-derived albedo and elevation. These remote sensing data, in addition to a Regional Atmospheric Climate Model (RACMO) run at 27 km resolution, account for the diverse drivers of surface melt across Antarctica, facilitating effective generalization beyond the training region of the Antarctic Peninsula. A comparison of SUPREME with a dynamically downscaled RACMO run at 5.5 km over the Antarctic Peninsula shows high accuracy, with average yearly RMSE and bias of 5.5 mm w.e. yr^{-1} and 4.5 mm w.e. yr^{-1} , respectively. Validation at five automatic weather stations reveals SUPREME's marked improvement with substantially lower average RMSE (81 mm w.e.) compared to RACMO 27 km (129 mm w.e.). Beyond the training region, SUPREME aligns more closely with remote sensing products associated with surface melt than super-resolution models lacking physical constraints. While further validation of SUPREME is needed, our study highlights the potential of super-resolution techniques with physical constraints for high-resolution surface melt monitoring in Antarctica, providing insights into the impacts of localized melting on processes affecting ice shelf integrity such as hydrofracturing.

4.1. INTRODUCTION

Reductions in both thickness (Gudmundsson *et al.*, 2019) and extent (Greene *et al.*, 2022) of floating ice shelves have contributed to an increasing mass loss of the Antarctic Ice Sheet (IMBIE, 2018; Shepherd *et al.*, 2012). A recent study by Davison *et al.* (2023) revealed that over 40% of Antarctic ice shelves have lost mass between 1997 and 2021. While around two-thirds of this volume loss was attributed to basal melting (Davison *et al.*, 2023), surface melt is anticipated to play a more significant role in ice shelf shrinkage and weakening in the coming decades under continued atmospheric warming in all future climate scenarios (Gilbert & Kittel, 2021; Trusel *et al.*, 2015). The presence of surface meltwater reduces albedo (Lenaerts *et al.*, 2017) and firn air content (Kuipers Munneke *et al.*, 2014), creating positive feedback loops that generate additional surface melt and consequently increase meltwater ponding. This ponding poses a threat to ice shelf stability through surface meltwater-induced flexure and hydrofracturing (Banwell & Macayeal, 2015; Banwell *et al.*, 2019; Scambos *et al.*, 2009).

Nonetheless, accurately quantifying meltwater volumes on the Antarctic Ice Sheet is posing a significant challenge. Direct assessment of melt from ice core stratigraphy (e.g., Abram *et al.*, 2013; Das & Alley, 2008) and in-situ surface energy balance observations (e.g., Jakobs *et al.*, 2020; Kuipers Munneke, Van den Broeke, *et al.*, 2012) provide robust quantitative melt records, but these records are sparse. Remote sensing observations, while capable of offering measurements continent-wide, usually provide only binary data indicating whether melting has occurred or not, without quantifying the meltwater volume (de Roda Husman, Lhermitte, *et al.*, 2024; de Roda Husman *et al.*, 2022). Trusel *et al.* (2013) made a notable exception by employing the Quick Scatterometer (QuikSCAT) to measure annual meltwater volumes. Unfortunately, QuikSCAT ceased operation in 2009. Recently, also Banwell *et al.* (2023) made an effort to derive meltwater volumes from passive and active microwave sensors, but only by applying a physics-based snow model to the binary melt observations derived from remote sensing data, meltwater volumes could be estimated. Hence, besides in-situ observations and a few remote sensing methods, our understanding of past, present, and future surface melt volumes relies heavily on regional climate models (RCMs) such as the Regional Atmospheric Climate Model (RACMO) (van Wessem *et al.*, 2018) and Modèle Atmosphérique Régional (MAR) (Agosta *et al.*, 2019). Nevertheless, with a spatial resolution of typically 25–30 kilometers, RCMs face limitations in capturing the intricate interplay between melting and albedo, and have difficulty representing small-scale, high-melt features like blue ice, rocks, and ponds (Arthur *et al.*, 2022; Kingslake *et al.*, 2017; Lenaerts *et al.*, 2017).

Hence, there is a necessity for downscaling techniques that reproduce the critical details of surface melt that are currently lacking in RCMs. A frequently employed technique is statistical downscaling, a method that enhances the resolution of RCM variables, typically by leveraging their linear correlation with elevation. Recently, statistical downscaling has been employed to generate high-resolution surface mass balance (SMB) variables for Antarctica (Gallée *et al.*, 2011), including snowfall (Ghilain *et al.*, 2022) and surface melt (Noël *et al.*, 2023). Similarly, over Greenland,

SMB components have been subject to statistical downscaling in studies by Hanna *et al.* (2005, 2008, 2011), Franco *et al.* (2012), Noël *et al.* (2016), and Tedesco *et al.* (2023). However, in areas where the correlation of an SMB component with elevation is weak, statistical downscaling may not provide additional benefits (Van de Berg *et al.*, 2020). Another commonly used method, dynamical downscaling, entails running a model in a nested domain with higher spatial resolution and represents a prevalent design approach for many RCMs (Box & Rinke, 2003; Fettweis *et al.*, 2017; Noël *et al.*, 2016). Dynamical downscaling requires that physical parameterizations are adjusted in a finer grid (Hourdin *et al.*, 2017; Schmidt *et al.*, 2017). It relies on physical formulations rather than empirical relationships and correlations, but it comes with a significant computational cost (Fyke *et al.*, 2018). Hence, both statistical and dynamical downscaling methods have their limitations, prompting us to explore an alternative approach for downscaling surface melt from an RCM: deep learning.

In this study, we introduce SUPREME (SUPER-REsolution-based Melt Estimation over Antarctica), a method to refine RACMO from a 27 km horizontal resolution to a more detailed 5.5 km resolution, employing a physically-informed deep learning super-resolution technique. Super-resolution techniques have been successfully used to refine image details (Dong *et al.*, 2016; Goodfellow *et al.*, 2014; Shi *et al.*, 2016). Their potential for geophysical application has been demonstrated in Antarctic studies, including the downscaling of global climate models (van der Meer *et al.*, 2023), bedrock topography (Leong & Horgan, 2020), and sea ice motion (Petrou *et al.*, 2018). Super-resolution methods distinguish themselves by their adeptness at preserving intricate details without being constrained by potentially limiting linear statistical assumptions or high computational costs for predictions. Despite such advantages, super-resolution models may not generalize well beyond their training region (Jiang *et al.*, 2022). This could be particularly problematic for its application to surface melt, given the notable variations in melt triggers and patterns observed across Antarctica (de Roda Husman *et al.*, 2022; Hu *et al.*, 2022). To enhance spatial transferability, alongside RACMO 27 km, we include observations that are physically associated with surface melt—specifically, albedo and elevation from remote sensing data—into our super-resolution model. Albedo is linked to surface reflectivity, while elevation accounts for altitude-related temperature variations – both critical factors in determining the extent and intensity of surface melt (Giesen & Oerlemans, 2012). The incorporation of remote sensing data into the super-resolution model involves transitioning from a single-image super-resolution model, which depends solely on the low-resolution counterpart of the desired high-resolution output (Yang *et al.*, 2014), to a multi-image super-resolution model that integrates multiple input features (Kawulok *et al.*, 2019).

4.2. DATA

4.2.1. RACMO 27 KM AND 5.5 KM

We employ surface melt volume data from two RACMO datasets, both belonging to version 2.3p2, with horizontal resolutions of approximately 27 km (van Wessem

et al., 2018) and 5.5 km (van Wessem *et al.*, 2016). The RACMO 27 km dataset serves as one of the input features for the super-resolution model, while the RACMO 5.5 km dataset, covering the Antarctic Peninsula exclusively, serves as the reference data (or “ground truth”) for training the super-resolution model.

RACMO 27 km combines the atmospheric dynamics from the High-Resolution Limited Area Model (HIRLAM) (Undén *et al.*, 2002) with the physical parameterizations of the European Centre for Medium-Range Weather Forecasts (ECMWF) global model (ECMWF, 2009). It is coupled bidirectionally with a multi-layer snow model that accounts for processes like melting, percolation, and refreezing in the snow (Ettema *et al.*, 2010). Additionally, the model incorporates a snow albedo scheme based on the evolution of snow grain size (Kuipers Munneke *et al.*, 2011) and a drifting snow scheme that simulates the redistribution and sublimation of suspended snow particles (Lenaerts *et al.*, 2012). For more detailed technical information about RACMO 27 km, we direct the reader to van Wessem, Reijmer, Morlighem, *et al.* (2014) and van Wessem, Reijmer, Lenaerts, *et al.* (2014). In 2018, RACMO 5.5 km was introduced as a designated run at 5.5 km over the Antarctic Peninsula. For this high-resolution run, RACMO was forced by ERA-Interim, using an updated surface topography for the Antarctic Peninsula (van Wessem *et al.*, 2016).

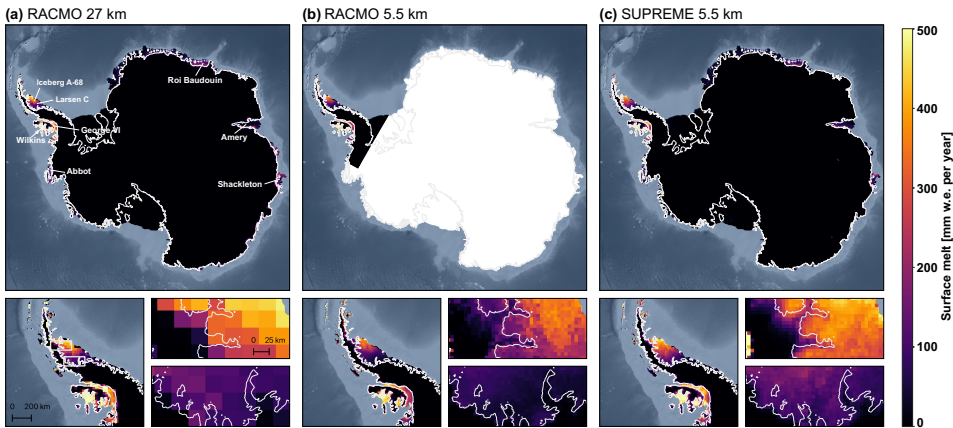


Figure 4.1: Surface melt volume comparison for the 2017–2018 melt season: (a) RACMO 27 km, (b) RACMO 5.5 km (van Wessem *et al.*, 2016), and (c) SUPREME (this study). Upper panels display Antarctic-wide scale, while lower panels provide close-ups of the Antarctic Peninsula. Since RACMO 5.5 km data are solely available for the Antarctic Peninsula, the white region indicates no data.

Both RACMO 27 km and 5.5 km data are available for the period spanning from 1979 to the present day. In our study, we focus on daily surface melt outputs between 2001 and 2019, measured in millimeters water equivalent (mm w.e.). While RACMO 27 km provides coverage across the entire Antarctic region (see Figure 4.1a), RACMO 5.5 km is limited to the Antarctic Peninsula (Figure 4.1b). In addition to differences in spatial coverage and horizontal resolutions, RACMO 5.5 km simulates lower surface melt values compared to RACMO 27 km. For the Antarctic Peninsula

over the period from 1979 to 2014, the annual surface melt volume showed a notable disparity, with RACMO 5.5 km recording 34 Gt yr^{-1} compared to RACMO 27 km's 57 Gt yr^{-1} (Kuipers Munneke, Picard, *et al.*, 2012; van Wessem *et al.*, 2016). Also throughout our study period from 2001 to 2019, RACMO 5.5 km reports melt values that are lower compared to RACMO 27 km (see Supplementary Figure 4.1), which is likely attributed to a cloud cover underestimation (van Wessem *et al.*, 2016). As our SUPREME model is calibrated on the RACMO 5.5 km reference dataset, this underestimation compared to RACMO 27 km is anticipated to persist. In follow-up studies, there is potential for retraining our developed super-resolution architecture using high-resolution surface melt reference data other than RACMO 5.5 km, such as from upcoming versions of RACMO or other RCMs like MAR.

4.2.2. PHYSICAL CONSTRAINTS

ALBEDO

In addition to RACMO 27 km, albedo and elevation are additional variables input into the super-resolution model. We use daily white-sky albedo, obtained from the MCD43A3 product on a spatial resolution of 500 meters, based on data from the Moderate Resolution Imaging Spectroradiometer (MODIS) (Schaaf *et al.*, 2002). This MCD43A3 product matches those in previous Antarctic studies (e.g., Lenaerts *et al.*, 2017; Tollenaar *et al.*, 2022). The dataset is stored in Google Earth Engine (GEE; Gorelick *et al.*, 2017) and consists of daily observations, which are generated as 16-day running means. To align with the resolution of the RACMO 5.5 km product, we employ bicubic interpolation to reproject the data to the Antarctic Polar Stereographic projection, and average the data to upsample it to a 5.5 km resolution. If albedo values are unavailable due to cloud cover, we substitute the pixel with the monthly median albedo value of that specific pixel.

However, since cloud cover can reach up to 90% on the Antarctic ice shelves (Lachlan-Cope, 2010), the use of the daily albedo input feature is limited. Therefore, the albedo Q5 input feature acts as an additional data source, highlighting the most extreme melt patterns on an annual basis. We compute the 5th percentile (Q5) albedo for each pixel during every melt season, defined as spanning from July 1 to June 30 of the following year.

ELEVATION

The final input feature for the super-resolution model is a static elevation map sourced from the TanDEM-X PolarDEM. This map provides gap-free elevation data for 2013–2014 over Antarctica at a spatial resolution of 90 meters (Wessel *et al.*, 2021). Similar to the MODIS albedo data, we employ bicubic interpolation to reproject the dataset onto the Antarctic Polar Stereographic projection, and apply averaging to upsample the data to a resolution of 5.5 km. We neglect elevation changes and assume constant topography since the elevation changes over the studied time period are relatively small and are not expected to significantly impact atmospheric dynamics.

4.2.3. VALIDATION DATA

AUTOMATIC WEATHER STATIONS

SUPREME is assessed against five automatic weather stations (AWS): AWS14, AWS15, AWS17, AWS18, and Neumayer (refer to Figure 4.2 for their locations). The five selected AWS have multiyear data records without any gaps and have experienced surface melt during our study period. AWS14 and AWS15 are located at the center of the Larsen C Ice Shelf, AWS17 on the remnant of the Larsen B Ice Shelf, AWS18 at the grounding line of the Larsen C Ice Shelf, and Neumayer at the Ekström Ice Shelf. Meteorological observations from the five AWS are forced into a surface energy balance (SEB) model, enabling the calculation of surface melt. The SEB model and configuration are the same as used by Jakobs *et al.* (2020). In addition, the measured longwave radiation is corrected for window heating as described in Smeets *et al.* (2018), and measured shortwave radiation is corrected for the zero offset as described in Foken (2021).

RACMO 2 km

The SUPREME melt product is compared with another downscaled RACMO product besides RACMO 5.5 km, referred to as RACMO 2 km, as developed by Noël *et al.* (2023). RACMO 2 km was obtained through a statistical-downscaling approach applied to RACMO 27 km, resulting in a spatial resolution of 2 km. RACMO 2 km data are available on a daily resolution, but in this study, we only use annual melt values (from July 1 to June 30 for the years spanning from 2001 to 2019).

QUIKSCAT

We compare SUPREME's annual melt volumes with QuikSCAT data for eight melt seasons, spanning from 2001–2002 to 2008–2009. QuikSCAT observations for Antarctica are available from 1999–2009 at a 4.45 km resolution (Trusel *et al.*, 2013). The product relies on the annual sum of backscatter intensity reduction, calibrated with AWS observations.

PASSIVE MICROWAVE REMOTE SENSING

We also compare SUPREME to data from PMW sensors, also known as radiometers. PMWs provide binary melt data (i.e., melt or no-melt) that allow for the calculation of cumulative melt days within a melt season. We use cumulative melt days using a dataset from Picard and Fily (2006), which contains daily observations that distinguish between melt and no-melt on a 25 by 25 km² spatial resolution. This binary melt product was generated by applying a melt detection algorithm (Picard & Fily, 2006; Torinesi *et al.*, 2003) to data from the scanning Multichannel Microwave Radiometer (SMMR) and three Special Sensor Microwave Imager (SSM/I) instruments (Picard & Fily, 2006).

OPTICAL REMOTE SENSING

Finally, we compare SUPREME with a melt-slush product derived from optical remote sensing (Dell *et al.*, 2022, 2024). This product is particularly effective in

detecting melt presence in regions with low firn air content, where the meltwater is clearly visible in optical imagery, in contrast to microwave sensors. Dell *et al.* (2022, 2024) developed a product for surface melt and slush based on the visible and near-infrared (NIR) bands of Landsat 8 observations covering the Antarctic ice shelves. The slush and melt dataset (Dell *et al.*, 2024) offers monthly data spanning from 2013 to 2021, resulting in six overlapping melt seasons with SUPREME (from 2013–2014 to 2018–2019). To streamline the comparison, we aggregate the monthly data to create a single optical remote sensing product for each melt season, indicating the number of months with either melt or slush per pixel. The melt and slush dataset, with a 30 meter spatial resolution, is too detailed for a straightforward visual comparison with SUPREME's 5.5 km resolution. To address this, we apply maximum interpolation to downscale the optical remote sensing product to a 5.5 km resolution. This process involves assigning the value representing the highest number of months within each 5.5 km pixel area.

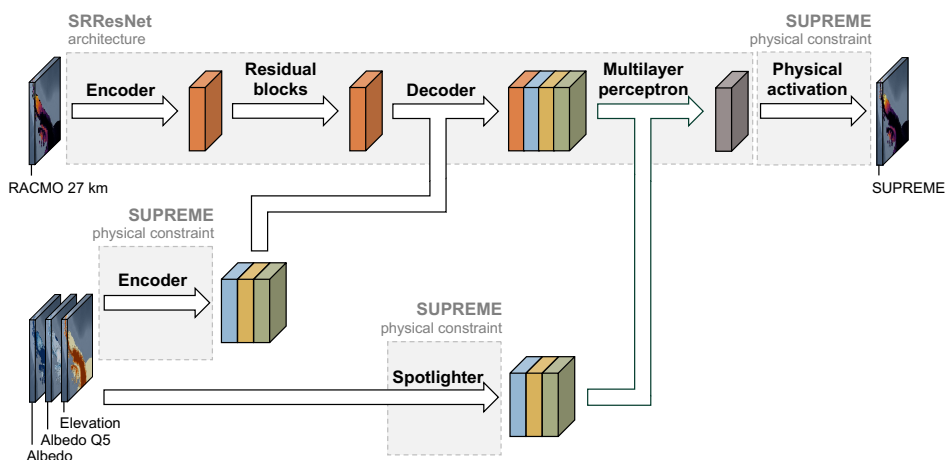


Figure 4.2: Overview of super-resolution model architecture. The model incorporates the SRResNet architecture along with three additional physical constraints. The processed data were color-coded: orange for daily RACMO 27 km, blue for daily albedo, yellow for annual 5th percentile albedo, and green for elevation.

4.3. METHODS

4.3.1. PREPROCESSING

The super-resolution model is trained on the Antarctic Peninsula, which is divided into thirteen training patches as shown in Supplementary Figure 4.3. These patches, created for memory efficiency, are sized at 297 km by 297 km, which is the lowest common multiple of 5.5 km (for RACMO 5.5 km, albedo, and elevation) and 27 km (for RACMO 27 km): i.e., 5.5 km multiplied by 54, and 27 km by 11 both equal 297 km. We gather input features including daily RACMO 27 km, daily albedo, annual Q5 albedo, and a static elevation map for each of the training patches, along with

the daily RACMO 5.5 km reference data. To ensure that edge information receives equal consideration as central data, we apply padding. For RACMO 5.5 km, this entails adding ten pixels (equivalent to a 55 km border), while for RACMO 27 km, two pixels are added (equivalent to a 54 km border). After the training phase, the patches are clipped to maintain their central dimensions of 297 km by 297 km. After the padding, the preprocessed data are split into three sets: training (2001–2006), validation (2007–2010), and testing (2011–2019). The validation set is used during training to tune hyperparameters, while the testing set is reserved for evaluating the final performance of the trained model on unseen data. The split was primarily driven by the availability of AWS records, predominantly spanning from 2011 onwards. The distribution of the training, validation, and testing datasets are statistically similar, as confirmed by an Anderson-Darling test. This statistical assessment is designed to determine similarity in distribution (Scholz & Stephens, 1987). The Anderson-Darling test revealed that the datasets surpass a p-value of 0.05, indicating consistent distributions among the datasets.

4.3.2. SUPREME MODEL ARCHITECTURE

SRRESNET ARCHITECTURE

Our customized neural network architecture (Figure 4.2) builds upon the SRResNet, a neural network architecture specifically designed for image super-resolution tasks (Ledig *et al.*, 2017). In the first step of the SRResNet, the RACMO 27 data undergoes encoding through a single convolution operation. Specifically, a 3x3 filter is applied to the RACMO 27 km data to compute weighted sums, resulting in dimensionality reduction. The outcome of this encoding step produces feature maps that emphasize the large-scale spatial melt patterns, effectively translating the data from spatial melt values into abstract features.

The next step of the SRResNet involves the implementation of sixteen residual blocks applied to the encoded RACMO 27 km (He *et al.*, 2016). These blocks are constructed to allow the combination of the output layer of one layer with that of another layer situated deeper within the block. This design facilitates learning by enabling the model to concentrate on recognizing specific residual details, which pertain to the differences between the current prediction and the desired output (i.e., RACMO 5.5 km). Within the sixteen residual blocks, three operations are carried out. First, a convolutional layer with 3x3 kernels and 64 feature maps extracts spatial patterns from the input. Subsequently, batch normalization is applied to stabilize and accelerate training. Finally, an element-wise summation operation combined the output of a layer with the input of a deeper layer through a skip connection, allowing data to bypass multiple layers and address the vanishing gradients problem. This phenomenon occurs when gradients become extremely small during training, hindering the ability of deep neural networks to effectively learn from data (He *et al.*, 2016).

After the encoding steps and residual block processing, we merge the RACMO 27 km data with the encoded albedo and elevation data (Section 4.3.2). Subsequently, the data undergoes decoding, a process that transforms compressed or abstract features back into a more understandable format, effectively upsampling the data.

Once again, we follow a strategy similar to SRResNet, employing six deconvolution layers with 3x3 kernels, complemented by Parametric Rectified Linear Unit (PReLU) as the activation function. The decoded data are combined with the spotlighted data from SUPREME (Section 4.3.2). Following this, we implement the final step in the standard SRResNet architecture: the multilayer perceptron, which involves connecting every neuron in one layer to every neuron in the next layer through a single convolution operation with a 1x1 kernel. Although this step forms the final stage in the conventional SRResNet, as well as in many other neural networks, we introduce an additional step involving a physical activation function, as detailed in Section 4.3.2.

PHYSICAL CONSTRAINTS

The SRResNet is enriched using three physical constraints, each performing distinct tasks: the “encoder” adds daily albedo, annual Q5 albedo, and elevation data for feature extraction and dimensionality reduction, the “spotlighter” uses 3D-convolutions to analyze albedo and elevation patterns in latitude, longitude, and time, and the “physical activation” scales melt values based on elevation, leveraging the knowledge that lower elevations are associated with higher melt values (see Figure 4.2).

For the first physical constraint, the encoder, we apply a similar procedure to the encoding of RACMO 27 km data, as outlined in the SRResNet architecture, applying a convolution operation and PReLU activation function to extract meaningful patterns from the albedo and elevation data. Subsequently, we downscale the data to match the spatial resolution of the encoded RACMO 27 km data. This is accomplished through 2x2 average pooling, wherein the input data are divided into 2x2 regions, and the average of the values within each region is calculated. These encoded albedo and elevation data are combined with the encoded RACMO 27 km to undergo a decoding step explained in the SRResNet architecture section.

The spotlighter constrains the super-resolution model by the same data used in the encoder, which undergoes a 3D convolution for analysis across longitude, latitude, and time. The 3D convolution functions as a specialized filter, emphasizing important aspects of the data in both spatial and temporal domains. The resulting output is subsequently merged with the decoded RACMO 27 km, albedo, and elevation data. This step aids in capturing meaningful spatiotemporal features which are passed to the multilayer perceptron.

Recognizing the negative correlation between elevation and surface melt (Trusel *et al.*, 2012), and the positive feedback between albedo and surface melt (Jakobs *et al.*, 2019), we apply two correction functions that adjust pixels based on elevation and albedo, referred to as “physical activation”. The physical activation function for elevation increases surface melt values for pixels with low elevation, and reduces surface melt values for pixels at higher elevations. In the re-scaling process, each high-resolution surface melt pixel generated as the final output of the SRResNet architecture is multiplied by a custom sigmoid-like function. These sigmoid functions are created by analyzing the albedo Q5 and elevation data for annual surface melt values from RACMO 5.5 km, RACMO 27 km, and QuikSCAT. Based on this

comparison, the sigmoid functions are plotted using visual inspection and serve as initial guides (see Supplementary Figure 4.6). During training, the weights of the model are updated based on learned weighting functions. The custom sigmoid-like functions have the following shape:

$$Out(\lambda, \phi) = In(\lambda, \phi) \times \frac{A}{1 + B \times e^{X(\lambda, \phi) - C}} \quad (4.1)$$

where $In(\lambda, \phi)$ is the final output of the SRResNet architecture, and λ and ϕ represent the longitude and latitude, respectively. The parameter A is set to 1.36, B is set to 0.005, and C is set to 1.0.

After adjusting the elevation values, we apply the albedo physical activation function, once more using a custom sigmoid-like function (Equation (4.1)). In this context, the parameter $In(\lambda, \phi)$ denotes the output of the elevation physical activation function, while $X(\lambda, \phi)$ represents annual albedo Q5 data, varying both spatially and on a yearly basis. The values assigned to the albedo Q5 physical-activation functions are as follows: A is set to 1.0, B is set to 0.05, and C is set to 37.0.

4.3.3. TRAINING

During training, the RMSprop optimizer (Reddy *et al.*, 2018) is employed, starting with a learning rate of 10^{-3} . An exponential learning rate decay is implemented to dynamically adjust the learning rate in later training epochs. The models are trained with a batch size of 16 over a span of 30 epochs. Early stopping is implemented to mitigate potential model overfitting, whereby it monitors training mean squared error (MSE) loss. If the MSE loss did not improve by at least the specified minimum threshold of 5×10^{-4} (mm w.e. yr^{-1})² for five consecutive epochs, the training process concludes prematurely. We experimented with alternative hyperparameters, such as learning rate, loss function, and optimizer, using the validation dataset, but found that the presented parameters produced the best results.

To evaluate the importance of physical constraints, we train different models: one incorporating all three physical constraints (referred to as SUPREME), another without any physical constraint (referred to as SRResNet), and additional models with exclusive use of each individual physical constraint—SUPREME_{only encoder}, SUPREME_{only spotlighter}, and SUPREME_{only physical activation}. Additionally, we train two models to evaluate the importance of the remote sensing input features on the downscaled surface melt product, which we denote as SUPREME_{no albedo} and SUPREME_{no elevation}. In SUPREME_{no albedo}, we omit the albedo input features, retaining only RACMO 27 km and elevation as inputs. In SUPREME_{no elevation}, we exclude elevation, keeping only RACMO 27 km and albedo. In SRResNet, we exclude all remote sensing features, using only RACMO 27 km as an input feature.

4.3.4. POST-PROCESSING

Using the trained models from Section 4.3.3, we produce the SUPREME results and the results for which one or more input features or physical constraints were excluded. The output from the super-resolution models includes patches with

padding, which are subsequently clipped to form patches with dimensions of 54 x 54 pixels. Despite the applied padding on patch edges, some patches exhibit pronounced transitions, resulting in a ‘checkerboard’ effect. To address this, we reposition all patches 27 km left and right relative to their original positions and recalculate the results. Subsequently, we average the outcomes from the three runs to obtain the final SUPREME results. Finally, we sum all the individual days to create aggregated products per melt season, measured in mm w.e. per year. Due to memory constraints, we evaluate only the melt products per melt season rather than at a higher temporal resolution.

4.3.5. EVALUATION

Evaluating SUPREME poses a considerable challenge. There is no observational dataset providing Antarctic-wide surface melt data at such a high spatial resolution for the past two decades. Consequently, we have to rely on various available products to assess the performance of SUPREME. We compare SUPREME with in-situ data (AWS), another downscaled RACMO product (RACMO 2 km), and various remote sensing products (QuikSCAT, PMW remote sensing, and a melt-slush product from optical remote sensing), as was described in Section 4.2.3.

Moreover, we also conduct a comparative analysis of SUPREME against RACMO 5.5 km, focusing exclusively on the Antarctic Peninsula, where RACMO 5.5 km data are available. We compare SUPREME and RACMO 5.5 km for the testing period from 2010 to 2019 and employ four key metrics: coefficient of determination (R^2), Root Mean Square Error (RMSE), bias, and Pearson Correlation Coefficient (PCC). Firstly, R^2 is a statistical measure indicating the proportion of the variance in the reference data that can be explained by the prediction data in a regression model. Secondly, the RMSE gives us an understanding of the average size of the differences between predicted and observed values, effectively quantifying the overall performance of the model by taking into account both the bias and variance of the errors. A lower RMSE signifies a better fit of the model to the data. Thirdly, bias refers to the systematic deviation of the super-resolution model predictions from the observed values. The bias provides insight into any consistent overestimation or underestimation tendencies present in the model’s predictions compared to the reference data. Finally, the PCC evaluates the linear relationship between predicted and observed values, with a scale ranging from -1 to 1 . A PCC of 1 indicates a perfect positive linear relationship, signifying that the model accurately captures the temporal variability of the data. These four metrics collectively offer a comprehensive evaluation of our model’s performance. While R^2 measures how well a regression model fits the observed data, RMSE provides the overall accuracy, bias evaluates the systematic errors or deviations in predictions compared to the true value, and PCC assesses the linear relationship.

4.4. RESULTS

In the results section, we begin by analyzing the performance of SUPREME on the testing dataset. At the end of Section 4.4.1, we demonstrate that the testing

metrics closely align with the training metrics, indicating that the model generalizes effectively. Subsequently, in the remaining results (Sections 4.4.2 – 4.4.5), we incorporate the training region and period for further analysis, while consistently indicating instances where data were included in the training of the super-resolution model.

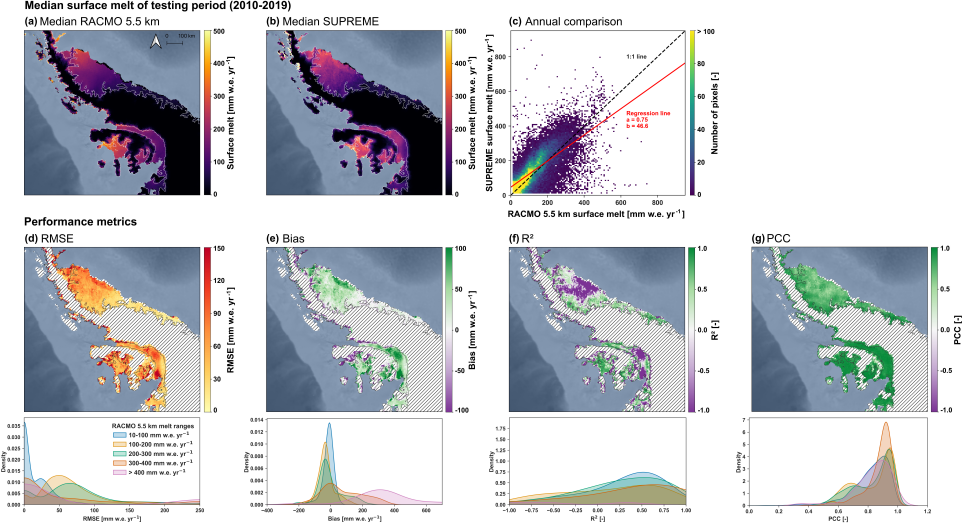


Figure 4.3: Comparison of RACMO 5.5 km and SUPREME over the Antarctic Peninsula for the testing period (2010-2019), with median melt values for RACMO 5.5 km in (a), median melt values for SUPREME in (b), and a scatter plot with annual RACMO 5.5 km and SUPREME melt values and regression line in (c). The performance metrics with the root mean square error (RMSE), bias, coefficient of determination (R^2), and Pearson correlation coefficient (PCC) are shown in (d), (e), (f), and (g), respectively, where the upper panels show spatial maps and the bottom panels show the distribution of the data in kernel density estimate (KDE) plots, displaying the data per melt regime based on the median RACMO 5.5 km melt values. Pixels with surface melt rates below $10 \text{ mm w.e. yr}^{-1}$ and pixels elevated more than 1700 meters above sea level are excluded from the analyses, as their inclusion could artificially enhance the performance metrics.

4.4.1. PERFORMANCE ON TESTING DATASET

SUPREME demonstrates strong performance during the testing melt seasons from 2010 to 2019 when compared to the reference data from RACMO 5.5 km, as illustrated by the performance metrics displayed in Figure 4.3. Notably, SUPREME exhibits slightly higher melt values in specific regions, including the northern part of the Larsen C Ice Shelf, the collapsed A-68 iceberg in 2017 (Braakmann-Folgmann *et al.*, 2022), George VI, and Wilkins ice shelves (see Figure 4.3a and 4.3b). For the locations of iceberg A-68, Wilkins, and George VI ice shelves see Figure 4.1. These areas align with locations exhibiting higher RMSE (Figure 4.3d) and bias (Figure 4.3e) values. RMSE and bias values vary noticeably among different melt regimes

(i.e., 10–100, 100–200, 200–300, 300–400, and over 400 mm w.e. yr⁻¹). The highest RMSE and bias are found for the high melt regime (exceeding 400 mm w.e. yr⁻¹), with median values of 103 and 325 mm w.e. yr⁻¹, respectively. This indicates that SUPREME's performance could be improved, particularly for high melt rates. The lowest R² values (Figure 4.3f) are observed for both low and high melt regimes, specifically at the center of the Larsen C Ice Shelf, and the center and south of George VI Ice Shelves, with values around -1, indicating that SUPREME does not adequately capture the variability in surface melt observed in RACMO 5.5 km.

The PCC (Figure 4.3g) is less dependent on the melt regimes and has a median value of 0.86, indicating a high level of correlation between the annual melt values predicted by RACMO 5.5 km and SUPREME for most of the Antarctic Peninsula. At the grounding zone of the Larsen C Ice Shelf and the George VI Ice Shelf, the PCC surpasses 0.90, underlining a particularly strong correlation in these regions.

To assess the performance of SUPREME and RACMO 5.5 km during the training (2001–2002 to 2006–2007) and non-training (2007–2008 to 2018–2019) periods, we conducted a paired t-test. We compared the yearly mean RMSE values between RACMO 5.5 km and SUPREME for the six melt seasons of the training period against two segments of the non-training period: the first segment (2007–2008 to 2012–2013) and the second segment (2013–2014 to 2018–2019). The results indicate no significant difference in RMSE between RACMO 5.5 km and SUPREME for both the training and non-training periods. Supplementary Table 4.1 presents the yearly average performance metrics of surface melt for the Antarctic Peninsula and Larsen C during the training (2001–2002 to 2006–2007) and non-training (2007–2008 to 2018–2019) periods.

4.4.2. COMPARISON OF SUPREME AND RACMO 27 KM

TEMPORAL ANALYSIS

Figure 4.4 shows consistent year-to-year area-integrated variability among RACMO 27 km and SUPREME (with a PCC > 0.95 for all study regions), despite notable quantitative differences in the modeled values. Between 2001–2002 and 2018–2019, the RACMO 27 km model projects an annual surface melt over the entire Antarctic Ice Sheet of 98.5 and a standard deviation of the inter-annual variability of ± 22.0 Gt, whereas the SUPREME model reports lower numbers at 79.5 ± 14.9 Gt yr⁻¹ (Figure 4.4a). For the Antarctic Peninsula (Figure 4.4b) and Larsen C (Figure 4.4c), RACMO 27 km yields higher annual melt values (37.3 ± 10.7 Gt and 13.6 ± 4.6 Gt, respectively) than SUPREME (34.6 ± 9.1 Gt and 12.4 ± 4.1 Gt, respectively). When comparing RACMO 27 km and SUPREME in the remainder of the ice sheet, we observe similar annual surface melt values for most ice shelves. However, a notable exception is Shackleton (Figure 4.4f), where RACMO 27 km reports approximately 2 Gt more surface melt (6.0 ± 2.2 Gt) compared to SUPREME (4.3 ± 1.4 Gt).

SPATIAL ANALYSIS

To get a better understanding of when and where RACMO 27 km tends to result in higher surface melt values than SUPREME, we can examine the spatial patterns of

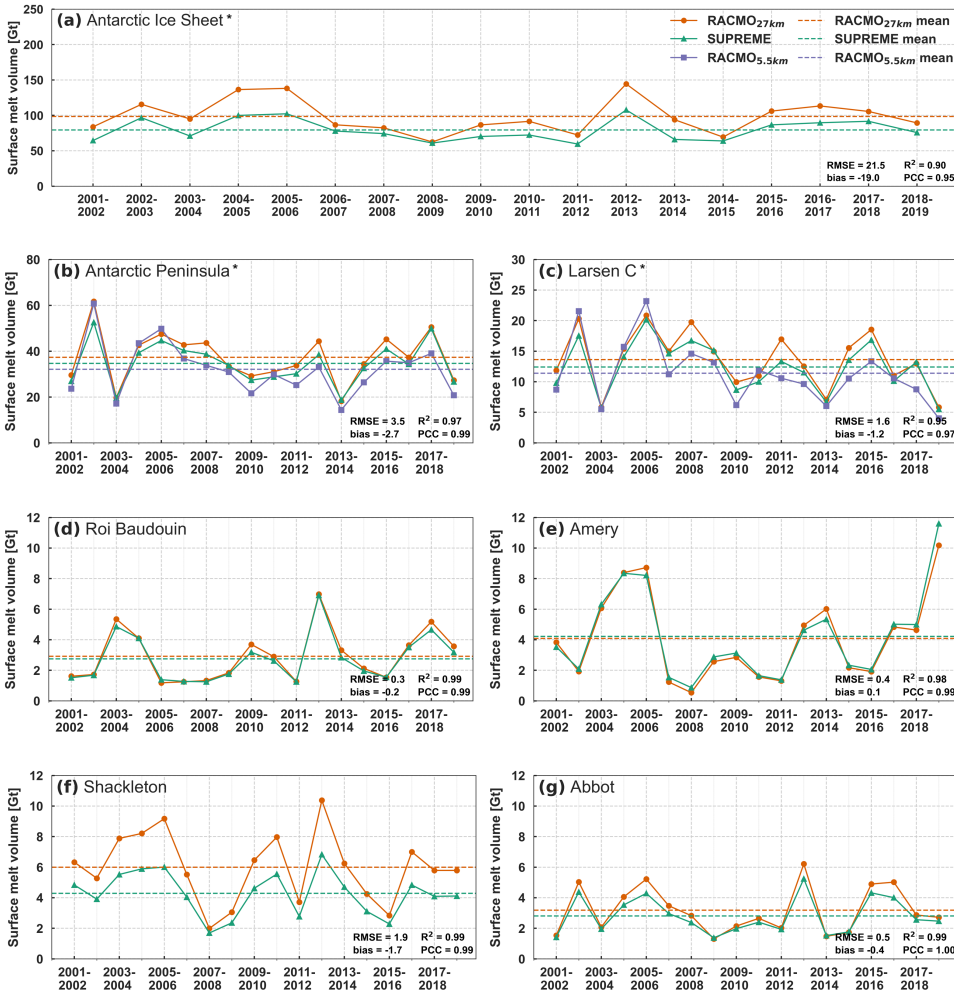


Figure 4.4: Temporal evolution of surface melt for the melt seasons from 2001 to 2019, represented by RACMO 27 km (in orange), SUPREME (in green), and RACMO 5.5 km (in purple), with dashed lines representing the 2001–2019 mean. RACMO 5.5 km data are exclusively available for the Antarctic Peninsula (b) and Larsen C (c). For the Antarctic-wide time series (a), and specific locations including Roi Baudouin (d), Amery (e), Shackleton (f), and Abbot (g), only RACMO 27 km and SUPREME data are depicted. Caution is advised when interpreting the datasets marked with an asterisk (a–c), as a part of these data were used in training SUPREME. The extent of the selected regions can be found in Supplementary Figure 4.4. Relevant statistics used to compare RACMO 27 km and SUPREME, including root mean square error (RMSE), bias, coefficient of determination (R^2), and Pearson correlation coefficient (PCC), are listed.

Larsen C (Figure 4.5a), Roi Baudouin (Figure 4.5b), Amery (Figure 4.5c), Shackleton (Figure 4.5d), and Abbot (Figure 4.5e) ice shelves. These five ice shelves are selected

for closer examination due to their relatively high surface melt rates.

The lower surface melt values in SUPREME compared to RACMO 27 km presented in Figure 4.4 are not uniform; rather, surface melt exhibits localized patterns of both lower and higher melt values. Lower surface melt values for SUPREME are observed over the Larsen C Ice Shelf, especially during the melt season of 2011–2012, as well as across all melt seasons over the Shackleton Ice Shelf. One exception is the northern part of the Shackleton Ice Shelf, where SUPREME shows a peak in surface melt with an average annual value of approximately 600 mm w.e., while RACMO 27 km has an average of around 160 mm w.e. annually. These high melt values for SUPREME can likely be attributed to the extremely low albedo values in the vicinity of this area (see Supplementary Figure 4.5), connected to a persistent polynya adjacent to the Shackleton Ice Shelf (Nihashi & Ohshima, 2015). With median albedo values of this open water of around 0.1, SUPREME most likely misidentifies this phenomenon as intense surface melt. For specific areas within the grounding zone, SUPREME consistently demonstrates higher melt values than RACMO 27 km. This is especially evident during the high melt season of 2012–2013 for the center part of the grounding zone of Roi Baudouin, the eastern part of Amery, and the northern part of Abbot ice shelves.

DATA SPREAD ANALYSIS

Figure 4.6 quantifies the surface melt values of RACMO 27 km and SUPREME, distinguishing between values on the floating ice shelf and in the grounding zone (see Supplementary Figure 4.4 for precise locations). The surface melt range in RACMO 27 km and SUPREME is assessed using the 5th (Q5) and 95th (Q95) percentiles. Notably, there is a consistently wider range of surface melt in SUPREME compared to RACMO 27 km, observed in both the ice shelf and grounding zone. In contrast, the mean and median values for both ice shelves and grounding zones are generally higher in RACMO 27 km compared to SUPREME (except for the Amery Ice Shelf), reaffirming the lower melt volumes in SUPREME in comparison to RACMO 27 km.

Examining the floating ice shelves, the most substantial discrepancy between RACMO 27 km and SUPREME is observed on the Shackleton Ice Shelf. RACMO 27 km shows a Q5–Q95 range of 73 to 159 mm w.e. yr^{-1} , while SUPREME exhibits a wider range spanning from 2 to 659 mm w.e. yr^{-1} (Figure 4.6d). The elevated melt values (Q95) in SUPREME for the Shackleton Ice Shelf are also visually evident in Figure 5, particularly in the northern sector of the shelf. Also, on the grounding zone, SUPREME consistently displays a larger Q5–Q95 range compared to RACMO 27 km. The most pronounced differences are seen in the cases of Amery (Figure 4.6c) and Abbot (Figure 4.6e). RACMO 27 km shows a Q95 value of 195 mm w.e. yr^{-1} for Amery, while SUPREME yields a higher value of 385 mm w.e. yr^{-1} . The contrast is even more pronounced for Abbot, with RACMO 27 km at 165 mm w.e. yr^{-1} and SUPREME at 711 mm w.e. yr^{-1} .

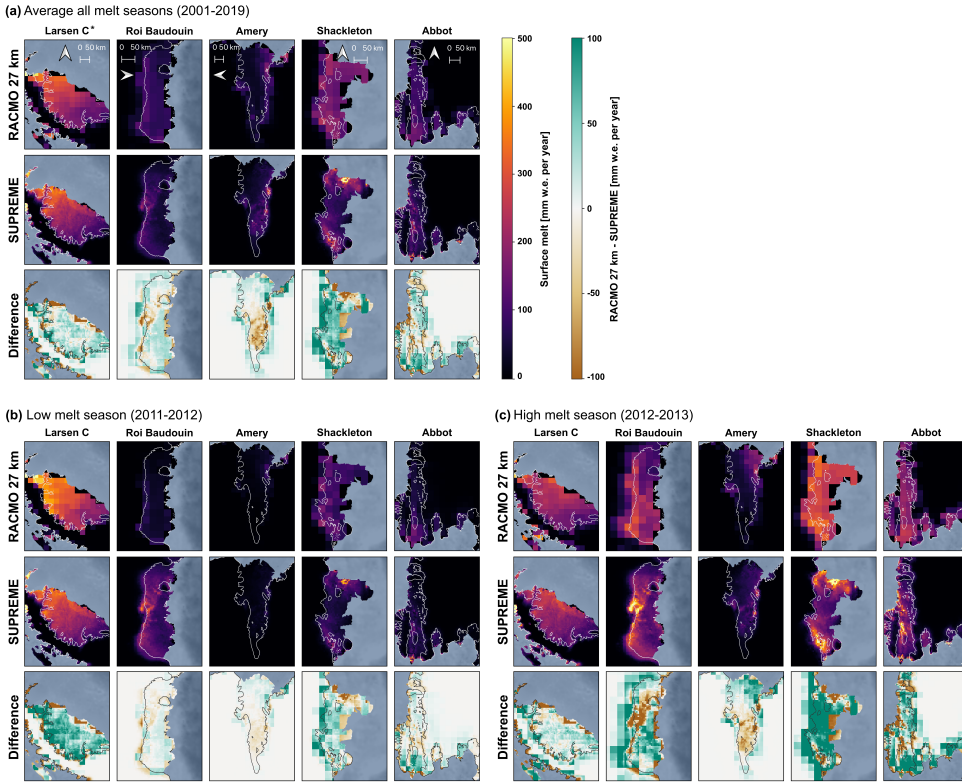


Figure 4.5: Surface melt for (a) the average of melt seasons of 2001–2019, (b) low melt season 2011–2012, and high melt season 2012–2013 for RACMO 27 km, SUPREME, and the difference between RACMO 27 km and SUPREME. Caution is advised when interpreting the datasets marked with an asterisk (i.e., Larsen C, panel a), as a part of these data were used in training SUPREME.

4.4.3. COMPARISON OF SUPREME AND AWS

Figure 4.7 presents a comparison between RACMO 5.5 km, RACMO 27 km, and SUPREME with five AWS. Notably, SUPREME exhibits a lower RMSE than RACMO 27 km for all five AWS, and a lower absolute bias for AWS14, AWS15, and AWS18. The largest difference between SUPREME and RACMO 27 km is observed for AWS18 (Figure 4.7d). For this AWS, SUPREME yields an RMSE of $87 \text{ mm w.e. yr}^{-1}$ and a bias of $23 \text{ mm w.e. yr}^{-1}$, compared to the $244 \text{ mm w.e. yr}^{-1}$ RMSE and $-216 \text{ mm w.e. yr}^{-1}$ bias for RACMO 27 km. Due to its coarse resolution, RACMO 27 km fails to resolve the surface melt in areas with highly variable topography, such as around AWS18. This AWS is situated near the grounding line of the Larsen C ice shelf, east of the Antarctic Peninsula mountain range, and is prone to föhn events that contribute to surface melt (Kuipers Munneke *et al.*, 2018; Wiesenekker *et al.*, 2018).

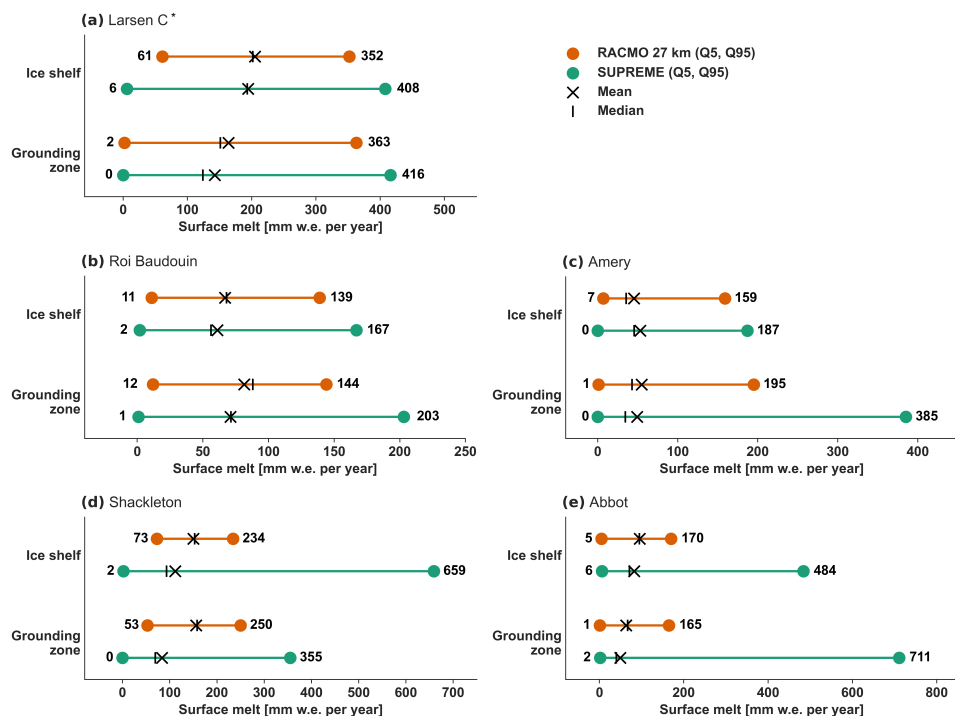


Figure 4.6: The range of surface melt values for the ice shelves and grounding zones, showing the mean (crosses), median (vertical lines), 5th (Q5), and 95th (Q95) percentile values, for the melt seasons spanning from 2001 to 2019. The data are presented for both RACMO 27 km (in orange) and SUPREME (in green) at the ice shelf and grounding zone of (a) Larsen C, (b) Roi Baudouin, (c) Amery, (d) Shackleton, and (e) Abbot. Caution is advised when interpreting the datasets marked with an asterisk (i.e., Larsen C in panel a), as a part of these data were used in training SUPREME.

4.4.4. COMPARISON OF SUPREME AND OTHER SURFACE MELT PRODUCTS

Given that RACMO 5.5 km data are limited to the Antarctic Peninsula, a comprehensive Antarctic-wide assessment between SUPREME and RACMO 5.5 km dataset is not feasible. Here, we proceeded to compare SUPREME with other melt products, i.e., RACMO 2 km, QuikSCAT, PMW remote sensing, and an optical remote sensing product that provides information on both melt and slush. Both RACMO 2 km and QuikSCAT offer quantitative data on surface melt in mm w.e., whereas PMW and optical remote sensing techniques provide binary outputs without specific quantification of melt volume.

Each of the validation datasets has distinct underlying methodologies (as was explained in Section 4.2.3), resulting in large disparities in local surface melt patterns, as illustrated in Figure 4.8. In addition, Figure 4.9 illustrates the comparison between SUPREME and the validation products using both a scatter plot and several

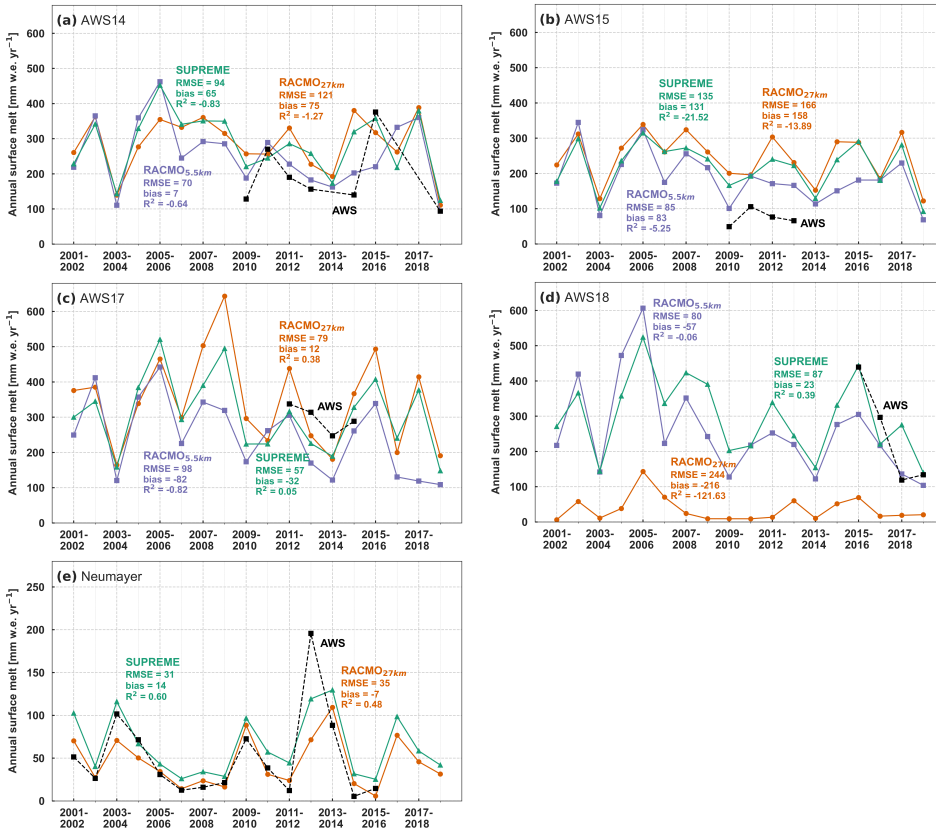


Figure 4.7: Surface melt per melt season by RACMO 27 km (in orange), SUPREME (in green), RACMO 5.5 km (in purple), and automatic weather stations (AWS) (in black). Data are collected from five automatic weather stations: AWS14 (a), AWS15 (b), AWS17 (c), AWS18 (d), and Neumayer (e). The Root Mean Squared Error (RMSE), bias, and coefficient of determination (R^2) are represented by the color of the respective model in comparison to AWS measurements. Supplementary Figure 4.2 displays the locations of the AWS.

performance metrics. In the period from 2001 to 2009 (Figure 4.8a and Figure 4.9a), the Larsen C Ice Shelf should be considered with caution, as this dataset was used during training of SUPREME. For the Roi Baudouin Ice Shelf, both QuikSCAT and PMW data reveal higher surface melt levels in the eastern region (150 mm w.e. yr⁻¹ and 35 melt days yr⁻¹, respectively) compared to the western area (75 mm w.e. yr⁻¹ and 20 melt days yr⁻¹, respectively). This gradient, however, is not as clearly discernible in the RACMO 27 km, RACMO 2 km, or SUPREME datasets. Also, the R^2 values are low when comparing SUPREME to QuikSCAT (-2.18), and slightly higher but still very low for RACMO 27 km (-1.77) and RACMO 2 km (-0.98), as illustrated in Figure 4.9a. For the Amery Ice Shelf, both SUPREME and RACMO 2 km display some high surface melt values (250 mm w.e. yr⁻¹), particularly on the

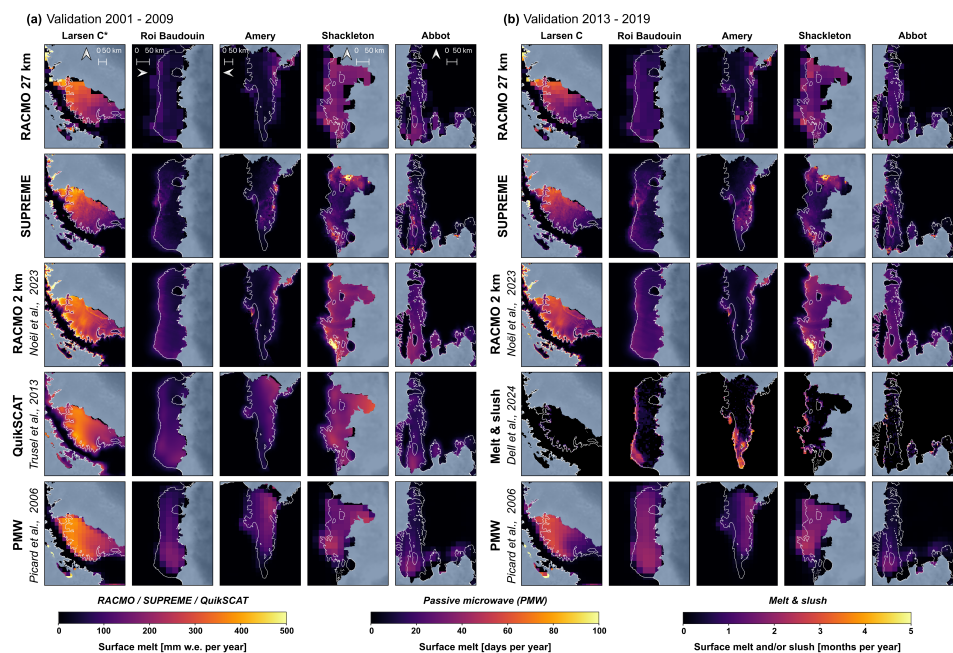
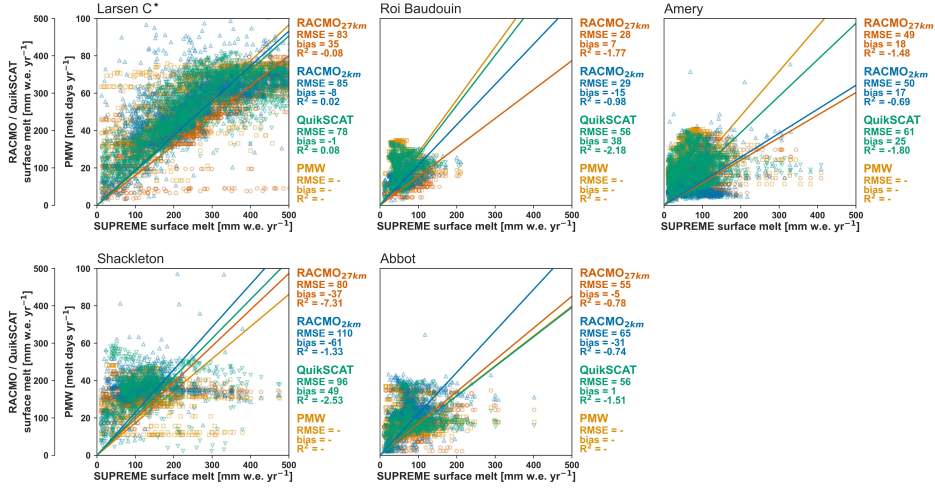


Figure 4.8: Spatial comparison of SUPREME to validation datasets across two distinct periods: (a) 2001–2009 and (b) 2013–2019, encompassing Larsen C, Roi Baudouin, Shackleton ice shelves, and Mary Byrd Land. For the 2001–2009 period, SUPREME is compared to RACMO 27 km, RACMO 2 km, QuikSCAT, and passive microwave (PMW) remote sensing (note that the latter employs a different unit than the other methods). In the 2013–2019 period, SUPREME is compared to RACMO 27 km, RACMO 2 km, a surface melt and slush product from optical remote sensing, and PMW remote sensing (both optical and PMW measurements employ different units than the other methods). Caution is advised when interpreting the dataset marked with an asterisk (i.e., SUPREME, Larsen C, 2001–2009), as a part of these data were used during the training of SUPREME.

southern part of the ice shelf. Likewise, QuikSCAT and PMW also show increased melt in the southern region ($150 \text{ mm w.e. yr}^{-1}$ and $40 \text{ melt days yr}^{-1}$, respectively), but the precise locations with the highest melt differ. QuikSCAT shows the highest melt values toward the southeast, whereas PMW tends toward the center-south, gradients that are not present in SUPREME. It is worth noting that RACMO 27 km and QuikSCAT and RACMO 27 km report surface melt below $200 \text{ mm w.e. yr}^{-1}$ for Amery, while SUPREME and RACMO 2 km register values exceeding $500 \text{ mm w.e. yr}^{-1}$. The smoother representation of surface melt by RACMO 27 km and QuikSCAT, attenuating peak values, is likely a result of their coarser spatial resolutions (i.e., 27 km for RACMO 27 km, and 25 km as a native spatial resolution for QuikSCAT). Likewise, the Shackleton Ice Shelf displays elevated melt values in SUPREME and RACMO 2 km, exceeding 400 mm w.e. at the southern grounding line. Moreover, in the northern region, SUPREME shows melting rates exceeding $500 \text{ mm w.e. yr}^{-1}$. The high surface melt values at the southern grounding line of the Shackleton

(a) Validation 2001-2009



(b) Validation 2013-2019

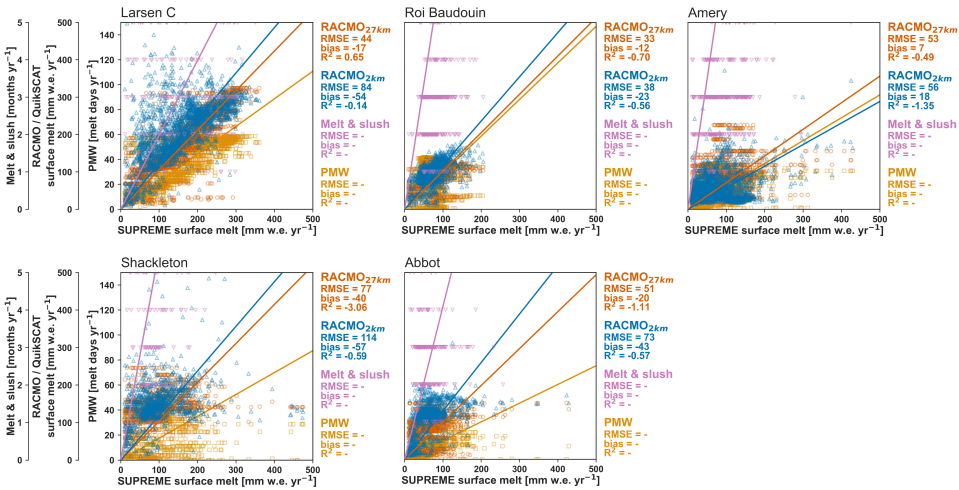


Figure 4.9: Comparison of SUPREME to validation datasets across two distinct periods: (a) 2001–2009 and (b) 2013–2019, encompassing Larsen C, Roi Baudouin, Shackleton ice shelves, and Mary Byrd Land, complementing Figure 4.8. The scatter plots compare SUPREME with validation products (i.e., RACMO 27 km, RACMO 2 km, QuikSCAT, passive microwave (PMW) remote sensing, and surface melt and slush product), with each line representing the least-square fit. The Root Mean Squared Error (RMSE), bias, and coefficient of determination (R^2) are represented by the color of the respective validation data in comparison to SUPREME, for PMW and the melt and slush product only the R^2 is included. Caution is advised when interpreting the datasets marked with an asterisk (i.e., Larsen C, panel a), as a part of these data were used in training SUPREME. Supplementary Figure 4.4 shows the spatial extents analyzed.

Ice Shelf are also observed in other validation products, exceeding 250 mm w.e. yr^{-1} in QuikSCAT, and 40 melt days yr^{-1} in PMW. For the Abbot Ice Shelf, the most substantial melt values are concentrated in the southern region bordering the Amundsen Sea. Here, SUPREME depicts surface melt values exceeding 400 mm w.e. yr^{-1} , whereas RACMO 27 km, RACMO 2 km, and QuikSCAT melt values remain under 200 mm w.e. yr^{-1} .

Moving to the second comparison period (2013–2019) in Figure 4.8b and Figure 4.9b, we compare SUPREME to RACMO 27 km, RACMO 2 km, a melt and slush product derived from optical imagery, and PMW. As noted in Section 4.2.3, since optical imagery detects meltwater solely when slushy or ponded water is present, they do not represent wet snow that may later refreeze within the firn layer. Therefore, SUPREME is expected to show similar melt patterns to the optical melt and slush product only in locations characterized by a low firn air content, where meltwater accumulates at the surface. Figure 4.8b shows that the melt and slush product predominantly reveals high values around the grounding line, indeed often corresponding to locations with supraglacial melt lake presence (e.g., Stokes *et al.*, 2019). Some of these locations align with high melt values detected in SUPREME, such as the central part of the grounding line of the Roi Baudouin Ice Shelf and the southern part of the grounding line of the Amery Ice Shelf, where surface melt values range between 250 and 500 mm w.e. yr^{-1} . For the Roi Baudouin Ice Shelf, the RMSE values are relatively low compared to the other ice shelves, standing at 33 mm w.e. yr^{-1} for RACMO 27 km and 38 mm w.e. yr^{-1} for RACMO 2 km, as illustrated in Figure 4.9b. However, there are also instances where there is not a clear overlap between surface melt in the melt and slush product and SUPREME, as observed over the western part of the Amery Ice Shelf. Here, in the optical remote sensing product, melt or slush is detected on average for at least three months per year, while RACMO 27 km, SUPREME, RACMO 2 km, and the PMW product show low melt values around 50–100 mm w.e. yr^{-1} or 5 melt days yr^{-1} . Similar to the 2001–2009 period, there are also variations in melt patterns between PMW and SUPREME for 2013–2019, with PMW displaying a smoother surface melt pattern with fewer high-resolution details compared to SUPREME. For both the Shackleton and Abbot ice shelves, we observe relatively large RMSE values, ranging from 51 to 114 mm w.e. yr^{-1} .

4.4.5. IMPORTANCE OF PHYSICAL CONSTRAINTS

In Sections 4.4.2, 4.4.3, and 4.4.4, we exclusively presented SUPREME, which uses the SRResNet model architecture along with three physical constraints to incorporate remote sensing data. To assess the importance of these individual physical constraints, Figure 4.10a presents models trained exclusively with each physical constraint (SUPREME_{only encoder}, SUPREME_{only spotlighter}, SUPREME_{only physical activation}). Additionally, models with all physical constraints but only one of the remote sensing input features are depicted (SUPREME_{no albedo}, SUPREME_{no elevation}). Figure 4.10b showcases SUPREME with all three physical constraints alongside SRResNet without any physical constraints. Additionally, Supplementary Figure 4.7 shows the mean, median, and spread of the datasets presented in Figure 4.10, and Supplementary

Table 4.2 shows the performance metrics of the different super-resolution models compared to RACMO 27 km.

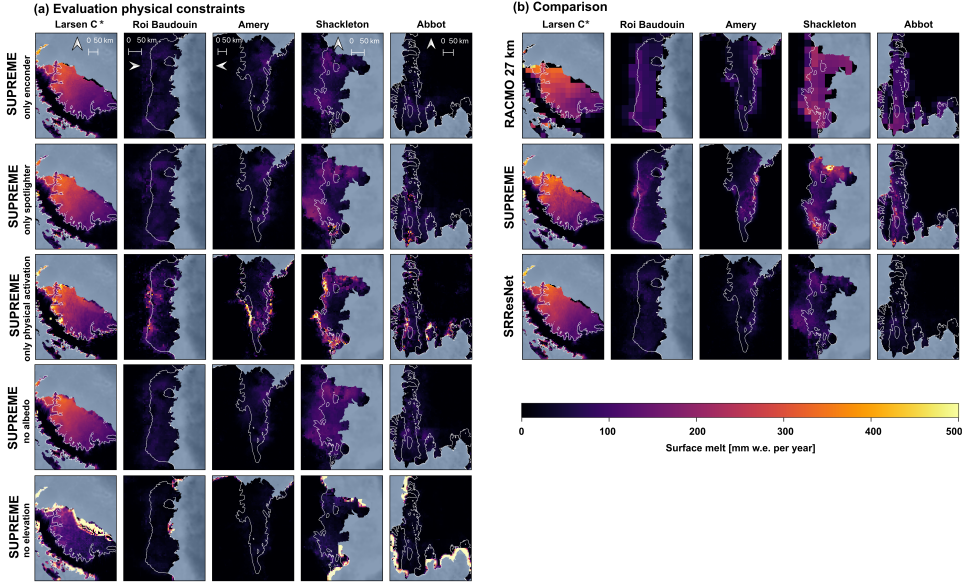


Figure 4.10: Evaluating the performance of surface melt for the average of melt seasons of 2001-2019 across different model architectures. (a) SUPREME with individual physical constraints (only encoder, only spotlighter, only physical activation), and SUPREME with the exclusion of albedo and elevation input features from the model architectures, respectively. (b) Comparative data featuring RACMO 27 km, SUPREME with all physical constraints and input features, and SRResNet without any physical constraint and with both albedo and elevation excluded from the model architecture. Caution is advised when interpreting the datasets marked with an asterisk (i.e., Larsen C in panels a and b), as a part of these data were used in training SUPREME.

The physical constraints responsible for integrating encoded albedo and elevation data into the model architecture (SUPREME_{only encoder}), incorporating spotlighted albedo and elevation data (SUPREME_{only spotlighter}), and applying the physical activation function (SUPREME_{only physical activation}) demonstrate a similar melt pattern as SUPREME and RACMO 27 km over the Larsen C Ice Shelf, exhibiting a south-north melt trend ranging from roughly 100 to 400 mm w.e. yr^{-1} . However, beyond the Antarctic Peninsula, SUPREME_{only encoder}, SUPREME_{only spotlighter}, and SUPREME_{only physical activation} compare less favorably to SUPREME and RACMO 27 km. The median annual melt values over the Roi Baudouin, Amery, Shackleton, and Abbot ice shelves are higher for SUPREME (averaging 61 mm w.e. yr^{-1}) and RACMO 27 km (averaging 88 mm w.e. yr^{-1}), compared to SUPREME_{only encoder} (averaging 37 mm w.e. yr^{-1}), SUPREME_{only spotlighter} (averaging 50 mm w.e. yr^{-1}), and SUPREME_{only physical activation} (averaging 44 mm w.e. yr^{-1}) (see Supplementary Figure 4.7). In comparison to RACMO 27 km on an Antarctic-wide scale, SUPREME exhibits an RMSE of 32 mm w.e. yr^{-1} , while SUPREME_{only encoder} shows a

slightly higher value at 33 mm w.e. yr^{-1} . However, SUPREME_{only spotlighter} and SUPREME_{only physical activation} exhibit notably higher RMSE values of 55 mm w.e. yr^{-1} and 53 mm w.e. yr^{-1} respectively (see Supplementary Table 4.2).

Similar observations apply to models that lack either albedo (SUPREME_{no albedo}) or elevation (SUPREME_{no elevation}), as they do not generalize well beyond the Antarctic Peninsula. These models also tend to underestimate surface melt compared to SUPREME and RACMO 27 km, as shown by their median annual melt values over the Roi Baudouin, Amery, Shackleton, and Abbot ice shelves for SUPREME_{no albedo} (averaging 49 mm w.e. yr^{-1}) and SUPREME_{no elevation} (averaging 23 mm w.e. yr^{-1}) (see Supplementary Figure 4.7). When compared to RACMO 27 km across Antarctica, SUPREME shows an RMSE of 32 mm w.e. yr^{-1} , akin to SUPREME_{no albedo}. However, SUPREME_{no elevation} displays a notably higher RMSE of 60 mm w.e. yr^{-1} (see Supplementary Table 4.2).

Besides the finding that models lacking physical constraints or input features display less melt on the ice shelves compared to RACMO 27 km and SUPREME, there are also discrepancies in spatial patterns. The SUPREME model, incorporating all input features, shows heightened melt values in the grounding zones, aligning with observations from the validation datasets (Figure 4.8). However, models without albedo data (i.e., SUPREME_{no albedo} and SRResNET) indicate surface melt extending up to 50 km inland. This pattern persists with SUPREME_{only encoder} and SUPREME_{only spotlighter}. This is most clearly visible in the case of the Shackleton Ice Shelf, where values range between 50 and 150 mm w.e. yr^{-1} , whereas RACMO 27 km, SUPREME, and the validation datasets in Figure 4.8 demonstrate values close to zero mm w.e. yr^{-1} . Therefore, incorporating both albedo and elevation data is crucial for accurately representing melt patterns outside the training region.

4.5. DISCUSSION

Our study illustrated that SUPREME, which incorporates physical constraints derived from albedo and elevation observations, outperforms models that lack such constraints. Notably, the single-image super-resolution model, SRResNet, which was trained solely on RACMO 27 km, and the models lacking at least one physical constraint, exhibited poor performance outside of the Antarctic Peninsula. The melt patterns observed in these models differed notably from those seen in RACMO 27 km, RACMO 2 km, or QuikSCAT, with most showing less surface melt (Supplementary Figure 4.7). On the other hand, in some cases, models lacking albedo (i.e., SUPREME_{no albedo}) or albedo and elevation (i.e., SRResNet) led to increased melting further inland, which was not present in other melt products. This poor performance underscored the need to integrate both albedo and elevation data in an efficient manner into the super-resolution model in order to produce an accurate downscaled surface melt product. The incorporation of additional input features, such as climate variables like wind speed and direction, could potentially enhance the super-resolution product even further.

Integrating remote sensing data through deep learning into the downscaling of RCMs presents considerable promise for multiple research purposes. Our

approach could serve as a proof-of-concept and be extended to other studies. Firstly, besides RACMO 27 km, our developed super-resolution algorithm could be extended to other RCMs like MAR (Agosta *et al.*, 2019). Secondly, the potential application of super-resolution techniques extends across diverse datasets, including observations, model simulations, and emulated data (Vandal *et al.*, 2017). Lastly, the super-resolution architecture is not limited to surface melt; it can enhance various other RCM variables. A critical advancement for Antarctica could involve applying such a super-resolution technique not only to surface melt but also to basal melt (e.g., Burgard *et al.*, 2023), bed topography (e.g., Cai *et al.*, 2023), or sea ice motion (e.g., Petrou *et al.*, 2018). In this study, albedo and elevation are identified as relevant remote sensing data for downscaling surface melt, given their correlation with surface melt. However, downscaling other variables from RCMs may require the incorporation of completely different remote sensing data, depending on the physical processes that influence those variables. For example, in the case of downscaling surface temperature, Li *et al.* (2019) demonstrated the value of including elevation, reflectance from optical remote sensing, vegetation indices, and elevation in the downscaling process.

When assessing the downscaled surface melt product developed with the SUPREME architecture, we observe favorable comparisons against RACMO 5.5 km, AWS, and various remote sensing products associated with surface melt. Over the Antarctic Peninsula, SUPREME performed well, exhibiting a bias of $-22 \text{ mm w.e. yr}^{-1}$ for melt pixels when compared to RACMO 5.5 km. Additionally, in comparison to AWS, SUPREME exhibited an average RMSE of $81 \text{ mm w.e. yr}^{-1}$, outperforming RACMO 27 km, which had an average RMSE of $129 \text{ mm w.e. yr}^{-1}$. However, evaluating SUPREME's performance beyond the Antarctic Peninsula presented challenges. We conducted comparisons with RACMO 2 km, QuikSCAT, PMW remote sensing, and an optical remote sensing-derived melt and slush product. The substantial discrepancies between these datasets made direct assessments challenging. Although some melt patterns, such as elevated surface melt along the grounding zones of the studied ice shelves, were consistent with most of the other products, others, like the heightened melt values north of the Shackleton Ice Shelf, were distinctive to SUPREME and appeared to be an artifact due to low albedo values from the nearby ocean. Conducting follow-up studies to further compare SUPREME against validation data, such as with RACMO data downscaled using different techniques, e.g., a more detailed comparison with the statistically-downscaled RACMO product by Noël *et al.* (2023), other RCMs like MAR (Agosta *et al.*, 2019), or quantitative meltwater products from PMW (currently available for Greenland from Zheng *et al.*, 2022), may provide additional insights into meltwater volumes on Antarctica. Additionally, while this study focused on annual surface melt volumes due to memory constraints, future research is planned to study the intra-annual surface melt dynamics of SUPREME and compare them across various validation datasets.

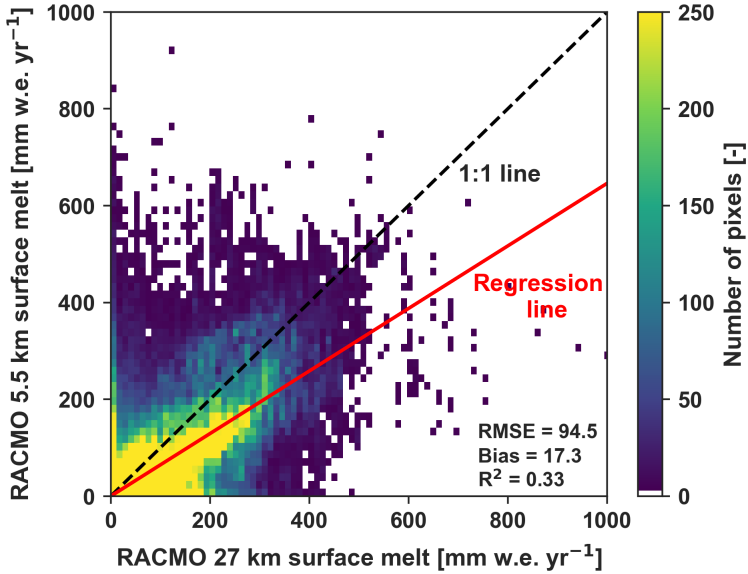
Opting for deep learning over traditional statistical or dynamical downscaling methods to enhance the resolution of RCMs, SUPREME uses the capabilities of deep learning to capture complex patterns and non-linear dependencies in the data. While statistical and dynamical downscaling methods have played instrumental

roles in climate research (e.g., Ahmed *et al.*, 2013; Noël *et al.*, 2016, 2023; Themeßl *et al.*, 2012), deep learning offers an alternative downscaling approach by incorporating diverse datasets without the need for statistical linear relationships and integrating good generalization capabilities for efficient climate parameter downscaling. However, significant steps still need to be taken, as the inherent “black box” nature of deep learning poses challenges in interpreting deep learning models. Anticipated efforts in enhancing the interpretability of the model are expected to refine its overall effectiveness and integration into climate research methodologies (Guidotti *et al.*, 2018; La Rocca & Perna, 2022; Savage, 2022).

4.6. CONCLUSION

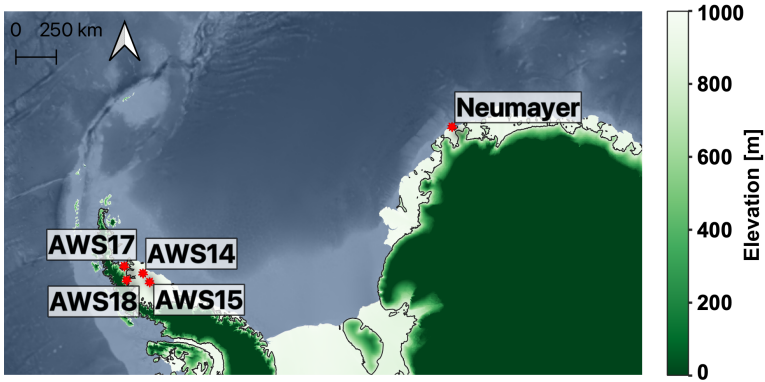
The relatively coarse spatial resolution in RCMs is insufficient for accurately capturing small-scale variations in surface melt across the Antarctic Ice Sheet. In response, we adapted the super-resolution architecture of SRResNet with physical constraints to create SUPREME, a physically-constrained super-resolution model that incorporates remote sensing data—specifically albedo and elevation—into the architecture. Using the SUPREME architecture, the surface melt component from RACMO at 27 km was downscaled to 5.5 km resolution. SUPREME achieved excellent out-of-sample performance within the training region, encompassing the Antarctic Peninsula, as validated by comparisons with AWS and RACMO 5.5 km. Outside the training region, SUPREME exhibited year-to-year variations that closely mirrored those of RACMO 27 km for individual ice shelves and on an Antarctic-wide scale, while also providing additional spatial details absent in RACMO 27 km. Moreover, comparing SUPREME with other melt products, like RACMO 2 km, QuikSCAT, PMW remote sensing, and optical remote sensing, showed similar melt patterns. This study underscores the potential of multi-image super-resolution in downscaling climate variables. Beyond the input features and model architecture examined in this research, numerous other combinations deserve exploration to further enhance the resolution of RCMs.

4.7. SUPPLEMENTARY MATERIALS

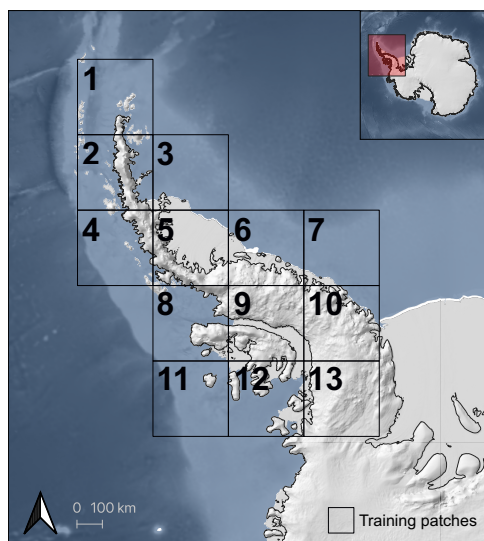


4

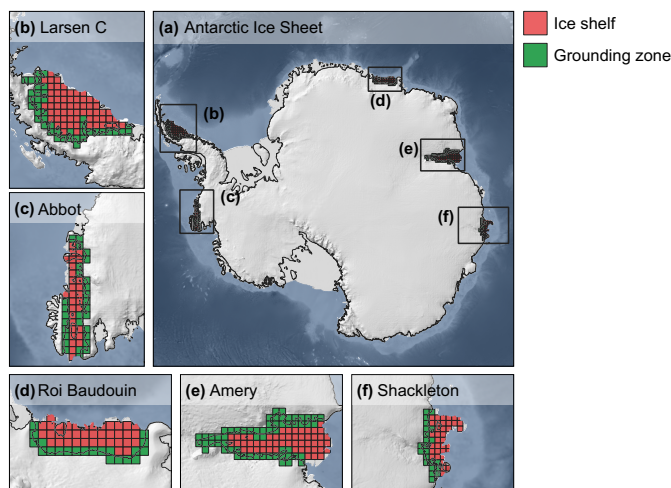
Supplementary Figure 4.1: Relation between RACMO 27 km and RACMO 5.5 km surface melt. The red line indicates the regression line, while the black dashed line shows the 1:1 line, highlighting RACMO 5.5 km's tendency to underestimate surface melt compared to RACMO 27 km. RMSE and bias are in mm w.e. yr⁻¹.



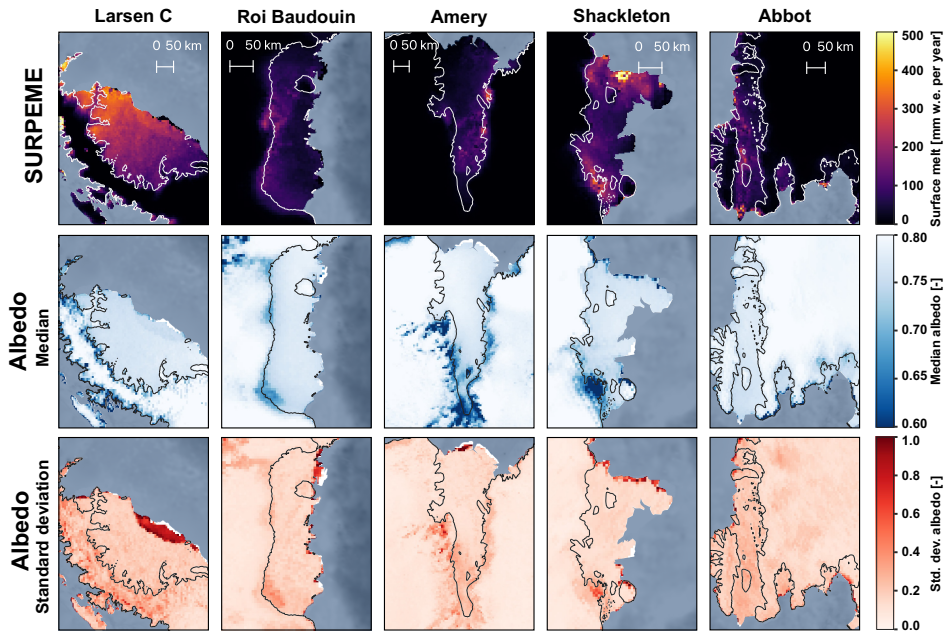
Supplementary Figure 4.2: Locations of the five AWS used in this study. For additional details on the AWS, see Jakobs *et al.* (2020). Elevation in the background map is from the Reference Elevation Model of Antarctica (REMA) (Howat *et al.*, 2019).



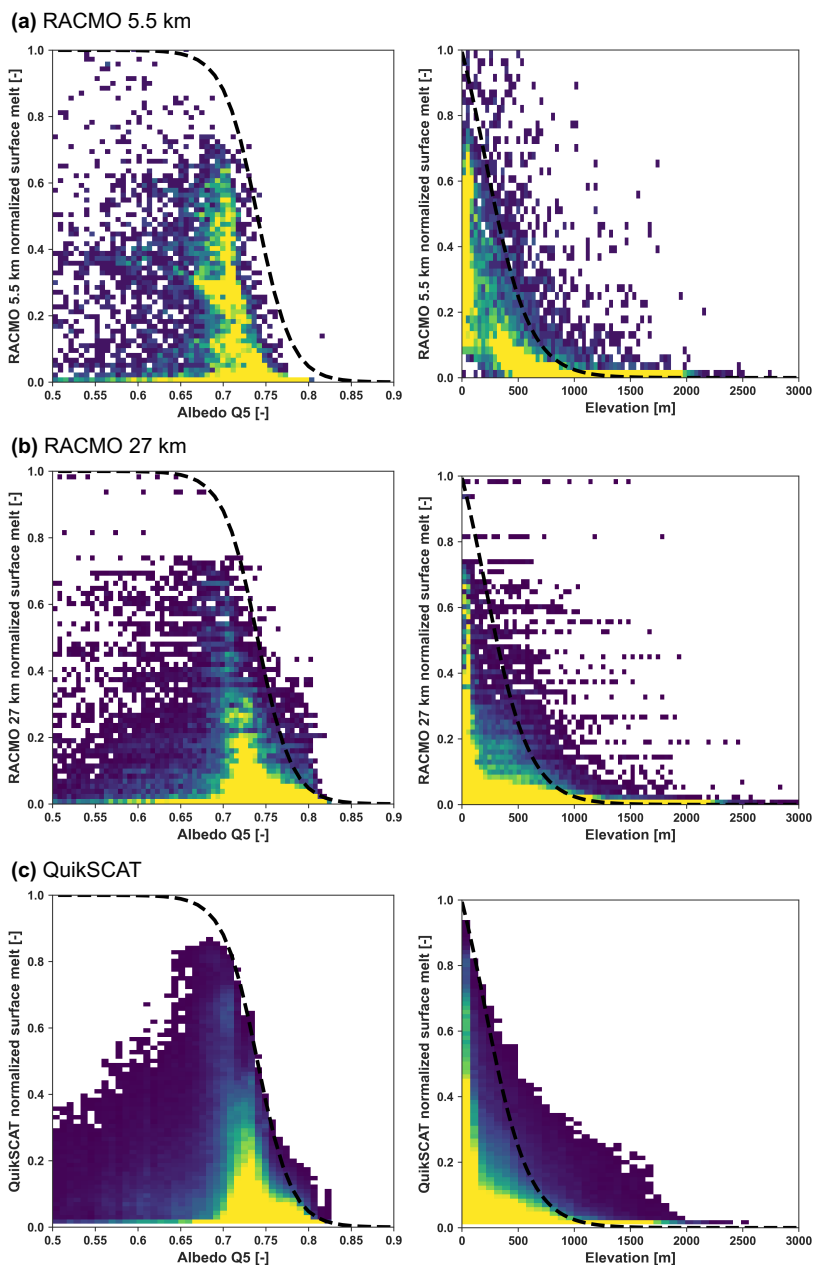
Supplementary Figure 4.3: Location of the thirteen patches used in training the super-resolution models, all positioned on the Antarctic Peninsula. The red box in the upper right corner highlights the specific location of the Antarctic Peninsula, with a background image of the Cryosat-2 elevation map (Helm *et al.*, 2014).



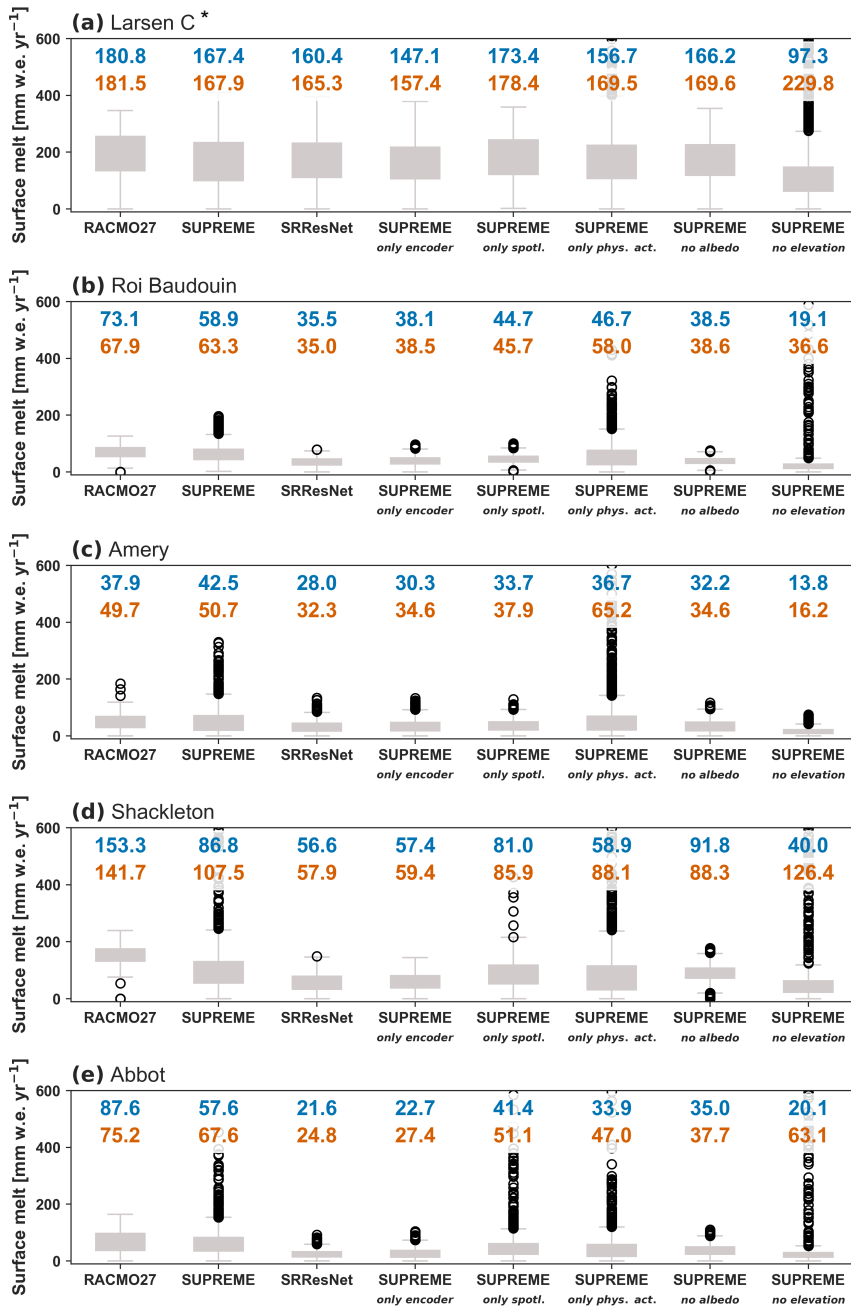
Supplementary Figure 4.4: Overview of the five highlighted regions in this study, featuring an Antarctic-wide perspective (a) along with specific views of Larsen C (b), Abbot (c), Roi Baudouin (d), Amery (e), and Shackleton (f) ice shelves. The pixels in this figure have a 27 km resolution matching the RACMO 27 km resolution, and for data with 5.5 km resolution (albedo, elevation, RACMO 5.5 km), all data within these pixels were considered. Region-wide assessments involved selecting all pixels, ice shelf-wide assessments only considered the red pixels, and grounding zone assessments focused solely on the green ones.



Supplementary Figure 4.5: The mean surface melt for SUPREME (a), along with the median (b) and standard deviation (c) of albedo for 2001–2019. Caution is advised when interpreting the datasets marked with an asterisk (i.e., Larsen C), as a part of these data were used in training SUPREME.



Supplementary Figure 4.6: The two physical activation functions (albedo Q5 and elevation) implemented in the SUPREME architecture are depicted by black dashed lines. The weighted scatter plot represents normalized surface melt data for (a) RACMO 5.5 km between 2001–2019 on the Antarctic Peninsula, (b) RACMO 27 km between 2001–2019 Antarctic-wide, and (c) QuikSCAT between 2001 and 2009 Antarctic-wide.



Supplementary Figure 4.7: Boxplots of yearly average surface melt for the melt seasons of 2001–2019 at every pixel across different model architectures, with median (in blue) and mean (in orange) values in mm w.e. yr⁻¹. Corresponding spatial maps are provided in Figure 4.10, and the spatial extents analyzed are shown in Supplementary Figure 4.4. Caution is advised when interpreting the datasets marked with an asterisk (i.e., Larsen C in panel a), as a part of these data were used in training SUPREME.

Table 4.1: Analysis of the yearly average RMSE and bias of SUPREME compared to RACMO 5.5 km and RACMO 27 km within the training period (2001–2006) and the subsequent period (2007–2019). RMSE and bias are in mm w.e. yr^{-1} . The spatial extents analyzed are shown in Supplementary Figure 4.4.

| (a) Data used during training (2001–2006) | | | |
|---|------|------|-------|
| Comparison | RMSE | Bias | R^2 |
| SUPREME vs RACMO 5.5 km (Antarctic Peninsula) | 4.8 | −1.4 | 0.96 |
| SUPREME vs RACMO 27 km (Antarctic Peninsula) | 4.4 | −3.4 | 0.99 |
| SUPREME vs RACMO 5.5 km (Larsen C) | 2.6 | −0.7 | 0.89 |
| SUPREME vs RACMO 27 km (Larsen C) | 1.6 | −1.2 | 0.97 |

| (b) Data not used during training (2007–2019) | | | |
|---|------|------|-------|
| Comparison | RMSE | Bias | R^2 |
| SUPREME vs RACMO 5.5 km (Antarctic Peninsula) | 5.5 | 4.5 | 0.84 |
| SUPREME vs RACMO 27 km (Antarctic Peninsula) | 2.8 | −2.1 | 0.96 |
| SUPREME vs RACMO 5.5 km (Larsen C) | 2.5 | 1.8 | 0.73 |
| SUPREME vs RACMO 27 km (Larsen C) | 1.5 | −1.1 | 0.93 |

Table 4.2: Antarctic-wide performance metrics of deep learning model architectures compared to RACMO 27 km. RMSE and bias are in mm w.e. yr^{-1} .

| Model architecture | RMSE | Bias | R^2 |
|---|------|------|-------|
| SUPREME | 32.1 | 6.7 | 0.77 |
| SRResNet | 33.0 | 9.1 | 0.79 |
| SUPREME _{only encoder} | 32.5 | 8.1 | 0.80 |
| SUPREME _{only spotlighter} | 54.5 | −1.6 | 0.51 |
| SUPREME _{only physical activation} | 53.3 | 2.06 | 0.59 |
| SUPREME _{no albedo} | 32.1 | 8.4 | 0.80 |
| SUPREME _{no elevation} | 60.4 | 8.4 | 0.41 |

BIBLIOGRAPHY

- Abram, N. J., Mulvaney, R., Wolff, E. W., Triest, J., Kipfstuhl, S., Trusel, L. D., Vimeux, F., Fleet, L., & Arrowsmith, C. (2013). Acceleration of snow melt in an Antarctic Peninsula ice core during the twentieth century. *Nature Geoscience*, 6(5), 404–411.
- Agosta, C., Amory, C., Kittel, C., Orsi, A., Favier, V., Gallée, H., Van den Broeke, M. R., Lenaerts, J., van Wessem, J. M., Van de Berg, W. J., et al. (2019). Estimation of the Antarctic surface mass balance using the regional climate model MAR (1979–2015) and identification of dominant processes. *The Cryosphere*, 13(1), 281–296.
- Ahmed, K. F., Wang, G., Silander, J., Wilson, A. M., Allen, J. M., Horton, R., & Anyah, R. (2013). Statistical downscaling and bias correction of climate model outputs for climate change impact assessment in the US northeast. *Global and Planetary Change*, 100, 320–332.
- Arthur, J. F., Stokes, C. R., Jamieson, S. S., Rachel Carr, J., Leeson, A. A., & Verjans, V. (2022). Large interannual variability in supraglacial lakes around East Antarctica. *Nature communications*, 13(1), 1–12.
- Banwell, A. F., & Macayeal, D. R. (2015). Ice-shelf fracture due to viscoelastic flexure stress induced by fill/drain cycles of supraglacial lakes. *Antarctic Science*, 27(6), 587–597.
- Banwell, A. F., Wever, N., Dunmire, D., & Picard, G. (2023). Quantifying Antarctic-Wide Ice-Shelf Surface Melt Volume Using Microwave and Firn Model Data: 1980 to 2021. *Geophysical Research Letters*, 50(12), e2023GL102744.
- Banwell, A. F., Willis, I. C., Macdonald, G. J., Goodsell, B., & MacAyeal, D. R. (2019). Direct measurements of ice-shelf flexure caused by surface meltwater ponding and drainage. *Nature communications*, 10(1), 1–10.
- Box, J. E., & Rinke, A. (2003). Evaluation of Greenland ice sheet surface climate in the HIRHAM regional climate model using automatic weather station data. *Journal of Climate*, 16(9), 1302–1319.
- Braakmann-Folgmann, A., Shepherd, A., Gerrish, L., Izzard, J., & Ridout, A. (2022). Observing the disintegration of the A68A iceberg from space. *Remote Sensing of Environment*, 270, 112855.
- Burgard, C., Jourdain, N. C., Mathiot, P., Smith, R. S., Schäfer, R., Caillet, J., Finn, T. S., & Johnson, J. E. (2023). Emulating Present and Future Simulations of Melt Rates at the Base of Antarctic Ice Shelves With Neural Networks. *Journal of Advances in Modeling Earth Systems*, 15(12).
- Cai, Y., Wan, F., Lang, S., Cui, X., & Yao, Z. (2023). Multi-branch deep neural network for bed topography of Antarctica super-resolution: Reasonable integration of multiple remote sensing data. *Remote Sensing*, 15(5), 1359.
- Das, S. B., & Alley, R. B. (2008). Rise in frequency of surface melting at Siple Dome through the Holocene: Evidence for increasing marine influence on the climate of West Antarctica. *Journal of Geophysical Research: Atmospheres*, 113(D2).
- Davison, B. J., Hogg, A. E., Gourmelen, N., Jakob, L., Wuite, J., Nagler, T., Greene, C. A., Andreasen, J., & Engdahl, M. E. (2023). Annual mass budget of Antarctic ice shelves from 1997 to 2021. *Science Advances*, 9(41), eadi0186.

- Dell, R., Banwell, A. E., Willis, I. C., Arnold, N. S., Halberstadt, A. R. W., Chudley, T. R., & Pritchard, H. D. (2022). Supervised classification of slush and ponded water on Antarctic ice shelves using Landsat 8 imagery. *Journal of Glaciology*, 68(268), 401–414.
- Dell, R., Willis, I., Arnold, N., Banwell, A., & de Roda Husman, S. (2024). Substantial contribution of slush to meltwater area across Antarctic ice shelves. *Nature Geoscience*, 1–7.
- de Roda Husman, S., Hu, Z., van Tiggelen, M., Dell, R., Bolibar, J., Lhermitte, S., Wouters, B., & Kuipers Munneke, P. (2024). Physically-informed super-resolution downscaling of Antarctic surface melt. *Journal of Advances in Modeling Earth Systems*, 16(7), e2023MS004212.
- de Roda Husman, S., Hu, Z., Wouters, B., Kuipers Munneke, P., Veldhuijsen, S., & Lhermitte, S. (2022). Remote Sensing of Surface Melt on Antarctica: Opportunities and Challenges. *IEEE Journal of Selected Topics in Applied Earth Observations and Remote Sensing*.
- de Roda Husman, S., Lhermitte, S., Bolibar, J., Izeboud, M., Hu, Z., Shukla, S., van der Meer, M., Long, D., & Wouters, B. (2024). A high-resolution record of surface melt on Antarctic ice shelves using multi-source remote sensing data and deep learning. *Remote Sensing of Environment*, 301, 113950.
- Dong, C., Loy, C. C., & Tang, X. (2016). Accelerating the super-resolution convolutional neural network. *Computer Vision–ECCV 2016: 14th European Conference, Amsterdam, The Netherlands, October 11–14, 2016, Proceedings, Part II 14*, 391–407.
- ECMWF. (2009). IFS Documentation CY33R1 – Part IV: Physical Processes [IFS Documentation].
- Ettema, J., Van den Broeke, M., Van Meijgaard, E., Van de Berg, W., Box, J., & Steffen, K. (2010). Climate of the Greenland ice sheet using a high-resolution climate model–Part 1: Evaluation. *The Cryosphere*, 4(4), 511–527.
- Fettweis, X., Box, J. E., Agosta, C., Amory, C., Kittel, C., Lang, C., van As, D., Machguth, H., & Gallée, H. (2017). Reconstructions of the 1900–2015 Greenland ice sheet surface mass balance using the regional climate MAR model. *The Cryosphere*, 11(2), 1015–1033.
- Foken, T. (2021). *Springer handbook of atmospheric measurements*. Springer Nature.
- Franco, B., Fettweis, X., Lang, C., & Erpicum, M. (2012). Impact of spatial resolution on the modelling of the Greenland ice sheet surface mass balance between 1990–2010, using the regional climate model MAR. *The Cryosphere*, 6(3), 695–711.
- Fyke, J., Sergienko, O., Löfverström, M., Price, S., & Lenaerts, J. T. (2018). An overview of interactions and feedbacks between ice sheets and the Earth system. *Reviews of Geophysics*, 56(2), 361–408.
- Gallée, H., Agosta, C., Gentil, L., Favier, V., & Krinner, G. (2011). A downscaling approach toward high-resolution surface mass balance over Antarctica. *Surveys in geophysics*, 32(4), 507–518.
- Ghilain, N., Vannitsem, S., Dalaiden, Q., Goosse, H., De Cruz, L., & Wei, W. (2022). Large ensemble of downscaled historical daily snowfall from an earth system model to 5.5 km resolution over Dronning Maud Land, Antarctica. *Earth System Science Data*, 14(4), 1901–1916.
- Giesen, R., & Oerlemans, J. (2012). Calibration of a surface mass balance model for global-scale applications. *The Cryosphere*, 6(6), 1463–1481.
- Gilbert, E., & Kittel, C. (2021). Surface melt and runoff on Antarctic ice shelves at 1.5 C, 2 C, and 4 C of future warming. *Geophysical Research Letters*, 48(8), e2020GL091733.
- Goodfellow, I., Pouget-Abadie, J., Mirza, M., Xu, B., Warde-Farley, D., Ozair, S., Courville, A., & Bengio, Y. (2014). Generative adversarial nets. *Advances in neural information processing systems*, 27.

- Gorelick, N., Hancher, M., Dixon, M., Ilyushchenko, S., Thau, D., & Moore, R. (2017). Google Earth Engine: Planetary-scale geospatial analysis for everyone. *Remote sensing of Environment*, 202, 18–27.
- Greene, C. A., Gardner, A. S., Schlegel, N.-J., & Fraser, A. D. (2022). Antarctic calving loss rivals ice-shelf thinning. *Nature*, 609(7929), 948–953.
- Gudmundsson, G. H., Paolo, F. S., Adusumilli, S., & Fricker, H. A. (2019). Instantaneous Antarctic ice sheet mass loss driven by thinning ice shelves. *Geophysical Research Letters*, 46(23), 13903–13909.
- Guidotti, R., Monreale, A., Ruggieri, S., Turini, F., Giannotti, F., & Pedreschi, D. (2018). A survey of methods for explaining black box models. *ACM computing surveys (CSUR)*, 51(5), 1–42.
- Hanna, E., Huybrechts, P., Cappelen, J., Steffen, K., Bales, R. C., Burgess, E., McConnell, J. R., Peder Steffensen, J., Van den Broeke, M., Wake, L., et al. (2011). Greenland Ice Sheet surface mass balance 1870 to 2010 based on Twentieth Century Reanalysis, and links with global climate forcing. *Journal of Geophysical Research: Atmospheres*, 116(D24).
- Hanna, E., Huybrechts, P., Janssens, I., Cappelen, J., Steffen, K., & Stephens, A. (2005). Runoff and mass balance of the Greenland ice sheet: 1958–2003. *Journal of Geophysical Research: Atmospheres*, 110(D13).
- Hanna, E., Huybrechts, P., Steffen, K., Cappelen, J., Huff, R., Shuman, C., Irvine-Fynn, T., Wise, S., & Griffiths, M. (2008). Increased runoff from melt from the Greenland Ice Sheet: a response to global warming. *Journal of Climate*, 21(2), 331–341.
- He, K., Zhang, X., Ren, S., & Sun, J. (2016). Deep residual learning for image recognition. *Proceedings of the IEEE conference on computer vision and pattern recognition*, 770–778.
- Helm, V., Humbert, A., & Miller, H. (2014). Elevation and elevation change of Greenland and Antarctica derived from CryoSat-2. *The Cryosphere*, 8(4), 1539–1559.
- Hourdin, F., Mauritsen, T., Gettelman, A., Golaz, J.-C., Balaji, V., Duan, Q., Folini, D., Ji, D., Klocke, D., Qian, Y., et al. (2017). The art and science of climate model tuning. *Bulletin of the American Meteorological Society*, 98(3), 589–602.
- Howat, I. M., Porter, C., Smith, B. E., Noh, M.-J., & Morin, P. (2019). The reference elevation model of Antarctica. *The Cryosphere*, 13(2), 665–674.
- Hu, Z., Sun, Y., Kuipers Munneke, P., Lhermitte, S., & Zhu, X. (2022). Towards a spatially transferable super-resolution model for downscaling Antarctic surface melt. *NeurIPS 2022 Workshop on Tackling Climate Change with Machine Learning*.
- IMBIE. (2018). Mass balance of the Antarctic Ice Sheet from 1992 to 2017. *Nature*, 558(7709), 219–222.
- Jakobs, C. L., Reijmer, C. H., Kuipers Munneke, P., König-Langlo, G., & Van den Broeke, M. R. (2019). Quantifying the snowmelt–albedo feedback at Neumayer Station, East Antarctica. *The Cryosphere*, 13(5), 1473–1485.
- Jakobs, C. L., Reijmer, C. H., Smeets, C. P., Trusel, L. D., Van de Berg, W. J., Van den Broeke, M. R., & van Wessem, J. M. (2020). A benchmark dataset of in situ Antarctic surface melt rates and energy balance. *Journal of Glaciology*, 66(256), 291–302.
- Jiang, J., Shu, Y., Wang, J., & Long, M. (2022). Transferability in deep learning: A survey. *arXiv preprint arXiv:2201.05867*.
- Kawulok, M., Benecki, P., Piechaczek, S., Hrynczenko, K., Kostrzewa, D., & Nalepa, J. (2019). Deep learning for multiple-image super-resolution. *IEEE Geoscience and Remote Sensing Letters*, 17(6), 1062–1066.

- Kingslake, J., Ely, J. C., Das, I., & Bell, R. E. (2017). Widespread movement of meltwater onto and across Antarctic ice shelves. *Nature*, 544(7650), 349–352.
- Kuipers Munneke, P., Luckman, A., Bevan, S., Smeets, C., Gilbert, E., Van den Broeke, M., Wang, W., Zender, C., Hubbard, B., Ashmore, D., et al. (2018). Intense winter surface melt on an Antarctic ice shelf. *Geophysical Research Letters*, 45(15), 7615–7623.
- Kuipers Munneke, P., Picard, G., Van den Broeke, M., Lenaerts, J., & Van Meijgaard, E. (2012). Insignificant change in Antarctic snowmelt volume since 1979. *Geophysical Research Letters*, 39(1).
- Kuipers Munneke, P., Van den Broeke, M., King, J., Gray, T., & Reijmer, C. (2012). Near-surface climate and surface energy budget of Larsen C ice shelf, Antarctic Peninsula. *The Cryosphere*, 6(2), 353–363.
- Kuipers Munneke, P., Van den Broeke, M., Lenaerts, J., Flanner, M., Gardner, A., & Van de Berg, W. (2011). A new albedo parameterization for use in climate models over the Antarctic Ice Sheet. *Journal of Geophysical Research: Atmospheres*, 116(D5).
- Kuipers Munneke, P., Ligtenberg, S. R., Van den Broeke, M. R., & Vaughan, D. G. (2014). Firn air depletion as a precursor of antarctic ice-shelf collapse. *Journal of Glaciology*, 60(220), 205–214.
- La Rocca, M., & Perna, C. (2022). Opening the black box: Bootstrapping sensitivity measures in neural networks for interpretable machine learning. *Stats*, 5(2), 440–457.
- Lachlan-Cope, T. (2010). Antarctic clouds. *Polar Research*, 29(2), 150–158.
- Ledig, C., Theis, L., Huszár, F., Caballero, J., Cunningham, A., Acosta, A., Aitken, A., Tejani, A., Totz, J., Wang, Z., et al. (2017). Photo-realistic single image super-resolution using a generative adversarial network. *Proceedings of the IEEE conference on computer vision and pattern recognition*, 4681–4690.
- Lenaerts, J., Lhermitte, S., Drews, R., Ligtenberg, S., Berger, S., Helm, V., Smeets, C., Van den Broeke, M., Van de Berg, W. J., Van Meijgaard, E., et al. (2017). Meltwater produced by wind–albedo interaction stored in an East Antarctic ice shelf. *Nature climate change*, 7(1), 58–62.
- Lenaerts, J., Van den Broeke, M., Déry, S., Van Meijgaard, E., Van de Berg, W., Palm, S. P., & Sanz Rodrigo, J. (2012). Modeling drifting snow in Antarctica with a regional climate model: 1. Methods and model evaluation. *Journal of Geophysical Research: Atmospheres*, 117(D5).
- Leong, W. J., & Horgan, H. J. (2020). DeepBedMap: A deep neural network for resolving the bed topography of Antarctica. *The Cryosphere*, 14(11), 3687–3705.
- Li, W., Ni, L., Li, Z.-l., Duan, S.-B., & Wu, H. (2019). Evaluation of machine learning algorithms in spatial downscaling of MODIS land surface temperature. *IEEE Journal of Selected Topics in Applied Earth Observations and Remote Sensing*, 12(7), 2299–2307.
- Nihashi, S., & Ohshima, K. I. (2015). Circumpolar mapping of Antarctic coastal polynyas and landfast sea ice: Relationship and variability. *Journal of climate*, 28(9), 3650–3670.
- Noël, B., Van de Berg, W. J., Machguth, H., Lhermitte, S., Howat, I., Fettweis, X., & Van den Broeke, M. R. (2016). A daily, 1 km resolution data set of downscaled Greenland ice sheet surface mass balance (1958–2015). *The Cryosphere*, 10(5), 2361–2377.
- Noël, B., van Wessem, J. M., Wouters, B., Trusel, L., Lhermitte, S., & Van den Broeke, M. R. (2023). Higher Antarctic ice sheet accumulation and surface melt rates revealed at 2 km resolution. *Nature Communications*, 14(1), 7949.
- Petrou, Z. I., Xian, Y., & Tian, Y. (2018). Towards breaking the spatial resolution barriers: An optical flow and super-resolution approach for sea ice motion estimation. *ISPRS journal of photogrammetry and remote sensing*, 138, 164–175.

- Picard, G., & Fily, M. (2006). Surface melting observations in Antarctica by microwave radiometers: Correcting 26-year time series from changes in acquisition hours. *Remote sensing of environment*, 104(3), 325–336.
- Reddy, S., Reddy, K. T., & Vallikumari, V. (2018). Optimization of deep learning using various optimizers, loss functions and dropout. *Int. J. Recent Technol. Eng*, 7, 448–455.
- Savage, N. (2022). Breaking into the black box of artificial intelligence. *Nature*.
- Scambos, T. A., Fricker, H. A., Liu, C.-C., Bohlander, J., Fastook, J., Sargent, A., Massom, R., & Wu, A.-M. (2009). Ice shelf disintegration by plate bending and hydro-fracture: Satellite observations and model results of the 2008 Wilkins ice shelf break-ups. *Earth and Planetary Science Letters*, 280(1-4), 51–60.
- Schaaf, C. B., Gao, F., Strahler, A. H., Lucht, W., Li, X., Tsang, T., Strugnell, N. C., Zhang, X., Jin, Y., Muller, J.-P., et al. (2002). First operational BRDF, albedo nadir reflectance products from MODIS. *Remote sensing of Environment*, 83(1-2), 135–148.
- Schmidt, G. A., Bader, D., Donner, L. J., Elsaesser, G. S., Golaz, J.-C., Hannay, C., Molod, A., Neale, R. B., & Saha, S. (2017). Practice and philosophy of climate model tuning across six US modeling centers. *Geoscientific Model Development*, 10(9), 3207–3223.
- Scholz, F. W., & Stephens, M. A. (1987). K-sample Anderson–Darling tests. *Journal of the American Statistical Association*, 82(399), 918–924.
- Shepherd, A., Ivins, E. R., Barletta, V. R., Bentley, M. J., Bettadpur, S., Briggs, K. H., Bromwich, D. H., Forsberg, R., Galin, N., Horwath, M., et al. (2012). A reconciled estimate of ice-sheet mass balance. *Science*, 338(6111), 1183–1189.
- Shi, W., Caballero, J., Huszár, F., Totz, J., Aitken, A. P., Bishop, R., Rueckert, D., & Wang, Z. (2016). Real-time single image and video super-resolution using an efficient sub-pixel convolutional neural network. *Proceedings of the IEEE conference on computer vision and pattern recognition*, 1874–1883.
- Smeets, P. C. J. P., Kuipers Munneke, P., van As, D., Van den Broeke, M. R., Boot, W., Oerlemans, H., Snellen, H., Reijmer, C. H., & van de Wal, R. S. W. (2018). The K-transect in west Greenland: Automatic weather station data (1993–2016). *Arctic, Antarct. Alp. Res.*, 50(1), S100002.
- Stokes, C. R., Sanderson, J. E., Miles, B. W., Jamieson, S. S., & Leeson, A. A. (2019). Widespread distribution of supraglacial lakes around the margin of the East Antarctic Ice Sheet. *Scientific reports*, 9(1), 13823.
- Tedesco, M., Colosio, P., Fettweis, X., & Cervone, G. (2023). A computationally efficient statistically downscaled 100 m resolution Greenland product from the regional climate model MAR. *The Cryosphere Discussions*, 2023, 1–27.
- Thiemeßl, M. J., Gobiet, A., & Heinrich, G. (2012). Empirical-statistical downscaling and error correction of regional climate models and its impact on the climate change signal. *Climatic Change*, 112, 449–468.
- Tollenaar, V., Zekollari, H., Lhermitte, S., Tax, D. M., Debaille, V., Goderis, S., Claey, P., & Pattyn, F. (2022). Unexplored Antarctic meteorite collection sites revealed through machine learning. *Science advances*, 8(4), eabj8138.
- Torinesi, O., Fily, M., & Genthon, C. (2003). Variability and trends of the summer melt period of Antarctic ice margins since 1980 from microwave sensors. *Journal of Climate*, 16(7), 1047–1060.
- Trusel, L., Frey, K. E., & Das, S. B. (2012). Antarctic surface melting dynamics: Enhanced perspectives from radar scatterometer data. *Journal of Geophysical Research: Earth Surface*, 117(F2).

- Trusel, L., Frey, K. E., Das, S. B., Karnauskas, K. B., Kuipers Munneke, P., Van Meijgaard, E., & Van den Broeke, M. R. (2015). Divergent trajectories of Antarctic surface melt under two twenty-first-century climate scenarios. *Nature Geoscience*, 8(12), 927–932.
- Trusel, L., Frey, K. E., Das, S. B., Kuipers Munneke, P., & Van den Broeke, M. (2013). Satellite-based estimates of Antarctic surface meltwater fluxes. *Geophysical Research Letters*, 40(23), 6148–6153.
- Undén, P., Rontu, L., Jarvinen, H., Lynch, P., Calvo Sánchez, F. J., Cats, G., Cuxart, J., Eerola, K., Fortelius, C., García-Moya, J. A., et al. (2002). HIRLAM-5 scientific documentation.
- Van de Berg, W. J., van Meijgaard, E., & van Uft, L. H. (2020). The added value of high resolution in estimating the surface mass balance in southern Greenland. *The Cryosphere*, 14(6), 1809–1827.
- van der Meer, M., de Roda Husman, S., & Lhermitte, S. (2023). Deep learning regional climate model emulators: A comparison of two downscaling training frameworks. *Journal of Advances in Modeling Earth Systems*, 15(6), e2022MS003593.
- Vandal, T., Kodra, E., Ganguly, S., Michaelis, A., Nemani, R., & Ganguly, A. R. (2017). DeepSD: Generating high resolution climate change projections through single image super-resolution. *Proceedings of the 23rd acm sigkdd international conference on knowledge discovery and data mining*, 1663–1672.
- van Wessem, J. M., Ligtenberg, S. R. M., Reijmer, C. H., Van de Berg, W. J., Van den Broeke, M. R., Barrand, N. E., Thomas, E. R., Turner, J., Wuite, J., Scambos, T. A., & van Meijgaard, E. (2016). The modelled surface mass balance of the Antarctic Peninsula at 5.5 km horizontal resolution. *The Cryosphere*, 10(1), 271–285.
- van Wessem, J. M., Reijmer, C., Lenaerts, J., Van de Berg, W., Van den Broeke, M., & Van Meijgaard, E. (2014). Updated cloud physics in a regional atmospheric climate model improves the modelled surface energy balance of Antarctica. *The Cryosphere*, 8(1), 125–135.
- van Wessem, J. M., Reijmer, C., Morlighem, M., Mouginot, J., Rignot, E., Medley, B., Joughin, I., Wouters, B., Depoorter, M., Bamber, J., et al. (2014). Improved representation of East Antarctic surface mass balance in a regional atmospheric climate model. *Journal of Glaciology*, 60(222), 761–770.
- van Wessem, J. M., Van de Berg, W. J., Noël, B. P., Van Meijgaard, E., Amory, C., Birnbaum, G., Jakobs, C. L., Krüger, K., Lenaerts, J., Lhermitte, S., et al. (2018). Modelling the climate and surface mass balance of polar ice sheets using RACMO2–Part 2: Antarctica (1979–2016). *The Cryosphere*, 12(4), 1479–1498.
- Wessel, B., Huber, M., Wohlfart, C., Bertram, A., Osterkamp, N., Marschalk, U., Gruber, A., Reuß, F., Abdullahi, S., Georg, I., et al. (2021). TanDEM-X PolarDEM 90 m of Antarctica: Generation and error characterization. *The Cryosphere*, 15(11), 5241–5260.
- Wiesenekker, J. M., Kuipers Munneke, P., Van den Broeke, M. R., & Smeets, C. P. (2018). A multidecadal analysis of Föhn winds over Larsen C ice shelf from a combination of observations and modeling. *Atmosphere*, 9(5), 172.
- Yang, C.-Y., Ma, C., & Yang, M.-H. (2014). Single-image super-resolution: A benchmark. *Computer Vision–ECCV 2014: 13th European Conference, Zurich, Switzerland, September 6–12, 2014, Proceedings, Part IV* 13, 372–386.
- Zheng, L., Cheng, X., Shang, X., Chen, Z., Liang, Q., & Wang, K. (2022). Greenland Ice Sheet daily surface melt flux observed from space. *Geophysical Research Letters*, 49(6), e2021GL096690.

5

DRAINING OR REFREEZING? A SPATIOTEMPORAL DEEP LEARNING MODEL USING SENTINEL-1 FOR TRACKING MELTWATER LAKE EVOLUTION ON ANTARCTICA

**Sophie de Roda Husman, Stef Lhermitte, Theofani
Psomouli, Meike van Noord, Bert Wouters**

This chapter has not been published.

ABSTRACT

Antarctic ice shelves are increasingly at risk due to ocean warming and atmospheric warming, with the latter leading to surface melting and the formation of meltwater lakes. While some lakes refreeze, others drain into fractures, potentially destabilizing ice shelves and raising sea levels. Traditional monitoring using optical satellite imagery is limited by cloud cover, hindering the tracking of lake changes. This study introduces ConvLSTM, a spatiotemporal deep learning model designed to analyze lake evolution throughout a melt season. Initially trained on Greenland data from earlier studies that identified refreezing and draining lakes, the model was then applied to Antarctica. Using optical imagery to identify lake locations, the trained ConvLSTM model used Sentinel-1 time series data to predict lake evolution and detect refreezing and draining lakes during both the strong (2019–2020) and weak (2020–2021) melt seasons. During the 2019–2020 season, 1346 lakes were identified (65% refreezing, 35% draining), and in the 2020–2021 season, 1599 lakes were detected (99% refreezing, 1% draining). No clear links were found between lake behaviors and ice shelf parameters, indicating the need for further research and model refinement. This study marks an initial step in leveraging deep learning and Sentinel-1 data to monitor supraglacial lake evolution on Antarctic ice shelves.

5.1. INTRODUCTION

SUPRAGLACIAL lakes form when meltwater collects in surface depressions on glaciers and ice sheets. These lakes have been widespread on the floating ice shelves surrounding the Antarctic continent for decades (Bell *et al.*, 2018; Glasser & Scambos, 2008; Kingslake *et al.*, 2017). In Antarctica, supraglacial lakes typically refreeze at the end of the melt season (Arthur *et al.*, 2020). However, there are instances where lakes slowly or rapidly drain (Arthur *et al.*, 2020; Leeson *et al.*, 2020; Trusel *et al.*, 2022).

Refreezing often starts with the formation of ice lids that grow outward from the lake centers, eventually leading to complete refreezing (Arthur *et al.*, 2020; Langley *et al.*, 2016); however, in some cases, lakes may maintain a liquid water core (Dunmire *et al.*, 2020; Koenig *et al.*, 2015; Law *et al.*, 2020; Miles *et al.*, 2017). When meltwater refreezes in situ, there is no mass change at the surface. On the other hand, the drainage of lakes can significantly impact ice flow rates and ice shelf stability.

Drainage can occur slowly over the ice surface through supraglacial channels or rapidly through the ice via crevasses driven by the weight of the water, a process known as hydrofracture (Nye, 1957). In Greenland, draining lakes route water to the base of the ice sheet, increasing hydraulic pressure and temporarily lifting the ice off the bed, enhancing basal sliding and ice flow rates (Christoffersen *et al.*, 2018; Maier *et al.*, 2023; Tedesco *et al.*, 2013; Tuckett *et al.*, 2019; Zwally *et al.*, 2002). Although there is no direct evidence of hydrofracturing beneath lakes on grounded Antarctic ice (Bell *et al.*, 2018), draining lakes can still pose a hazard to ice-shelf stability by acting as concentrated loads that flex and weaken the floating ice (Banwell *et al.*, 2013; MacAyeal & Sergienko, 2013; Scambos *et al.*, 2009). Numerical models, laboratory simulations, and in-situ observations suggest that the loading and unloading associated with lake filling and draining lead to ice shelf flexing and fracture formation both within and outside lake basins (Banwell *et al.*, 2013, 2024; Beltaos, 2002). A modeling study by Banwell *et al.* (2013) suggested that if these fractures intersect other nearby lake basins, a chain reaction of further lake-drainage events may be initiated, potentially contributing to large-scale ice shelf break-up. Ice shelves that have undergone significant thinning due to surface and ocean-driven ablation at the ice-shelf base (Gudmundsson *et al.*, 2019; Pritchard *et al.*, 2012; Reese *et al.*, 2018) may be particularly vulnerable to break-up due to hydrofracturing (Banwell *et al.*, 2013; Pattyn *et al.*, 2018; Scambos *et al.*, 2000). Therefore, monitoring lake dynamics in Antarctica throughout the melt season is increasingly important, including refreezing and draining events.

Most studies on the dynamics of supraglacial lakes are based on the analysis of optical satellite imagery (Langley *et al.*, 2016; Leeson *et al.*, 2013; McMillan *et al.*, 2007; Williamson *et al.*, 2018). However, optical sensors have limitations as they cannot capture images through clouds or in darkness, restricting the number of useful scenes available for analysis. Radar imagery can overcome some of these limitations. Several studies on the Greenland Ice Sheet have demonstrated that Synthetic Aperture Radar (SAR) data from Sentinel-1 can be effectively used to identify lake drainages (Benedek & Willis, 2021; Miles *et al.*, 2017; D. Zhu *et al.*, 2023).

Supraglacial lakes in SAR imagery appear as low backscatter because liquid water increases the absorption of radar signals and also contributes to surface forward scattering. As the lake surface starts to freeze, the scattering caused by bubbles trapped in the ice increases, resulting in higher backscatter intensity. Similarly, lake drainage events have been observed to follow a pattern of low to high backscatter, however, the increase in backscatter is more abrupt and intense than refreezing lakes due to the rough, debris-laden lake bottom after drainage (Benedek & Willis, 2021; Johansson & Brown, 2012; Miles *et al.*, 2017). While Benedek and Willis (2021) used a statistical method based on Z-score, and Miles *et al.* (2017) used a method based on Sentinel-1 thresholds, these approaches have shown efficacy only for a few individual lakes. Implementing these methods on a continent-wide scale is challenging due to several factors that affect radar backscatter, including speckle noise and varying viewing angles, which contribute to the heterogeneity of the Sentinel-1 time series (White *et al.*, 2015).

Deep learning is effective at capturing non-linear patterns (LeCun *et al.*, 2015), making it valuable in fields such as weather nowcasting (Shi *et al.*, 2015), traffic flow prediction (Lv *et al.*, 2014), medical imaging (Litjens *et al.*, 2017), and stock prediction (Ding *et al.*, 2015), where handling complex, non-linear data is essential. In this research, a ConvLSTM (Convolutional Long Short-Term Memory) model shows promise for learning both spatial and temporal information from Sentinel-1 time series. ConvLSTM combines two deep learning techniques: Convolutional Neural Networks (CNNs), which are good at identifying patterns in images, and LSTM networks, which are good at understanding sequences over time. By merging these two methods, ConvLSTM can track how features change in space and time simultaneously. This architecture is commonly used for tasks like object detection in videos (e.g., Song *et al.*, 2018), and similarly, it could be applied to analyze the evolution of meltwater lakes in Antarctica from Sentinel-1 time series, treating the data as a sequence of spatiotemporal frames.

Here, we develop a deep learning algorithm to classify the evolution of supraglacial lakes over a melt season (i.e., refreezing or draining) using Sentinel-1 data, guided by optical imagery to pinpoint lake locations. For this, we use a ConvLSTM model, which is able to learn both the spatial and temporal information from the Sentinel-1 time series. We train, validate, and test the algorithm on data from Greenland and subsequently apply it on an Antarctic-wide scale across two melt seasons: the relatively strong 2019–2020 melt season (e.g., Banwell *et al.*, 2021; Moussavi *et al.*, 2020) and the relatively weak 2020–2021 melt season (e.g., de Roda Husman *et al.*, 2024). Additionally, we assess various ice properties, such as lake area, lake volume, velocity, and thickness, to determine if there are discernible differences between refreezing and draining lakes.

5.2. DATA AND METHODS

5.2.1. IDENTIFYING LOCATIONS OF LAKES

We employ Sentinel-1 SAR data for our ConvLSTM deep learning model and, to reduce data download and processing, first identify all lake centroids. To train,

test, and validate the model, we use Sentinel-1 time series data from lakes on the Greenland Ice Sheet, leveraging its established role in prior research on supraglacial lake dynamics. The lake locations in Greenland are identified based on previously published studies. Once developed, the model is applied to Antarctica using Sentinel-1 data to predict lake behavior, with lake locations identified using optical imagery.

LAKES ON THE GREENLAND ICE SHEET

To collect the training and validation lake centroids, we use lake shapefiles provided by Zheng *et al.* (2023), which combine optical and SAR data to detect supraglacial lakes on a Greenland-wide scale. We use lakes from the 2021 melt season, identified as an average season within the analyzed melt seasons from 2017–2022 by Zheng *et al.* (2023). Employing Sentinel-2 (Level-1C) and Landsat 8 (Collection 2 Tier 2 TOA reflectance) imagery via Google Earth Engine (GEE), we filter for optical imagery for the lakes with clear visibility (at least 90% non-clouded). From the extensive inventory of supraglacial lakes identified by Zheng *et al.* (2023) (i.e., 5032 lakes in the 2021 melt season), we manually curate a subset showing distinct refreezing or draining patterns throughout the melt season. Due to limited resources, only 10% of Zheng's identified lakes are analyzed, and not all could be classified, as many were either obscured by clouds or difficult to categorize as draining or refreezing. The selection process, led by Sophie de Roda Husman and validated by co-authors Stef Lhermitte and Bert Wouters, results in a dataset comprising 64 refreezing and 49 draining lakes. This dataset, which includes lake centroids of draining and refreezing lakes, is split into training and validation sets in an 80:20 ratio.

For the testing data, we use an independent dataset from Glen *et al.* (2024), which was derived from Landsat-8 and Sentinel-2 imagery over the Greenland Ice Sheet, specifically focusing on the Russell/Leverett glacier catchment. Besides the outline of the lakes, this dataset includes drainages and refreezing labels. The lakes are from both the relatively weak 2018 and the relatively strong 2019 melt seasons, providing a robust evaluation framework for our model. We use all lakes identified by Glen *et al.* (2024), which equals to 250 refreezing lakes and 1760 draining lakes. Figure 5.1 provides an overview of the refreezing and draining lakes used for training, validation, and testing the model.

LAKES ON THE ANTARCTIC ICE SHEET

We use Sentinel-2 (Level-1C) data from GEE to identify the lakes on the Antarctic Ice Sheet for which we apply the trained ConvLSTM model. This approach allows us to run the model only on identified lake locations rather than across the entire Antarctic Ice Sheet. We filter all Sentinel-2 images during the Antarctic melt seasons from November to March of 2019–2020 and 2020–2021 by a maximum cloud coverage of 30% and a minimum sun elevation of 20° (Tuckett *et al.*, 2021). The Sentinel-2 data is organized into time windows of 10 days, resulting in spatial-time windows comprising a mosaic of up to seven images, clipped to a tile.

For each Sentinel-2 image, we assess the maximum extent and depth of lakes, using a band-threshold-based method developed by Moussavi *et al.* (2020) and

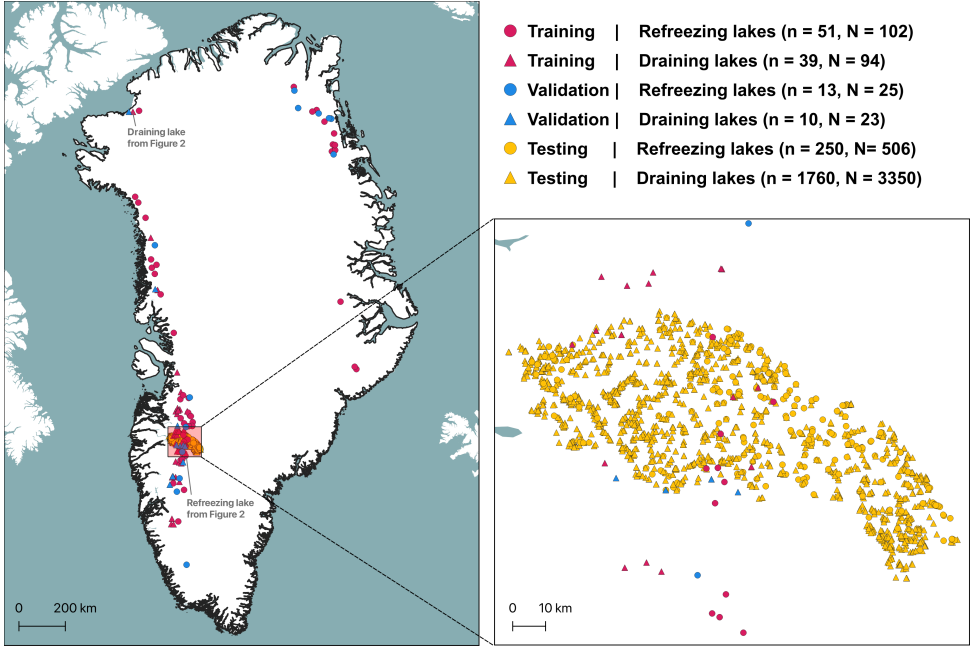


Figure 5.1: Overview of the training, validation, and testing lakes used for developing the ConvLSTM model, with refreezing lakes indicated by circles and draining lakes by triangles. Training and validation data were manually selected based on a Greenland-wide study on supraglacial lakes by Zheng *et al.* (2023), while testing data were classified in a study by Glen *et al.* (2024) for the Russell/Leverett glacier catchment, as highlighted in the inset. The variable ‘n’ in the legend indicates the total number of lakes, while ‘N’ represents the total number of Sentinel-1 time series, which can exceed ‘n’ if a lake appears in multiple orbits.

further refined and automated by Tuckett *et al.* (2021). This method involves combining different bands of the satellite images to create new bands, applying thresholds to obtain masks for meltwater, rocks, and clouds, and finally estimating the depth by considering the albedo and reflectance of water in a physically-based model. The lake masks from individual spatial-time windows are combined to create a maximum lake extent and lake depth for each observed melt season.

We only select larger lakes for our analysis because the dynamics of smaller lakes are difficult to capture with Sentinel-1’s 10-meter spatial resolution. Moreover, Krawczynski *et al.* (2009) found that only larger lakes, approximately 250–800 m across and 2–5 m deep, contain a sufficient volume of water to drive a water-filled crack to the base of an idealized 1 km-thick ice sheet. Therefore, we filter for lakes with an extent larger than 500,000 m² and a volume of 100,000 m³.

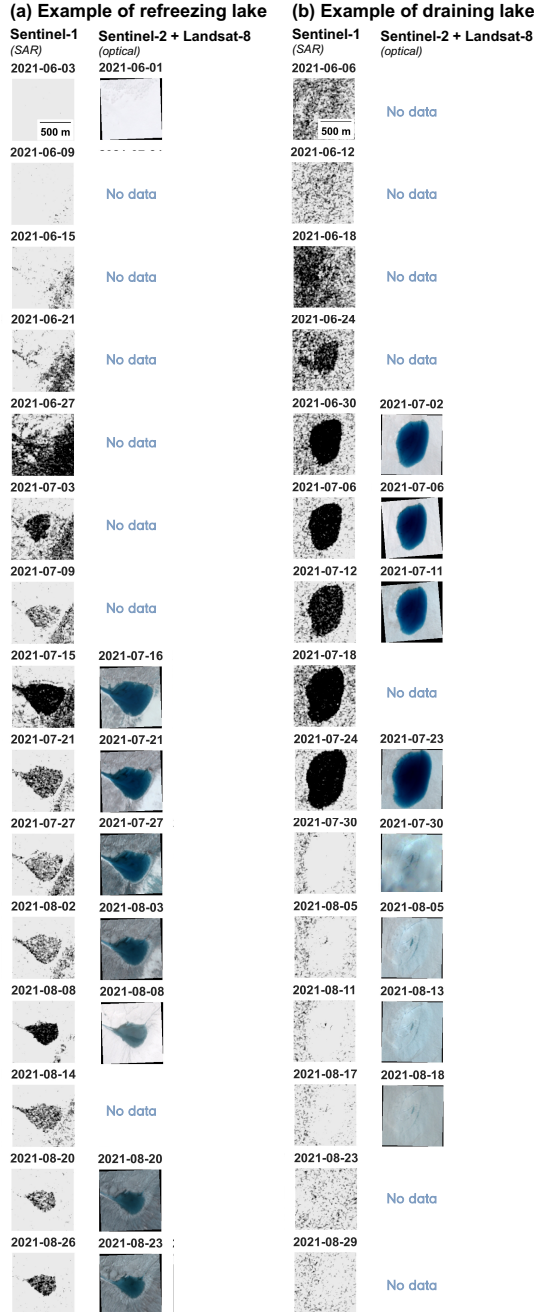


Figure 5.2: Overview of a (a) refreezing and (b) draining lake, displaying Sentinel-1 (SAR) and Sentinel-2/Landsat-8 (optical) time series selected from the training dataset. The optical images are aligned with the closest SAR image in time. In cases where optical images were unavailable due to cloud cover, a “No data” label was assigned in the optical time series. The location of the refreezing and draining lakes are marked in Figure 5.1.

5.2.2. SENTINEL-1 TIME SERIES

Now that the lake locations are known, we download Sentinel-1 images with a pixel spacing of 10 by 10 meters, acquired in Interferometric Wide (IW) mode. For Antarctica, these images are exclusively available in HH (horizontal-horizontal) polarization. Although HV (horizontal-vertical) polarization could offer advantages for distinguishing between draining and refreezing lakes (Benedek & Willis, 2021; Miles *et al.*, 2017), it is primarily available in Extra Wide (EW) mode for most locations, which has a coarser pixel spacing of 25 by 25 meters or 40 by 40 meters. This coarser resolution limits the detectability of small lakes across most of Antarctica.

Therefore, we retrieve HH-polarized Sentinel-1 time series based on the centroids of the selected training, validation, and testing lakes and the application lakes (Section 5.2.1). Utilizing 1000 by 1000 meter bounding boxes around these centroids, we access Sentinel-1 data from GEE. We split the Sentinel-1 data by orbit, accounting for varying backscatter intensities attributable to differing viewing geometries. Some lakes fall within multiple orbits, resulting in more time series than individual lakes.

For the training, validation, and testing lakes in Greenland, our dataset comprises 102 refreezing and 94 draining lake time series for training, 25 refreezing and 23 draining lake time series for validation, and 506 refreezing and 3350 draining lake time series for testing. An example of Sentinel-2 and Landsat-8 imagery, along with Sentinel-1 time series for a draining lake and a refreezing lake can be found in Figure 5.2.

For the Sentinel-1 time series of the training, validation, and testing lakes our time interval is set between 1 May and 1 August, though the exact start and end dates are orbit-dependent. Given that the revisit time of Sentinel-1, when combining data from Sentinel-1A and Sentinel-1B, is six days, this results in a minimum of 16 scenes, which corresponds to the length of the Sentinel-1 time series we used. If 17 scenes were available for a specific orbit, we did not use the last image, as ConvLSTM architectures require consistent dimensions. Hence, the shape of the Sentinel-1 time series is 16 (length), by 100 (width, corresponding to 1000 m), by 100 (height, corresponding to 1000 m), and has one label (draining or refreezing), as shown in Figure 5.3. To standardize the Sentinel-1 time series inputs for the ConvLSTM model, we normalized each time series by scaling values between the respective 2.5th and 97.5th percentiles within the time series. This normalization procedure mitigates the influence of varying viewing angles across orbits, ensuring consistent input for the model.

Similar to the training, validation, and testing data, we create time series of 16 scenes for the identified lakes on Antarctica. For Antarctica, these scenes are selected between December 15 and March 15, although the exact start and end dates vary depending on the orbit. We obtain data for 1346 lakes for the 2019–2020 melt season and 1599 lakes for the 2020–2021 melt season.

5.2.3. DEVELOPING CONVLSTM MODEL ON GREENLAND ICE SHEET

Our deep learning model, designed to classify draining and refreezing lakes in one melt season, is based on a ConvLSTM architecture (Shi *et al.*, 2015). The ConvLSTM

model leverages both convolutional and LSTM layers to capture spatial and temporal features from Sentinel-1 SAR data. This dual capability is crucial for analyzing time series data with complex spatial and temporal features, such as the dynamic evolution of supraglacial lakes.

The ConvLSTM model is constructed using several key layers, inspired by the model defined in Shi *et al.* (2015). The architecture starts with a ConvLSTM2D layer, which employs 64 filters with a kernel size of 3x3 and a rectified linear unit (ReLU) activation function to capture spatiotemporal features. This is followed by a batch normalization layer to standardize the output and improve training stability, and a dropout layer with a rate of 0.2 to prevent overfitting. A max pooling layer is then used to reduce the spatial dimensions by a factor of two. The data are then flattened, converting the 2D matrix to a 1D vector. Finally, the model includes a dense hidden layer with 128 neurons and a ReLU activation, followed by an output layer with a single neuron and a sigmoid activation for binary classification. The output is a value between 0 and 1, where 0 indicates refreezing and 1 indicates draining. We use a threshold of 0.5 to classify the predictions into refreezing and draining classes.

The model is compiled using the Adam optimizer and binary cross-entropy loss function (Goodfellow, 2016). To improve convergence, an exponential decay learning rate scheduler is employed to adjust the learning rate over the training epochs, starting at 0.001 with decay steps of 1000 and a decay rate of 0.9. The model is trained over 50 epochs, with the learning rate scheduler ensuring optimal learning rates throughout the training process. Early stopping is based on the validation loss to prevent overfitting. We employed a grid search on the validation data to identify the optimal hyperparameters (optimizer, loss function, learning rate, filters, kernel size) based on the highest validation accuracy achieved, and the values presented here proved to be the best.

We evaluate the performance of the model on the testing data using a confusion matrix and a variety of metrics, including accuracy, precision, recall, and F1-score. The detailed performance analysis ensures the robustness and reliability of our classification algorithm.

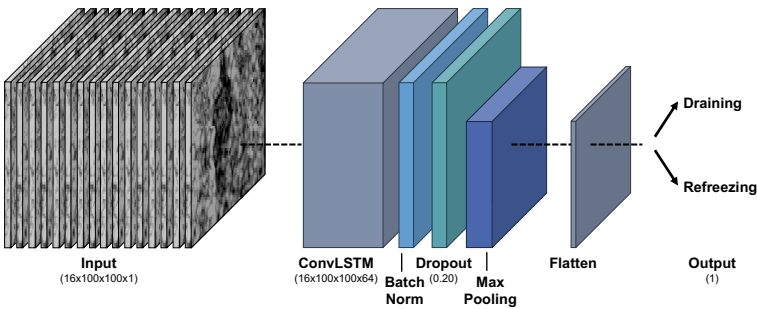


Figure 5.3: Conceptual overview of the ConvLSTM model: it takes as input a time series comprising sixteen Sentinel-1 scenes and outputs a label indicating either refreezing or draining.

5.2.4. ASSESSING SENSITIVITY OF CONV LSTM MODEL

To assess whether the ConvLSTM model effectively learns both spatial and temporal patterns, we perturb the test dataset, which includes lakes classified by Glen *et al.* (2024), and evaluate the model's performance. For the spatial perturbations, we adjust the backscatter intensities of the Sentinel-1 time series by decreasing and increasing each input time series to 75% and 125% of their original values, respectively. For temporal perturbations, we randomly shuffle each time series.

After perturbing the test data, we apply the trained ConvLSTM model, as described in Section 5.2.3, to make predictions. By comparing the accuracies of the original and perturbed classifications, we assess whether the ConvLSTM model has learned from the spatial and temporal dynamics present in the refreezing and draining lakes of the training dataset.

5.2.5. APPLYING CONV LSTM MODEL ON ANTARCTIC ICE SHEET

After training, validating, and testing the ConvLSTM model, we apply it on an Antarctic-wide scale for the relatively strong 2019–2020 and the relatively weak 2020–2021 melt seasons (Banwell *et al.*, 2021; de Roda Husman *et al.*, 2024; Moussavi *et al.*, 2020). We apply the trained ConvLSTM model to all identified lakes in Antarctica and classify the lakes as refreezing or draining using a threshold of 0.5.

5.2.6. SUPRAGLACIAL LAKE AND ICE SHELF PARAMETERS

To understand which types of lakes refreeze and which drain, we compare the predicted lake locations with two lake parameters (i.e., maximum lake area and maximum lake volume) and three ice shelf parameters (i.e., ice flow speed, ice thickness, and firn air content). Paired t-tests are employed to assess whether statistically significant differences exist between refreezing and draining lakes concerning these lake and ice shelf parameters.

Firstly, determining maximum lake area and volume, using the method developed by Moussavi *et al.* (2020) (see Section 5.2.1), will indicate whether smaller or larger lakes on Antarctica more frequently drain or refreeze. Secondly, ice flow speed data from MEASUREs InSAR-based Antarctica ice velocity map (Mouginot *et al.*, 2012; Rignot *et al.*, 2011) may indicate whether lakes on ice undergoing significant stresses are more likely to drain or refreeze. Thirdly, ice thickness information from Bedmap2 (Fretwell *et al.*, 2013) helps understand the behavior of lakes on thinner or thicker ice. Finally, firn air content, derived from the IMAU Firn Densification Model (IMAU-FDM) for the average of 1979–2020 (Veldhuijsen *et al.*, 2023), plays a critical role in influencing water infiltration and retention processes, providing insights into the behavior of lakes on firn with varying firn air content.

5.3. RESULTS

5.3.1. TESTING THE DEVELOPED CONV LSTM

The developed ConvLSTM model is tested using refreezing and draining lakes identified in the study by Glen *et al.* (2024); refer to Figure 5.1 for their geographical

distribution. The testing dataset consists of draining and refreezing lakes observed during both weak (2018) and strong (2019) melt seasons on the Russell/Leverett glacier catchment of the Greenland Ice Sheet. Performance metrics in Table 5.1 and confusion matrices in Figure 5.4 illustrate robust results across both seasons. Notably, the weak melt season shows slightly better performance with an accuracy of 84.2% compared to 79.7% for the strong melt season. However, a McNemar test, which is used to determine if there are significant differences between two binary classifications (McNemar, 1947), shows that there is no significant difference ($p > 0.05$) between the two melt seasons.

Table 5.1: Performance metrics (accuracy, precision, recall, F1-score) of the trained ConvLSTM model on an unseen testing dataset for the weak (2018) and strong (2019) melt seasons, using lakes classified in a study by Glen *et al.* (2024). The dataset includes 250 refreezing lakes and 1760 draining lakes in Greenland.

| | Weak melt season (2018) | Strong melt season (2019) |
|-----------|-------------------------|---------------------------|
| Accuracy | 84.2% | 79.7% |
| Precision | 94.7% | 97.4% |
| Recall | 84.3% | 79.5% |
| F1-score | 89.2% | 87.5% |

To evaluate the model’s sensitivity, we perform analyses in both the spatial and temporal domains, as outlined in Table 5.2. In the spatial domain, we adjust the backscatter intensity of the Sentinel-1 time series by increasing and decreasing it. We anticipate that these changes will have minimal impact on accuracy, since the model should focus on the evolution of the lake rather than the specific intensity values. This expectation is supported by the fact that the model encountered the same lake multiple times during training, with varying backscatter intensities due to different orbits. Indeed, these spatial perturbations do not decrease accuracy and even result in a slight improvement compared to the original dataset. This indicates that the ConvLSTM model is robust to spatial variations.

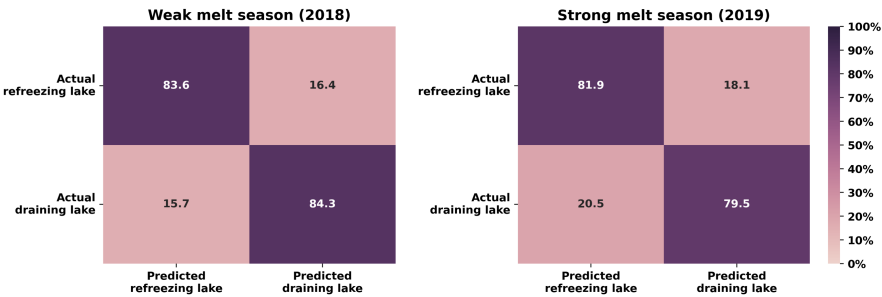


Figure 5.4: Confusion matrices of the testing dataset for weak (2018) and strong (2019) melt seasons, using classified lakes from a study by Glen *et al.* (2024), with 250 refreezing lakes and 1760 draining lakes on Greenland.

In the temporal domain, we perform perturbations by randomly shuffling the Sentinel-1 time series. This is expected to reduce accuracy, as the ConvLSTM model relies on the temporal order of the data. Indeed, random shuffling lowers the accuracy to 71.0% from 84.2% for the 2018 melt season, and to 67.0% from 79.7% for the 2019 melt season. This drop in accuracy suggests that the model is sensitive to the sequence of the time series, indicating its capability to effectively capture temporal patterns.

Table 5.2: Accuracy of the trained ConvLSTM model on the perturbed testing dataset for the weak (2018) and strong (2019) melt seasons, using lakes classified in a study by Glen *et al.* (2024). The perturbations are categorized into (a) spatial and (b) temporal.

| (a) Spatial perturbations | | |
|---------------------------------|-------------------------|---------------------------|
| | Weak melt season (2018) | Strong melt season (2019) |
| Increased backscatter intensity | 90.8% | 86.6% |
| Decreased backscatter intensity | 84.8% | 94.4% |

| (b) Temporal perturbations | | |
|-------------------------------|-------------------------|---------------------------|
| | Weak melt season (2018) | Strong melt season (2019) |
| Randomly shuffled time series | 71.0% | 67.2% |

5.3.2. PREDICTED REFREEZING AND DRAINING LAKES ON ANTARCTICA

Figure 5.5 shows the predicted refreezing and draining lakes for the two studied Antarctic melt seasons. Most lakes are classified as refreezing, yet predictions vary notably between the two seasons. For the relatively strong 2019–2020 melt season, 1346 lakes are identified, with 65% refreezing and 35% draining. In contrast, for the relatively weak 2020–2021 melt season, 1599 lakes are identified, with almost all lakes refreezing (99%) and only 1% draining. During the 2019–2020 melt season, draining lakes are identified all over Antarctica, with the majority located in the Antarctic Peninsula, Amery, and Shackleton ice shelves. In the 2020–2021 melt season, the lakes are confined to the Amery Ice Shelf and Victoria Land. The locations of the identified supraglacial lakes overlap with other studies, such as the study by Arthur *et al.* (2020), which is expected, as they also used the method from Moussavi *et al.* (2020) to identify lakes.

Comparing our predictions with existing data on refreezing and draining lakes is challenging, as such data are not yet available for Antarctica. However, we can compare our findings with Jourdain *et al.* (2024), who identified surface conditions necessary for hydrofracturing using regional climate model simulations. They assessed whether local runoff over a 10-year period exceeded a certain threshold, indicating potential for ice shelf hydrofracturing. While this is not a perfect comparison—particularly since our model does not differentiate between slow and rapid (i.e., hydrofracturing) drainages—it provides a preliminary assessment. Jourdain

et al. (2024) identified several ice shelves on the Antarctic Peninsula, such as Larsen A, B, C, George VI, and Wilkins, as being likely to experience hydrofracturing before 2015. For other ice shelves, where we identified drainages in 2019–2020, Jourdain *et al.* (2024) also predict vulnerability to hydrofracturing before 2050 under the SSP2–4.5 scenario. These include the Roi Baudouin, Amery, and Shackleton ice shelves. However, on other ice shelves such as Cosgrove and Riiser-Larsen, where we have identified drainages, Jourdain *et al.* (2024) project them to become vulnerable to hydrofracturing only after 2100.

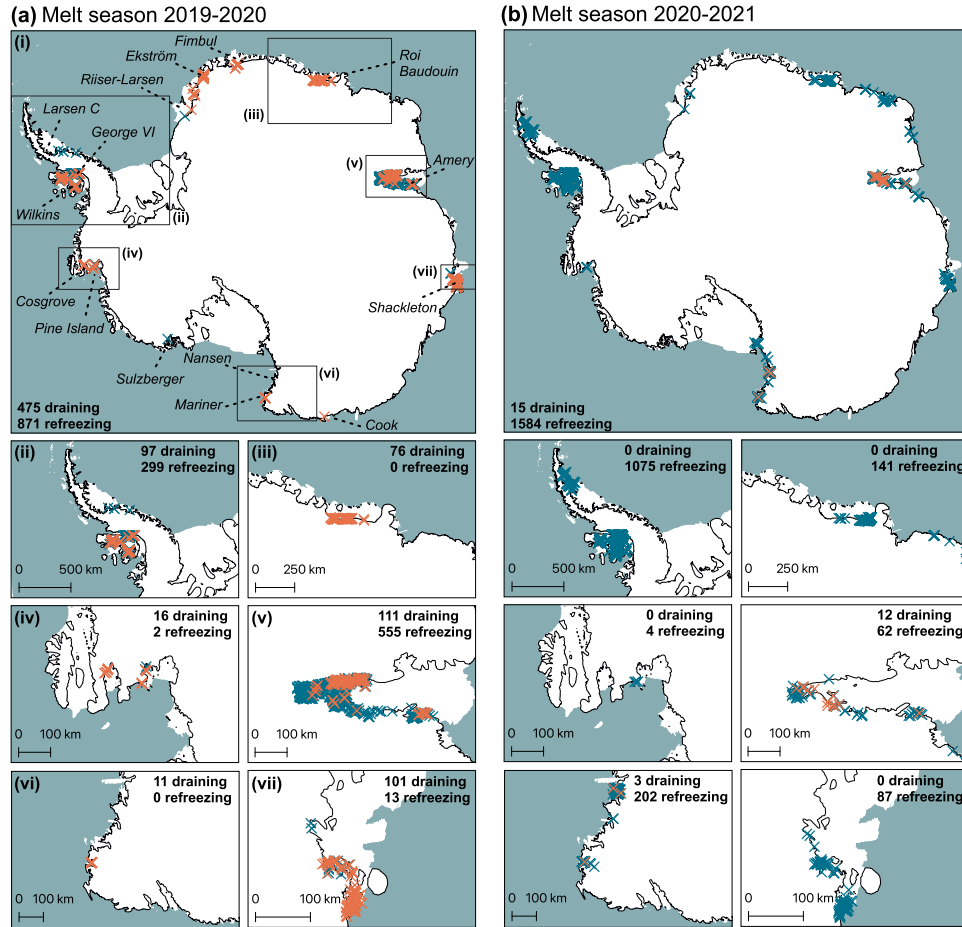


Figure 5.5: The classified draining (orange circles) and refreezing (blue crosses) lakes using the ConvLSTM model, with panels (i) presenting an overview of the Antarctic Ice Sheet, and panels (ii) presenting the Antarctic Peninsula, panels (iii) Dronning Maud Land, (iv) Marie Byrd Land, (v) Amery Ice Shelf, (vi) Victoria Land, and (vii) Shackleton Ice Shelf. The labels in each panel show the number of identified draining and refreezing lakes for the respective melt season. In panels (a)–(i), the names of the ice shelves mentioned are those referred to throughout the manuscript.

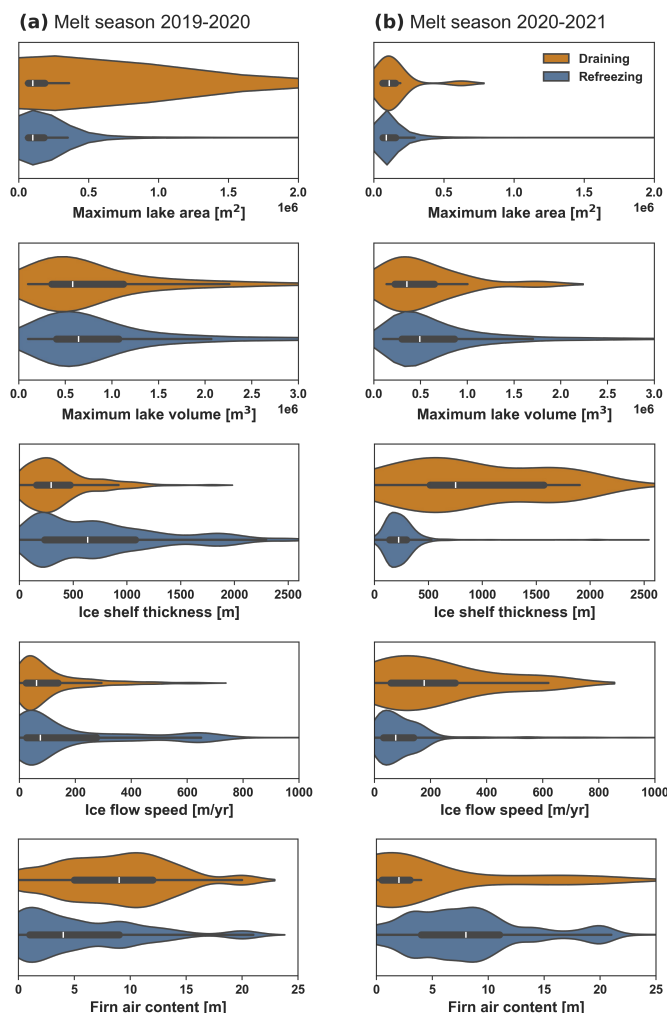


Figure 5.6: Violin plots showing identified draining lakes (in orange) and refreezing lakes (in blue) in Antarctica for the (a) 2019–2020 and (b) 2020–2021 melt seasons, depicting maximum lake area, maximum lake volume, ice shelf thickness, ice flow speed, and firn air content.

5.3.3. RELATION OF REFREEZING AND DRAINING LAKES TO LAKE AND ICE SHELF PARAMETERS

Figure 5.6 compares the identified draining and refreezing lakes to parameters of lake characteristics (maximum area and volume) and ice shelf characteristics (thickness, ice flow speed, and firn air content). The lake area and volume were significantly ($p < 0.05$) larger during the relatively strong 2019–2020 melt season compared to the relatively weak 2020–2021 melt season, with median areas of $100 \times 10^3 \text{ m}^2$ and $89 \times 10^3 \text{ m}^2$, and median volumes of $620 \times 10^3 \text{ m}^3$ and $492 \times 10^3 \text{ m}^3$, respectively. However,

when comparing the lake areas and volumes between drainages and refreezing lakes, there is no significant ($p > 0.05$) difference.

In terms of ice shelf thickness, ice flow speed, and firn air content, notable differences between the two melt seasons reveal contrasting patterns. During the 2019–2020 melt season, draining occurred on thinner ice shelves (median of 295 m) compared to refreezing lakes (median of 634 m), showing a significant difference ($p < 0.05$). Conversely, in 2020–2021, there were minimal drainages, but when present, they occurred on thicker ice shelves (median of 752 m) compared to refreezing lakes (median of 223 m). However, with only 15 draining lakes identified in 2020–2021, representing less than 1% of the studied lakes in that melt season, drawing conclusions from this relatively weak melt season is challenging.

Regarding ice flow speed, drainages in 2019–2020 occurred on slower-flowing ice shelves (median of 61 m/year) compared to refreezing lakes (median of 74 m/year), which is a statistically significant difference ($p < 0.05$). In contrast, for 2020–2021, drainages were observed on faster-flowing ice (median of 177 m/year) compared to refreezing (median of 76 m/year), although this difference is not significant ($p > 0.05$).

Similarly, for firn air content, during 2019–2020 drainages were associated with higher firn air content (median of 9 m) compared to refreezing lakes (median of 4 m), with a significant difference ($p < 0.05$). In 2020–2021, the pattern reversed, with drainages occurring on ice shelves with more depleted firn layers (median of 2 m) compared to refreezing lakes (median of 8 m), also showing a significant difference ($p < 0.05$).

5.4. DISCUSSION

5.4.1. FROM PROOF OF CONCEPT TO OPERATIONAL PRODUCT

The Antarctic-wide maps in Figure 5.5 reveal significant differences in lake evolution between the 2019–2020 and 2020–2021 melt seasons. Although the ConvLSTM model demonstrated good performance on the unseen testing dataset, achieving accuracies of 84.2% in 2018 and 79.7% in 2019 for the Greenland Ice Sheet (Table 5.1), confidently relying on the Antarctic-wide maps remains challenging. For instance, Sentinel-2 observations show that the 2020–2021 melt season had more lakes (1599) compared to the much stronger 2019–2020 season (1346). However, the lakes from the weaker 2020–2021 season were smaller in both area and volume (see Figure 5.6). Additionally, the ConvLSTM model based on Sentinel-1 data revealed a large difference in the ratio of refreezing to draining lakes: 475 draining lakes in 2019–2020 compared to only 15 in 2020–2021. Validating these results is challenging due to frequent cloud cover in Antarctica, which limits the availability of optical imagery.

A major limitation of the current ConvLSTM model is the small size of the training dataset, which included only 51 refreezing lakes and 39 draining lakes. By prioritizing the high quality of the training data and hand-picking the draining and refreezing lakes, we severely limited the overall dataset size. Therefore, to transition from a proof of concept to an operational product, we recommend using a larger training dataset from both Greenland and Antarctica. This could be achieved by manually

collecting more data or by employing a semi-supervised learning method (X. J. Zhu, 2005).

Due to the limitations of optical data in Antarctica, we believe SAR data, such as Sentinel-1, is a promising additional dataset for identifying draining and refreezing lakes in Antarctica. Beyond studying time series of radar backscatter, Li *et al.* (2021) demonstrated in a case study on the Amery and Roi Baudouin ice shelves that Interferometric SAR (InSAR) patterns, which involve studying the phase difference between two SAR images, can be used to identify refreezing and draining lakes. Hence, InSAR could provide valuable additional information in future studies for identifying refreezing and draining lakes.

However, it is important to note that we did not rely solely on SAR data; we also used optical data to identify lake locations in this study. While SAR-based methods can identify supraglacial lakes in Antarctica (e.g., Dirscherl *et al.*, 2021), they cannot yet, if ever, reliably determine lake volumes due to the rapid saturation of the SAR signal. This saturation complicates the differentiation between small and significant amounts of liquid water. Consequently, optical data remains indispensable for accurate lake volume measurement.

5.4.2. GREENLAND AS TRAINING DOMAIN FOR PREDICTING LAKE EVOLUTION ON ANTARCTICA

Given the distinct characteristics of lakes between the Greenland and Antarctic ice sheets, one might question whether Greenland can serve as a suitable region for training, validating, and testing the ConvLSTM model before its application to Antarctica. Although the sensitivity study in Section 5.3.1 demonstrated that the model is robust to spatial variations in Greenland—indicating that fluctuations in backscatter values do not impact performance—and that it successfully learns from the temporal sequence of the time series, differences in lake evolution between Antarctica and Greenland may still pose challenges.

Banwell *et al.* (2014) conducted a comparative study of lakes at Paakitsoq (West Greenland) and on the Larsen B Ice Shelf (Antarctic Peninsula), revealing significant diversity in lake types despite the study's relatively small scale. While the total number and average area of lakes were comparable in both regions, lakes on Larsen B were shallower and more uniform in size compared to those at Paakitsoq. The higher standard deviations of lake area and volume in the Paakitsoq region indicate greater variability in lake depths and areas compared to Larsen B. This variability is likely attributed to the substantial elevation gradient in the Paakitsoq region, ranging from approximately 400 m at the ice margin to 1500 m inland, in contrast to the minimal elevation gradient on the Larsen B Ice Shelf (Banwell *et al.*, 2014).

In addition to differences in lake shape, area, and volume, there are also variations in the timing of lake formation and the onset of refreezing or draining. Dirscherl *et al.* (2021) demonstrated that lakes in Antarctica typically form at the end of December or early January and disappear by early February, resulting in a lifetime of approximately one to 1.5 months. In Greenland, most lakes have longer lifetimes, typically spanning from June to August, totaling around three months, as shown by McMillan *et al.* (2007).

For training, validating, and testing the ConvLSTM model, the diversity of lakes in Greenland is advantageous as it captures a broader range of lake types. However, the differences in the timing of lake onset and offset between Greenland and Antarctica pose challenges for the ConvLSTM model, which learns refreezing and draining patterns based on the Greenlandic time series. Ideally, the model should also be trained with Antarctic refreezing and draining lakes to ensure robust performance, underscoring the need for more studies on Antarctic lakes.

5.4.3. INHERENT LIMITATIONS OF OUR MODEL

Besides the need to augment the ConvLSTM model training with additional samples (see Section 5.4.1) and integrate Antarctic data (see Section 5.4.2), there are also inherent limitations to what this type of deep learning model, trained on Sentinel-1 time series, can address. We discuss two main limitations in Sections 5.4.3 and 5.4.3.

SLOW OR RAPID DRAINAGES?

In this study, we split the Sentinel-1 time series per orbit, resulting in a temporal interval of six days for each training, validation, testing, and application sample. At this resolution, distinguishing between the two types of drainage identified by Selmes *et al.* (2011) is challenging: (i) slow drainage over more than two days, likely through existing channels to moulins; and (ii) rapid drainage in less than two days, typically via hydrofracturing and the formation of new moulins. Selmes *et al.* (2011, 2013) used optical remote sensing data to show that from 2005 to 2009, refreezing was the most common mode in Greenland (46%), followed by slow drainage (34%), rapid drainage (13%), and lakes that remained unidentified due to cloud cover (7%). Applying this distinction between fast and slow drainage to Antarctica would be valuable. To achieve this, Sentinel-1 images need correction for look angle and incidence angle to utilize the full Sentinel-1 time series without the need to split per orbit. Depending on the location in Antarctica, this could result in multiple images per week, since many lakes are present across multiple orbits (see Figure 3.2 in Chapter 3 for a map of Sentinel-1 temporal resolution). Additionally, future SAR satellites, such as Sentinel-1C and -1D (Torres *et al.*, 2017) and NASA-ISRO SAR Mission (NISAR; NISAR, 2018), could enhance temporal resolution once they are launched. Combining all these SAR images from different orbits and satellites might result in a time series with higher temporal resolution, allowing us to distinguish between the durations of draining.

DRAINAGE TO THE BED?

Our current approach does not provide insights into the hydrology of drained meltwater. Both slow and rapid drainage events create pathways to the bed (i.e., moulins), which can remain open throughout the melt season, allowing diurnally varying meltwater inflows to reach the bed (Banwell *et al.*, 2013). Unlike rapid drainage, slow-draining lakes do not facilitate rapid water delivery to the ice sheet bed. The subglacial hydrologic system's capacity to adapt to consistent inputs suggests that slow drainage events may induce less basal sliding than pulsed inputs

from rapid drainage events (Bartholomew *et al.*, 2012; Schoof, 2010), highlighting the importance of distinguishing between these drainage modes.

In Greenland, rapid surface water delivery to the bed has been observed to reduce basal friction and temporarily increase ice flow velocities by up to tenfold (Tedesco *et al.*, 2013). Similar processes have been hypothesized for East Antarctica (Langley *et al.*, 2016), with recent studies documenting speed-up events on the Antarctic Peninsula (Tuckett *et al.*, 2019), suggesting that surface meltwater may influence the subglacial hydrological system. Projected warming is expected to increase hydrofracturing events on ice shelves (Gilbert & Kittel, 2021; Jourdain *et al.*, 2024), emphasizing the critical need to monitor the distribution and evolution of supraglacial lake dynamics and hydrology.

5.5. CONCLUSION

In this study, we developed a spatiotemporal deep learning model, specifically ConvLSTM, to identify refreezing and draining lakes across Antarctica during both a relatively strong (2019–2020) and a relatively weak (2020–2021) melt season. Supraglacial lake locations were identified using optical images, and Sentinel-1 time series data were utilized to train and apply the ConvLSTM model. Initially developed using data from the Greenland Ice Sheet, the model was subsequently applied to the Antarctic Ice Sheet.

During the relatively strong 2019–2020 melt season, 1346 lakes were identified, with 65% refreezing and 35% draining. In contrast, the weaker 2020–2021 melt season saw the identification of 1599 lakes, predominantly refreezing (99%) with only 1% draining. We observed no clear relationships between lake characteristics and ice shelf parameters for refreezing and draining lakes, indicating that further research is needed to uncover the distinct patterns. Further model refinement is crucial to draw definitive conclusions, necessitating expansion of the training dataset. This study marks an initial step in monitoring the evolution of supraglacial lakes during Antarctic melt seasons, leveraging Sentinel-1 data and a spatiotemporal deep learning model as valuable tools.

BIBLIOGRAPHY

- Arthur, J. F., Stokes, C., Jamieson, S. S., Carr, J. R., & Leeson, A. A. (2020). Recent understanding of Antarctic supraglacial lakes using satellite remote sensing. *Progress in Physical Geography: Earth and Environment*, 44(6), 837–869.
- Banwell, A. F., Caballero, M., Arnold, N. S., Glasser, N. F., Mac Cathles, L., & MacAyeal, D. R. (2014). Supraglacial lakes on the Larsen B ice shelf, Antarctica, and at Paakitsoq, West Greenland: a comparative study. *Annals of Glaciology*, 55(66), 1–8.
- Banwell, A. F., Datta, R. T., Dell, R. L., Moussavi, M., Brucker, L., Picard, G., Shuman, C. A., & Stevens, L. A. (2021). The 32-year record-high surface melt in 2019/2020 on the northern George VI Ice Shelf, Antarctic Peninsula. *The Cryosphere*, 15(2), 909–925.
- Banwell, A. F., MacAyeal, D. R., & Sergienko, O. V. (2013). Breakup of the Larsen B Ice Shelf triggered by chain reaction drainage of supraglacial lakes. *Geophysical Research Letters*, 40(22), 5872–5876.
- Banwell, A. F., Willis, I. C., Stevens, L. A., Dell, R. L., & MacAyeal, D. R. (2024). Observed meltwater-induced flexure and fracture at a doline on George VI Ice Shelf, Antarctica. *Journal of Glaciology*, 1–14.
- Bartholomaeus, T. C., Anderson, R. S., & Anderson, S. P. (2008). Response of glacier basal motion to transient water storage. *Nature Geoscience*, 1(1), 33–37.
- Bartholomew, I., Nienow, P., Sole, A., Mair, D., Cowton, T., & King, M. A. (2012). Short-term variability in Greenland Ice Sheet motion forced by time-varying meltwater drainage: Implications for the relationship between subglacial drainage system behavior and ice velocity. *Journal of Geophysical Research: Earth Surface*, 117(F3).
- Bell, R. E., Banwell, A. F., Trusel, L. D., & Kingslake, J. (2018). Antarctic surface hydrology and impacts on ice-sheet mass balance. *Nature Climate Change*, 8(12), 1044–1052.
- Beltaos, S. (2002). Collapse of floating ice covers under vertical loads: test data vs. theory. *Cold Regions Science and Technology*, 34(3), 191–207.
- Benedek, C. L., & Willis, I. C. (2021). Winter drainage of surface lakes on the Greenland Ice Sheet from Sentinel-1 SAR imagery. *The Cryosphere*, 15(3), 1587–1606.
- Christoffersen, P., Bougamont, M., Hubbard, A., Doyle, S. H., Grigsby, S., & Pettersson, R. (2018). Cascading lake drainage on the Greenland Ice Sheet triggered by tensile shock and fracture. *Nature Communications*, 9(1), 1064.
- de Roda Husman, S., Lhermitte, S., Bolibar, J., Izeboud, M., Hu, Z., Shukla, S., van der Meer, M., Long, D., & Wouters, B. (2024). A high-resolution record of surface melt on Antarctic ice shelves using multi-source remote sensing data and deep learning. *Remote Sensing of Environment*, 301, 113950.
- Ding, X., Zhang, Y., Liu, T., & Duan, J. (2015). Deep learning for event-driven stock prediction. *Twenty-fourth international joint conference on artificial intelligence*.
- Dirscherl, M., Dietz, A. J., Kneisel, C., & Kuenzer, C. (2021). A novel method for automated supraglacial lake mapping in Antarctica using Sentinel-1 SAR imagery and deep learning. *Remote Sensing*, 13(2), 197.

- Dunmire, D., Lenaerts, J., Banwell, A., Wever, N., Shragge, J., Lhermitte, S., Drews, R., Pattyn, F., Hansen, J., Willis, I., et al. (2020). Observations of buried lake drainage on the Antarctic Ice Sheet. *Geophysical research letters*, 47(15), e2020GL087970.
- Fretwell, P., Pritchard, H. D., Vaughan, D. G., Bamber, J. L., Barrand, N. E., Bell, R., Bianchi, C., Bingham, R., Blankenship, D. D., Casassa, G., et al. (2013). Bedmap2: improved ice bed, surface and thickness datasets for Antarctica. *The cryosphere*, 7(1), 375–393.
- Gilbert, E., & Kittel, C. (2021). Surface melt and runoff on Antarctic ice shelves at 1.5 C, 2 C, and 4 C of future warming. *Geophysical Research Letters*, 48(8), e2020GL091733.
- Glasser, N., & Scambos, T. A. (2008). A structural glaciological analysis of the 2002 Larsen B ice-shelf collapse. *Journal of Glaciology*, 54(184), 3–16.
- Glen, E., Leeson, A. A., Banwell, A. F., Maddalena, J., Corr, D., Noël, B., & McMillan, M. (2024). A comparison of supraglacial meltwater features throughout contrasting melt seasons: Southwest Greenland. *EGUsphere*, 2024, 1–31.
- Goodfellow, I. (2016). Deep learning.
- Gudmundsson, G. H., Paolo, F. S., Adusumilli, S., & Fricker, H. A. (2019). Instantaneous Antarctic ice sheet mass loss driven by thinning ice shelves. *Geophysical Research Letters*, 46(23), 13903–13909.
- Johansson, A. M., & Brown, I. A. (2012). Observations of supra-glacial lakes in west Greenland using winter wide swath Synthetic Aperture Radar. *Remote sensing letters*, 3(6), 531–539.
- Jourdain, N. C., Amory, C., Kittel, C., & Durand, G. (2024). Changes in Antarctic surface conditions and potential for ice shelf hydrofracturing from 1850 to 2200. *EGUsphere*, 2024, 1–34.
- Kingslake, J., Ely, J. C., Das, I., & Bell, R. E. (2017). Widespread movement of meltwater onto and across Antarctic ice shelves. *Nature*, 544(7650), 349–352.
- Koenig, L. S., Lampkin, D., Montgomery, L., Hamilton, S., Turrin, J., Joseph, C., Moutsafa, S., Panzer, B., Casey, K., Paden, J. D., et al. (2015). Wintertime storage of water in buried supraglacial lakes across the Greenland Ice Sheet. *The Cryosphere*, 9(4), 1333–1342.
- Krawczynski, M., Behn, M., Das, S., & Joughin, I. (2009). Constraints on the lake volume required for hydro-fracture through ice sheets. *Geophysical Research Letters*, 36(10).
- Langley, E. S., Leeson, A. A., Stokes, C. R., & Jamieson, S. S. (2016). Seasonal evolution of supraglacial lakes on an East Antarctic outlet glacier. *Geophysical Research Letters*, 43(16), 8563–8571.
- Law, R., Arnold, N., Benedek, C., Tedesco, M., Banwell, A., & Willis, I. (2020). Over-winter persistence of supraglacial lakes on the Greenland Ice Sheet: Results and insights from a new model. *Journal of Glaciology*, 66(257), 362–372.
- LeCun, Y., Bengio, Y., & Hinton, G. (2015). Deep learning. *nature*, 521(7553), 436–444.
- Leeson, A. A., Forster, E., Rice, A., Gourmelen, N., & van Wessem, J. (2020). Evolution of supraglacial lakes on the Larsen B ice shelf in the decades before it collapsed. *Geophysical Research Letters*, 47(4), e2019GL085591.
- Leeson, A. A., Shepherd, A., Sundal, A. V., Johansson, A. M., Selmes, N., Briggs, K., Hogg, A. E., & Fettweis, X. (2013). A comparison of supraglacial lake observations derived from MODIS imagery at the western margin of the Greenland Ice Sheet. *Journal of Glaciology*, 59(218), 1179–1188.
- Li, W., Lhermitte, S., & López-Dekker, P. (2021). The potential of synthetic aperture radar interferometry for assessing meltwater lake dynamics on Antarctic ice shelves. *The Cryosphere*, 15(12), 5309–5322.

- Litjens, G., Kooi, T., Bejnordi, B. E., Setio, A. A. A., Ciompi, F., Ghafoorian, M., Van Der Laak, J. A., Van Ginneken, B., & Sánchez, C. I. (2017). A survey on deep learning in medical image analysis. *Medical image analysis*, 42, 60–88.
- Lv, Y., Duan, Y., Kang, W., Li, Z., & Wang, F.-Y. (2014). Traffic flow prediction with big data: A deep learning approach. *Ieee transactions on intelligent transportation systems*, 16(2), 865–873.
- MacAyeal, D. R., & Sergienko, O. V. (2013). The flexural dynamics of melting ice shelves. *Annals of Glaciology*, 54(63), 1–10.
- Maier, N., Andersen, J. K., Mouginot, J., Gimbert, F., & Gagliardini, O. (2023). Wintertime supraglacial lake drainage cascade triggers large-scale ice flow response in Greenland. *Geophysical Research Letters*, 50(4), e2022GL102251.
- McMillan, M., Nienow, P., Shepherd, A., Benham, T., & Sole, A. (2007). Seasonal evolution of supra-glacial lakes on the Greenland Ice Sheet. *Earth and Planetary Science Letters*, 262(3–4), 484–492.
- McNemar, Q. (1947). Note on the sampling error of the difference between correlated proportions or percentages. *Psychometrika*, 12(2), 153–157.
- Miles, K. E., Willis, I. C., Benedek, C. L., Williamson, A. G., & Tedesco, M. (2017). Toward monitoring surface and subsurface lakes on the Greenland ice sheet using Sentinel-1 SAR and Landsat-8 OLI imagery. *Frontiers in Earth Science*, 5, 251152.
- Mouginot, J., Scheuchl, B., & Rignot, E. (2012). Mapping of ice motion in Antarctica using synthetic-aperture radar data. *Remote Sensing*, 4(9), 2753–2767.
- Moussavi, M., Pope, A., Halberstadt, A. R. W., Trusel, L. D., Cioffi, L., & Abdalati, W. (2020). Antarctic supraglacial lake detection using Landsat 8 and Sentinel-2 imagery: Towards continental generation of lake volumes. *Remote Sensing*, 12(1), 134.
- NISAR. (2018). *NASA-ISRO SAR (NISAR) Mission Science Users' Handbook* (tech. rep.). NASA Jet Propulsion Laboratory.
- Nye, J. F. (1957). The distribution of stress and velocity in glaciers and ice-sheets. *Proceedings of the Royal Society of London. Series A. Mathematical and Physical Sciences*, 239(1216), 113–133.
- Pattyn, F., Ritz, C., Hanna, E., Asay-Davis, X., DeConto, R., Durand, G., Favier, L., Fettweis, X., Goelzer, H., Gollledge, N. R., et al. (2018). The Greenland and Antarctic ice sheets under 1.5 C global warming. *Nature climate change*, 8(12), 1053–1061.
- Pritchard, H., Ligtenberg, S. R., Fricker, H. A., Vaughan, D. G., Van den Broeke, M. R., & Padman, L. (2012). Antarctic ice-sheet loss driven by basal melting of ice shelves. *Nature*, 484(7395), 502–505.
- Reese, R., Gudmundsson, G. H., Levermann, A., & Winkelmann, R. (2018). The far reach of ice-shelf thinning in Antarctica. *Nature Climate Change*, 8(1), 53–57.
- Rignot, E., Mouginot, J., & Scheuchl, B. (2011). Ice flow of the Antarctic ice sheet. *Science*, 333(6048), 1427–1430.
- Scambos, T. A., Fricker, H. A., Liu, C.-C., Bohlander, J., Fastook, J., Sargent, A., Massom, R., & Wu, A.-M. (2009). Ice shelf disintegration by plate bending and hydro-fracture: Satellite observations and model results of the 2008 Wilkins ice shelf break-ups. *Earth and Planetary Science Letters*, 280(1–4), 51–60.
- Scambos, T. A., Hulbe, C., Fahnestock, M., & Bohlander, J. (2000). The link between climate warming and break-up of ice shelves in the Antarctic Peninsula. *Journal of Glaciology*, 46(154), 516–530.
- Schoof, C. (2010). Ice-sheet acceleration driven by melt supply variability. *Nature*, 468(7325), 803–806.

- Selmes, N., Murray, T., & James, T. (2011). Fast draining lakes on the Greenland Ice Sheet. *Geophysical Research Letters*, 38(15).
- Selmes, N., Murray, T., & James, T. (2013). Characterizing supraglacial lake drainage and freezing on the Greenland Ice Sheet. *The Cryosphere Discussions*, 7(1), 475–505.
- Shi, X., Chen, Z., Wang, H., Yeung, D.-Y., Wong, W.-K., & Woo, W.-c. (2015). Convolutional LSTM network: A machine learning approach for precipitation nowcasting. *Advances in neural information processing systems*, 28.
- Song, H., Wang, W., Zhao, S., Shen, J., & Lam, K.-M. (2018). Pyramid dilated deeper ConvLSTM for video salient object detection. *Proceedings of the European conference on computer vision (ECCV)*, 715–731.
- Tedesco, M., Willis, I. C., Hoffman, M. J., Banwell, A. F., Alexander, P., & Arnold, N. S. (2013). Ice dynamic response to two modes of surface lake drainage on the Greenland ice sheet. *Environmental Research Letters*, 8(3), 034007.
- Torres, R., Lokas, S., Di Cosimo, G., Geudtner, D., & Bibby, D. (2017). Sentinel 1 evolution: Sentinel-1C and-1D models. *2017 IEEE International Geoscience and Remote Sensing Symposium (IGARSS)*, 5549–5550.
- Trusel, L. D., Pan, Z., & Moussavi, M. (2022). Repeated tidally induced hydrofracture of a supraglacial lake at the Amery Ice Shelf grounding zone. *Geophysical Research Letters*, 49(7), e2021GL095661.
- Tuckett, P. A., Ely, J. C., Sole, A. J., Lea, J. M., Livingstone, S. J., Jones, J. M., & van Wessem, J. M. (2021). Automated mapping of the seasonal evolution of surface meltwater and its links to climate on the Amery Ice Shelf, Antarctica. *The Cryosphere Discussions*, 2021, 1–35.
- Tuckett, P. A., Ely, J. C., Sole, A. J., Livingstone, S. J., Davison, B. J., van Wessem, J. M., & Howard, J. (2019). Rapid accelerations of Antarctic Peninsula outlet glaciers driven by surface melt. *Nature Communications*, 10(1), 4311.
- Veldhuijsen, S. B., Van de Berg, W. J., Brils, M., Kuipers Munneke, P., & Van den Broeke, M. R. (2023). Characteristics of the 1979–2020 Antarctic firn layer simulated with IMAU-FDM v1. 2A. *The Cryosphere*, 17(4), 1675–1696.
- White, L., Brisco, B., Dabboor, M., Schmitt, A., & Pratt, A. (2015). A collection of SAR methodologies for monitoring wetlands. *Remote sensing*, 7(6), 7615–7645.
- Williamson, A. G., Banwell, A. F., Willis, I. C., & Arnold, N. S. (2018). Dual-satellite (Sentinel-2 and Landsat 8) remote sensing of supraglacial lakes in Greenland. *The Cryosphere*, 12(9), 3045–3065.
- Zheng, L., Li, L., Chen, Z., He, Y., Mo, L., Chen, D., Hu, Q., Wang, L., Liang, Q., & Cheng, X. (2023). Multi-sensor imaging of winter buried lakes in the Greenland Ice Sheet. *Remote Sensing of Environment*, 295, 113688.
- Zhu, D., Zhou, C., Zhu, Y., Wang, T., & Zhang, C. (2023). Monitoring of supraglacial lake distribution and full-year changes using multisource time-series satellite imagery. *Remote Sensing*, 15(24), 5726.
- Zhu, X. J. (2005). Semi-supervised learning literature survey.
- Zwally, H. J., Abdalati, W., Herring, T., Larson, K., Saba, J., & Steffen, K. (2002). Surface melt-induced acceleration of Greenland ice-sheet flow. *Science*, 297(5579), 218–222.

6

OUTLOOK

THE research presented in this thesis is centered around a single goal: improving the mapping of surface melt on Antarctica. I examined where and when the melting occurs (Chapters 2 and 3), assessed the volume of melt (Chapter 4), and traced the pathways of meltwater lakes (Chapter 5).

Antarctic surface melt research has evolved significantly from the laborious process of spending hours processing a few satellite images for a limited region in the nineties, to the current capability of analyzing surface melt across Antarctica at a continent-wide scale within seconds. This progress is attributed to the increasing availability of remote sensing data, more powerful computer hardware, and application of deep learning techniques. However, in this “big data era”, the large volume of data presents a challenge, as having more data does not necessarily make it easier to untangle a problem.

In this chapter, I briefly describe the initial state and available tools for Antarctic surface melt research at the onset of this research (Section 6.1) and outline my contributions and the current state of the field (Section 6.2). Finally, the focus shifts to the future, with three proposed research directions that could further advance our understanding and application of surface melt mapping on Antarctica (Section 6.3).

6.1. FROM WHERE WE WERE...

Although the first meltwater detection algorithm for Antarctica is more than 30 years old (Zwally & Fiegles, 1994), meltwater detection remained a relatively low priority in the cryosphere community during the following two decades, partly due to the prevailing view that meltwater was largely confined to specific regions (Doake & Vaughan, 1991; Scambos *et al.*, 2000; Vaughan & Doake, 1996). The realization that Antarctic meltwater is widespread along the margins (Bell *et al.*, 2018; Kingslake *et al.*, 2017; Kuipers Munneke *et al.*, 2012) sparked a surge in research on Antarctic surface meltwater. Alongside the growing recognition of the extensive melt extent in Antarctica, there has also been an increasing realization of its potential impacts on ice shelf stability (Lai *et al.*, 2020), which has led to a notable rise in interest in Antarctic surface melt. According to the Web of Science, the number of annual papers on ‘Antarctica’ and ‘surface melt’ surged from fewer than 20 between 1990 and 2006 to 55 between 2007 and 2017, and then to over 100 from 2018 to 2023.

The increase in Antarctic surface melt research has been supported by a rapid rise in satellite data availability. More than half a century after the launch of the first satellite, a large number of satellites have been developed and launched, providing a vast volume of data for various applications. The number of satellites and the quality of the data they collect are continually improving. The introduction of cloud-based platforms, such as Google Earth Engine, has enabled faster and more extensive analysis of satellite data than ever before. As a clear indication of this progress, Google Earth Engine was used in more research papers between 2020 and 2022 than in the entire previous decade (Pérez-Cutillas *et al.*, 2023).

Alongside the large increase in interest in Antarctic surface melt, the availability of remote sensing data, and the emergence of cloud-based platforms for easy access to remote sensing data, deep learning has emerged as a powerful tool to improve

surface melt mapping in Antarctica. Deep neural networks enable the effective processing of large-scale remote sensing data, extraction of meaningful patterns, and accurate predictions (X. Zhu *et al.*, 2017). Especially for a complex phenomenon like surface melt, which is nonlinear and not fully understood, deep learning can offer valuable insights where conventional physical models or statistical thresholds may fall short.

6.2. ... TO WHERE WE ARE NOW

Throughout this research, I leveraged the abundance of remote sensing data, cloud computing capabilities, and deep learning techniques to enhance our understanding of surface melt in Antarctica. In Section 6.2.1, my specific contributions to the scientific community are outlined per dissertation chapter. In Section 6.2.2, I provide a broader overview of the current scientific landscape of surface meltwater in Antarctica.

6.2.1. SUMMARY OF THIS RESEARCH

Chapter 2 described a comparative analysis of four sensors and satellite missions (MODIS, Sentinel-1, ASCAT, and SSMIS) commonly utilized for melt detection in Antarctica. This study was the first Antarctic-wide assessment of these satellite datasets. This assessment revealed large discrepancies in melt detection among the sensors, sometimes leading to conflicting results. The primary contribution highlights the inadequacy of relying on a single satellite mission for accurate surface melt mapping. I pinpointed specific areas and instances where sensor discrepancies were most pronounced. Another contribution to the scientific community is an overview of four potential approaches for sensor fusion, aimed at enhancing melt detection and moving away from reliance on a single sensor for detection.

Chapter 3 introduced UMelt, a high-resolution surface melting record with multiple applications for the scientific community. The UMelt record can be used to better understand the processes leading to ice shelf instability. Additionally, since UMelt provides detailed information on surface melt occurrences at specific locations and times, it can aid in the interpretation of in-situ data such as ice cores. Finally yet importantly, UMelt can be employed to refine regional climate models by comparing modeled surface melt with UMelt data.

Chapter 4 introduced a method for downscaling surface melt from a regional climate model. The study emphasized the advantages of integrating remote sensing data into the super-resolution model, thereby enhancing the model's accuracy. Apart from downscaling surface melt, this physics-informed super-resolution approach shows potential for downscaling various other cryospheric processes, such as firn air content or basal melt. While further validation of the downscaled surface volume dataset is needed, the study highlights the potential of super-resolution techniques with physical constraints for high-resolution surface melt mapping in Antarctica, providing insights into the impacts of localized melting on processes affecting ice shelf integrity such as hydrofracturing.

In Chapter 5, a method for monitoring the development of surface lakes in Antarctica was presented, offering a first data product that enables the analysis of lake drainage on an Antarctic-wide scale. Previously, such analyses were limited to idealized scenarios or specific lakes. However, with the dataset developed in this chapter, comprehensive stability modeling studies can now be conducted on an Antarctic-wide scale. Additionally, this method helps in gaining a better understanding of where drainages occur. Although I have investigated common ice shelf properties related to lake drainages, such as thickness and stress fields, there is an opportunity to expand this analysis to encompass additional factors like firn air content, fracture density, or tidal movement.

6.2.2. WHERE THE FIELD STANDS TODAY

Over the last decades, there has been substantial progress in observing surface melt in Antarctica. In recent years, advancements in deep learning have enabled the creation of numerous new maps that track surface melt presence across the continent, allowing us to assess the diurnal cycle of meltwater at sub-kilometer resolution on an Antarctic-wide scale (de Roda Husman, Lhermitte, *et al.*, 2024; Niu *et al.*, 2023; Q. Zhu *et al.*, 2023, 2024). In addition to tracking meltwater presence, initial efforts have been made to quantify Antarctic meltwater volume at higher resolutions. These efforts include using downscaling regional climate models (de Roda Husman, Hu, *et al.*, 2024; Noël *et al.*, 2023), running regional climate models at finer resolutions (van Dalum *et al.*, 2024), and integrating remote sensing data with models of snow microstructure and snowpack layering (Banwell *et al.*, 2023). The field is clearly advancing rapidly in enhancing our mapping capabilities.

Despite these advances, a key challenge remains: assessing the exact influence of surface melt on ice shelves. To address this, we must trace the path of meltwater and establish whether it moves laterally across the ice shelf, refreezes at a certain depth within the snow, firn, or ice layers, drains to the bed, or follows a combination of these routes. Over the past few years, smaller aspects of Antarctic hydrology have been disentangled, such as understanding whether meltwater remains as slushy snow or forms meltwater lakes (Dell *et al.*, 2024), whether these lakes move laterally across the ice shelves (Dell *et al.*, 2020), or whether the water is displaced to the subsurface as a buried lake (Dunmire *et al.*, 2020) or aquifer (Di Biase *et al.*, 2024). Additionally, a preliminary attempt has been made to assess whether meltwater lakes refreeze or drain (Chapter 5). However, achieving a comprehensive understanding of meltwater hydrology and its impact on Antarctic ice shelves requires an integrated effort, combining field measurements, modeling, and remote sensing observations from scientists across various disciplines.

6.3. ... AND WHERE TO GO FROM HERE

In this section, I propose three future research directions that could advance the scientific community's understanding of surface melt and its impact on Antarctic ice shelves. Section 6.3.1 presents an approach to estimate surface melt volume using only remote sensing data. Section 6.3.2 presents a method for assessing the current

impact of meltwater lake drainage on ice shelf stability, based on observed meltwater lakes from remote sensing imagery. Finally, Section 6.3.3 explores how past ice shelf and iceberg calving could be studied using (downscaled) remote sensing imagery to better understand the sensitivity of ice shelves.

6.3.1. FROM SURFACE MELT EXTENT TO SURFACE MELT VOLUME

Remote sensing of Antarctic surface melt has traditionally been assessed more in terms of its extent rather than volume. This is due to limitations in satellite data, such as the quick saturation of signals in the presence of liquid water, making accurate quantification challenging. While binary melt products like UMelt offer valuable insights, they cannot differentiate between small and large melt quantities, which are crucial for validating regional climate models and ultimately improving our sea level rise projections. Another challenge in deriving meltwater volumes from satellite data lies in distinguishing between newly formed melt and existing liquid water. Despite appearing similar in satellite signals, it is crucial not to misinterpret existing liquid water as surface melt, as this would result in an overestimation of the total amount of meltwater produced.

Due to the limitations of assessing surface melt volumes using remote sensing, current assessments of Antarctic melt volume rely on regional climate models such as Modèle Atmosphérique Régional (MAR; Agosta *et al.*, 2019), Regional Atmospheric Climate Model (RACMO; van Wessem *et al.*, 2018), or downscaled alternatives like SUPREME (de Roda Husman, Hu, *et al.*, 2024) and RACMO 2 km (Noël *et al.*, 2023). While these melt products are validated using data from automatic weather stations, this validation is limited to specific points. An Antarctic-wide validation is only feasible when comparing regional climate models to independent data. Beyond the historical QuikSCAT melt product (Trusel *et al.*, 2013) and remote sensing products that combine remote sensing data with SNOWPACK (Banwell *et al.*, 2023), it would be valuable to develop an independent, purely remote sensing-based melt product. Such a product not only provides a valuable validation benchmark for regional climate models but also serves as a standalone resource for monitoring and understanding Antarctic melt dynamics.

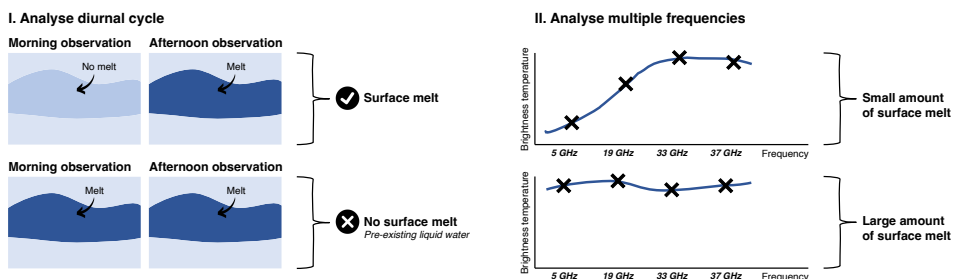


Figure 6.1: Proposed methodology for analysing melt volumes using satellite data, including: (1) analysing both morning and afternoon satellite observations, and (2) analysing multiple satellite frequencies.

In this dissertation, the detection of melt presence was based on a single frequency and time period from remote sensing data (Chapters 2 and 3). To create a remote sensing-based melt volume product, I propose a novel approach that leverages multiple remote sensing products and frequencies. Firstly, diurnal observations (from sensors such as ASCAT and SSMIS) offer insights into differentiating newly formed and pre-existing meltwater. If meltwater is pre-existing, morning and afternoon observations should be similar. Conversely, newly formed meltwater typically appears in the afternoon, allowing us to compute only the newly produced meltwater based on diurnal differences. Secondly, by comparing multiple frequencies from passive microwave data (e.g., 5, 19, 33, 37, and 85 GHz in the case of SSMIS), it might be possible to estimate meltwater volumes. The lower the frequency, the longer the wavelength, and the deeper the penetration depth. Hence, one would expect high brightness temperatures for all frequencies in the case of large meltwater accumulation and lower brightness temperatures at the low frequencies for shallower meltwater. The use of multiple frequencies to determine meltwater volumes was demonstrated by Zheng *et al.* (2022) for Greenland, utilizing a deep learning model with 19 GHz and 37 GHz passive microwave measurements. A visual representation of this proposed methodology, which uses the diurnal cycle and multiple frequencies of remote sensing data, is provided in Figure 6.1, serving as a guide for future research in this field.

6.3.2. IMPACT OF DETECTED LAKE DRAINAGES ON ICE SHELF STABILITY

Drainage events from meltwater lakes can induce flexure in the ice shelf, leading to the formation of fractures both within and beyond the lake basin. This process may trigger further drainage events and contribute to large-scale ice shelf breakup (Banwell *et al.*, 2013; Beltaos, 2002). While theoretical models (Banwell & MacAyeal, 2015; Banwell *et al.*, 2013; MacAyeal & Sergienko, 2013; MacAyeal *et al.*, 2015) and field observations in Greenland (Stevens *et al.*, 2024; Tedesco *et al.*, 2013) and Antarctica (Banwell *et al.*, 2019, 2024) have simulated and observed these effects, no study has yet examined the Antarctic-wide impact of draining lakes. Improved understanding of when and where lake drainage events occur in Antarctica is crucial for enhancing predictions of future ice shelf dynamics.

To address this gap, we propose studying the effect of lake drainages using actual, observed drainage events, for example, with the method demonstrated in Chapter 5. The impact of these drainages on ice shelves can be analyzed using a Finite Element Model (FEM). In this FEM model, the Antarctic Ice Sheet should be represented using realistic thickness data (e.g., Bedmachine; Morlighem, 2022) and strain values derived from velocity data (e.g., ITS_LIVE; Gardner *et al.*, 2019). A viscoelastic model of ice shelf flexure (MacAyeal *et al.*, 2015), assuming that total deformation is the sum of elastic and viscous components, could be used, along with thin-plate approximation formulas. To simulate the load of the lake, parameters such as area, volume, and duration of loading should be obtained (Chapter 5), along with other ice property parameters set based on laboratory experiments (e.g., Jellinek & Brill, 1956). Von Mises stresses will then be computed at the location of the lake drainage, which can be derived from Chapter 5. Values exceeding a critical threshold of 70

kPa (Albrecht & Levermann, 2012) could indicate potential fracture damage to the ice shelf.

Figure 6.2 presents a case study using parameters from MacAyeal *et al.* (2015) and data from a specific lake at the Shackleton Ice Shelf that drained in January 2020 (data from a study by Sommer *et al.*, 2024), analyzed using Ansys finite element analysis software (Madenci & Guven, 2015). An Antarctic-wide adaptation of such a FEM modeling study will provide valuable insights into the potential impacts of draining lakes on ice shelf stability. For instance, it could assess under which lake volumes and distributions the Von Mises stresses exceed the critical threshold of 70 kPa, potentially leading to ice shelf destabilization.

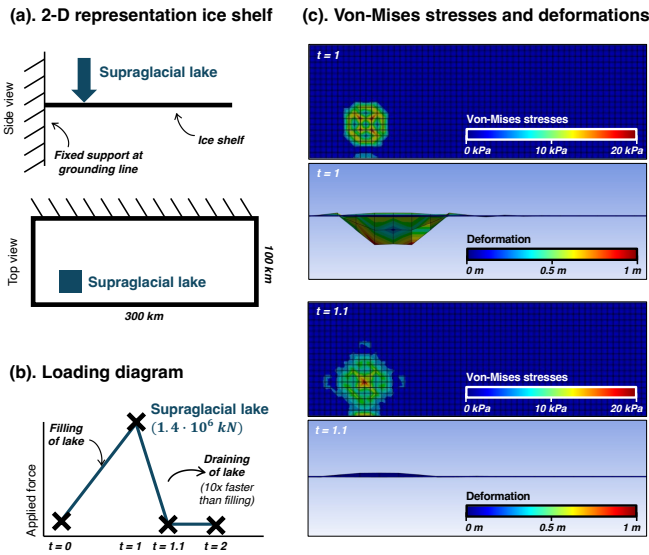


Figure 6.2: Simplistic 2-D representation of supraglacial lake loading and draining in FEM software (Ansys). (a) Simplified model of the Shackleton Ice Shelf featuring a supraglacial lake. (b) Loading diagram illustrating the filling and draining of a supraglacial lake, identified by Sommer *et al.* (2024) as the largest draining lake on the Shackleton Ice Shelf during the 2019–2020 melt season. (c) Von Mises stress and (exaggerated) deformation plots created using Ansys.

6.3.3. SENSITIVITY OF ICE SHELVES TO A CHANGING CLIMATE

To obtain the most realistic projections for sea level rise, an “ice shelf collapse forecaster” would be ideal. However, I believe creating such a forecaster is infeasible due to the complex interactions of processes. While we can now attribute the collapse of ice shelves such as Larsen B and Wilkins to a chain reaction of hydrofracturing lakes (Banwell *et al.*, 2013; Scambos *et al.*, 2009), sea ice loss, and ocean swell (Massom *et al.*, 2018), forecasting the next ice shelf collapse remains beyond our capability. Hindsight bias often makes past events seem easier to predict than future ones, leading to an overestimation of our forecasting capabilities.

Instead, a more realistic approach would be to assess the sensitivity of each ice shelf to potential causes of weakening. In recent years, we have identified several precursors and triggers of ice shelf collapse, including low firn air content (Kuipers Munneke *et al.*, 2014), hydrofracturing (Banwell *et al.*, 2013), ocean swell and reduced sea ice (Massom *et al.*, 2018), ice shelf damage (Lhermitte *et al.*, 2020) and basal melting (Pritchard *et al.*, 2012). However, we likely do not yet have a comprehensive understanding of all contributing factors.

I propose a detailed study of past iceberg calving events to gain the most comprehensive understanding possible of the factors contributing to ice shelf weakening. Although icebergs are smaller components of ice shelves, they provide a valuable source of information due to the abundance of available data. To illustrate the difference between ice shelf collapses and iceberg calving events: while there have been only a few significant ice shelf collapses in recent decades (e.g., Wordie Ice Shelf in 1989, Larsen Inlet in 1989, Prince Gustav Ice Shelf in 1995, Larsen A Ice Shelf in 1995, Larsen B Ice Shelf in 2002, Jones Ice Shelf in 2003, Wilkins Ice Shelf in 2008, and Conger Ice Shelf in 2022), the U.S. National Ice Center recorded 2688 iceberg calving events in just one year (January to December 2023). Icebergs drift northwards away from Antarctica after they calve, moving into warmer climates. The reasons for the further disintegration of icebergs can also serve as indicators of the stability of ice shelves in a warming climate. Therefore, understanding when and why these icebergs calve may help identify additional factors contributing to ice shelf instability that have yet to be recognized.

To better identify the precursors and triggers of iceberg calving and disintegration, a detailed analysis of historical satellite imagery is essential. By leveraging deep learning techniques to downscale coarse satellite images, as demonstrated in Chapter 3, we can obtain more detailed insights. Super-resolution techniques can enhance the resolution of satellite data on critical parameters such as sea ice presence, basal melt, surface melt, structural damage, and oceanic and wave conditions. Although this approach may not directly predict the next ice shelf collapse, it has the potential to uncover new triggers for ice shelf weakening. This, in turn, could improve their representation in climate models and lead to more accurate projections of sea level rise.

BIBLIOGRAPHY

- Agosta, C., Amory, C., Kittel, C., Orsi, A., Favier, V., Gallée, H., Van den Broeke, M. R., Lenaerts, J., van Wessem, J. M., Van de Berg, W. J., et al. (2019). Estimation of the Antarctic surface mass balance using the regional climate model MAR (1979–2015) and identification of dominant processes. *The Cryosphere*, 13(1), 281–296.
- Albrecht, T., & Levermann, A. (2012). Fracture field for large-scale ice dynamics. *Journal of Glaciology*, 58(207), 165–176.
- Banwell, A. F., & Macayeal, D. R. (2015). Ice-shelf fracture due to viscoelastic flexure stress induced by fill/drain cycles of supraglacial lakes. *Antarctic Science*, 27(6), 587–597.
- Banwell, A. F., MacAyeal, D. R., & Sergienko, O. V. (2013). Breakup of the Larsen B Ice Shelf triggered by chain reaction drainage of supraglacial lakes. *Geophysical Research Letters*, 40(22), 5872–5876.
- Banwell, A. F., Wever, N., Dunmire, D., & Picard, G. (2023). Quantifying Antarctic-Wide Ice-Shelf Surface Melt Volume Using Microwave and Firn Model Data: 1980 to 2021. *Geophysical Research Letters*, 50(12), e2023GL102744.
- Banwell, A. F., Willis, I. C., Macdonald, G. J., Goodsell, B., & MacAyeal, D. R. (2019). Direct measurements of ice-shelf flexure caused by surface meltwater ponding and drainage. *Nature communications*, 10(1), 1–10.
- Banwell, A. F., Willis, I. C., Stevens, L. A., Dell, R. L., & MacAyeal, D. R. (2024). Observed meltwater-induced flexure and fracture at a doline on George VI Ice Shelf, Antarctica. *Journal of Glaciology*, 1–14.
- Bell, R. E., Banwell, A. F., Trusel, L. D., & Kingslake, J. (2018). Antarctic surface hydrology and impacts on ice-sheet mass balance. *Nature Climate Change*, 8(12), 1044–1052.
- Beltaos, S. (2002). Collapse of floating ice covers under vertical loads: test data vs. theory. *Cold Regions Science and Technology*, 34(3), 191–207.
- Dell, R., Arnold, N., Willis, I., Banwell, A., Williamson, A., Pritchard, H., & Orr, A. (2020). Lateral meltwater transfer across an Antarctic ice shelf. *The Cryosphere*, 14(7), 2313–2330.
- Dell, R., Willis, I., Arnold, N., Banwell, A., & de Roda Husman, S. (2024). Substantial contribution of slush to meltwater area across Antarctic ice shelves. *Nature Geoscience*, 1–7.
- de Roda Husman, S., Hu, Z., van Tiggelen, M., Dell, R., Bolibar, J., Lhermitte, S., Wouters, B., & Kuipers Munneke, P. (2024). Physically-informed super-resolution downscaling of Antarctic surface melt. *Journal of Advances in Modeling Earth Systems*, 16(7), e2023MS004212.
- de Roda Husman, S., Lhermitte, S., Bolibar, J., Izeboud, M., Hu, Z., Shukla, S., van der Meer, M., Long, D., & Wouters, B. (2024). A high-resolution record of surface melt on Antarctic ice shelves using multi-source remote sensing data and deep learning. *Remote Sensing of Environment*, 301, 113950.
- Di Biase, V., Kuipers Munneke, P., Veldhuisen, S., de Roda Husman, S., Van den Broeke, M., Noël, B., Buth, L., & Wouters, B. (2024). Probability of firn aquifer presence

- in antarctica by combining remote sensing and regional climate model data. *Geophysical Research Letters*, 51(15), e2024GL109367.
- Doake, C., & Vaughan, D. G. (1991). Rapid disintegration of the Wordie Ice Shelf in response to atmospheric warming. *Nature*, 350(6316), 328–330.
- Dunmire, D., Lenaerts, J., Banwell, A., Wever, N., Shragge, J., Lhermitte, S., Drews, R., Pattyn, F., Hansen, J., Willis, I., et al. (2020). Observations of buried lake drainage on the Antarctic Ice Sheet. *Geophysical research letters*, 47(15), e2020GL087970.
- Gardner, A. S., Fahnestock, M. A., & Scambos, T. A. (2019). ITS_LIVE Regional Glacier and Ice Sheet Surface Velocities, version 1 [Dataset]. *National Snow and Ice Data Center*.
- Jellinek, H., & Brill, R. (1956). Viscoelastic properties of ice. *Journal of Applied Physics*, 27(10), 1198–1209.
- Kingslake, J., Ely, J. C., Das, I., & Bell, R. E. (2017). Widespread movement of meltwater onto and across Antarctic ice shelves. *Nature*, 544(7650), 349–352.
- Kuipers Munneke, P., Picard, G., Van den Broeke, M., Lenaerts, J., & Van Meijgaard, E. (2012). Insignificant change in Antarctic snowmelt volume since 1979. *Geophysical Research Letters*, 39(1).
- Kuipers Munneke, P., Ligtenberg, S. R., Van den Broeke, M. R., & Vaughan, D. G. (2014). Firn air depletion as a precursor of antarctic ice-shelf collapse. *Journal of Glaciology*, 60(220), 205–214.
- Lai, C.-Y., Kingslake, J., Wearing, M. G., Chen, P.-H. C., Gentine, P., Li, H., Spergel, J. J., & van Wessem, J. M. (2020). Vulnerability of Antarctica's ice shelves to meltwater-driven fracture. *Nature*, 584(7822), 574–578.
- Lhermitte, S., Sun, S., Shuman, C., Wouters, B., Pattyn, F., Wuite, J., Berthier, E., & Nagler, T. (2020). Damage accelerates ice shelf instability and mass loss in Amundsen Sea Embayment. *Proceedings of the National Academy of Sciences*, 117(40), 24735–24741.
- MacAyeal, D. R., & Sergienko, O. V. (2013). The flexural dynamics of melting ice shelves. *Annals of Glaciology*, 54(63), 1–10.
- MacAyeal, D. R., Sergienko, O. V., & Banwell, A. F. (2015). A model of viscoelastic ice-shelf flexure. *Journal of Glaciology*, 61(228), 635–645.
- Madenci, E., & Guven, I. (2015). *The finite element method and applications in engineering using ANSYS®*. Springer.
- Massom, R. A., Scambos, T. A., Bennetts, L. G., Reid, P., Squire, V. A., & Stammerjohn, S. E. (2018). Antarctic ice shelf disintegration triggered by sea ice loss and ocean swell. *Nature*, 558(7710), 383–389.
- Morlighem, M. (2022). Measures BedMachine Antarctica, version 3 [Dataset]. *NASA Nat. Snow Ice Data Center Distrib. Active Arch. Center, Boulder, CO, USA, Tech. Rep.*
- Niu, L., Tang, X., Yang, S., Zhang, Y., Zheng, L., & Wang, L. (2023). Detection of Antarctic surface meltwater using sentinel-2 remote sensing images via U-net with attention blocks: A case study over the amery ice shelf. *IEEE Transactions on Geoscience and Remote Sensing*, 61, 1–13.
- Noël, B., van Wessem, J. M., Wouters, B., Trusel, L., Lhermitte, S., & Van den Broeke, M. R. (2023). Higher Antarctic ice sheet accumulation and surface melt rates revealed at 2 km resolution. *Nature Communications*, 14(1), 7949.
- Pérez-Cutillas, P., Pérez-Navarro, A., Conesa-García, C., Zema, D. A., & Amado-Álvarez, J. P. (2023). What is going on within Google Earth Engine? A systematic review and meta-analysis. *Remote sensing applications: Society and environment*, 29, 100907.
- Pritchard, H., Ligtenberg, S. R., Fricker, H. A., Vaughan, D. G., Van den Broeke, M. R., & Padman, L. (2012). Antarctic ice-sheet loss driven by basal melting of ice shelves. *Nature*, 484(7395), 502–505.

- Scambos, T. A., Fricker, H. A., Liu, C.-C., Bohlander, J., Fastook, J., Sargent, A., Massom, R., & Wu, A.-M. (2009). Ice shelf disintegration by plate bending and hydro-fracture: Satellite observations and model results of the 2008 Wilkins ice shelf break-ups. *Earth and Planetary Science Letters*, 280(1-4), 51–60.
- Scambos, T. A., Hulbe, C., Fahnestock, M., & Bohlander, J. (2000). The link between climate warming and break-up of ice shelves in the Antarctic Peninsula. *Journal of Glaciology*, 46(154), 516–530.
- Sommer, J., Izeboud, M., de Roda Husman, S., Wouters, B., & Lhermitte, S. (2024). Brief Communications: Tides and Damage as Drivers of Lake Drainages on Shackleton Ice Shelf.
- Stevens, L. A., Das, S. B., Behn, M. D., McGuire, J. J., Lai, C.-Y., Joughin, I., Larochelle, S., & Nettles, M. (2024). Elastic stress coupling between supraglacial lakes. *Journal of Geophysical Research: Earth Surface*, 129(5), e2023JF007481.
- Tedesco, M., Willis, I. C., Hoffman, M. J., Banwell, A. F., Alexander, P., & Arnold, N. S. (2013). Ice dynamic response to two modes of surface lake drainage on the Greenland ice sheet. *Environmental Research Letters*, 8(3), 034007.
- Trusel, L., Frey, K. E., Das, S. B., Kuipers Munneke, P., & Van den Broeke, M. (2013). Satellite-based estimates of Antarctic surface meltwater fluxes. *Geophysical Research Letters*, 40(23), 6148–6153.
- van Dalum, C. T., Van de Berg, W. J., Gadde, S. N., van Tiggelen, M., van der Drift, T., van Meijgaard, E., van Uft, L. H., & Van den Broeke, M. R. (2024). First results of the polar regional climate model RACMO2.4. *EGUsphere*, 2024, 1–36.
- van Wessem, J. M., Van de Berg, W. J., Noël, B. P., Van Meijgaard, E., Amory, C., Birnbaum, G., Jakobs, C. L., Krüger, K., Lenaerts, J., Lhermitte, S., et al. (2018). Modelling the climate and surface mass balance of polar ice sheets using RACMO2–Part 2: Antarctica (1979–2016). *The Cryosphere*, 12(4), 1479–1498.
- Vaughan, D. G., & Doake, C. S. (1996). Recent atmospheric warming and retreat of ice shelves on the Antarctic Peninsula. *Nature*, 379(6563), 328–331.
- Zheng, L., Cheng, X., Shang, X., Chen, Z., Liang, Q., & Wang, K. (2022). Greenland Ice Sheet daily surface melt flux observed from space. *Geophysical Research Letters*, 49(6), e2021GL096690.
- Zhu, Q., Guo, H., Zhang, L., Liang, D., Liu, X., Zhou, H., & Gou, Y. (2023). High-resolution spatio-temporal analysis of snowmelt over Antarctic Peninsula ice shelves from 2015 to 2021 using SAR images. *International Journal of Digital Earth*, 16(1), 825–846.
- Zhu, Q., Guo, H., Zhang, L., Liang, D., Wu, Z., de Roda Husman, S., & Du, X. (2024). Automated surface melt detection over the Antarctic from Sentinel-1 imagery using deep learning. *International Journal of Applied Earth Observation and Geoinformation*, 130, 103895.
- Zhu, X., Tuia, D., Mou, L., Xia, G.-S., Zhang, L., Xu, F., & Fraundorfer, F. (2017). Deep learning in remote sensing: A comprehensive review and list of resources. *IEEE geoscience and remote sensing magazine*, 5(4), 8–36.
- Zwally, H. J., & Fiegles, S. (1994). Extent and duration of Antarctic surface melting. *Journal of Glaciology*, 40(136), 463–475.

CODE AND DATA AVAILABILITY

UMELT RESOURCES

SCRIPTS

The scripts used to develop UMelt are available on [GitHub](#).

DAILY DATA RECORD

The UMelt daily data record includes morning (6 AM) and afternoon (6 PM) observations at a 500 m spatial resolution for melt seasons from 2016–2021.

- **GeoTIFF files:** Available via [4TU.ResearchData](#).
- **Google Earth Engine assets:** Use the following link format: `https://code.earthengine.google.com/?asset=projects/phd-detectionsurfacemelt/assets/UMelt_Antarctica/MeltSeasonXXXX/UMelt_AllData_MeltSeasonXXXX`
Replace XXXX with the desired melt season (e.g., 1617 for 2016–2017). Example scripts are available on [GitHub](#).

YEARLY DATA RECORD

Yearly melt occurrence data for individual seasons are also accessible:

- **GeoTIFF files:** Available via [4TU.ResearchData](#).
- **Google Earth Engine assets:** Use the following link format: `https://code.earthengine.google.com/?asset=projects/phd-detectionsurfacemelt/assets/UMelt_Antarctica/MeltSeasonXXXX/UMelt_MeltFraction_MeltSeasonXXXX`
Replace XXXX with the desired melt season (e.g., 1617 for 2016–2017). Example scripts are available on [GitHub](#).

INTERACTIVE TOOL

An interactive tool to explore the presence of surface melt anywhere in Antarctica on a specific day or during a melt season is available as a [Google Earth Engine application](#).

SUPREME RESOURCES

SCRIPTS

The scripts used to develop SUPREME are available on [GitHub](#).

YEARLY DATA RECORD

A record of surface melt (in millimeters water equivalent per year) on an Antarctic-wide scale. It offers surface melt data at a spatial resolution of 5.5 kilometers for each melt year (1 July - 30 June), covering the period from 2001 to 2019.

- **GeoTIFF files:** Available via [4TU.ResearchData](#).

SILAKENET RESOURCES

SCRIPTS

The scripts used to develop the data products in Chapter 5 are available on [GitHub](#).

The product is still under development, so as of the end of 2024, the data has not yet been stored at [4TU.ResearchData](#) or any other repository.

LIST OF PUBLICATIONS

PUBLICATIONS

- **de Roda Husman, S.**, Hu, Z., van Tiggelen, M., Dell, R., Bolibar, J., Lhermitte, S., Wouters, B., & Kuipers Munneke, P. (2024). Physically-informed super-resolution downscaling of Antarctic surface melt. *Journal of Advances in Modeling Earth Systems*. <https://doi.org/10.1029/2023MS004212>
- Di Biase, V., Kuipers Munneke, P., Veldhuijsen, S.B.M., **de Roda Husman, S.**, van den Broeke, M.R., Noël, B., Buth, L.G., Wouters, B. (2024). Probability of firn aquifer presence in Antarctica by combining remote sensing and regional climate model data. *Geophysical Research Letters*. <https://doi.org/10.1029/2024GL109367>
- Shukla, S., Wouters, B., Picard, G., Wever, N., Izeboud, M., **de Roda Husman, S.**, Kausch, T., Veldhuijsen, S., Mätzler, C., & Lhermitte, S. (2024). Large variability in dominant scattering from Sentinel-1 SAR in East Antarctica: challenges and opportunities. *IEEE Journal of Selected Topics in Applied Earth Observations and Remote Sensing*. <https://doi.org/10.1109/JSTARS.2024.3438233>
- Dell, R., Willis, I. C., Arnold, N., Banwell, A., & **de Roda Husman, S.** (2024). Substantial contribution of slush to meltwater area across Antarctic ice shelves. *Nature Geoscience*. <https://doi.org/10.1038/s41561-024-01466-6>
- Zhu, Q., Guo, H., Zhang, L., Liang, D., Wu, Z., **de Roda Husman, S.**, & Du, X. (2024). Automated surface melt detection over the Antarctic from Sentinel-1 imagery using deep learning. *International Journal of Applied Earth Observation and Geoinformation*. <https://doi.org/10.1016/j.jag.2024.103895>
- The Firn Symposium team (2024). Firn on ice sheets. *Nature Reviews Earth & Environment*. <https://doi.org/10.1038/s43017-023-00507-9>
- **de Roda Husman, S.**, Lhermitte, S., Bolibar, J., Izeboud, M., Hu, Z., Shukla, S., van der Meer, M., Long, D., & Wouters, B. (2024). A high-resolution record of surface melt on Antarctic ice shelves using multi-source remote sensing data and deep learning. *Remote Sensing of Environment*. <https://doi.org/10.1016/j.rse.2023.113950> **Best Climate Action Paper 2023, TU Delft.**
- van der Meer, M., **de Roda Husman, S.**, & Lhermitte, S. (2023). Deep learning regional climate model emulators: A comparison of two downscaling training frameworks. *Journal of Advances in Modeling Earth Systems*. <https://doi.org/10.1029/2022MS003593>
- **de Roda Husman, S.**, Hu, Z., Wouters, B., Kuipers Munneke, P., Veldhuijsen, S., & Lhermitte, S. (2022). Remote sensing of surface melt on Antarctica: opportunities and challenges. *IEEE Journal of Selected Topics in Applied Earth Observations and Remote Sensing*. <https://doi.org/10.1109/JSTARS.2022.3216953>

- **de Roda Husman, S.**, van der Sanden, J.J., Lhermitte, S. & Eleveld, M.A. (2021). Integrating intensity and context for improved supervised river ice classification from dual-pol Sentinel-1 SAR data. *International Journal of Applied Earth Observation and Geoinformation*. <https://doi.org/10.1016/j.jag.2021.102359>

UNDER REVIEW

- Izeboud, M., Lhermitte, S., **de Roda Husman, S.**, & Wouters, B. (2024). Antarctic ice shelves vulnerable to damage in future climate warming. *Nature Climate Change*.
- Sommer, J., Izeboud, M. **de Roda Husman, S.**, Wouters, B., & Lhermitte, S. (2024). Brief communications: Tides and damage as drivers of lake drainages on Shackleton Ice Shelf. *EGUsphere [preprint]*.
- Nicola, L., Frøystad, R., Juarez-Martinez, A., Menthon, M., Moraes Luzardi, A. C., Turner, K. A., Wilson, S. F., Karlsson, N. B., van den Akker, T., Ambelorun, A., Andernach, M., Bentley, M. J., Bianchi, G., Bird, L., Carter, C., Castillo-Llarena, A., Coffey, N., Dawson, E., **de Roda Husman, S.**, ... Keisling, B. (2024). Where do we want the glaciology community to be in 2073? EDI challenges and visions from the 2023 Karthaus Summer School. *Journal of Glaciology*.
- Buth, L. G., Di Biase, V., Kuipers Munneke, P., Lhermitte, S., Veldhuijsen, S. B., **de Roda Husman, S.**, van den Broeke, M. R., & Wouters, B. (2023). Sentinel-1 detection of perennial firn aquifers in the Antarctic Peninsula. *EGUsphere [preprint]*.

CONFERENCE CONTRIBUTIONS

ORAL PRESENTATIONS

- Shukla, S., Wouters, B., Picard, G., Wever, N., Izeboud, M., **de Roda Husman, S.**, Kausch, T., Veldhuijsen, S., Matzler, C., & Lhermitte, S. (2024, May). Sentinel-1 reveals large variability of dominant scattering in a drifting snow-dominated environment of East Antarctica. *EGU General Assembly 2024*, Vienna, Austria.
- **de Roda Husman, S.**, Lhermitte, S., Bolibar, J., Izeboud, M., Hu, Z., Shukla, S., van der Meer, M., Long, D.G., & Wouters, B. (2023, December). UMelt: A novel high-resolution record of surface melt on Antarctic ice shelves. *AGU Fall Meeting, December*. San Francisco, United States of America. **Outstanding student presentation award.**
- **de Roda Husman, S.**, Hu, Z., Kuipers Munneke, P., van Tiggelen, M., Lhermitte, S., & Wouters, B. (2023, April). The added value of remote sensing data in downscaling regional climate models. *EGU General Assembly 2023*, Vienna, Austria.
- Di Biase, V., Kuipers Munneke, P., Wouters, B., & **de Roda Husman, S.** (2023, April). Antarctic firn aquifers detection algorithm based on satellite and regional climate model data. *EGU General Assembly 2023*, Vienna, Austria.
- Lhermitte, S., Wouters, B., & **HiRISE team**. (2023, April). The triggers for Conger Ice Shelf demise: Long-term weakening vs. short-term collapse. *EGU General Assembly 2023*, Vienna, Austria.
- **de Roda Husman, S.**, Hu, Z., Lhermitte, S., Wouters, B., Veldhuijsen, S., & Kuipers Munneke, P. (2022, September). Zooming in on Antarctic surface melt from space. *Forum for Research of Ice Shelf Processes meeting, FRISP*, New Castle, United Kingdom.
- **de Roda Husman, S.**, Lhermitte, S., & Wouters, B. (2022, May). Zooming in on Antarctic Surface Melt from Space. *Poolsymposium*, Den Haag, The Netherlands.
- **de Roda Husman, S.**, Lhermitte, S., & Wouters, B. (2022, May). Remote sensing of surface melt on Antarctica: Opportunities and challenges. *International Firn Workshop*, Online.
- **de Roda Husman, S.**, Hu, Z., Lhermitte, S., Wouters, B., & Kuipers Munneke, P. (2022, May). Earth Observation for surface melt monitoring over Antarctic ice shelves: Opportunities and challenges. *EGU General Assembly 2022*, Online.
- **de Roda Husman, S.**, Lhermitte, S., & Wouters, B. (2021, December). Towards improved spatio-temporal resolution surface meltwater detection on the Antarctic ice shelves from the synergy of active and passive microwave remote sensing. *AGU Fall Meeting 2021*, Online.

POSTER PRESENTATIONS

- **de Roda Husman, S.**, Lhermitte, S., Psomouli, T., van Noord, M., Bambler, J., Zhu, X.X., & Wouters, B. (2024, April). Draining or refreezing? Investigating meltwater lake evolution through deep learning. *EGU General Assembly 2024*, Vienna, Austria.
- Di Biase, V., Kuipers Munneke, P., **de Roda Husman, S.**, Veldhuijsen, S., van den Broeke, M., Wouters, B., & Noël, B. (2024, April). Firn aquifers in Antarctica: High-resolution mapping highlights predominance in the Antarctic Peninsula. *EGU General Assembly 2024*, Vienna, Austria.
- **de Roda Husman, S.**, Lhermitte, S., Psomouli, T., van Noord, M., Bambler, J., Zhu, X.X., & Wouters, B. (2024, February). Draining or refreezing? A spatiotemporal deep learning model using Sentinel-1 for tracking meltwater lake evolution in Antarctica. *AI4EO Winter School*, Biberwier, Austria.

CONVENER

- Session: Hydrology of ice sheets, ice shelves and glaciers (2024, April). Convener: Hewitt, I., Co-conveners: Racz, G.C., Banwell, A., **de Roda Husman, S.**, & Buzzard, S. (2024, May). *EGU General Assembly 2024*, Vienna, Austria.
- Session: Measuring firn properties remotely (2022, May). Conveners: Simonsen, S., & **de Roda Husman, S.** (2022, May). *International Firn Workshop*, Online.

MEDIA COVERAGE

NEWSPAPERS, MAGAZINES, AND BLOGS

- Zeespiegelstijging door smeltend Antarctica (2024, November). **Geo.brief**. [Link](#)
- Zoveel meter stijgt de zeespiegel als de Zuidpool smelt (2024, November). **Algemeen Dagblad**. [Link](#)
- Delftse onderzoeker weet smeltgat in klimaatmodellen te verkleinen (2024, April). **EW Magazine**. [Link](#)
- Slapende reus Antarctica smelt (2024, March). **Telegraaf & Dagblad van het Noorden**. [Link](#)
- The giant awakens: a high-resolution record of Antarctic surface melting (2024, March). **Stories of Science, TU Delft**. [Link](#)
- The IPCC report also has something positive (2023, March). **Delta, TU Delft**. [Link](#)
- Copernicus Sentinels help classify river ice (2020, May). **Sentinel Success Stories, European Space Agency**. [Link](#)

VIDEO, RADIO, AND PODCASTS

- We dachten dat de Zuidpool nooit zou smelten, totdat... (2024, November). **De Universiteit van Nederland**. [Link video](#), [Link podcast](#)
- Hoe smeltmeertjes het afbreken van ijsplaten versnellen (2024, March). **Wetenschap Vandaag, BNR Nieuwsradio**. [Link](#)
- Radio interview (2024, March). **Omroep Delft**.

SOCIAL MEDIA

- Twitter take-over week (2023, March). **@NL_Wetenschap**. [Link](#)
- Educational TikTok account **@Zuidpool_Sophie**. [Link](#)

CURRICULUM VITAE

Sophie DE RODA HUSMAN



Besides climate research, here is a short list of things I like: pretty data visualizations, camping, handstands, hiking in the mountains, eggplants and all Ottolenghi dishes, tapas, podcasts, board games, arthouse cinemas, thyme tea, mosaics, and cava/prosecco/champagne (everything bubbly).

| | |
|------------|--|
| 2021–2024 | Ph.D. in Geoscience & Remote Sensing Delft University of Technology, The Netherlands |
| 2024 | Research Fellowship in Artificial Intelligence Technical University of Munich, Germany |
| 2017–2020 | M.Sc. in Geoscience & Remote Sensing Delft University of Technology, The Netherlands |
| 2016–2017 | Minor in Civil Engineering Technical University of Madrid, Spain |
| 2013–2017 | B.Sc. in Civil Engineering Delft University of Technology, The Netherlands |
| 2007–2013 | High School Het Amsterdams Lyceum, The Netherlands |
| 04–12–1994 | Born in Amsterdam, the Netherlands |